molecules

Special Issue Reprint

Advances in Molecular Modeling in Chemistry, 2nd Edition

Edited by
Heng Zhang and Shiling Yuan

mdpi.com/journal/molecules

MDPI

Advances in Molecular Modeling in Chemistry, 2nd Edition

Advances in Molecular Modeling in Chemistry, 2nd Edition

Guest Editors

Heng Zhang
Shiling Yuan

MDPI

Basel • Beijing • Wuhan • Barcelona • Belgrade • Novi Sad • Cluj • Manchester

Guest Editors

Heng Zhang
School of Chemistry and Chemical Engineering
Shandong University
Jinan
China

Shiling Yuan
School of Chemistry and Chemical Engineering
Shandong University
Jinan
China

Editorial Office
MDPI AG
Grosspeteranlage 5
4052 Basel, Switzerland

This is a reprint of the Special Issue, published open access by the journal *Molecules* (ISSN 1420-3049), freely accessible at: https://www.mdpi.com/journal/molecules/special_issues/U093E8X113.

For citation purposes, cite each article independently as indicated on the article page online and as indicated below:

Lastname, A.A.; Lastname, B.B. Article Title. *Journal Name* **Year**, *Volume Number*, Page Range.

ISBN 978-3-7258-6398-3 (Hbk)
ISBN 978-3-7258-6399-0 (PDF)
https://doi.org/10.3390/books978-3-7258-6399-0

Contents

About the Editors

Heng Zhang

Heng Zhang is a Senior Experimentalist and Master's Supervisor at the School of Chemistry and Chemical Engineering, Shandong University. He earned his Ph.D. in Physical Chemistry from Shandong University in 2022, following earlier M.E. (Chemical Engineering) and B.S. (Chemistry) degrees from the same institution. His research focuses on molecular simulation, with applications in petroleum chemistry, environmental interfaces, antifouling materials, and chemical education.

Shiling Yuan

Shiling Yuan is a professor and doctoral supervisor at the School of Chemistry and Chemical Engineering, Shandong University. He earned his B.S. in Analytical Chemistry from the Shandong Institute of Building Materials (1993), his M.S. in Colloid Chemistry under Prof. Guiying Xu (1998), and his Ph.D. in Theoretical Chemistry under Academician Yuansheng Jiang (2003) from Shandong University. His research integrates molecular simulation with experimental studies, focusing on colloid and interface science, oilfield chemistry, biomolecular systems, and electrochemical energy storage.

molecules

MDPI

Article

Mechanistic Study of Oil Adsorption Behavior and CO_2 Displacement Mechanism Under Different pH Conditions

Xinwang Song [1], Yang Guo [1], Yanchang Chen [1] and Shiling Yuan [1,2,*]

[1] Shandong Key Laboratory of Green Electricity & Hydrogen Science and Technology, School of Chemical Engineering, Shandong Institute of Petroleum and Chemical Technology, Dongying 257061, China; 2022126@sdipct.edu.cn (X.S.); cumt-guoyang@cumt.edu.cn (Y.G.); chenyanchang@sdipct.edu.cn (Y.C.)
[2] School of Chemistry and Chemical Engineering, Shandong University, Jinan 250100, China
* Correspondence: shilingyuan@sdu.edu.cn

Abstract: Enhanced oil recovery (EOR) via CO_2 flooding is a promising strategy for improving hydrocarbon recovery and carbon sequestration, yet the influence of pH on solid–liquid interfacial interactions in quartz-dominated reservoirs remains poorly understood. This study employs molecular dynamics (MD) simulations to investigate the pH-dependent adsorption behavior of crude oil components on quartz surfaces and its impact on CO_2 displacement mechanisms. Three quartz surface models with varying ionization degrees (0%, 9%, 18%, corresponding to pH 2–4, 5–7, and 7–9) were constructed to simulate different pH environments. The MD results reveal that aromatic hydrocarbons exhibit significantly stronger adsorption on quartz surfaces at high pH, with their maximum adsorption peak increasing from 398 kg/m^3 (pH 2–4) to 778 kg/m^3 (pH 7–9), while their alkane adsorption peaks decrease from 764 kg/m^3 to 460 kg/m^3. This pH-dependent behavior is attributed to enhanced cation–π interactions that are facilitated by Na^+ ion aggregation on negatively charged quartz surfaces at high pH, which form stable tetrahedral configurations with aromatic molecules and surface oxygen ions. During CO_2 displacement, an adsorption–stripping–displacement mechanism was observed: CO_2 first forms an adsorption layer on the quartz surface, then penetrates the oil phase to induce the detachment of crude oil components, which are subsequently displaced by pressure. Although high pH enhances the Na^+-mediated weakening of oil-surface interactions, which leads to a 37% higher diffusion coefficient (8.5×10^{-5} cm^2/s vs. 6.2×10^{-5} cm^2/s at low pH), the tighter packing of aromatic molecules at high pH slows down the displacement rate. This study provides molecular-level insights into pH-regulated adsorption and CO_2 displacement processes, highlighting the critical role of the surface charge and cation–π interactions in optimizing CO_2-EOR strategies for quartz-rich reservoirs.

Keywords: oil adsorption behavior; CO_2 flooding; pH effect; molecular dynamics simulation; quartz surface; interfacial interactions

1. Introduction

The increasing global demand for energy has led to a growing interest in enhancing the efficiency of hydrocarbon recovery from subsurface reservoirs [1]. Conventional primary and secondary recovery methods often leave a significant fraction of hydrocarbons trapped within the porous rock matrix, which necessitates the development and optimization of tertiary recovery techniques, which are collectively known as enhanced oil recovery (EOR) methods [2–4]. Among the various EOR strategies, carbon dioxide (CO_2) flooding has emerged as a promising approach due to its potential to improve oil mobility,

reduce reservoir pressure, and contribute to carbon sequestration efforts [5–7]. Despite the technological advancements in CO_2-EOR, the intricate physicochemical interactions at the solid–liquid interface, particularly in heterogeneous reservoir environments, remain inadequately understood [8–10]. Such interactions are critical in determining the ultimate recovery efficiency of this method, especially in formations with considerable mineral compositions such as quartz.

Quartz, as a predominant component in many sandstone reservoirs, provides a chemically active surface that can interact with crude oil components [11–14]. The adsorption behavior of oil constituents on mineral surfaces can significantly influence oil displacement processes [15,16]. Adsorption not only alters the wettability of the rock but also dictates the extent of oil entrapment and mobilization during EOR operations. Previous experimental and theoretical studies have highlighted that the chemical composition of crude oil, especially its content of polar and aromatic molecules, plays a pivotal role in its interfacial interactions with reservoir minerals [17–20]. However, the effect of environmental conditions, particularly pH, on these interactions and the subsequent CO_2 flooding performance remains poorly characterized. Under different pH conditions, the quartz surface undergoes protonation or deprotonation, which leads to variations in the surface hydrophilicity and charge density. At low pH, the protonation of Si-OH groups reduces the surface charge, while at high pH, deprotonation enhances the negative surface charge, potentially strengthening interactions with polar or aromatic oil components [21,22]. These complex interplays suggest that pH could serve as a critical control factor in tailoring the efficiency of CO_2-driven oil recovery processes. Nevertheless, direct experimental investigations into these phenomena are challenging due to the nanoscale nature of the interactions and the complexity of real reservoir conditions.

Molecular dynamics (MD) simulations offer a powerful computational tool to unravel molecular-level mechanisms that govern adsorption and displacement phenomena at mineral–fluid interfaces. Kirch et al. combined molecular dynamics simulations and machine learning to predict oil–brine interfacial tensions, highlighting the dominant roles of oil properties and salinity [23]. Xue and colleagues used MD simulations to investigate CO_2–octane displacement and miscibility in calcite nanoslits, revealing strong CO_2–calcite interactions that enhance oil recovery and CO_2 sequestration [24]. Lu and colleagues combined microscopic visualization experiments and MD simulations to reveal how hybrid CO_2 thermal systems decompose heavy oil aggregates, enhance oil recovery, and optimize gas/steam ratios for improved EOR performance [25]. Wang et al. used molecular dynamics simulations with modified combination rules to study the phase behavior and interfacial properties of CO_2+n–decane systems, revealing that CO_2-preferential adsorption in quartz nanopores enhances oil displacement and influences molecular diffusion [26]. The motivation for this study stems from the need to elucidate the pH-dependent adsorption behavior of crude oil on quartz surfaces and its impact on CO_2-EOR efficiency. While experimental studies have provided valuable insights into macroscopic EOR performance, they often lack the resolution to capture molecular-scale phenomena.

In this study, MD simulations were employed to investigate the adsorption behavior of crude oil components on quartz surfaces under different pH environments and to evaluate the influence of these interactions on subsequent CO_2 displacement processes (Figure 1). Specifically, the distribution of crude oil within silica slits under different environmental conditions, as well as the occurrence states of various crude oil molecules on quartz surfaces, were investigated. Subsequently, the mechanisms of interaction between CO_2 and crude oil in tight reservoirs and their effects on the miscibility behavior of the CO_2 were summarized, and the miscibility and displacement mechanisms of CO_2 molecules were examined in

detail. Finally, the kinetic parameters of crude oil components during the displacement process under different pH conditions were evaluated.

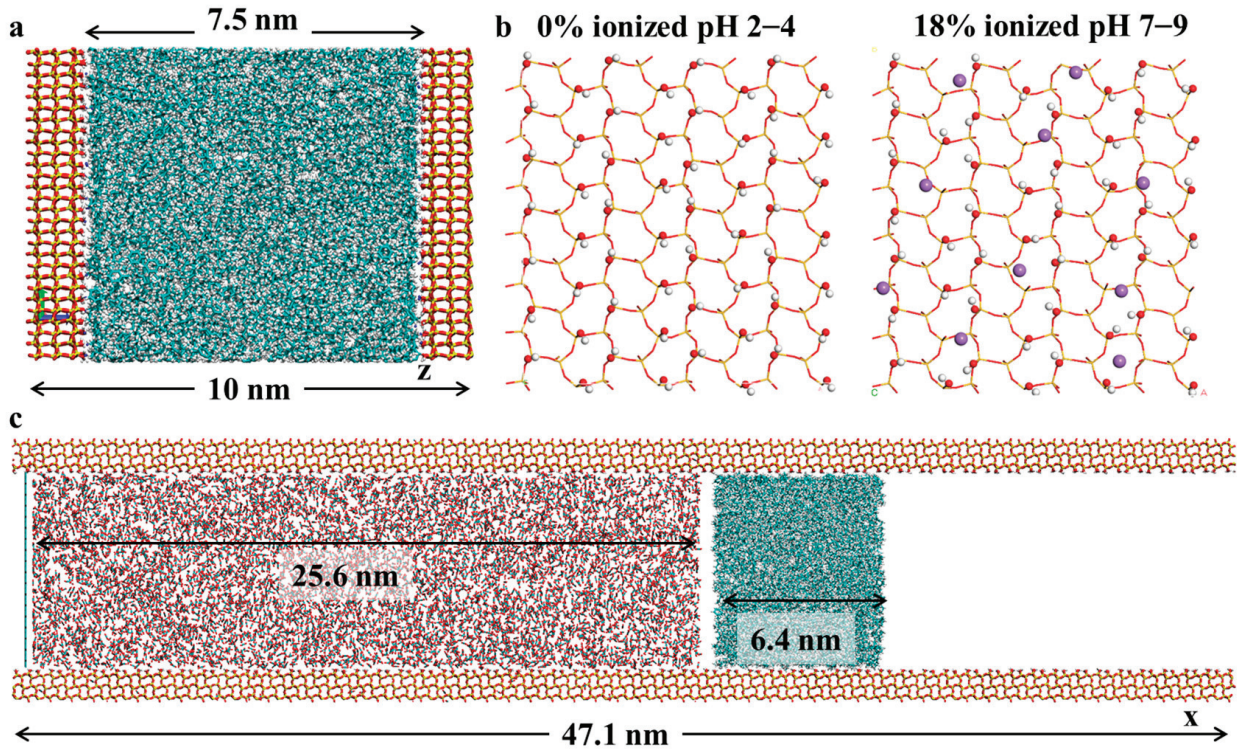

Figure 1. (**a**) Initial model of light crude oil adsorption on the silica surface. (**b**) Silica surface models under different pH conditions. (**c**) Initial structure of the CO_2 flooding model. Yellow, purple, red, cyan, and white spheres represent Si, Na, O, C, and H atoms, respectively.

2. Results and Discussion

2.1. Distribution of Crude Oil Within Silica Slits

In this section, the distribution states of different types of crude oil molecules within quartz pores under various pH conditions were first investigated. At the start of our molecular dynamics simulations, the hydrocarbon molecules were randomly and homogeneously distributed within the pore space between the quartz surfaces. Figure 2a presents the final equilibrium results after sufficient simulation time. The snapshots from molecular dynamics simulations shown in Figure 2a revealed that alkanes, cycloalkanes, and aromatics were mainly distributed in two regions within the quartz pores: the bulk region and the surface region [27,28]. In the bulk region, these molecules were freely dispersed, exhibiting a high tendency for diffusion. In contrast, near the surface, significant interactions between the molecules and the quartz surface were observed, and these were characterized by stronger adsorption behavior and reduced diffusion tendencies. To further quantify the distribution of crude oil molecules within the quartz slits, the density profiles along the z-direction were calculated, as presented in Figure 2b–d. Overall, the distribution of crude oil molecules in the bulk region of the quartz slit appeared relatively uniform, being primarily concentrated within the range of 2.3–7.4 nm, approximately 1.5 nm away from the quartz surfaces. At the quartz surfaces, pronounced adsorption peaks were observed for all types of crude oil molecules. Specifically, the alkanes formed two distinct adsorption layers at the quartz surface, which indicated relatively strong interactions with the surface. In contrast, the cycloalkanes and aromatics each formed a single, tightly adsorbed layer, which highlighted differences in the surface adsorption behavior among the different molecular types. A comparison of the adsorption behaviors under different pH conditions revealed

that the distribution of crude oil molecules in the bulk region remained relatively stable as the pH increased, with the densities of the alkanes, cycloalkanes, and aromatics in the bulk region being maintained at approximately 467 kg/m^3, 148 kg/m^3, and 65 kg/m^3, respectively. However, the adsorption behavior at the quartz surface was significantly affected by the pH. As the pH increased, the adsorption peaks of the alkanes at the quartz surface gradually decreased, while those of the aromatics progressively increased. Specifically, the maximum adsorption peak for the alkanes at the quartz surface decreased from 764 kg/m^3 to 460 kg/m^3, whereas the maximum adsorption peak for the aromatics increased from 398 kg/m^3 to 778 kg/m^3. These results demonstrate that pH markedly influences the adsorption characteristics of various crude oil components on quartz surfaces.

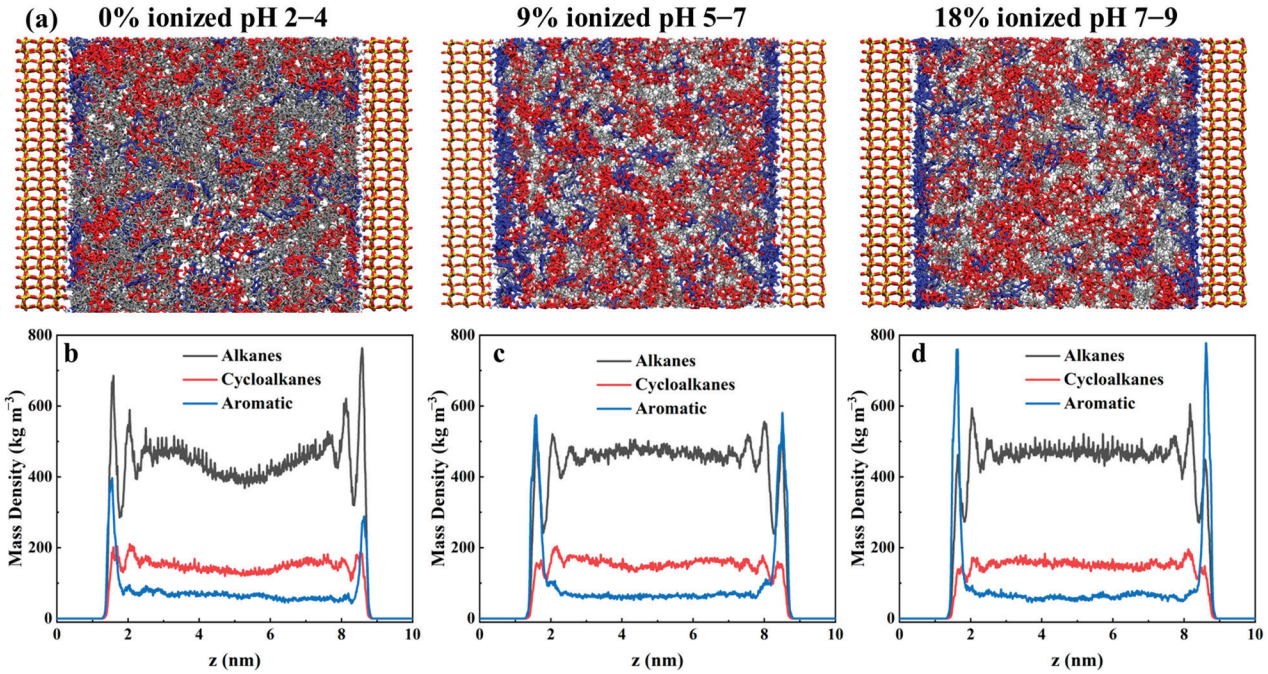

Figure 2. (**a**) Snapshots of the distribution of crude oil molecules within quartz pores under different pH conditions. To distinguish different types of crude oil molecules, alkanes are colored gray, cycloalkanes are colored red, and aromatics are colored blue. Density distributions of various crude oil molecules within the quartz pores under (**b**) pH 2–4, (**c**) pH 5–7, and (**d**) pH 7–9 conditions.

The surface adsorption behavior of crude oil, which determines its release and flow characteristics in reservoirs, was directly linked to the recoverability and ultimate recovery rate of the crude oil in the reservoir [29,30]. Therefore, the occurrence of different crude oil molecules on quartz surfaces is quantitatively investigated in this section. As shown in Figure 1, three crude oil components (alkanes, cycloalkanes, and aromatic hydrocarbons) were observed to reside on the quartz surface. To further elucidate their behavior on the quartz surface, the contact area proportions of these three components with the quartz surface were calculated under various pH conditions (Figure 3a). It was found through quantitative analysis that the surface contact behavior of these molecules was significantly influenced by different pH environments. A higher contact area with the quartz surface (40.7%) was exhibited by the alkane molecules under low-pH conditions, which was significantly reduced (to 15.8%) under high-pH conditions. A consistent decrease in the surface contact area (from 15.8% to 11.5%) was also observed for the cycloalkane molecules as the pH increased. Conversely, a marked increase in the surface contact area (from 22.7% to 47.8%) was noted for the aromatic hydrocarbon molecules under high-pH conditions, which indicates that stronger interactions with the quartz surface were facilitated in alkaline

environments. It was also suggested that aromatic hydrocarbon molecules in the confined oil layers displaced alkane and cycloalkane molecules as the environmental pH increased. This intermolecular substitution effect was found to alter not only the adsorption properties of the quartz surface but also potentially the overall reservoir development strategies. To provide a more intuitive representation of the distribution of aromatic hydrocarbon molecules on the quartz surface, their two-dimensional distribution was calculated and visualized via the *gmx densmap* tool. As depicted in Figure 3b–d, a monolayer adsorption pattern was generally exhibited by the adsorption of aromatic hydrocarbon molecules on the quartz surface. Under low-pH conditions, a relatively sparse distribution and lower adsorption density were observed for the aromatic hydrocarbon molecules on the quartz surface. However, as the pH increased, the surface adsorption density of the aromatic hydrocarbon molecules was found to gradually increase, which indicated a stronger adsorption tendency.

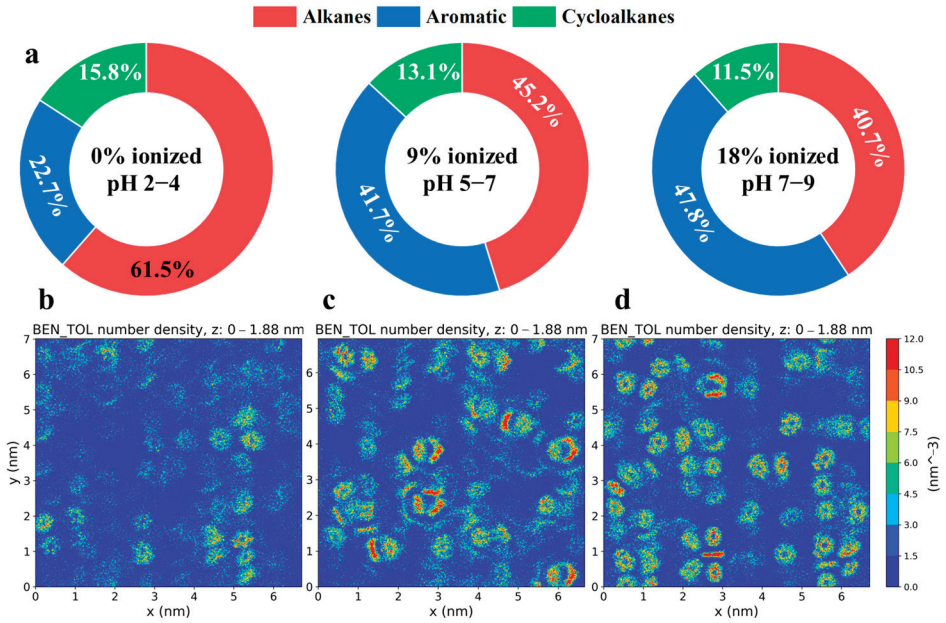

Figure 3. (**a**) Variation in the adsorption proportion of different types of crude oil molecules on the quartz surface as a function of pH. Two-dimensional density distribution maps of aromatic compounds adsorbed on the quartz surface under (**b**) pH 2–4, (**c**) pH 5–7, and (**d**) pH 7–9 conditions.

The reasons for the increased adsorption of aromatic hydrocarbon molecules on quartz surfaces with a rising pH were further investigated. It was considered that the pH environment primarily altered the charge state of the quartz surface, with a higher negative charge typically being exhibited under high-pH conditions [31,32]. On one hand, the π-electron cloud in aromatic hydrocarbon molecules could impart a certain degree of negative charge, which could potentially lead to repulsive forces between these negative charges. However, the adsorption of aromatic hydrocarbon molecules on the quartz surface was still facilitated through mechanisms such as π–π stacking and hydrophobic interactions, owing to their unique structure. On the other hand, an increase in pH was found to potentially modify the ionic strength in the oil layer, allowing Na^+ ions to aggregate more readily at the surface. This aggregation was hypothesized to enhance the attraction of aromatic hydrocarbon molecules in the oil layer through cation–π interactions. To validate these hypotheses, the density distribution of Na+ ions on the upper and lower quartz surfaces in the oil layer was calculated, as shown in Figure 4a. It was observed that, under pH 5–7 conditions, a relatively broad adsorption peak (approximately 0.2 nm) was formed by the Na^+ ions on the quartz surface. However, as the pH of the oil layer environment

increased to 7–9, the adsorption peak of the Na^+ ions became narrower (approximately 0.1 nm), with a significantly enhanced peak intensity. This change indicated that the Na^+ ions were more densely aggregated on the quartz surface under high-pH conditions, which thereby increased the potential for cation–π interactions and significantly enhanced the adsorption density on the quartz surface. To provide a more intuitive representation of this interaction mechanism, the composite structures formed by the Na^+ ions and aromatic hydrocarbon molecules on the quartz surface were visualized, as shown in Figure 4c,d. Through the repeated examination of interaction snapshots, the composite structures involving Na^+ ions were broadly categorized into two types. In the first type, as depicted in Figure 4c, the Na^+ ions were simultaneously engaged in ion–pair interactions with negatively charged oxygen ions in ionized silanol groups on the quartz surface and in cation–π interactions with a nearby aromatic hydrocarbon molecule. In this configuration, the Na^+ ions acted as an intermediary bridge, promoting the adsorption of aromatic hydrocarbon molecules on the quartz surface. In the second type, as shown in Figure 4d, the Na^+ maintained ion–pair interactions with negatively charged oxygen ions in ionized silanol groups on the quartz surface while attracting two surrounding aromatic hydrocarbon molecules. A stable tetrahedral interaction configuration was formed through the synergistic ion–pair and cation–π interactions among the quartz surface, Na^+ ions, and aromatic hydrocarbon molecules, which enabled the stable adsorption of aromatic hydrocarbon molecules on the quartz surface, with a reduced likelihood of dissociation. In summary, the enhanced enrichment of the aromatic hydrocarbon molecules on the quartz surface under high-pH conditions was attributed to the aggregation effect of Na^+ ions and the strengthened cation–π interactions.

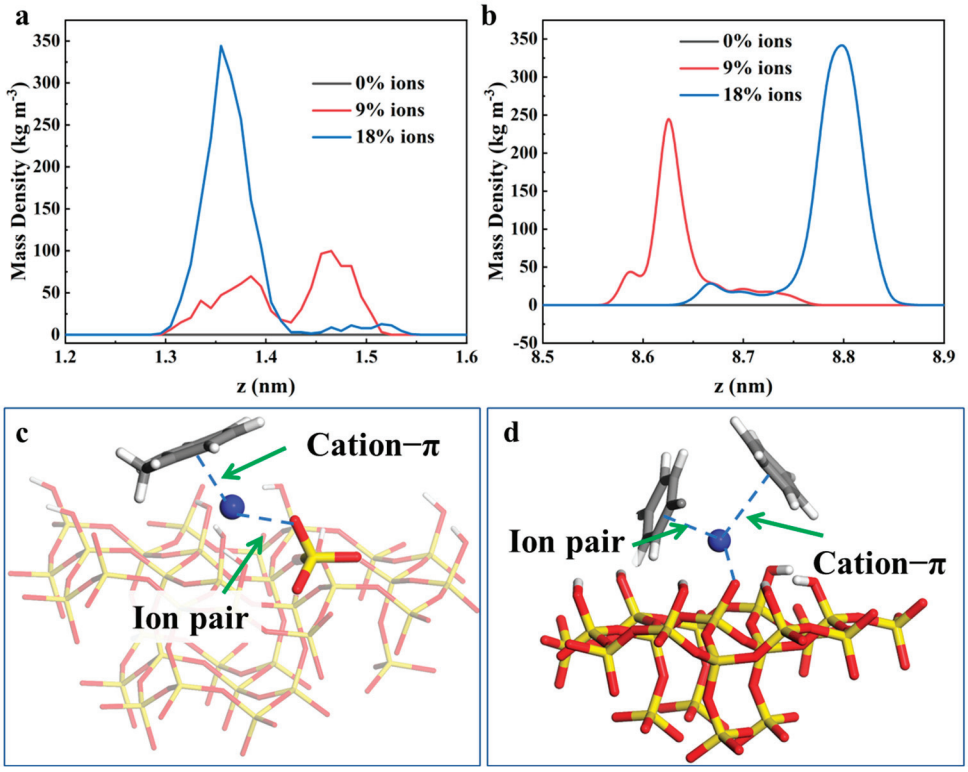

Figure 4. Distribution density of Na^+ ions near the (**a**) lower and (**b**) upper surfaces of quartz. (**c**,**d**) Adsorption configurations formed by Na^+ ions and aromatic hydrocarbon molecules on the quartz surface. Yellow denotes silicon (Si) atoms, blue denotes sodium (Na) atoms, red denotes oxygen (O) atoms, and gray denotes carbon (C) atoms.

2.2. CO_2 Displacement Process Under Different pH Conditions

The interaction between CO_2 and crude oil in tight reservoirs, along with its impact on the miscible phase behavior, was characterized by complex mechanisms, although accurate analysis at the nanoscale remained a challenge [33,34]. In this section, the mechanism of the displacement of crude oil in nanopores by CO_2 is investigated using molecular dynamics methods. The oil phase shown in Figure 5 corresponds to the equilibrated hydrocarbon mixture from Figure 2, including alkanes, cycloalkanes, and aromatic hydrocarbons. However, in Figure 5, all oil components are uniformly colored cyan without further differentiation by molecular type. The dynamic behavior of CO_2 in displacing crude oil under different pH conditions was visualized in Figure 5. Due to the differing amounts of CO_2 on the left and right sides of the oil film in the initial configuration, a pressure differential was induced, which resulted in a unidirectional displacement of the oil phase (CO_2 was present only on the left side of the oil phase, while the right side contained no CO_2). As shown in Figure 5, as the simulation progressed, the oil phase exhibited overall displacement behavior under both pH conditions, which confirmed the effectiveness of CO_2 in oil displacement. However, as the simulation advanced, the strong attractive interactions between the crude oil and the quartz surface were found to significantly hinder the efficiency of CO_2 displacement. Specifically, these strong attractive interactions impeded the interfacial detachment process between the CO_2 and the oil phase, preventing CO_2 from rapidly and effectively stripping crude oil from the quartz surface. Consequently, a substantial number of crude oil molecules remained tightly adsorbed on the quartz surface, which reduced the fluidity of the crude oil and the displacement efficiency of the CO_2. This phenomenon indicated that, when optimizing CO_2-enhanced oil recovery techniques, not only the interactions between CO_2 and crude oil but also the influence of reservoir surface adsorption effects need to be thoroughly considered. Additionally, the displacement effect under high-pH conditions was limited by a slower displacement rate. In contrast, the oil phase displacement under low-pH conditions was observed to be more rapid, which suggested that the displacement efficiency of the CO_2 was significantly enhanced under low-pH conditions. This observation highlighted the pronounced influence of pH on the flow velocity of the oil phase during the CO_2 displacement process.

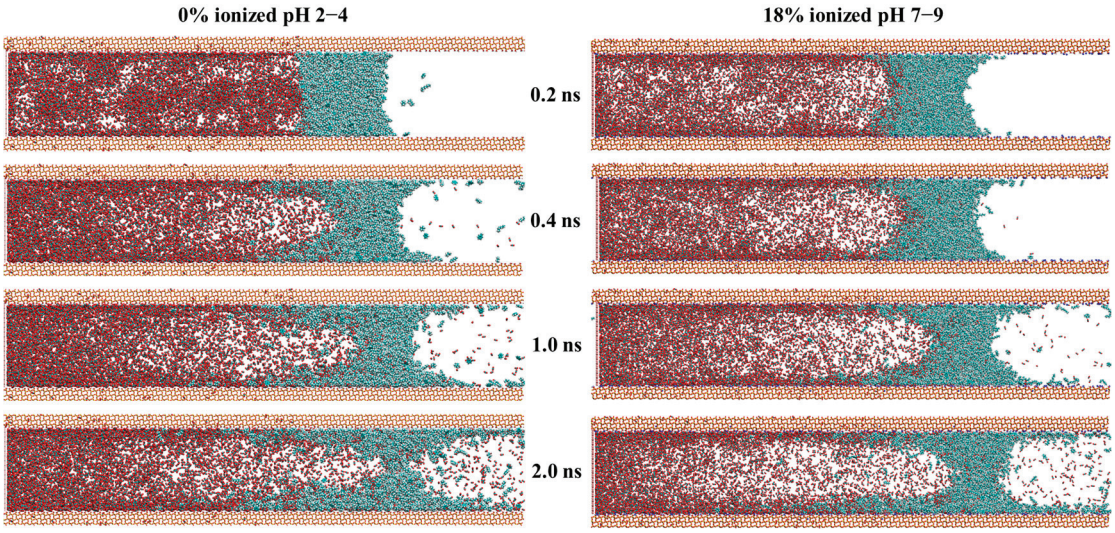

Figure 5. Snapshots of the CO_2 displacement process within the quartz pore during 0.2–2.0 ns. Red indicates CO_2 molecules, cyan represents oil-phase molecules, and the top and bottom slab structures simulate the oil reservoir matrix.

The miscible and displacement mechanisms of CO_2 molecules were further investigated in detail. From Figure 5, it can be seen that the initial step of CO_2 displacement was characterized by the miscible behavior between the CO_2 molecules and crude oil components, which indicated that CO_2 miscible displacement could be applied in reservoirs with significant pressure gradients. The initial miscible behavior is visualized in Figure 6. At 2 ps after the simulation began, a clear and stable oil–gas interface with a distinct boundary was observed (Figure 6a). As the simulation progressed, CO_2 molecules gradually penetrated the oil phase, and miscible phenomena began to emerge. Initially, the CO_2 molecules were primarily concentrated near the oil–gas interface, making preliminary contact with oil phase molecules. Over time, the CO_2 molecules were observed to diffuse further into the oil phase interior, engaging in increased interactions with crude oil molecules. This miscible phenomenon suggested that the dissolution and diffusion of CO_2 in the oil phase progressively increased, which facilitated the displacement and mixing of the oil phase. Following the miscible phase, the CO_2 displacement behavior was captured in simulation snapshots, as shown in Figure 6b. It was determined from the figure that the overall displacement mechanism could be summarized as an "adsorption-stripping-displacement" process. At the onset of the simulation, CO_2 molecules were first adsorbed onto the quartz pore surface, forming an adsorption layer. This process is illustrated in Figure 4b, which shows that CO_2 molecules were significantly aggregated on the quartz pore surface (4 ps), interacting with the pore wall to form a stable adsorption layer. The adsorption phase laid the foundation for the subsequent displacement process. As the simulation advanced, CO_2 molecules began to diffuse within the crude oil phase and gradually penetrated the gaps within the quartz pores (14 ps). At this stage, interactions between the CO_2 and crude oil molecules on the quartz surface were observed, which led to the detachment of crude oil molecule edges, which then entered the oil phase. The key to the stripping stage was that crude oil components were successfully detached from the quartz surface through the dissolution and diffusion of CO_2 molecules. Subsequently, under the driving force of external pressure, the stripped crude oil components were progressively displaced. During this process, the continuous injection of CO_2 and the applied pressure promoted the movement and mixing of the detached crude oil components within the pore space, and an effective displacement process was thereby achieved. Crude oil molecules were gradually propelled forward under the action of CO_2, completing the overall displacement process.

The kinetic parameters of oil components during the displacement process under different pH conditions were quantitatively compared to evaluate the influence of pH on CO_2 flooding. The mean square displacement (MSD) of the oil components throughout the entire displacement process was first calculated, as shown in Figure 7a. It was observed that the oil components exhibited a higher MSD under pH 7–9 conditions, with a diffusion coefficient of 8.5×10^{-5} cm^2 s^{-1}, which represents an approximately 37% increase compared to the diffusion coefficient of 6.2×10^{-5} cm^2 s^{-1} at pH 2–4. This indicated that the displacement efficiency of CO_2 increased with a rising pH. The calculation of time-dependent diffusion coefficients (Figure 7b) further supported this conclusion. This behavior was attributed to the increased negative charge density on the quartz surface under high-pH conditions, which promoted the aggregation of Na+ ions and consequently weakened the adsorption interactions between the oil components and the quartz surface. The weakened adsorption enabled more free movement of the oil molecules within the pore space, which led to enhanced diffusion. In addition, the high pH environment might have altered the viscosity of the pore fluid or the interactions between the fluid and the oil phase, further facilitating the diffusion of oil molecules. These results demonstrated that the pH exerted a significant influence on the dynamic behavior of the oil components, and

the higher diffusion coefficients and MSD values under high-pH conditions revealed the potential advantage of CO_2 flooding under alkaline environments.

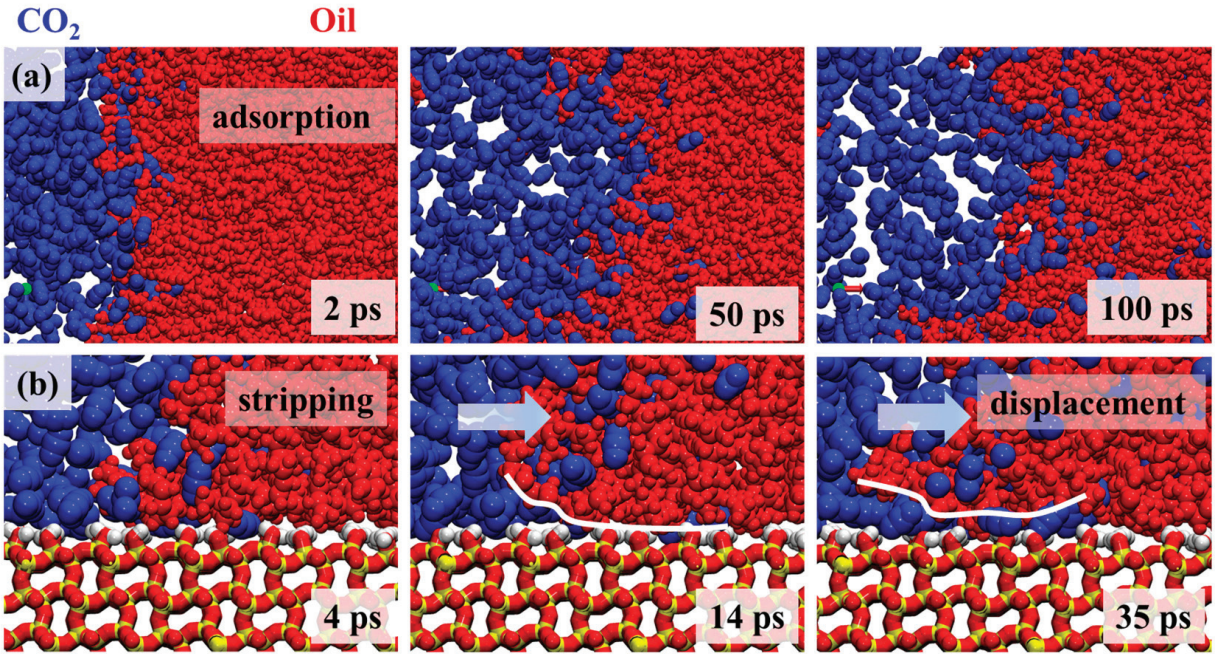

Figure 6. (**a**) Miscible phase behavior of CO_2 molecules and crude oil. (**b**) Stripping and displacement behavior of CO_2 molecules on the quartz surface. Blue represents CO_2 molecules and red represents crude oil molecules.

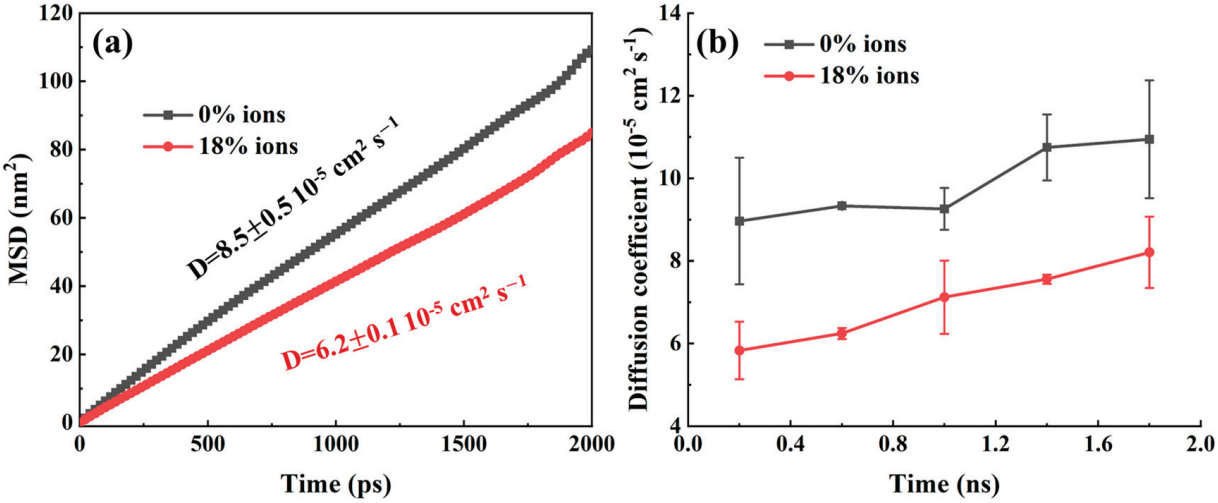

Figure 7. (**a**) Mean square displacement and diffusion coefficient of oil phase molecules during their advancement within the pore. (**b**) Diffusion coefficients of oil phase molecules at different time stages.

3. Methodology

In this section, an adsorption model of crude oil components in tight reservoirs is constructed, as shown in Figure 1a, where silica is selected to represent the reservoir solid. The main focus of this study was to investigate the adsorption mechanisms under different pH conditions; therefore, silica models responsive to various pH environments were developed. As illustrated in Figure 1b, pH primarily affects the degree of ionization on the silica surface. Three silica surface models with different ionization degrees were established, corresponding to 0%, 9%, and 18% ionization and representing pH ranges of 2–4, 5–7, and 7–9, respectively [21,22,35]. A certain proportion of alkane, cycloalkane, and

aromatic molecules was subsequently placed between the reservoir solids to simulate the adsorption behavior of different crude oil components. The oil phase was modeled using a representative mixture of alkanes, cycloalkanes, and aromatics (heptane: 165, octane: 188, nonane: 170, cycloheptane: 174, cyclohexane: 165, benzene: 107, toluene: 93.) which reflects typical SARA fractions in crude oil [36]. The hydrocarbon molecules were initially placed in a central region between two parallel silica surfaces that formed a nanopore. Care was taken to ensure no initial overlap and to maintain sufficient spacing between molecules to avoid artificial steric effects. The system was then equilibrated under NPT conditions before production runs. Molecular dynamics simulations were conducted under the NPT ensemble for 20 ns. The system was equilibrated under the NPT ensemble, where the number of particles (N), the pressure (P), and the temperature (T) were maintained as constant, which allowed for the realistic simulation of fluid behavior under reservoir conditions. To simplify this study, a nanopore model (Figure 1c) was constructed to approximate the matrix environment of tight reservoirs, while ensuring that the thickness of the pore walls exceeded the cutoff radius of the potential function. The number of CO_2 molecules introduced into the simulation system was determined based on the target density of CO_2 at ambient pressure (1 atm) and 358 K, which reflects post-injection diffusion or surface-exposed environments in enhanced oil recovery scenarios [8,37].

Given that the pore size in tight reservoirs typically ranges from 3 to 8 nm, the pore size in this work was set to 7.5 nm, as shown in Figure 1a. A graphene layer was positioned at the starting point on the left side of the simulated lattice to prevent carbon dioxide molecules from crossing the left periodic boundary [38,39]. MD simulations were performed using the GROMACS software 2019 package, employing the General Amber Force Field (GAFF) [40]. The CO_2 molecules were modeled using the EPM2 model. The simulation temperature was maintained at 358 K using the V-rescale thermostat [41]. The temperature of 358 K (85 °C) was selected to approximate realistic reservoir conditions typically encountered in deep or intermediate-depth tight reservoirs. A cutoff distance of 1.2 nm was applied. The LINCS algorithm was used to constrain bonds involving hydrogen atoms [42], with a time step of 2 fs. Long-range electrostatic interactions were calculated using the particle mesh ewald (PME) method. Trajectory visualization was carried out using the VMD software [43].

4. Conclusions

This study was conducted to investigate the adsorption behavior of crude oil on quartz surfaces under varying pH conditions and its impact on the CO_2 displacement process using molecular dynamics simulations. The main conclusions can be summarized as follows: (1) Crude oil molecules were primarily distributed in the pore bulk phase and on the surface within quartz pores, with the adsorption peak of aromatic hydrocarbons on the quartz surface being significantly higher than that of other components. Moreover, the adsorption of aromatic hydrocarbons was enhanced as the pH increased. (2) Under high-pH conditions, the aggregation of Na+ ions on the quartz surface was found to strengthen cation–π interactions, which further attracted aromatic hydrocarbon molecules and led to the formation of a denser adsorption layer on the quartz surface. (3) The CO_2 displacement process was characterized as an "adsorption-stripping-displacement" mechanism. An adsorption layer of CO_2 was initially formed on the quartz surface, which was followed by its penetration into the oil phase, where interactions with crude oil molecules occurred, resulting in the detachment of crude oil components. Ultimately, the detached crude oil components were effectively displaced under the influence of external pressure. (4) The displacement effect under high-pH conditions was limited by a slower displacement rate, whereas the oil phase displacement under low-pH conditions was observed to be more

rapid. This was attributed to the tighter packing of aromatic hydrocarbon molecules on the quartz surface under high-pH conditions.

Building on the molecular insights gained in this study, future research should focus on systematically exploring the influence of varying hydrocarbon compositions and more complex oil mixtures on the adsorption and displacement behaviors within nanoporous media. Additionally, experimental validation of the simulation results could be pursued, and alternative strategies for improving displacement techniques, such as the integration of other chemical agents or enhanced CO_2 injection methods, could be investigated to achieve more efficient reservoir development.

Author Contributions: Conceptualization, S.Y.; Methodology, X.S.; Software, Y.C. and S.Y.; Validation, Y.G.; Resources, X.S.; Data curation, Y.C.; Writing—original draft, X.S.; Writing—review & editing, Y.G.; Project administration, S.Y.; Funding acquisition, X.S. All authors have read and agreed to the published version of the manuscript.

Funding: This work was supported by the Research Start-up Fund Project of Shandong Institute of Petroleum and Chemical Technology (2023SS017): Construction of nanoemulsion system based on amphoteric surfactants and its oil displacement mechanism.

Institutional Review Board Statement: Not applicable.

Informed Consent Statement: Not applicable.

Data Availability Statement: The original contributions presented in this study are included in the article. Further inquiries can be directed to the corresponding authors.

Conflicts of Interest: The authors declare no conflict of interest.

References

1. Wang, S.; Yao, X.; Feng, Q.; Javadpour, F.; Yang, Y.; Xue, Q.; Li, X. Molecular insights into carbon dioxide enhanced multi-component shale gas recovery and its sequestration in realistic kerogen. *Chem. Eng. J.* **2021**, *425*, 130292. [CrossRef]
2. Liu, Y.; Shang, Y.; Yan, Z.; Li, H.; Wang, Z.; Li, Z.; Liu, Z. Pim1 kinase provides protection against high glucose-induced stress and apoptosis in cultured dorsal root ganglion neurons. *Neurosci. Res.* **2021**, *169*, 9–16. [CrossRef] [PubMed]
3. Clarkson, C.R.; Haghshenas, B.; Ghanizadeh, A.; Qanbari, F.; Williams-Kovacs, J.D.; Riazi, N.; Debuhr, C.; Deglint, H.J. Nanopores to megafractures: Current challenges and methods for shale gas reservoir and hydraulic fracture characterization. *J. Nat. Gas Sci. Eng.* **2016**, *31*, 612–657. [CrossRef]
4. Dordzie, G.; Balhoff, M. A review of chemical methods and testing techniques for enhanced oil recovery in shale reservoirs. *Fuel* **2025**, *394*, 135060. [CrossRef]
5. Li, L.; Su, Y.; Hao, Y.; Zhan, S.; Lv, Y.; Zhao, Q.; Wang, H. A comparative study of CO_2 and N_2 huff-n-puff EOR performance in shale oil production. *J. Pet. Sci. Eng.* **2019**, *181*, 106174. [CrossRef]
6. Song, C.; Yang, D. Experimental and numerical evaluation of CO_2 huff-n-puff processes in Bakken formation. *Fuel* **2017**, *190*, 145–162. [CrossRef]
7. Li, L.; Wang, C.; Li, D.; Fu, J.; Su, Y.; Lv, Y. Experimental investigation of shale oil recovery from Qianjiang core samples by the CO_2 huff-n-puff EOR method. *RSC Adv.* **2019**, *9*, 28857–28869. [CrossRef] [PubMed]
8. Fang, T.; Zhang, Y.; Ding, B.; Yan, Y.; Zhang, J. Static and dynamic behavior of CO_2 enhanced oil recovery in nanoslits: Effects of mineral type and oil components. *Int. J. Heat Mass Transf.* **2020**, *153*, 119583. [CrossRef]
9. Falk, K.; Coasne, B.; Pellenq, R.; Ulm, F.-J.; Bocquet, L. Subcontinuum mass transport of condensed hydrocarbons in nanoporous media. *Nat. Commun.* **2015**, *6*, 6949. [CrossRef] [PubMed]
10. Lee, T.; Bocquet, L.; Coasne, B. Activated desorption at heterogeneous interfaces and long-time kinetics of hydrocarbon recovery from nanoporous media. *Nat. Commun.* **2016**, *7*, 11890. [CrossRef] [PubMed]
11. Khovental, P.; Kopanichuk, I.; Vishnyakov, A. Molecular simulation of quartz wetting in crude oil/brine system at reservoir conditions using a novel protocol for contact angle calculation. *Colloids Surf. A Physicochem. Eng. Asp.* **2025**, *708*, 135978. [CrossRef]
12. Li, B.; Sui, H.; Wang, D.; Wang, Y.; Zhang, F.; Yao, J. Molecular insights into CO_2 enhanced oil recovery and CO_2 storage in quartz nanopores. *Geoenergy Sci. Eng.* **2025**, *246*, 213640. [CrossRef]

13. Nie, H.; Liu, Q.; Li, P.; Li, P.; Ding, J.; Sun, C.; Zhai, C.; Zhao, J.; Jin, Z.; Dang, W. Quartz types, formation mechanism, and its effect on shale oil and gas enrichment: A review. *Earth-Sci. Rev.* **2025**, *261*, 105011. [CrossRef]
14. Zhang, T.; Zhao, J.; Kong, D.; Zhou, J.; Wang, X.; Wei, B. Solvent-responsive switching wettability of superoleophobic/superhydrophilic quartz sand filter medium facilitates rapidly oil/water separation and demulsification. *Colloids Surf. A Physicochem. Eng. Asp.* **2024**, *697*, 134418. [CrossRef]
15. Qu, Y.; Wang, Y. Effects of mineral type on competitive adsorption and miscibility of CO_2-oil system in tight reservoirs: A molecular dynamics study. *J. Mol. Liq.* **2025**, *423*, 127032. [CrossRef]
16. Tang, J.; Zhang, J.; Jia, Y.; Liu, W.; Xiao, C.; Guo, X.; Cheng, Q. The critical role of temperature on the CO_2 replacement characteristics within inorganic minerals in shale oil reservoirs. *J. Mol. Liq.* **2025**, *421*, 126865. [CrossRef]
17. Lin, X.; Zhang, Y.; Yang, Z.; Yue, W.; Zhang, R.; Qi, J.; Lu, H. pH-regulated superhydrophobic quartz sands for controllable oil-water separation. *J. Environ. Chem. Eng.* **2023**, *11*, 110818. [CrossRef]
18. Hong, Q.; Pang, Z.; Liu, X.; Wang, B.; Liu, D.; Liao, H.; Wang, L. Quantitative macro and micro analysis on enhanced oil recovery (EOR) mechanisms of multi-component composite steam flooding (MCCSF) based on image recognition algorithm. *Geoenergy Sci. Eng.* **2025**, *249*, 213766. [CrossRef]
19. Zhang, A.; Lu, Y. Confined transport property of multi-polar mixed shale oil components induced by interfacial effects within kerogen nanopores. *Fuel* **2025**, *393*, 134985. [CrossRef]
20. Wang, L.; Zou, R.; Yuan, Y.; Zhang, Y.; Zou, R.; Huang, L.; Liu, Y.; Meng, Z.; Chen, H. Dynamics of impure CO_2 and composite oil in mineral nanopores: Implications for shale oil recovery and gas storage performance. *Chem. Eng. J.* **2024**, *500*, 157421. [CrossRef]
21. Yuan, S.; Wang, Z.; Yuan, S. Insights into the pH-dependent interactions of sulfadiazine antibiotic with soil particle models. *Sci. Total Environ.* **2024**, *917*, 170537. [CrossRef] [PubMed]
22. Emami, F.S.; Puddu, V.; Berry, R.J.; Varshney, V.; Patwardhan, S.V.; Perry, C.C.; Heinz, H. Force Field and a Surface Model Database for Silica to Simulate Interfacial Properties in Atomic Resolution. *Chem. Mater.* **2014**, *26*, 2647–2658. [CrossRef]
23. Kirch, A.; Celaschi, Y.M.; de Almeida, J.M.; Miranda, C.R. Brine–Oil Interfacial Tension Modeling: Assessment of Machine Learning Techniques Combined with Molecular Dynamics. *ACS Appl. Mater. Interfaces* **2020**, *12*, 15837–15843. [CrossRef] [PubMed]
24. Xue, C.; Ji, D.; Wen, Y.; Luo, H.; Zhao, Y.; Li, Y. Promising combination of CO_2 enhanced oil recovery and CO_2 sequestration in calcite nanoslits: Insights from molecular dynamics simulations. *J. Mol. Liq.* **2023**, *391*, 123243. [CrossRef]
25. Lu, N.; Dong, X.; Wang, H.; Liu, H.; Chen, Z.; Li, Y.; Zeng, D. Hybrid CO_2 thermal system for post-steam heavy oil recovery: Insights from microscopic visualization experiments and molecular dynamics simulations. *Energy Geosci.* **2025**, *6*, 100394. [CrossRef]
26. Wang, R.; Peng, F.; Song, K.; Feng, G.; Guo, Z. Molecular dynamics study of interfacial properties in CO_2 enhanced oil recovery. *Fluid Phase Equilibria* **2018**, *467*, 25–32. [CrossRef]
27. Liu, F.; Gao, X.; Du, J.; Lin, L.; Hou, D.; Luo, J.; Zhao, J. Microscopic mechanism of enhancing shale oil recovery through CO_2 flooding- insights from molecular dynamics simulations. *J. Mol. Liq.* **2024**, *410*, 125593. [CrossRef]
28. Tang, X.; Xiao, S.; Lei, Q.; Yuan, L.; Peng, B.; He, L.; Luo, J.; Pei, Y. Molecular Dynamics Simulation of Surfactant Flooding Driven Oil-Detachment in Nano-Silica Channels. *J. Phys. Chem. B* **2019**, *123*, 277–288. [CrossRef] [PubMed]
29. Yan, H.; Yuan, S. Molecular Dynamics Simulation of the Oil Detachment Process within Silica Nanopores. *J. Phys. Chem. C* **2016**, *120*, 2667–2674. [CrossRef]
30. Xiong, Y.; Cao, T.; Chen, Q.; Li, Z.; Yang, Y.; Xu, S.; Yuan, S.; Sjöblom, J.; Xu, Z. Adsorption of a Polyaromatic Compound on Silica Surfaces from Organic Solvents Studied by Molecular Dynamics Simulation and AFM Imaging. *J. Phys. Chem. C* **2017**, *121*, 5020–5028. [CrossRef]
31. Patwardhan, S.V.; Emami, F.S.; Berry, R.J.; Jones, S.E.; Naik, R.R.; Deschaume, O.; Heinz, H.; Perry, C.C. Chemistry of Aqueous Silica Nanoparticle Surfaces and the Mechanism of Selective Peptide Adsorption. *J. Am. Chem. Soc.* **2012**, *134*, 6244–6256. [CrossRef] [PubMed]
32. Kumar, M.; Sengupta, A. A Molecular Simulation Study on Selective Adsorption of CO_2 from an Industrial Ternary Gas Mixture inside Porous Silica and Kaolinite Adsorbents. *Energy Fuels* **2025**, *39*, 8540–8566. [CrossRef]
33. Zhang, H.; Wang, R.; Guo, Z.; Feng, G. Molecular Insights into Effects of Methanol Additive on CO_2 Enhanced Oil Recovery in the Dead-End Nanopore. *ACS Appl. Energy Mater.* **2024**, *7*, 10251–10258. [CrossRef]
34. Liu, B.; Liu, W.; Pan, Z.; Yu, L.; Xie, Z.; Lv, G.; Zhao, P.; Chen, D.; Fang, W. Supercritical CO_2 Breaking Through a Water Bridge and Enhancing Shale Oil Recovery: A Molecular Dynamics Simulation Study. *Energy Fuels* **2022**, *36*, 7558–7568. [CrossRef]
35. Yuan, S.; Zhang, J.; Yu, X.; Zhu, X.; Zhang, N.; Yuan, S.; Wang, Z. Molecular Mechanisms of Humic Acid in Inhibiting Silica Scaling during Membrane Distillation. *Environ. Sci. Technol.* **2025**, *59*, 978–988. [CrossRef] [PubMed]
36. Kunieda, M.; Nakaoka, K.; Liang, Y.; Miranda, C.R.; Ueda, A.; Takahashi, S.; Okabe, H.; Matsuoka, T. Self-Accumulation of Aromatics at the Oil−Water Interface through Weak Hydrogen Bonding. *J. Am. Chem. Soc.* **2010**, *132*, 18281–18286. [CrossRef] [PubMed]

37. Fang, T.; Zhang, Y.; Liu, J.; Ding, B.; Yan, Y.; Zhang, J. Molecular insight into the miscible mechanism of CO_2/C10 in bulk phase and nanoslits. *Int. J. Heat Mass Transf.* **2019**, *141*, 643–650. [CrossRef]
38. Yan, Y.; Li, C.; Dong, Z.; Fang, T.; Sun, B.; Zhang, J. Enhanced oil recovery mechanism of CO_2 water-alternating-gas injection in silica nanochannel. *Fuel* **2017**, *190*, 253–259. [CrossRef]
39. Dong, T.; Harris, N.B. Pore Size Distribution and Morphology in the Horn River Shale, Middle and Upper Devonian, Northeastern British Columbia, Canada. *Electron Microsc. Shale Hydrocarb. Reserv.* **2013**, *102*, 67–79. [CrossRef]
40. Wang, J.; Wolf, R.M.; Caldwell, J.W.; Kollman, P.A.; Case, D.A. Development and testing of a general amber force field. *J. Comput. Chem.* **2004**, *25*, 1157–1174. [CrossRef] [PubMed]
41. Bussi, G.; Donadio, D.; Parrinello, M. Canonical sampling through velocity rescaling. *J. Chem. Phys.* **2007**, *126*, 014101. [CrossRef] [PubMed]
42. Hess, B.; Bekker, H.; Berendsen, H.J.C.; Fraaije, J.G.E.M. LINCS: A linear constraint solver for molecular simulations. *J. Comput. Chem.* **1997**, *18*, 1463–1472. [CrossRef]
43. Humphrey, W.; Dalke, A.; Schulten, K. VMD: Visual molecular dynamics. *J. Mol. Graph.* **1996**, *14*, 33–38. [CrossRef] [PubMed]

molecules

MDPI

Article

Atomistic Insights into the Influence of High Concentration H_2O_2/H_2O on Al Nanoparticles Combustion: ReaxFF Molecules Dynamics Simulation

Xindong Yu [1], Pengtu Zhang [2], Heng Zhang [1,3,*] and Shiling Yuan [1,2,*]

[1] Key Lab of Colloid and Interface Chemistry, Shandong University, Jinan 250100, China; 202212213@mail.sdu.edu.cn
[2] School of Chemical Engineering, Shandong Institute of Petroleum and Chemical Technology, Dongying 257061, China; ptzhang@sdipct.edu.cn
[3] Shandong Chambroad Holding Co., Ltd., Binzhou 256500, China
* Correspondence: zhangheng@sdu.edu.cn (H.Z.); shilingyuan@sdu.edu.cn (S.Y.)

Abstract: The combination of Al nanoparticles (ANPs) as fuel and H_2O_2 as oxidizer is a potential green space propellant. In this research, reactive force field molecular dynamics (ReaxFF-MD) simulations were used to study the influence of water addition on the combustion of Al/H_2O_2. The MD results showed that as the percentage of H_2O increased from 0 to 30%, the number of Al-O bonds on the ANPs decreased, the number of Al-H bonds increased, and the adiabatic flame temperature of the system decreased from 4612 K to 4380 K. Since the Al-O bond is more stable, as the simulation proceeds, the number of Al-O bonds will be significantly higher than that of Al-H and Al-OH bonds, and the Al oxides ($Al[O]_x$) will be transformed from low to high coordination. Subsequently, the combustion mechanism of the $Al/H_2O_2/H_2O$ system was elaborated from an atomic perspective. Both H_2O_2 and H_2O were adsorbed and chemically activated on the surface of ANPs, resulting in molecular decomposition into free radicals, which were then captured by ANPs. H_2 molecules could be released from the ANPs, while O_2 could not be released through this pathway. Finally, it was found that the coverage of the oxide layer reduced the rate of H_2O_2 consumption and H_2 production significantly, simultaneously preventing the deformation of the Al clusters' morphology.

Keywords: Al nanoparticles; ReaxFF; combustion; hydrogen peroxide

1. Introduction

In recent years, with the development of missiles and aerospace technologies, it has become essential to develop a green and high-efficiency propulsion system [1–4]. Conventional propellant fuels are primarily consisting of hydrazine (N_2H_4) and methylated derivatives of hydrazine, etc. However, their disadvantages, such as extremely high toxicity, carcinogenicity, high volatility, and risk of explosion, increase the cost and environmental impact of these propellants during production, storage, and transportation [5,6]. Therefore, the development of a more eco-friendly, lower-cost, and higher-performance propellant composition has been a topical issue in space science.

H_2O_2 has been used as a monopropellant and a non-volatile oxidizer for rockets since the 1940s [7–9]. Its complete decomposition releases only water vapor, oxygen, and heat, with minimal environmental impact. This propellant offers the aerospace industry an attractive approach to using green propellants with greatly reduced toxicity and low storage and disposal costs [10,11]. In monopropellant rocket systems, the decomposition and combustion efficiency of H_2O_2 can be improved by using multiphase catalysts [12]. In bipropellant rocket systems, high concentrations of hydrogen peroxide are used as oxidizers for different fuels (hydrocarbons, kerosene, alcohols, etc.) to increase specific impulse and develop high-energy, environmentally friendly propellant

formulations [13–18]. For example, Okninski reported a 3.5% improvement in specific impulse and a 70% gain in density-specific impulse by using 98% H_2O_2, compared to motors using N_2O as an oxidizer [19].

On the other hand, as the third most abundant element in the earth's crust, aluminum has a very high energy density (30.5 kJ/g), low application costs, and environmentally friendly and non-polluting use. For this reason, it is widely applied in various technological fields, including aerospace technology, automobiles, airplanes, and high-energy materials [20–22]. Among the composite propellants, Al powder is often used as a metal fuel to enhance the energy characteristics of propellants. The combination of ANPs with conventional oxidizers, such as ammonium perchlorate (AP), 1,3,5-trinitro-1,3,5-triazinane (RDX), 1,3,5,7-tetranitro-1,3,5,7-tetrazocane(HMX), 2,4,6-trinitrotoluene (TNT), etc. is also very widely used in application research [23–27].

By contrast, solid–liquid hybrid propellants with Al as the fuel and H_2O_2 as the oxidizer have been studied relatively little. Above all, solid–liquid hybrid systems are safer for transportation, storage, and operation than solid systems and liquid systems. Meanwhile, their specific impulse is generally higher than that of solid rockets, and the density-specific impulse is higher than that of liquid rockets. Moreover, ANPs can obtain a high exotherm (25.8 kJ/g) as well as yield only clean oxidation products (H_2O, H_2, O_2, and Al_2O_3) in the reaction with H_2O_2, which is why Al/H_2O_2 is a promising bipropellant for development [28–30].

Zaseck et al. showed that the size of the aluminum particles was the most dominant factor driving the combustion rate of the bipropellant, with the combustion rate exponent increasing from ∼0.5 to ∼1.0 as the diameter of the Al particles decreased from 12 μm to 3 μm. Furthermore, the concentration of H_2O_2 had an important effect on the combustion rate and combustion temperature, compared to the mixing ratio (O/F), which had the least effect on the combustion rate [29]. The effect of H_2O_2 on the combustion properties of aluminum-water mixtures was investigated by Sabourin et al. The linear combustion rate increased from 9.6 cm/s to 58 cm/s at 3.65 MPa as the mass fraction of H_2O_2 was increased from 0 to 32%, and the flame temperature increased by 600 K as the mass fraction of H_2O_2 was increased from 0 to 35% under chemically proportioned conditions [30]. According to research, H_2O_2 usually undergoes spontaneous decomposition, and the main product of decomposition is water. Hence, its concentration decreases over time, which has a great impact on the combustion efficiency of the propellant [12]. In addition, ANPs have a higher surface area relative to micron-sized Al particles, which contributes to faster oxidation, while ANPs rapidly form an oxide shell on the surface in the presence of an oxidizing agent, and the core-shell structure (Al@Al_2O_3) ultimately influences the adiabatic flame temperature and reaction mechanism of the Al/H_2O_2 reaction [31,32]. As a result, understanding the basic combustion mechanism of ANPs with H_2O_2 and the influence of the percentage of water content on the reaction is crucial for enhancing propulsion performance and energy efficiency.

Experimentally revealing the aforementioned combustion pathways, particularly at the molecular/atomic level, is still quite difficult. Yet ReaxFF-MD simulations provide much richer molecular/atomic details and have been widely used as an alternative to combustion and pyrolysis experiments, etc. [33–38]. For example, ReaxFF-MD simulations have successfully captured the atomic-level mass transfer and the reactive processes of the oxidation of ANPs under high-temperature and high-pressure oxygen atmospheres, which reveal the detailed mechanism of the oxidation of ANPs [39]. Zhao et al. revealed the reaction mechanism of molten Al nano-droplets (ANDP) with H_2O vapor at high temperatures from an atomic perspective using ReaxFF. The influence of temperature, ANDP particle size, and water vapor concentration on ANDP combustion was also considered [40]. Recently, the influence of ANPs as additives on the thermal decay mechanism of energetic materials (EMs) and the evolution of ANPs during the thermal decomposition of EMs have also been explored through reactive molecular dynamics simulations [41,42].

Here, this work will use ReaxFF-MD simulations to investigate the influence of adding different proportions of H_2O on the combustion of Al/H_2O_2 by analyzing the number of bonds, reaction products, intermediates, morphology of ANPs, and reaction trajectories of the whole reaction process. In addition, it aims to explore the combustion mechanism of $Al/H_2O_2/H_2O$ from the atomic perspective. The findings of this study will help to provide a theoretical basis for an in-depth study of Al/H_2O_2 combustion and guide the design of subsequent development of binary propulsion systems.

2. Results

2.1. Reactive Force Field (ReaxFF) Molecular Dynamics

ReaxFF is a molecular dynamics simulation method for chemical reactions, first proposed in 2001 by van Duin et al. [43]. In the model of the reactive force field, the concept of atom type in the classical force field no longer exists, and there is no connectivity between the atoms in the system; instead, at the current moment, connectivity is determined by calculating the bond order (BO) between any two atoms. As chemical bonds are broken and created, the list of atomic connectivity is updated. Thus, it is a molecular force field based on bond order [44,45]. The strength of the ReaxFF force field lies in its ability to handle chemical reaction processes in larger systems on longer time scales and with an accuracy approaching that of quantum chemical calculations. As a result, ReaxFF has been widely used in the field of materials science for more than two decades, in areas such as development and design.

2.2. Model Construction

All of the ReaxFF-MD simulations in this paper were performed in the large-scale atomic/molecular massively parallel simulator (LAMMPS) package [46,47]. This work uses the Al/C/H/O force field parameter set developed by Hong et al. [48]. The force field has been successfully used to reveal the influence of carbon coatings on the oxidation of ANPs and the combustion reaction of ANPs with oxidizing agents (O_2, H_2O, H_2O_2, etc.) [49,50]. First, an Al particle with a diameter of 2.8 nm and 675 atoms was constructed. The ANPs were then placed in periodic boxes of 10.0 nm × 10.0 nm × 10.0 nm by Packmol, which were surrounded by a random distribution of a predetermined amount of H_2O_2/H_2O molecules in different ratios [51]. The thickness of the vacuum layer between ANPs and H_2O_2/H_2O was set to 1.1 nm to prevent the initial chemisorption of molecules on the Al surface. The model construction process and specific parameters are shown in Table 1 and Figure 1, respectively.

Table 1. Model parameters of the simulation cells.

Molar Ratio (H_2O)	System Component	Size (Angstrom^3)	Total Atoms
0	$1000H_2O_2$ + 675Al	100 × 100 × 100	4675
10%	$900H_2O_2$ + $100H_2O$ + 675Al	100 × 100 × 100	4575
20%	$800H_2O_2$ + $200H_2O$ + 675Al	100 × 100 × 100	4475
30%	$700H_2O_2$ + $300H_2O$ + 675Al	100 × 100 × 100	4375

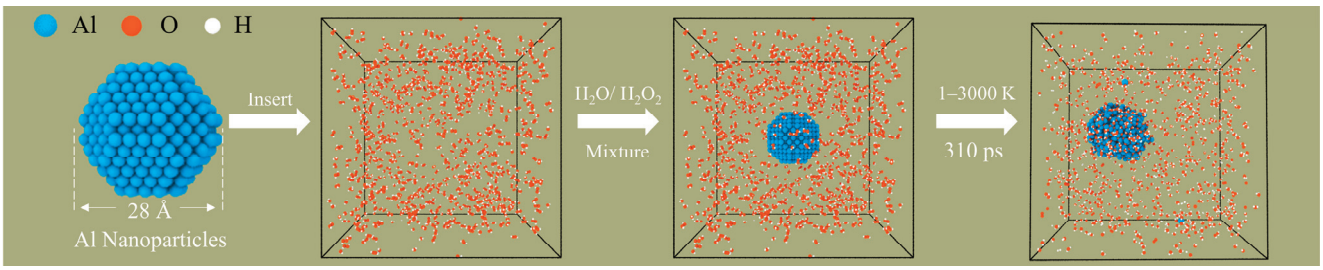

Figure 1. Model building and simulation process (aluminum, oxygen, and hydrogen are blue, orange, and white, respectively).

2.3. Computational Details and Post-Processing

For the sake of optimizing the system structure, the system was first simulated at 1 K for 10 ps, heated up to 3000 K at a rate of 30 K/ps, and then simulated at 3000 K for 200 ps. The simulations were performed under the canonical ensemble (NVT, where N, V, and T represent the total number of particles, the system volume, and the temperature, respectively), and the temperature of the system was controlled using a Nosé-Hoover thermostat, with a combined time for all simulations of 310 ps. In addition, a microcanonical ensemble (NVE) was performed for each system to simulate the change in temperature of the system in an adiabatic state with 250 ps. The time step for all simulated processes was set to 0.2 fs. Bond breakage and formation were determined by the method of the bond order cutoffs, where the cutoff value was set to 0.3.

According to the previous literature, the set values of the above parameters are reliable [44,48]. High temperature only affects the reaction rate and has little influence on the reaction mechanism in ReaxFF-MD simulations [52]. Hence, we used high-temperature simulations during the combustion process. Since the experimental time is much longer than the simulation time, the number of interatomic collisions is increased by increasing the temperature, which improves the combustion efficiency and reduces the simulation cost. Meanwhile, the evolution of chemical species and the number of bonds in the simulations were post-processed by using a Python program, and the simulation results were visualized with OVITO [53].

3. Discussion

3.1. Influence of the Addition of H_2O on the Combustion of ANPs in H_2O_2

Propulsion grade H_2O_2 has a long history of safe production and application in power and propulsion units, and optimum performance is obtained by using the highest concentration (i.e., 100% H_2O_2). Nevertheless, the experimental H_2O_2 contains a little water in a reduced concentration due to the compromise between the production cost and the performance obtained and the spontaneous decomposition of H_2O_2 over time. Therefore, we established four systems of Al/H_2O_2/H_2O with different percentages, containing 0, 10%, 20%, and 30% of water, respectively, and carried out combustion simulations at 310 ps for the four systems.

Al-O bonds and Al-H bonds are prevalent in the combustion of Al/H_2O_2, and the rate of its formation reflects the rate of production of aluminum oxide and aluminum hydride. Figure 2 shows the comparative analysis of the number of Al-O, and Al-H bonds in different systems, and it suggests that the generation curves of Al/H_2O_2/H_2O systems with different proportions are significant differences. As shown in Figure 2a, the number of Al-O bonds reaches an extreme value later, as the water content increases. In addition, the final amount of Al-O bonds produced decreases with increasing water. The growth curve of the Al-H bond is somewhat different in that it peaks first and then declines after reaching the maximum value (Figure 2b). This indicates that the intermediate product of the reaction is the Al-H bond, which breaks after reaching a maximum value to form other products. When the time exceeds 200 ps, the number of Al-H bonds levels off, and the reaction essentially reaches equilibrium. In contrast to the evolution in the number of Al-O bonds, there is a delay in reaching the maximum value of Al-H bonds as the proportion of H_2O to the reactants increases, and the final Al-H bonds produced increase with the water content.

H_2O_2 is more oxidizing than H_2O, and the addition of water changes the reaction mechanism of the Al/H_2O_2 mixture. The evolution of the number of major chemical bonds in the Al/H_2O_2/H_2O system with different water contents is shown in Figure S1 (Supplementary Materials). In the initial stage of the process, the decrease in the O-O bonds implies the consumption of H_2O_2, and the decrease followed by a slow rise in the H-O bonds implies the decomposition of H_2O_2 and H_2O, with subsequent regeneration of water. We also found that, as water increased, H-H bonds became more numerous, whereas O-O bonds became less. The H-H bond is mainly associated with the formation of the product

H_2, and the source of H_2 is formed due to the breaking of the Al-H bond. It suggests that the increase in water content increases the production of the product H_2 by influencing the number of Al-H bonds while hindering the production of O_2.

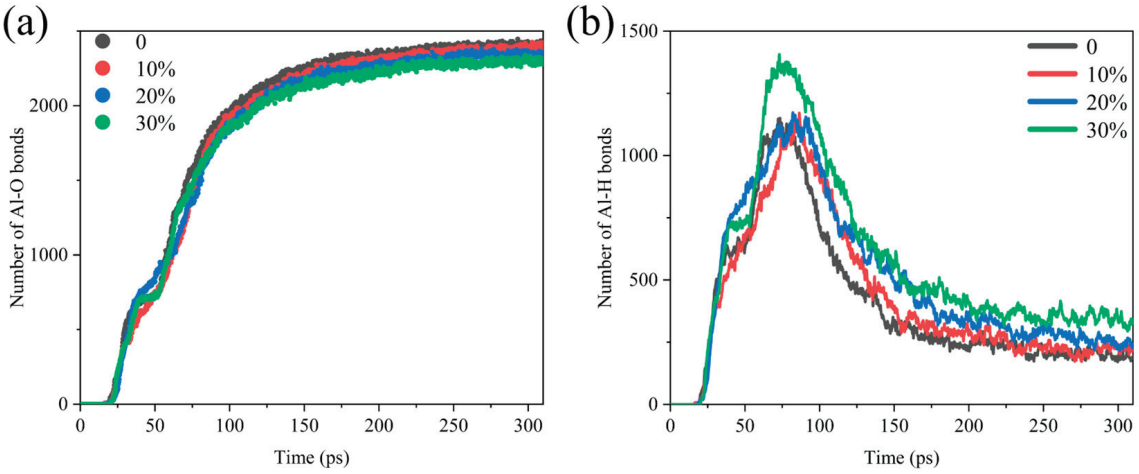

Figure 2. Comparative analysis of the number of (**a**) Al-O bonds and (**b**) Al-H bonds in the $Al/H_2O_2/H_2O$ system; 0, 10%, 20% and 30% represent the proportion of H_2O in each system.

Analyzing the evolution of the number of products is helpful in understanding the reaction mechanism of the $Al/H_2O_2/H_2O$ system. Al and its oxides are usually found in the form of clusters. Therefore, we count them by the number of chemical bonds. Here are the equations derived from the relationship between the number of molecules and the number of bonds.

$$N(Al\ (OH)_3) \approx (N_{bond}(O\text{-}H) - 2N(H_2O_2) - 2N(H_2O) - N(\bullet OH) - N(\bullet OOH))/3 \quad (1)$$

$$N(AlH_3) = (N_{bond}(Al\text{-}H))/3 \quad (2)$$

In this equation, $N(Al\ (OH)_3)$, $N(H_2O_2)$, $N(H_2O)$, $N(\bullet OH)$, $N(\bullet OOH)$, and $N(AlH_3)$ denote the number of molecules of $Al(OH)_3$, H_2O_2, H_2O, $\bullet OH$, $\bullet OOH$, and AlH_3. Meanwhile Nbond(O-H) and Nbond(Al-H) represent the number of O-H and Al-H bonds, respectively. There are very few molecules (e.g., H_4O_2) on the right-hand side of Equation (1), which can be ignored, so Equation (1) uses "≈". To investigate the influence of water addition on the Al/H_2O_2 reaction mechanism, we calculated the number of products of the Al/H_2O_2 system containing 30% H_2O as a function of time through codes and equations.

As shown in Figure 3, we can simply divide the whole reaction process into two stages. In the early stage of the reaction, H_2O and H_2O_2 were adsorbed onto the surface of the ANPs and reacted to form AlH_3, $Al\ (OH)_3$, and differently coordinated Al oxides ($Al[O]_1$, $Al[O]_2$, $Al[O]_3$, $Al[O]_4$, $Al[O]_5$). However, over time, as the adsorption sites on ANPs gradually decreased, Al-O, Al-H, and Al-OH bonds started to compete for the adsorption sites. Since the bond energy of Al-O (501.9 ± 10.6 kJ mol^{-1}) is far higher than that of Al-H (288.0 ± 13.0 kJ mol^{-1}), the bonding of Al-O bonds is more stable [54]. Thus, the H atoms began to be extruded from the ANPs at about 75 ps. The gradual decrease in the amount of AlH_3 and the steady increase in the number of Al-O bonds were accompanied by the transformation of the lower-coordinated Al oxides ($Al[O]_0$ and $Al[O]_1$) into higher-coordinated $Al[O]_3$, $Al[O]_4$, and $Al[O]_5$. With sufficient simulation time, it can be predicted that, eventually, the coordination number of the majority of Al oxides will become six, consistent with the coordination number of Al in the stable oxidation product Al_2O_3. Figure 3b reveals that H_2O_2 starts to decrease from around 20 ps until it is completely consumed at around 175 ps, while H_2O starts to decrease from around 23 ps until it reaches a minimal value at around 68 ps. This indicates that a bit of H_2O is also involved in the combustion reaction with Al, whereas the reactivity of H_2O is much lower than that of

H_2O_2, and more energy has to be absorbed to reach the reaction barrier of Al/H_2O, so the onset of the consumption of H_2O is slightly delayed compared to that of H_2O_2.

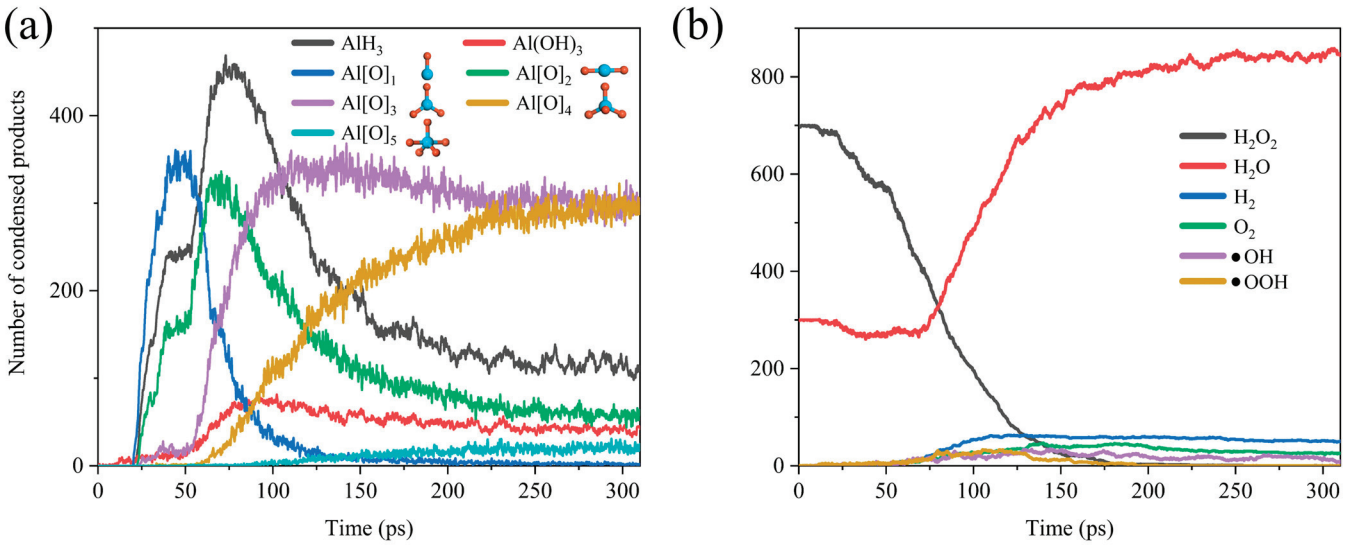

Figure 3. Evolution of (**a**) the products AlH_3, $Al(OH)_3$, $Al[O]_x$ and the configuration of the corresponding ligand oxides of Al (Al is blue, O is red) and (**b**) gas phase chemicals H_2O_2, H_2O, H_2, O_2, •OH, •OOH in Al/H_2O_2/H_2O (30%) system.

Interestingly, we compared the H_2O_2 consumption, H_2O, H_2, and O_2 formation curves for systems with different water contents. As seen in Figure 4, in the early stage of the reaction, the temperature was not too high for water to have much influence on the consumption of H_2O_2, but after about 50 ps, there was a difference in the rate of H_2O_2 consumption. The higher the proportion of H_2O, the lower the rate of consumption of H_2O_2. There was a slight decrease in the amount of water early on and a rapid increase in the number of water molecules after 55 ps, until it stabilized after about 200 ps (Figure 4b). It could be assumed that Al reacted with H_2O at the beginning of the reaction. As the reaction progressed, the system began to produce more H_2O than the number of H_2O molecules consumed, and the final yield of H_2O decreased as the concentration of H_2O_2 decreased. Figure 4c,d correspond to the analysis of the number of bonds in Figure S1, indicating that the increase in water content increases the production of the final product H_2 while hindering the production of O_2.

3.2. Atomic Perspective of the Reaction Mechanism of ANPs/H_2O_2/H_2O

We can observe the combustion of Al/H_2O_2 from an atomistic perspective by capturing the microscopic trajectory of the reaction. Figure 5 presents a snapshot of the reaction of H_2O_2 and H_2O on the ANPs surface in the Al/H_2O_2 system with 30% water. We found that both H_2O_2 and H_2O molecules were constantly approaching the ANPs and then were adsorbed on the surface. During this process, H_2O_2 and H_2O molecules were chemically activated, whereby the molecules decomposed into OH radicals and H radicals and were captured by ANPs. The Al-OH bond was unstable and quickly broke to form an Al-H bond with an Al-O bond. Hence, the number of Al-H and Al-O bonds was much higher than the number of Al-OH bonds as the simulation time increased.

ANPs and H_2O_2 are used as bipropellants mainly owing to the fact that the products of the reaction are green and non-polluting, so we focus on analyzing the generation routes of their products: H_2O, H_2, and O_2. Figure 6 shows a snapshot of H_2O generation from the surface of ANPs. We could see that the reaction starts with the O and H atoms on the ANPs, approaching each other to form Al-OH bonds, then combining with the H on the nearby ANPs to form H_2O, which is eventually desorbed from the surface of the ANPs.

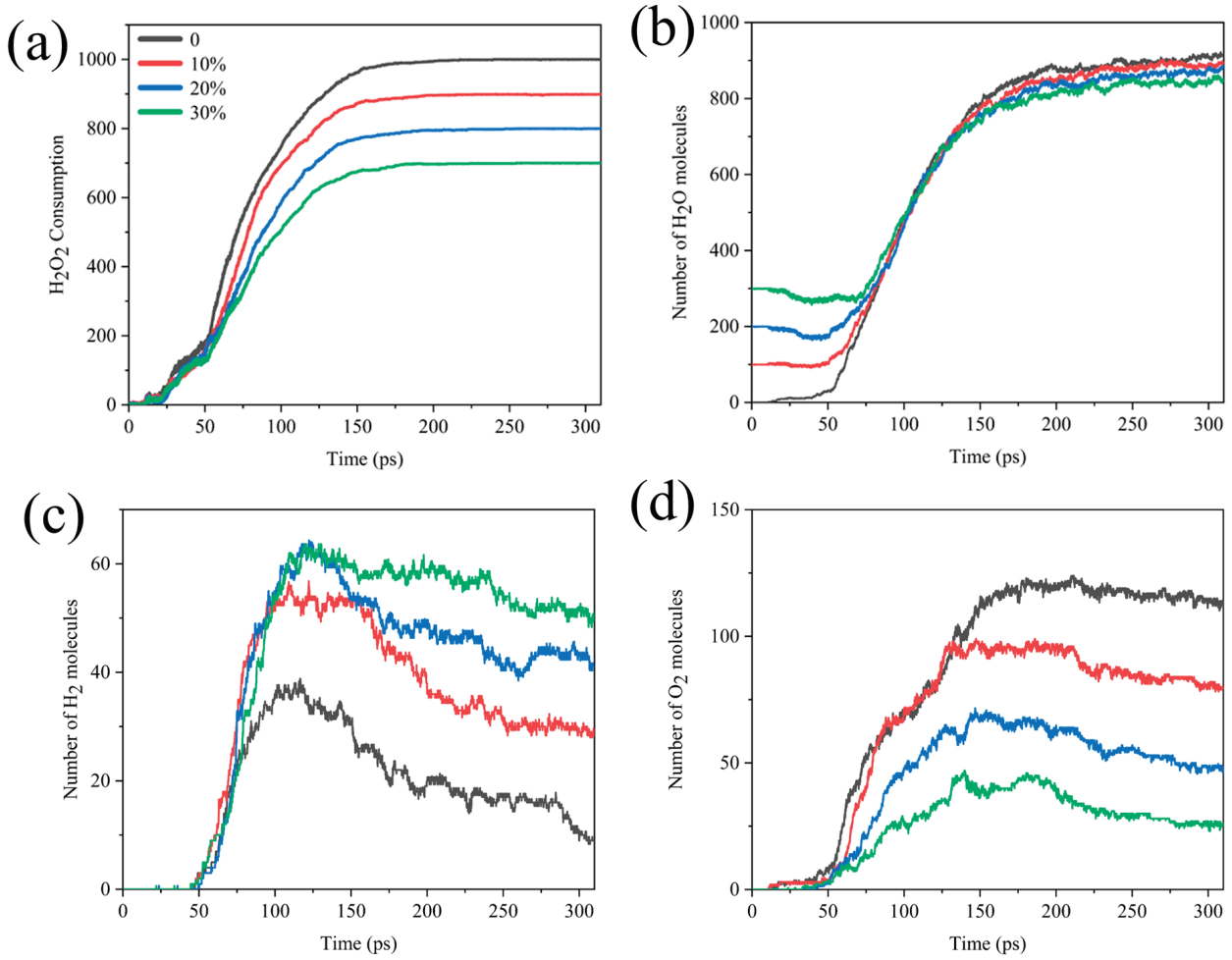

Figure 4. Comparison of (**a**) H_2O_2 molecular consumption and (**b**) H_2O, (**c**) H_2, (**d**) O_2 molecular formation curves in different Al/H_2O_2/H_2O systems.

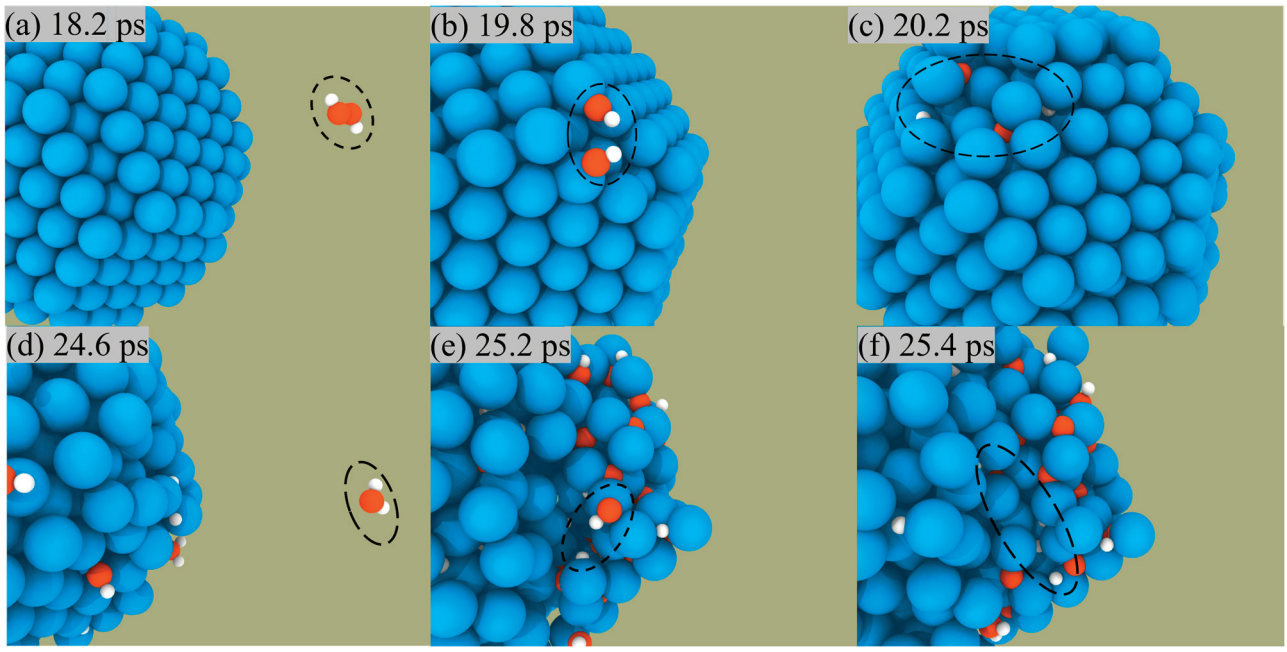

Figure 5. Snapshots of the reaction between H_2O_2 and the surface of ANPs (**a**–**c**), snapshots of the reaction between H_2O and the surface of ANPs (**d**–**f**) in Al/H_2O_2/H_2O (30%) system.

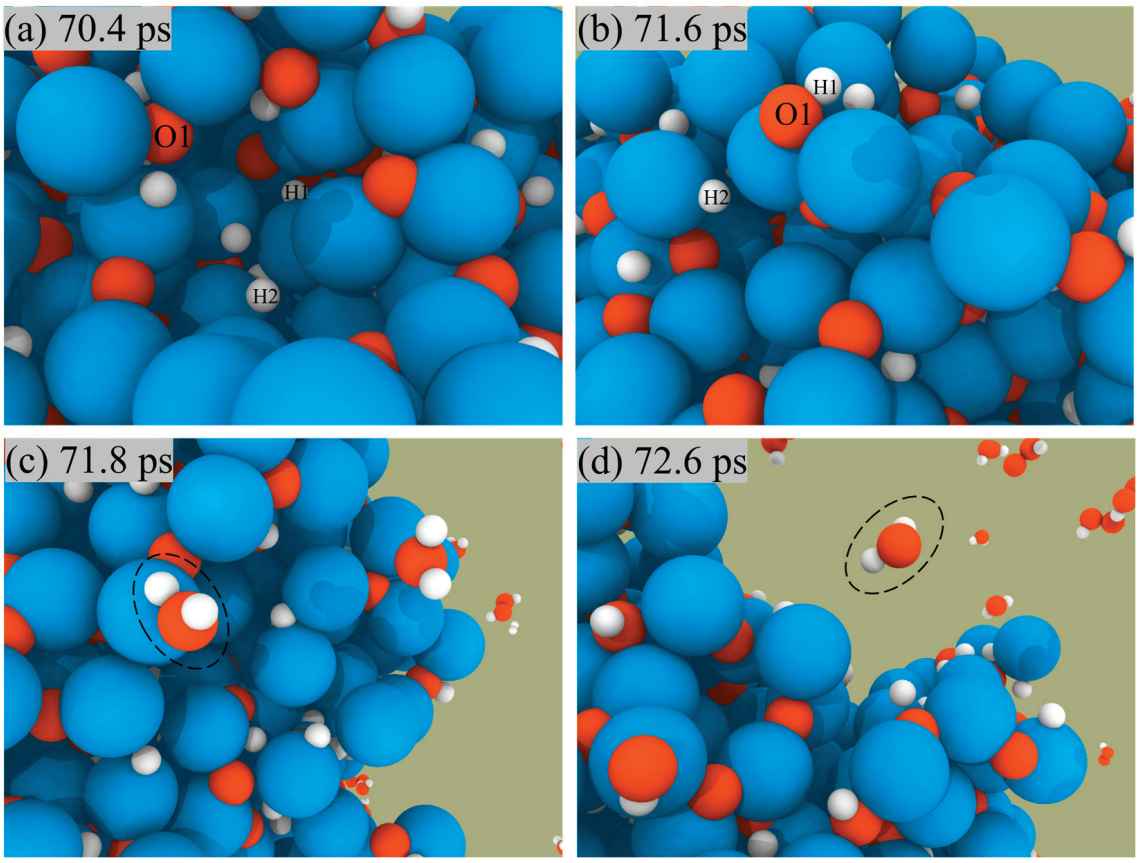

Figure 6. Snapshot of H_2O formation (**a**–**c**) and desorption (**d**) from the surface of ANPs in Al/H_2O_2/H_2O (30%) system.

The two paths for producing H_2 are shown in Figure 7. In the first pathway, the H atoms on the surface of ANPs come close to each other, then form H-H bonds, and finally release from the surface of ANPs to generate H_2 molecules. The other mechanism is that the free H radical approaches the H_2O_2 molecule in solution and then combines with an H of the H_2O_2 molecule to form an H_2 molecule and a peroxide hydroxyl radical (•OOH). The reaction proceeds as in Equation (3).

$$H + H_2O_2 \rightarrow H_2 + HO_2 \quad (3)$$

Since the number of H radicals is relatively small, H_2 is mainly generated by the first pathway.

Similarly, Figure 8 shows the two pathways for generating O_2. Nevertheless, unlike the production of H_2, O_2 does not release from the surface of ANPs, which also indicates that the Al-O bond is much more stable than the Al-H bond.

$$H_2O_2 + OH \rightarrow H_2O + HO_2 \quad (4)$$

$$HO_2 + OH \rightarrow H_2O + O_2 \quad (5)$$

$$HO_2 + H_2O \rightarrow H_3O + O_2 \quad (6)$$

Both mechanisms have the same reaction in the first stage, i.e., Equation (4), in which OH radicals in solution attack the H_2O_2 molecule to form an H_2O molecule and an OOH radical. The difference is that in the first mechanism, i.e., Equation (5), the OH radical attacks the OOH radical again followed by the generation of an H_2O molecule and an O_2 molecule. The second mechanism, Equation (6), involves the H_2O molecule continually

approaching the OOH radical and then seizing one of its H, eventually forming an H_3O radical with an O_2 molecule.

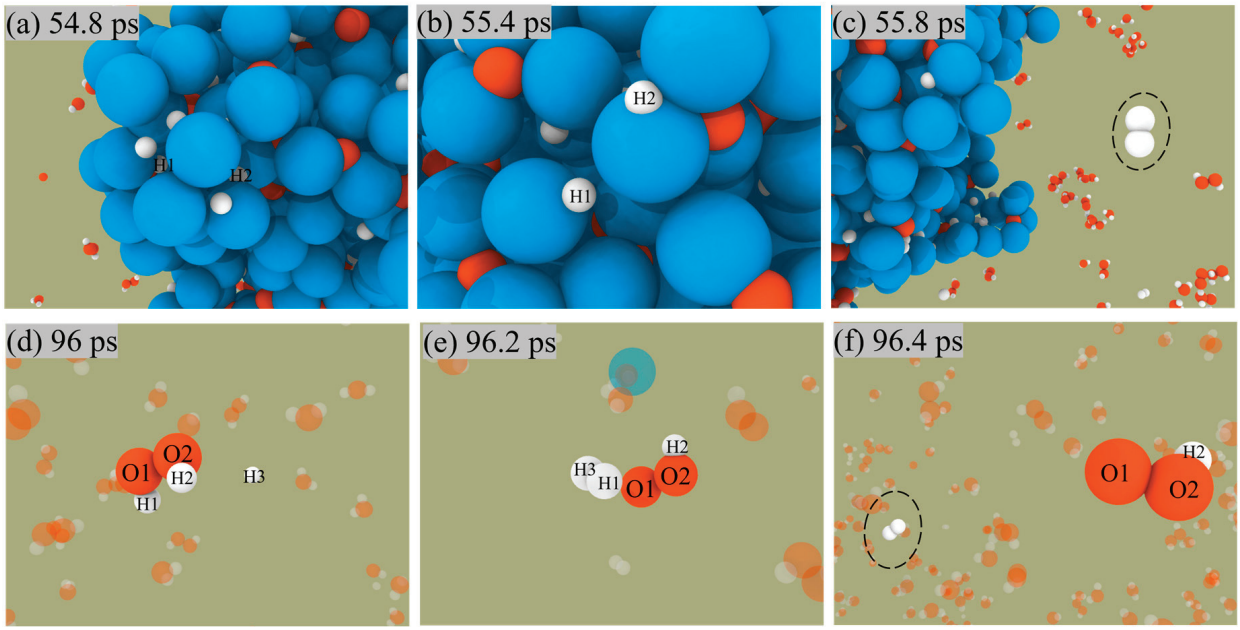

Figure 7. Snapshot of H_2 generation from ANPs surface (**a**–**c**) and solution (**d**–**f**) in Al/H_2O_2/H_2O (30%) system.

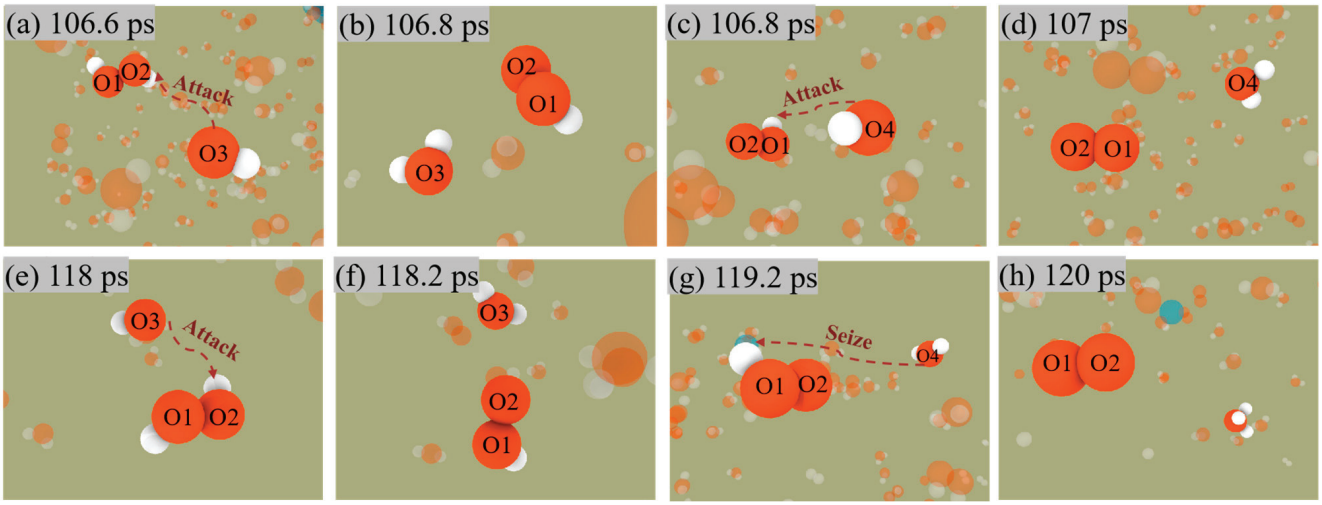

Figure 8. Snapshot of O_2 generation by the first mechanism (**a**–**d**) and the second mechanism (**e**–**h**) in Al/H_2O_2/H_2O (30%) system.

3.3. Adiabatic Combustion Processes in the ANPs/H_2O_2/H_2O System

Under experimental conditions, H_2O_2 usually contains water in varying proportions, so we wanted to investigate the influence of the addition of H_2O on the temperature at which Al/H_2O_2 burned. The simulation under the NVT ensemble and constant heating rate cannot reflect the influence of H_2O on combustion. To address this problem, we simulated 250 ps with an NVE ensemble to obtain the adiabatic flame temperature of the combustion. Figure 9a shows the evolution of temperature over time for systems containing different proportions of H_2O. We considered the equilibrium temperature at the end of the simulation as the adiabatic flame temperature of the combustion system. Then, it was found that the temperature of the systems all reached extreme values after 100 ps and remained stable, while the temperature of the adiabatic flame decreased with the increase

in the percentage of H_2O. This means that the adiabatic flame temperature decreased from 4612 K to 4380 K as the percentage of water increased from 0 to 30%.

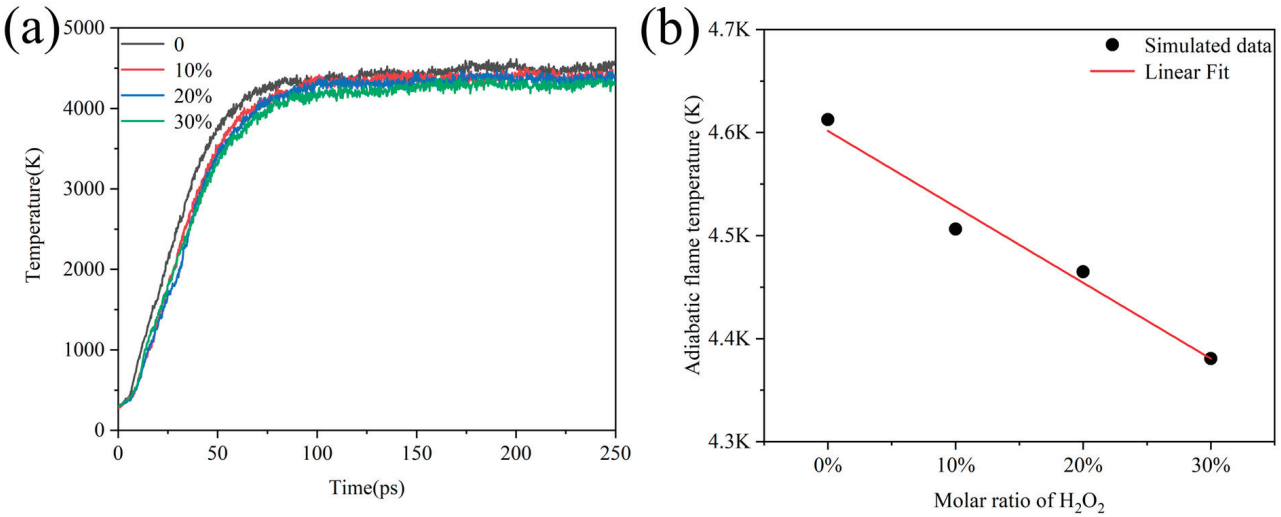

Figure 9. (**a**) Evolution of adiabatic flame temperature over time for $Al/H_2O_2/H_2O$ systems with different percentages and (**b**) linear fitting of adiabatic flame temperature to the ratio of H_2O under steady state combustion.

3.4. Influence of the Heating Speed on the Combustion of the System

To obtain reliable results of the simulations, we simulated the $Al/H_2O_2/H_2O$ (30%) system with 60 K/ps, 30 K/ps, and 15 K/ps heating speed. Figure 10 shows the comparative analysis of the number of Al-H bonds, Al-O bonds, H_2, and O_2 in systems with different heating speeds. As shown in Figure 10a,b, in the early stages of the reaction, the rate of Al-O and Al-H bond formation is positively correlated with the heating speed. The peak of the Al-H bonds is also delayed as the heating speed decreases. We also found a plateau in Al-O bonds formation at a heating rate of 15 K/ps. It is not difficult to notice that the rate of early Al-O bonds formation actually decreases briefly at 30 K/ps and 60 K/ps heating rates. This may be due to the fact that the final number of Al-O bonds is close to each other at temperatures of 750 K~1500 K, and the lower heating rate amplifies the appearance of this plateau period. At the heating rate of 60 K/ps, the yield of H_2 molecules is significantly reduced. This is attributed to the fact that the system reaches high temperatures early, prompting the reaction between H_2 molecules and O_2 molecules to form H_2O.

3.5. Influence of the Oxide Layer on the Combustion of the System

Considering the passivation of Al in the natural environment, we coated the surface of ANPs with an oxide layer in the simulation. Al particles with a diameter of 2.8 nm were placed in a periodic box of size 10.0 nm × 10.0 nm × 10.0 nm containing 200 O_2 molecules and then subjected to NVT simulations at 200 K for 50 ps, cycling six times. The detailed process is shown in Figure S2. Eventually, the $Al_{675}O_{314}/H_2O_2/H_2O$ system was obtained. The $Al_{675}O_{314}/H_2O_2/H_2O$ system was then simulated under the same simulation conditions as the $Al/H_2O_2/H_2O$ system.

As shown in Figure 11, we found that the coverage of the oxide layer resulted in a decrease in the reactive aluminum content of the ANPs, so the rate of H_2O_2 consumption decreased. Due to the existence of the oxide layer and the fact that the Al-O bond is more stable than the Al-H bond, the O atoms occupied the reaction site of the ANPs earlier, resulting in the H atoms on the ANPs reaching a maximum value earlier, and the H content on the Al was lower. Since the release of H_2 from the surface of ANPs is the most dominant source of H_2 in the product, ANPs that have been passivated contain more O atoms. Hence, the reaction favored the evolution of H_2O from the surface of ANPs over the production of H_2. The yield of H_2O increased in the systems with an oxide layer, while the yield of H_2

became poor. Understandably, due to the passivation of Al in the initial stage, the active aluminum content of the ANPs was reduced, the $Al_{675}O_{314}/H_2O_2/H_2O$ system was less energetic, the reaction released less energy (22% less compared to $Al_{675}/H_2O_2/H_2O$ (30%) system), and the adiabatic flame temperature decreased from 4357 K to 3256 K.

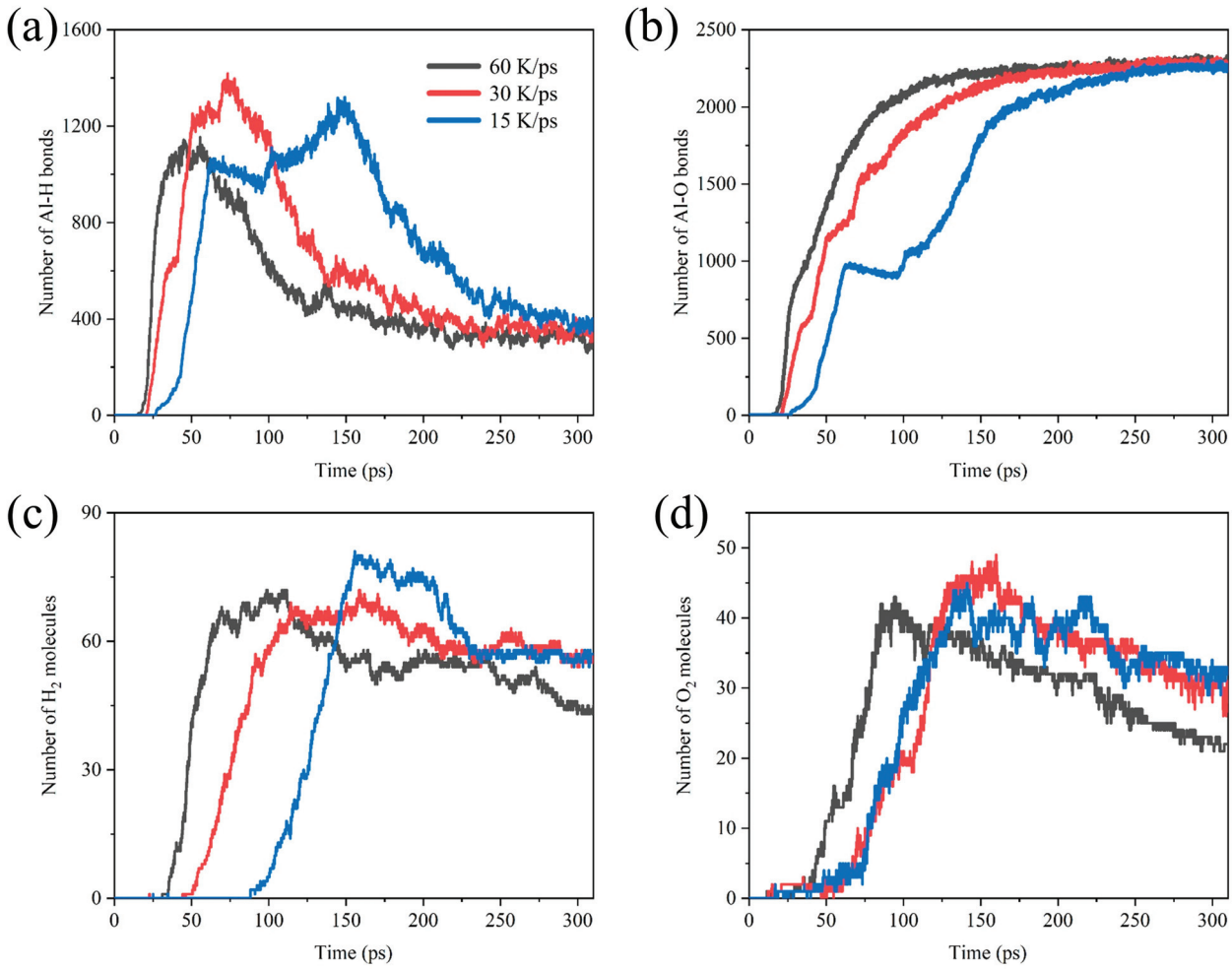

Figure 10. Comparative analysis of the number of (**a**) Al-H bonds, (**b**) Al-O bonds, (**c**) H_2 molecules, and (**d**) O_2 molecules in the $Al/H_2O_2/H_2O$ (30%) system with different heating speeds.

The evolution of the morphology of ANPs with different molar ratios of $Al/H_2O_2/H_2O$ systems and systems with oxide layer is shown in Figure 12. In connection with Figure 13, we found that the violent combustion of ANPs in the H_2O_2/H_2O system also changed its morphology. The temperature of the system gradually increased with time, and the epitaxial growth of the chain-like structure of ANPs became more apparent, accompanied by an increase in the internal voids. When the temperature reached the melting point of Al (about 933 K), many small fragments of Al clusters were also generated. However, as the system temperature continued to increase, the chain-like structure of ANPs gradually disappeared, the volume contracted, agglomeration occurred, and the number of Al clusters gradually decreased. The addition of H_2O also influences the morphological evolution of ANPs. At 50 ps, the morphology of ANPs in the $Al/H_2O_2/H_2O$ system with 30% H_2O was only slightly deformed. As the H_2O content decreased, the deformation of ANPs increased and even cavities were formed. In addition, the ANPs would also separate to form more and more small fragments. While the addition of the oxide layer reduced the reaction energy release of the system, the ANPs deformed even less and basically did not rupture or decompose into small fragments.

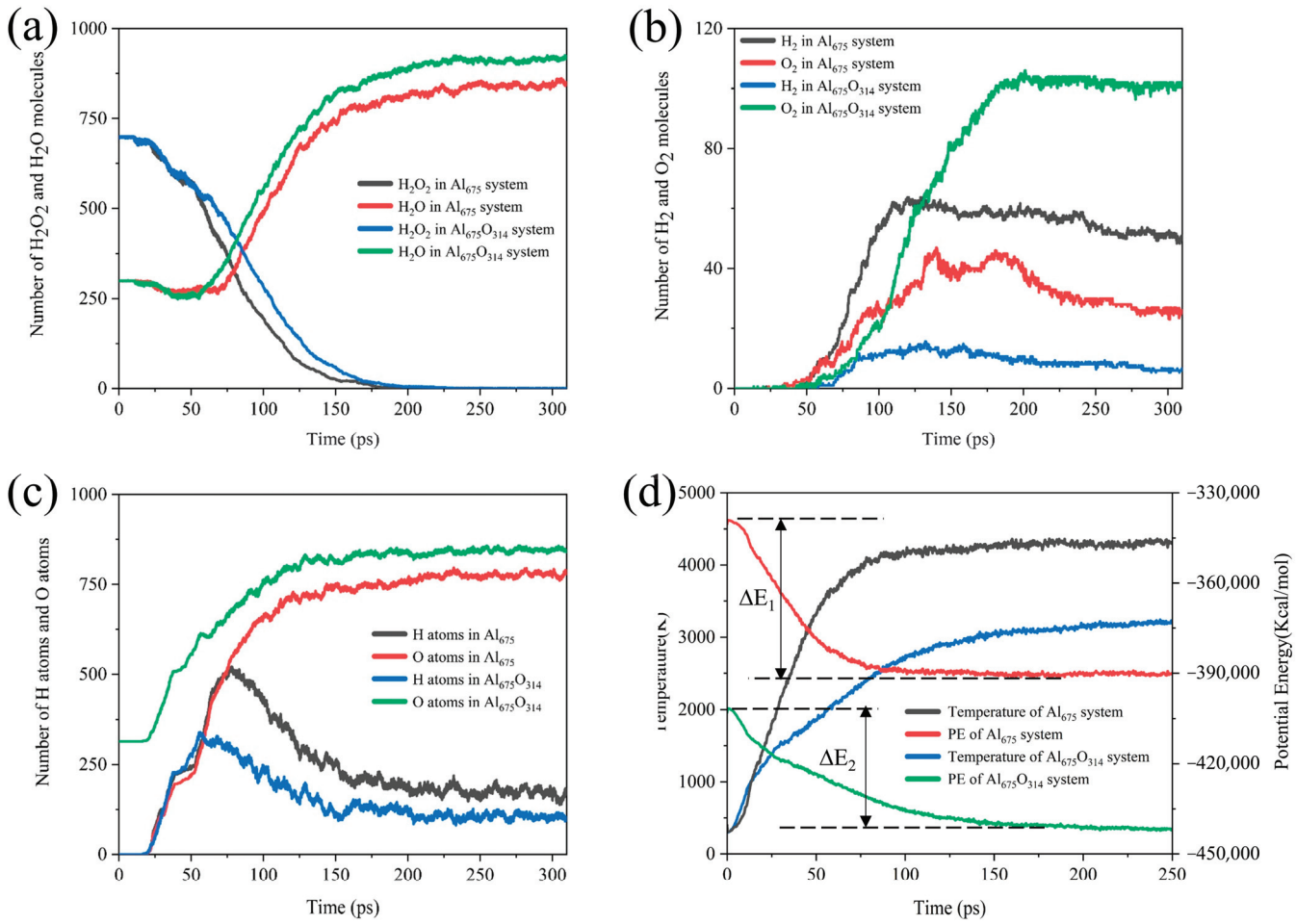

Figure 11. Evolution of (**a**) the amount of H_2O_2/H_2O, (**b**) H_2/O_2, (**c**) the H and O atoms on ANPs over time, and (**d**) the simulated temperature and potential energy over time under adiabatic conditions in the $Al_{675}/H_2O_2/H_2O$ (30%) system and $Al_{675}O_{314}/H_2O_2/H_2O$ (30%) system.

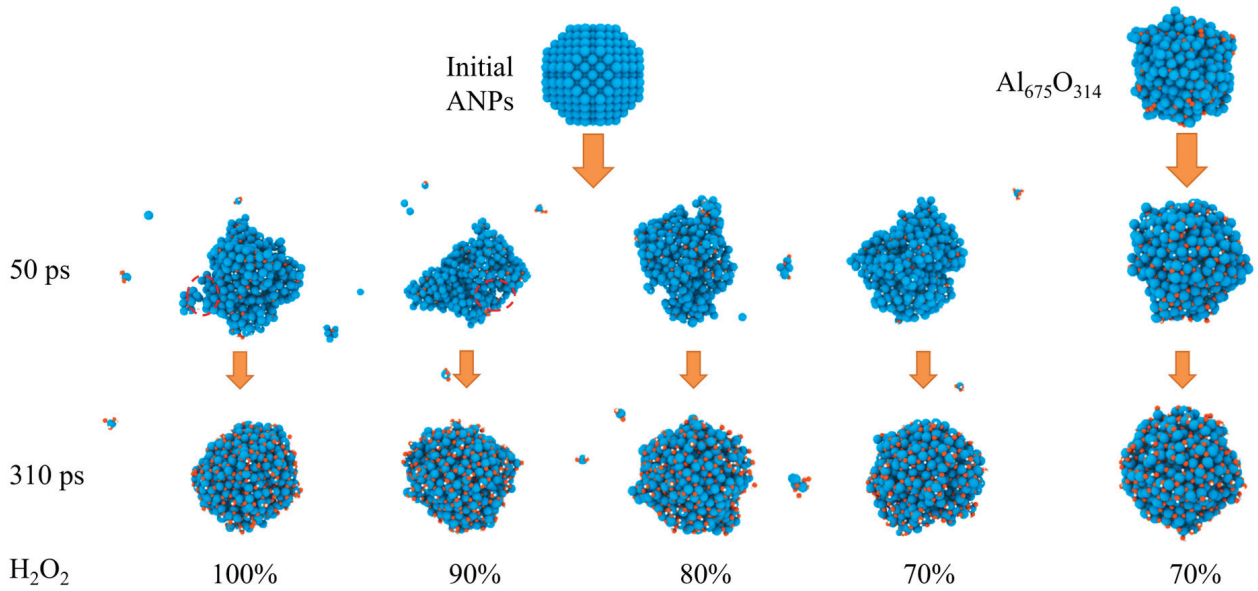

Figure 12. Evolution of the morphology of ANPs in systems with different molar ratios of $Al/H_2O_2/H_2O$ and in systems with an oxide layer (Al, oxygen, and hydrogen are blue, orange, and white, respectively).

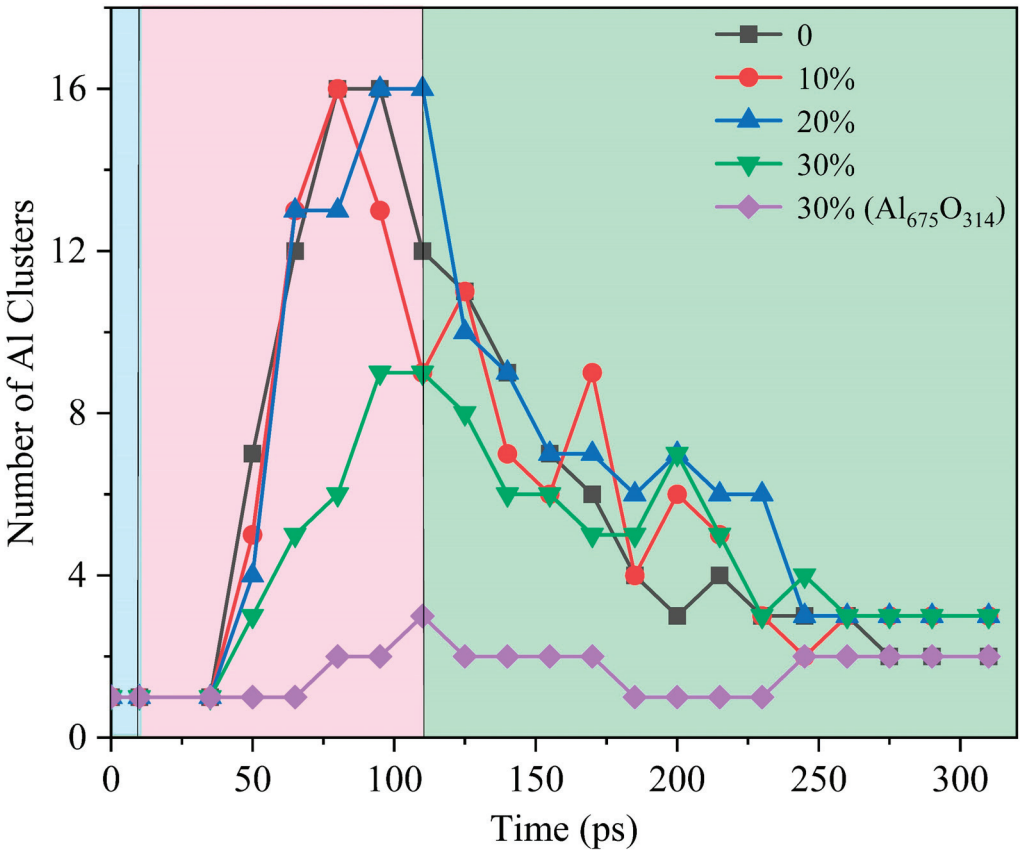

Figure 13. Evolution of the number of Al clusters in five systems (blue background for the configuration optimization phase, pink background for the heating phase, green background for the thermostatic phase).

4. Conclusions

In summary, we simulated the effect of H_2O addition on Al/H_2O_2 combustion by using the ReaxFF force field. Here are several significant findings and conclusions from this paper:

(1) With the percentage of H_2O increased from 0 to 30%, the number of Al-O bonds on the ANPs decreases, and the number of Al-H bonds increases. Meanwhile, the increase in the water content would increase the production of the final product H_2 and hinder the production of O_2.

(2) The combustion mechanism of the $Al/H_2O_2/H_2O$ system was investigated from an atomistic perspective. H_2O_2 molecules and H_2O molecules were adsorbed on the surface of ANPs, then chemically activated and decomposed into OH radicals and H radicals, which were finally captured by ANPs. The Al-O bond is more stable than the Al-H bond, which is why H_2O and H_2 could be generated and desorbed from the ANPs surface, while O_2 could not be generated through this pathway. H and O would compete for the reaction sites of ANPs, whereby the number of Al-O bonds would be far higher than that of Al-H and Al-OH bonds as the simulation proceeds, and $Al[O]_x$ would be converted from low to high coordination.

(3) The effect of the content of H_2O on the adiabatic flame of the $Al/H_2O_2/H_2O$ system was investigated. The results showed that the adiabatic flame temperature decreased from 4612 K to 4380 K as the percentage of water increased from 0 to 30%.

(4) In addition, the influence of different heating speed on the combustion of the system was investigated. The simulation results indicated that the heating speed only affected the early formation of Al-O and Al-H bonds, but not their final number. A high

heating rate promoted the reaction between the H_2 molecules and the O_2 molecules to form H_2O.

(5) Finally, the combustion of passivated ANPs with H_2O_2/H_2O was simulated. The coating of the oxide layer would reduce the rate of H_2O_2 consumption and H_2 production significantly while preventing drastic deformation of the ANPs' morphology.

Supplementary Materials: The following supporting information can be downloaded at: https://www.mdpi.com/article/10.3390/molecules29071567/s1. Figure S1: Evolution of the number of H-H, H-O, Al-H, Al-O, O-O bonds for each system. Figure S2: Formation of oxide layer on the surface of ANPs.

Author Contributions: Conceptualization, X.Y. and P.Z.; methodology, H.Z.; software, S.Y.; validation, X.Y., H.Z. and S.Y.; formal analysis, X.Y.; investigation, X.Y.; resources, P.Z.; data curation, H.Z.; writing—original draft preparation, X.Y.; writing—review and editing, S.Y.; visualization, X.Y.; supervision, H.Z.; project administration, S.Y. All authors have read and agreed to the published version of the manuscript.

Funding: This research was funded by the Carbon Neutrality Research Institute Fund (CNIF20220205) and Shandong Natural Science Foundation (ZR2021MB055).

Institutional Review Board Statement: Not applicable.

Informed Consent Statement: Not applicable.

Data Availability Statement: Data are contained within the article or Supplementary Materials.

Conflicts of Interest: Author Heng Zhang was employed by the company Shandong Chambroad Holding Co., Ltd. The remaining authors declare that the research was conducted in the absence of any commercial or financial relationships that could be construed as a potential conflict of interest.

References

1. Zhang, Q.H.; Shreeve, J.M. Ionic liquid propellants: Future fuels for space propulsion. *Chem. Eur. J.* **2013**, *19*, 15446–15451. [CrossRef] [PubMed]
2. Gohardani, A.S.; Stanojev, J.; Demaire, A.; Anflo, K.; Persson, M.; Wingborg, N.; Nilsson, C. Green space propulsion: Opportunities and prospects. *Prog. Aerosp. Sci.* **2014**, *71*, 128–149. [CrossRef]
3. Nosseir, A.E.S.; Cervone, A.; Pasini, A. Review of state-of-the-art green monopropellants: For propulsion systems analysts and designers. *Aerospace* **2021**, *8*, 20. [CrossRef]
4. Barato, F. Review of alternative sustainable fuels for hybrid rocket propulsion. *Aerospace* **2023**, *10*, 643. [CrossRef]
5. Santos, L.B.; Ribeiro, C.A.; Capela, J.M.V.; Crespi, M.S.; Pimentel, M.A.S.; De Julio, M. Kinetic parameters for thermal decomposition of hydrazine. *J. Therm. Anal. Calorim.* **2013**, *113*, 1209–1216. [CrossRef]
6. Kumar, P. Advances in phase stabilization techniques of AN using KDN and other chemical compounds for preparing green oxidizers. *Def. Technol.* **2019**, *15*, 949–957. [CrossRef]
7. Guseinov, S.L.; Fedorov, S.G.; Kosykh, V.A.; Storozhenko, P.A. Hydrogen peroxide decomposition catalysts used in rocket engines. *Russ. J. Appl. Chem.* **2020**, *93*, 467–487. [CrossRef]
8. Jung, S.; Choi, S.; Heo, S.; Kwon, S. Scaling of catalyst bed for hydrogen peroxide monopropellant thrusters using catalytic decomposition modeling. *Acta Astronaut.* **2021**, *187*, 167–180. [CrossRef]
9. Okninski, A.; Surmacz, P.; Bartkowiak, B.; Mayer, T.; Sobczak, K.; Pakosz, M.; Kaniewski, D.; Matyszewski, J.; Rarata, G.; Wolanski, P. Development of green storable hybrid rocket propulsion technology using 98% hydrogen peroxide as oxidizer. *Aerospace* **2021**, *8*, 234–257. [CrossRef]
10. Markandan, K.; Chin, J.K.; Cheah, K.H.; Tan, M.T.T. Recent developments in ceramic microthrusters and the potential applications with green propellants: A review. *Clean Technol. Environ. Policy* **2018**, *20*, 1941–1950. [CrossRef]
11. Wang, Z.D.; Herbinet, O.; Hansen, N.; Battin-Leclerc, F. Exploring hydroperoxides in combustion: History, recent advances and perspectives. *Prog. Energy Combust. Sci.* **2019**, *73*, 132–181. [CrossRef]
12. Parzybut, A.; Surmacz, P.; Gut, Z. Impact of hydrogen peroxide concentration on manganese oxide and platinum catalyst bed performance. *Aerospace* **2023**, *10*, 556. [CrossRef]
13. Cong, Y.; Zhang, T.; Li, T.; Suo, J.W.; Wang, X.D.; Ma, L.; Liang, D.B.; Lin, L.W. Propulsive performance of a hypergolic H_2O_2/kerosene bipropellant. *J. Propuls. Power* **2004**, *20*, 83–86. [CrossRef]
14. Li, X.T.; Tian, H.; Yu, N.J.; Cai, G.B. Experimental investigation of fuel regression rate in a HTPB based lab-scale hybrid rocket motor. *Acta Astronaut.* **2014**, *105*, 95–100. [CrossRef]
15. Tian, H.; Sun, X.L.; Guo, Y.D.; Wang, P.F. Combustion characteristics of hybrid rocket motor with segmented grain. *Aerosp. Sci. Technol.* **2015**, *46*, 537–547. [CrossRef]

16. Li, S.; Ge, Y.F.; Wei, X.L.; Li, T. Mixing and combustion modeling of hydrogen peroxide/kerosene shear-coaxial jet flame in lab-scale rocket engine. *Aerosp. Sci. Technol.* **2016**, *56*, 148–154. [CrossRef]
17. Li, H.X.; Ye, L.; Wei, X.L.; Li, T.; Li, S. The design and main performance of a hydrogen peroxide/kerosene coaxial-swirl injector in a lab-scale rocket engine. *Aerosp. Sci. Technol.* **2017**, *70*, 636–643. [CrossRef]
18. John, J.; Nandagopalan, P.; Baek, S.W.; Cho, S.J. Hypergolic ignition delay studies of solidified ethanol fuel with hydrogen peroxide for hybrid rockets. *Combust. Flame* **2020**, *212*, 205–215. [CrossRef]
19. Okninski, A. On use of hybrid rocket propulsion for suborbital vehicles. *Acta Astronaut.* **2018**, *145*, 1–10. [CrossRef]
20. Starik, A.M.; Savel'ev, A.M.; Titova, N.S. Specific features of ignition and combustion of composite fuels containing aluminum nanoparticles (Review). *Combust. Explos. Shock. Waves* **2015**, *51*, 197–222. [CrossRef]
21. Sundaram, D.S.; Yang, V.; Zarko, V.E. Combustion of nano aluminum particles (Review). *Combust. Explos. Shock. Waves* **2015**, *51*, 173–196. [CrossRef]
22. DeLuca, L.T. Overview of Al-based nanoenergetic ingredients for solid rocket propulsion. *Def. Technol.* **2018**, *14*, 357–365. [CrossRef]
23. Vadhe, P.P.; Pawar, R.B.; Sinha, R.K.; Asthana, S.N.; Rao, A.S. Cast aluminized explosives. *Combust. Explos. Shock. Waves* **2008**, *44*, 461–477. [CrossRef]
24. Kim, Y.; Park, Y.; Yoh, J.J. Slow and rapid thermal decomposition characteristics of enhanced blast explosives for burning in fuel-rich, oxygen-rich conditions. *Thermochim. Acta* **2019**, *678*, 178300. [CrossRef]
25. Pang, W.Q.; Fan, X.Z.; Wang, K.; Chao, Y.M.; Xu, H.X.; Qin, Z.; Zhao, F.Q. Al-based nano-sized composite energetic materials (Nano-CEMs): Preparation, characterization, and performance. *Nanomaterials* **2020**, *10*, 1039. [CrossRef] [PubMed]
26. Jayaraman, K.; Sivakumar, P.M.; Zarrabi, A.; Sivakumar, R.; Jeyakumar, S. Combustion characteristics of nanoaluminium-based composite solid propellants: An overview. *J. Chem.* **2021**, *2021*, 5520430. [CrossRef]
27. He, Q.Q.; Wang, J.; Mao, Y.F.; Cao, W.; Chen, J.; Nie, F.D. An effective strategy to improve combustion and pressure output performance of HMX/Al. *Combust. Flame* **2022**, *244*, 112281. [CrossRef]
28. Sabourin, J.L.; Risha, G.A.; Yetter, R.A.; Son, S.F.; Tappan, B.C. Combustion characteristics of nanoaluminum, liquid water, and hydrogen peroxide mixtures. *Combust. Flame* **2008**, *154*, 587–600. [CrossRef]
29. Zaseck, C.R.; Son, S.F.; Pourpoint, T.L. Combustion of micron-aluminum and hydrogen peroxide propellants. *Combust. Flame* **2013**, *160*, 184–190. [CrossRef]
30. Schmitt, M.M.; Bowden, P.R.; Tappan, B.C.; Henneke, D. Steady-state shock-driven reactions in mixtures of nano-sized aluminum and dilute hydrogen peroxide. *J. Energetic Mater.* **2018**, *36*, 266–277. [CrossRef]
31. Sundaram, D.S.; Yang, V. Combustion of micron-sized aluminum particle, liquid water, and hydrogen peroxide mixtures. *Combust. Flame* **2014**, *161*, 2469–2478. [CrossRef]
32. Chu, Q.Z.; Shi, B.L.; Liao, L.J.; Luo, K.H.; Wang, N.F.; Huang, C.G. Ignition and oxidation of core-shell Al/Al_2O_3 nanoparticles in an oxygen atmosphere: Insights from molecular dynamics simulation. *J. Phys. Chem. C* **2018**, *122*, 29620–29627. [CrossRef]
33. Ashraf, C.; van Duin, A.C.T. Extension of the ReaxFF combustion force field toward syngas combustion and initial oxidation kinetics. *J. Phys. Chem. A* **2017**, *121*, 1051–1068. [CrossRef] [PubMed]
34. Zeng, H.D.; Cheng, X.L.; Zhang, C.Y.; Lu, Z.P. Responses of core-shell Al/Al_2O_3 nanoparticles to heating: ReaxFF molecular dynamics simulations. *J. Phys. Chem. C* **2018**, *122*, 9191–9197. [CrossRef]
35. Hong, D.K.; Li, Z.H.; Si, T.; Guo, X. A study of the effect of H_2O on char oxidation during O_2/H_2O combustion using reactive dynamic simulation. *Fuel* **2020**, *280*, 118713. [CrossRef]
36. Liu, J.P.; Liu, P.G.; Wang, M.J.; Wang, W.C.; Lv, F.W.; Sun, R.C.; Yang, Y.X. Combustion of Al nanoparticles coated with ethanol/ether molecules by non-equilibrium molecular dynamics simulations. *Mater. Today Commun.* **2020**, *22*, 100819. [CrossRef]
37. Cheng, Y.X.; Zhao, Y.; Zhao, F.Q.; Xu, S.Y.; Ju, X.H.; Ye, C.C. ReaxFF simulations on the combustion of Al and n-butanol nanofluid. *Fuel* **2022**, *330*, 125465. [CrossRef]
38. Bai, Z.Z.; Jiang, X.Z.; Luo, K.H. Understanding mechanisms of pyridine oxidation with ozone addition via reactive force field molecular dynamics simulations. *Chem. Eng. Sci.* **2023**, *266*, 118290. [CrossRef]
39. Li, G.; Niu, L.L.; Hao, W.Z.; Liu, Y.; Zhang, C.Y. Atomistic insight into the microexplosion-accelerated oxidation process of molten aluminum nanoparticles. *Combust. Flame* **2020**, *214*, 238–250. [CrossRef]
40. Zhao, Y.; Ma, D.X.; Zhao, F.Q.; Xu, S.Y.; Ju, X.H. Atomic insights into the combustion behavior of Al nano-droplets with H_2O vapor at high temperature. *Appl. Surf. Sci.* **2022**, *586*, 152777. [CrossRef]
41. Hao, W.Z.; Li, G.; Niu, L.L.; Gou, R.J.; Zhang, C.Y. Molecular dynamics insight into the evolution of Al nanoparticles in the thermal decomposition of energetic materials. *J. Phys. Chem. C* **2020**, *124*, 10783–10792. [CrossRef]
42. Zhao, Y.; Mei, Z.; Zhao, F.Q.; Xu, S.Y.; Ju, X.H. Atomic perspectives revealing the evolution behavior of aluminum nanoparticles in energetic materials. *Appl. Surf. Sci.* **2021**, *563*, 150296. [CrossRef]
43. van Duin, A.C.T.; Dasgupta, S.; Lorant, F.; Goddard, W.A. ReaxFF: A reactive force field for hydrocarbons. *J. Phys. Chem. A* **2001**, *105*, 9396–9409. [CrossRef]
44. Chenoweth, K.; van Duin, A.C.T.; Goddard, W.A. ReaxFF reactive force field for molecular dynamics simulations of hydrocarbon oxidation. *J. Phys. Chem. A* **2008**, *112*, 1040–1053. [CrossRef] [PubMed]

45. Senftle, T.P.; Hong, S.; Islam, M.M.; Kylasa, S.B.; Zheng, Y.X.; Shin, Y.K.; Junkermeier, C.; Engel-Herbert, R.; Janik, M.J.; Aktulga, H.M.; et al. The ReaxFF reactive force-field: Development, applications and future directions. *npj Comput. Mater.* **2016**, *2*, 15011. [CrossRef]
46. Plimpton, S. Fast parallel algorithms for short-range molecular-dynamics. *J. Comput. Phys.* **1995**, *117*, 15011. [CrossRef]
47. Aktulga, H.M.; Fogarty, J.C.; Pandit, S.A.; Grama, A.Y. Parallel reactive molecular dynamics: Numerical methods and algorithmic techniques. *Parallel Comput.* **2012**, *38*, 245–259. [CrossRef]
48. Hong, S.; van Duin, A.C.T. Atomistic-scale analysis of carbon coating and its effect on the oxidation of aluminum nanoparticles by ReaxFF-molecular dynamics simulations. *J. Phys. Chem. C* **2016**, *120*, 9464–9474. [CrossRef]
49. Li, G.; Niu, L.L.; Xue, X.G.; Hao, W.Z.; Liu, Y.; Zhang, C.Y. Atomic perspective about the reaction mechanism and H_2 production during the combustion of Al nanoparticles/H_2O_2 bipropellants. *J. Phys. Chem. A* **2020**, *124*, 7399–7410. [CrossRef]
50. Dong, R.K.; Mei, Z.; Zhao, F.Q.; Xu, S.Y.; Ju, X.H. Initial oxidation of nano-aluminum particles by H_2O/H_2O_2: Molecular dynamics simulation. *Int. J. Hydrogen Energy* **2021**, *46*, 1234–1245. [CrossRef]
51. Martínez, L.; Andrade, R.; Birgin, E.G.; Martínez, J.M. PACKMOL: A package for building initial configurations for molecular dynamics simulations. *J. Comput. Chem.* **2009**, *30*, 2157–2164. [CrossRef] [PubMed]
52. Zheng, M.; Li, X.X.; Wang, M.J.; Guo, L. Dynamic profiles of tar products during Naomaohu coal pyrolysis revealed by large-scale reactive molecular dynamic simulation. *Fuel* **2019**, *253*, 910–920. [CrossRef]
53. Stukowski, A. Visualization and analysis of atomistic simulation data with OVITO-the Open Visualization Tool. *Model. Simul. Mater. Sci. Eng.* **2010**, *18*, 15012. [CrossRef]
54. Luo, Y.R.; Kerr, J.A. *Bond Dissociation Energies*; CRC Press: Boca Raton, FL, USA, 2012; Volume 89, p. 89.

molecules

MDPI

Article

Electronic Modulation of Cu Catalytic Interfaces by Functionalized Ionic Liquids for Enhanced CO_2 Reduction

Chuanhui Wang [1], Wei Zhou [1], Jiamin Ma [1], Zhi Wang [2,*] and Congyun Zhang [1,*]

[1] School of Environment and Geography, Qingdao University, Qingdao 266071, China; wch2022020768@163.com (C.W.); 13770594749@163.com (W.Z.); majiamin07@163.com (J.M.)
[2] School of Materials Science and Engineering, North University of China, Taiyuan 030051, China
* Correspondence: shikouri@163.com (Z.W.); zhangcy@qdu.edu.cn (C.Z.)

Abstract: The electrocatalytic CO_2 reduction reaction (CO_2RR) into value-added multi-carbon C_{2+} products holds significant promise for sustainable chemical synthesis and carbon-neutral energy cycles. Among the various strategies developed to enhance CO_2RR, the use of ionic liquids (ILs) has emerged as a powerful approach for modulating the local microenvironment and electronic structure of Cu-based metal catalysts. In this study, to unravel the molecular-level mechanisms underlying these enhancements, density functional theory calculations (DFTs) were employed to systematically explore how ILs with different terminal groups modulate the electronic reconstruction of the Cu surface, further affecting the *CO–*CO coupling and product selectivity. Electronic structure analyses reveal that ILs bearing polar moieties (–SH, –COOH) can synergistically enhance the interfacial electron accumulation and induce an upshift of the Cu d-band center, thereby strengthening *CO adsorption. In contrast, nonpolar IL (CH_3) exhibits negligible effects, underscoring the pivotal role of ILs' polarity in catalyst surface-state engineering. The free energy diagrams and transition state analyses reveal that ILs with polar groups significantly lower both the reaction-free energy and activation barrier associated with the *CO–*CO coupling step. This energetic favorability selectively inhibits the C_1 product pathways and hydrogen evolution reaction (HER), further improving the selectivity of C_2 products. These theoretical insights not only unveil the mechanistic origins of IL-induced performance enhancement but also offer predictive guidance for the rational design of advanced IL–catalyst systems for efficient CO_2 electroreduction.

Keywords: CO_2RR; ionic liquids; DFT; interface charge reconstruction; C–C coupling

1. Introduction

With the growing global demand for sustainable energy and the increasing emphasis on environmental protection [1,2], the electrocatalytic CO_2 reduction reaction (CO_2RR) has become a research hotspot [3,4]. Converting CO_2 into high value-added multi-carbon (C_{2+}) products can not only effectively alleviate the greenhouse effect but also achieve the recycling of carbon resources, providing a new approach for the energy transition [5,6]. Copper (Cu)-based materials are among the few metal catalysts capable of driving the electrochemical reduction in CO_2 toward C_{2+} products such as ethylene and ethanol [7,8]. Its distinct catalytic performance originates from a balanced *CO adsorption energy, which is sufficient to stabilize key reaction intermediates while still allowing for their subsequent C–C coupling. However, Cu-based materials still face several intrinsic challenges in the reduction in CO_2 to produce C_2 products. For example,

the product selectivity remains unsatisfactory, often yielding a complex mixture of hydrocarbons, which hinders the efficient isolation of a single high-purity target product [9,10]. In addition, there are also problems such as insufficient stability, high overpotential, and severe competition from side reactions such as hydrogen evolution [11,12], all of which collectively compromise the overall efficiency and practicality of Cu-mediated CO_2 reduction. In order to further enhance its catalytic performance and selectivity towards C_2 products, researchers have explored various strategies, including surface structure regulation (crystal plane regulation, vacancy engineering, changes in shape, size, roughness, etc.) [13–17], elemental doping (heteroatom doping and alloying) [18–21], regulation of the local microenvironment [22,23], as well as organic molecule modification (polymer binders or functional additives) [24,25]. Among these, the ionic liquid (IL)-modified system has shown great potential due to its unique customizable physical and chemical properties, including high electrochemical stability, excellent ionic conductivity, and good CO_2 solubility. In addition, the adjustable hydrophobicity of ILs can enhance the affinity for CO_2 and suppress the hydrogen evolution reaction (HER) [26,27].

ILs can achieve the microstructural regulation of Cu-based catalysts. For instance, 1-octyl-3-methylimidazolium chloride ([Omim]Cl) can act as a bifunctional reagent to prepare cuprous oxide nanoparticles with rough surfaces and oxygen vacancies [28]. These nanoparticles with such a unique structure are highly conducive to the adsorption of intermediates and facilitate the formation of C_{2+} products. In addition, ILs can also be used as electrolytes to regulate the interfacial microenvironment in electrochemical systems. ILs form a structured electric double layer at the electrode–electrolyte interface through the self-assembly of their cations and anions under applied potential [29,30]. This interfacial structure in turn influences the adsorption, stabilization, and transformation of CO_2RR intermediates [31–34]. Particularly, imidazolium-based ILs can form Im–CO_2 adducts with CO_2 reduction intermediates, thereby enhancing CO_2 adsorption and activation. Theoretical calculations corroborate these findings by revealing that ILs reduce the Gibbs free energy barriers associated with key intermediates and strengthen their adsorption energies, ultimately promoting more efficient catalytic activity.

ILs have exhibited remarkable functional advantages by virtue of the optimization of the catalyst structure and the regulation of the interfacial microenvironment. The adjustability of their cationic and anionic components has opened up broad space for the further precise control of catalytic activity and product selectivity. Shaikh and co-workers conducted kinetic calculations and demonstrated that varying amino acid-based anions influence the cycloaddition reaction with CO_2 and modulate electrostatic interactions [35]. The rational functionalization of Cu-based catalysts has been validated to facilitate for the direct cleavage of the C–O bond, thus maintaining a high selectivity for C_2H_4. Comparative studies on Cu electrodes modified with polyacrylic acid (PAA, with –COOH group) and polyvinylidene fluoride (PVDF, with –CF_2 group) reveal that Cu–PAA favors the formation of formic acid rather than Cu–PVDF (functionalized with –CF_2 group), whereas the Cu–PVDF system predominantly yields methane [36]. Moreover, adjusting the anionic components of polymerized ionic liquids (PILs) has been demonstrated to effectively modulate product distribution, highlighting the potential of molecular design strategies in steering CO_2RR selectivity [37]. Although the above examples illustrate that replacing the cations and anions in ionic liquids can accelerate the reaction and improve the reaction selectivity, most of these studies only remain at the macroscopic level of experiments. As for how the replacement of cations and anions affects the adsorption capacity of CO_2 step by step, as well as the subsequent coupling, bond-breaking, and hydrogenation processes, there is a lack of in-depth research on the specific principal mechanisms in between. We are in urgent

need of a means at the molecular level to uncover the essence of these influences, starting from the source of charges.

In the context of IL-modulated CO_2 electroreduction, density functional theory calculations (DFTs) [38] offer a robust theoretical framework for elucidating reaction pathways, quantifying energy barriers, identifying active sites, and capturing interfacial electronic interactions. For example, DFT calculations have demonstrated that the strong *CO absorption ability on $[BPy]BF_4$ is due to the charge accumulation around F^- [39]. Moreover, DFT analyses reveal that ILs can promote the *CO dimerization, a critical process in the formation of C_{2+} products [40]. Under certain IL-modified conditions, *CHO–*CHO coupling has also been identified as a thermodynamically favorable C–C bond formation pathway [41]. In addition, DFT can simulate solvent effects, interfacial interactions, and material stability. These insights are essential for understanding how ILs influence intermediate stabilization and transition-state energetics at the catalyst–electrolyte interface, thereby bridging molecular-level interactions with macroscopic catalytic performance and guiding the rational design of IL-integrated electrocatalytic systems.

Although DFT has achieved certain results in establishing the correlation between macroscopic experimental phenomena and reaction mechanisms at the molecular level, in the research field of ILs, there is still a lack of in-depth and comprehensive understanding of how the structural changes in IL functional groups affect the interfacial charge distribution, the stability of intermediates, and the C–C bonding energy barriers. The quantitative relationships between these group substitutions and key catalytic parameters, as well as the regulatory mechanisms of these group substitutions on the electrochemical reaction pathways, have not formed a systematic and complete theoretical framework. Therefore, starting from this point, we will study the influence of the groups on ILs on the catalytic reduction in CO_2 on the metal surface.

In this context, we focus on exploring the potential mechanisms of the catalytic performance of ILs with different functional groups in promoting the formation of C_2 products during the CO_2RR on the surface of Cu. Through the comprehensive application of DFT simulations, we systematically analyzed the microscopic processes of the interactions at the interface between Cu and ILs. The research results show that ILs achieve thermodynamic stability and kinetic acceleration by precisely regulating the interfacial microenvironment. At the electronic structure level, ILs adjust the charge distribution on the surface of Cu. IL (SH) and IL (COOH) transfer electrons to Cu, making the center of the d orbital of Cu closer to the Fermi level. This not only enhances the Cu–C interaction and stabilizes the *CO intermediate but also shortens the distance between C atoms. From an energy perspective, the modification of ILs (excluding IL (CH_3)) reduces the adsorption energy of intermediates. At the same time, it also reduces the thermodynamic energy difference and kinetic barriers of the C–C coupling step, ensuring the rapid progress of the rate-determining step (RDS) in CO_2RR. In addition, the interfacial charge microenvironment induced by ILs not only inhibits the conversion of CO_2 into C_1 products, thus increasing the selectivity of C_2 products, but also significantly suppresses the competitiveness of the HER through proton confinement and the inhibition of the *H desorption step. We have determined that Cu–IL (SH) is the most outstanding catalyst, which is due to the fact that the SH group transfers the most charge to Cu. So far, we have established the entire correlation system encompassing the functional groups, charge transfer, intermediate stability, coupling energy barrier, and product selectivity.

2. Simulation Details

We selected the Cu (1 0 0) surface [42,43] and designed several ILs with different terminal groups, including the mercapto group, carboxyl group, and methyl group, named 1-(3-mercaptopropyl)-3-methylimidazolium chloride (IL (SH)), 1-(3-carboxylpropyl)-3-methylimidazolium chloride (IL (COOH)), and 1-(3-butyl)-3-methylimidazolium chloride (IL (CH_3)). These were optimized and then placed on the Cu surface for surface optimization, named as Cu–IL (SH), Cu–IL (COOH), and Cu–IL (CH_3), respectively. Throughout the process, the Vienna Ab initio Simulation Package. 6.4.2 (VASP. 6.4.2) [44] was used to perform DFT calculations for the CO_2RR on the Cu surface and the Cu–IL interfaces modified by different types of ILs. The projector-augmented wave (PAW) [45] method was adopted to describe the interactions between ions and electrons, and the generalized gradient approximation (GGA) [46] with the Perdew–Burke–Ernzerhof (PBE) functional was used to calculate the energy and electronic structure properties of the materials. For the Cu (1 0 0) surface, a 6×6 supercell was used. To avoid the interactions between periodic units during the structural relaxation process, a vacuum space of more than 20 Å was set. During the optimization process, the bottom two layers of copper atoms were fixed, and other atoms were allowed to relax. To ensure the convergence of the total energy, the kinetic energy cutoff of the plane wave expansion was set to 500 eV, and all calculations used a Monkhorst-Pack $2 \times 2 \times 1$ K-point mesh [47]. The convergence criteria for force and energy were set to 0.01 eV/Å and 10^{-5} eV, respectively. In the frequency calculation, the energy convergence criterion was set to 10^{-7} eV. The electronic analysis used a $4 \times 4 \times 1$ K-point mesh. The Gibbs free energy (ΔG) for each step was calculated using the following formula: $\Delta G = \Delta E + \Delta E_{ZPE} - T\Delta S$, where ΔE is the adsorption energy of the adsorbate, T is the temperature (set to 300 K), and ΔE_{ZPE} and ΔS are the differences in zero-point energy and zero-point entropy, respectively. For the transition state calculation, the nudged elastic band (NEB) method was adopted [48], and it was checked whether the transition state had only one imaginary frequency. To obtain the influence mechanism of ILs on the charge distribution of the Cu surface, bader charge and differential charge calculations were carried out to describe the electron distribution on various Cu–IL catalysts and determine the optimal adsorption site of *CO. The adsorption energy of the *CO intermediate on the Cu–IL catalyst was defined as $E_{ads} = E_{total} - E_{surface} - E_{*CO}$, where E_{total} is the energy of the Cu or Cu–IL catalyst adsorbing *CO, $E_{surface}$ is the energy of the Cu surface or the Cu–IL catalyst, and E_{*CO} is the energy of the free *CO. The differential charge density of *CO adsorbed on the catalyst was defined as follows: $\Delta\rho = \rho_{A/B} - \rho_A - \rho_B$, where $\rho_{A/B}$ is the total charge density of *CO adsorbed on the Cu–IL catalyst, ρ_A is the charge density of the model after deleting the *CO intermediate from the total adsorption model, and ρ_B is the charge density of the model after removing the Cu or Cu–IL substrate from the total adsorption model.

The optimized structures of three ILs with different functional groups are shown in Figure $1a_1$–c_1. For the adsorption models of the three catalysts on the Cu base, we adhered to the principle of consistency and carried out adsorption at the same site. We designed several models with different bond lengths and bonding forms, optimized them, and found the optimal structures.

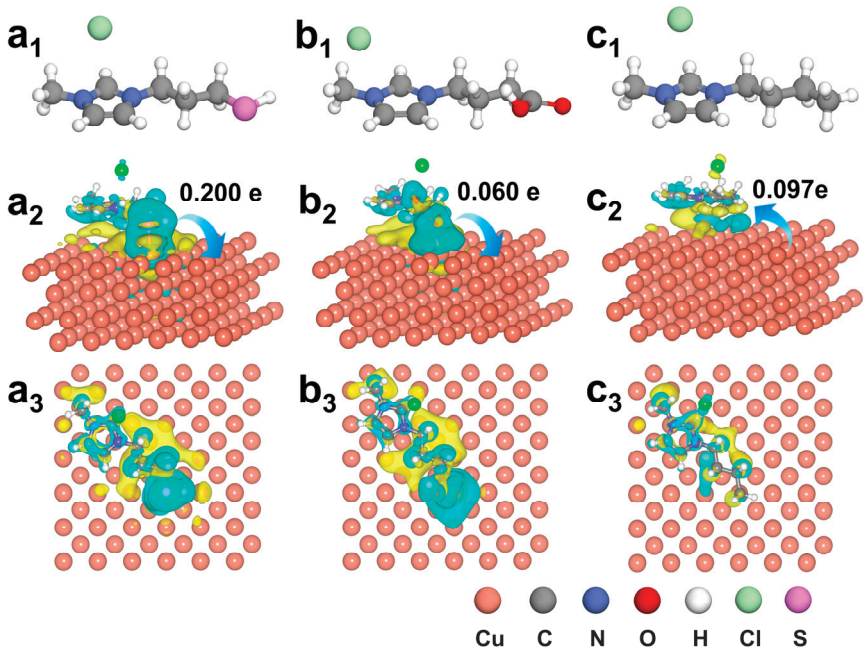

Figure 1. The configuration of ($\mathbf{a_1}$) IL (SH), ($\mathbf{b_1}$) IL (COOH), and ($\mathbf{c_1}$) Cu–IL (CH_3). The different charges of the ILs and Cu surfaces in three IL-modified catalyst systems, with cyan and yellow areas representing charge depletion and charge accumulation, respectively. ($\mathbf{a_2}$,$\mathbf{a_3}$) Cu–IL (SH), ($\mathbf{b_2}$,$\mathbf{b_3}$) Cu–IL (COOH), ($\mathbf{c_2}$,$\mathbf{c_3}$) the different charges of Cu–IL (CH_3).

3. Results and Discussion

3.1. Functional Group-Governed Electronic Reconstruction in IL-Modified Cu Catalysts

Based on the top view and side view configurations shown in Figures S1 and S2, the adsorption behavior of ILs on the Cu surface varies significantly with the nature of the functional group. Through systematic bader charge analysis (Figure S3) and differential charge density calculations (Figure 1), we quantitatively established distinct electron transfer patterns between IL modifiers and the Cu substrate. Notably, the Cu–IL (SH) system exhibits the most pronounced charge transfer with a net electron donation of 0.200 e from the IL (SH) to the Cu surface, followed by the Cu–IL (COOH) system, which transferred 0.060 e to the Cu. In contrast, Cu–IL (CH_3) displays an inverse charge transfer direction with 0.097 e migrating from Cu to the ILs. Bader charge analysis reveals significant interfacial electronic reorganization after the incorporation of different ILs, where Cu–IL (SH) manifests an enhanced electron accumulation surrounding the adsorption sites of Cu, whereas Cu–IL (CH_3) exhibits distinct electron depletion, demonstrating ligand-specific modulation of surface electron density. These results underscore the critical role of the functional group of the IL cation group in tuning interfacial charge distribution. This interfacial electronic reconstruction was further correlated with d-band center positioning through density of states (DOS) analysis (Figure 2). The calculated d-band center values followed the order of the d-band center size, as follows: Cu–IL (SH) (−2.326 eV) > Cu–IL (COOH) (−2.338 eV) > Cu (−2.342 eV) > Cu–IL (CH_3) (−2.347 eV). This systematic upshift of the Cu d-band center originates from electron donation by the ILs, which increases the electron occupancy of the Cu 3d orbitals. This charge transfer elevates the energy of antibonding states due to enhanced electron–electron repulsion and modified orbital overlap, thereby upshifting the d-band center. According to the d-band center theory, the elevated d-band center in Cu–IL (SH) suggests stronger adsorbate–substrate interactions due to the increased overlap between catalyst d-orbitals and adsorbate frontier molecular orbitals.

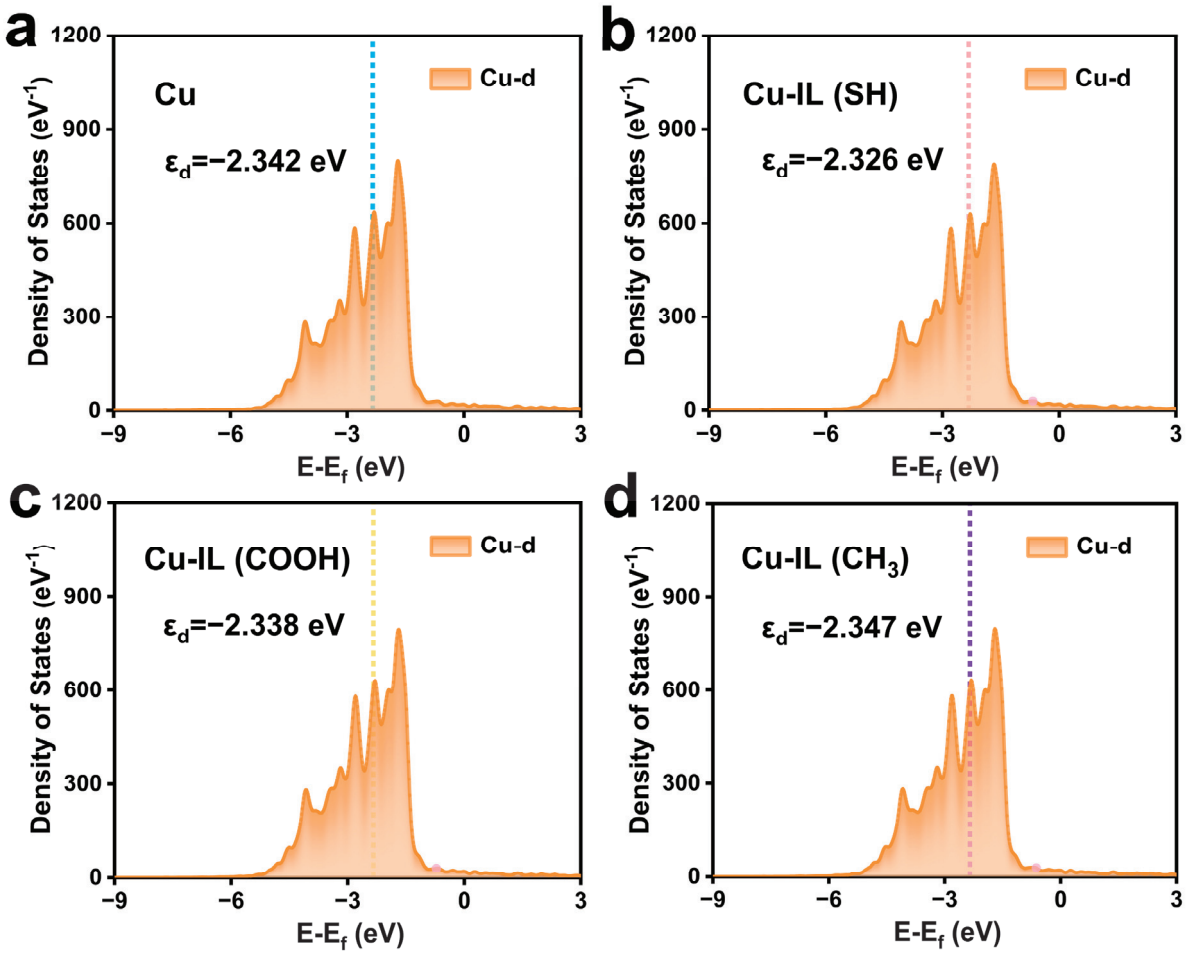

Figure 2. The DOS plots of the d orbital of Cu before *CO adsorption. (**a**) Cu, (**b**) Cu–IL (SH), (**c**) Cu–IL (COOH), and (**d**) Cu–IL (CH_3).

3.2. Electronic Structure Modulation and Intermediate Stabilization via IL-Modified Cu Surfaces

The electrocatalytic reduction in carbon dioxide to C_2 products is governed by two crucial stages: the C–C coupling step and the post-C–C coupling step, which are regarded as the RDS and the selectivity-determining step (SDS), respectively. For the rational design of catalysts, it is essential to understand how these steps are regulated by interfacial interactions. Against this backdrop, we systematically investigated the role of ionic liquids in regulating the adsorption configurations and energies of key intermediates during the electrocatalytic reduction in carbon dioxide. For different systems, we selected the pathway *CO + *CO → *COCO for analysis. We optimized the structures of the initial and final states of the coupling and analyzed data such as the adsorption capacity of the substrate for the intermediates, charge transfer, and transition-state energy barriers. The optimized structural models of the initial and final states of the *CO–*CO coupling are shown in Figures S4–S7.

We systematically investigated the evolution of the electronic structure of key intermediates on the pristine and IL-modified Cu surfaces. Differential charge density and bader charge analysis (Figures 3a–e and S8) demonstrates ligand-dependent charge redistribution upon *CO adsorption. For the Cu–IL (SH) catalyst, the Cu surface exhibits a charge depletion of approximately 0.715 e to the adsorbed *CO intermediates, compared to 0.520 e on the pristine Cu, indicating an enhanced electron donation capability. This enhancement can be attributed to the electron-donating nature of the –SH group, which facilitates electron density accumulation on the Cu surface and promotes subsequent transfer to the intermediates. In contrast, the –CH_3 group, being weakly electron-donating and

sterically non-polar, leads to reduced electron transfer, with only 0.408 e accumulated on the intermediates—less than that observed for pristine Cu. The –COOH group exhibits a moderate effect, resulting in an intermediate charge accumulation of 0.583 e. These results highlight the critical role of ILs' functional group's electronic properties in modulating interfacial charge redistribution and Cu–intermediate coupling strength.

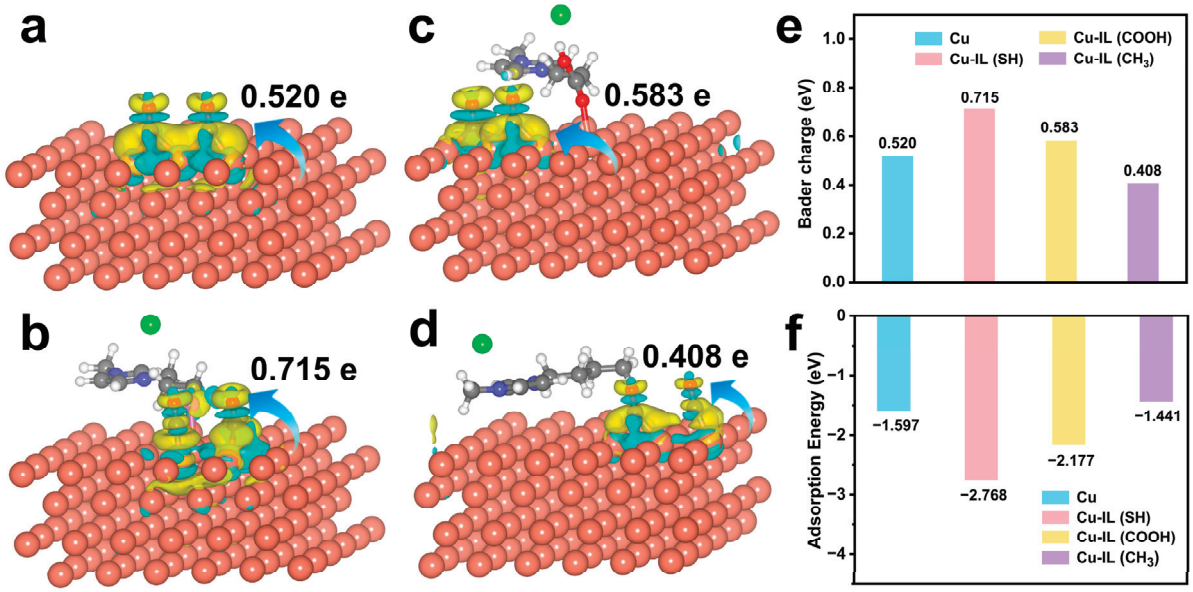

Figure 3. The different charges of the *CO + *CO and Cu/Cu–IL surfaces in pure Cu and three IL-modified catalyst systems in the initial state of C–C coupling. (**a**) The different charges of pristine Cu, (**b**) the different charges of Cu–IL (SH), (**c**) the different charges of Cu–IL (COOH), (**d**) the different charges of Cu–IL (CH_3). (**e**) The bader charge of *CO + *CO in the initial state of C–C coupling. (**f**) The adsorption energy of *CO + *CO on Cu/Cu–IL surfaces in the initial state of C–C coupling.

This functional group-dependent charge transfer behavior is closely correlated with the adsorption energy and observed d-band center shifts. The influence of IL functionalization on intermediate stabilization was first evaluated by comparing the adsorption energies of the *CO dimer configuration on different catalysts. The adsorption strength (Figure 3f) follows the following trend: Cu–IL (SH) (−2.768 eV) > Cu–IL (COOH) (−2.177 eV) > Cu (−1.597 eV) > Cu–IL (CH_3) (−1.441 eV). The significantly more negative adsorption energies for Cu–IL (SH) and Cu–IL (COOH) indicate stronger binding interactions with the intermediates, which enhance *CO surface coverage and reduce the spatial distance between adjacent *CO species, thereby promoting the probability of *CO–*CO coupling. This variation in adsorption energy is intrinsically correlated to the interfacial electronic structure, particularly the extent of charge transfer from the Cu surface to the adsorbates. Electron-donating functional groups such as –SH and –COOH promote substantial electron donation from the Cu substrate to the adsorbates, which facilitates intermediate stabilization. In contrast, the methyl-functionalized ILs suppress both intermediate stabilization and reaction site activation, underscoring their limited ability to activate key intermediates.

These observed charge transfer characteristics align well with the corresponding shifts in the Cu d-band center (Figure 4). Specifically, Cu–IL (SH) exhibits an upshift of the d-band center from −2.911 eV (pristine Cu) to −2.876 eV, followed by Cu–IL (COOH) (−2.903 eV), whereas Cu–IL (CH_3) causes a downshift to −2.922 eV, moving the d-band center further away from the Fermi. This trend reflects a weakened orbital overlap and reduced Cu–intermediate interaction. In comparison, the upshifted d-band centers in the Cu–IL (SH) and Cu–IL (COOH) systems bring the Cu d orbitals closer in energy to the

molecular orbitals of *CO, thus enhancing orbital hybridization and leading to stronger Cu–C bonding and more favorable adsorption geometries.

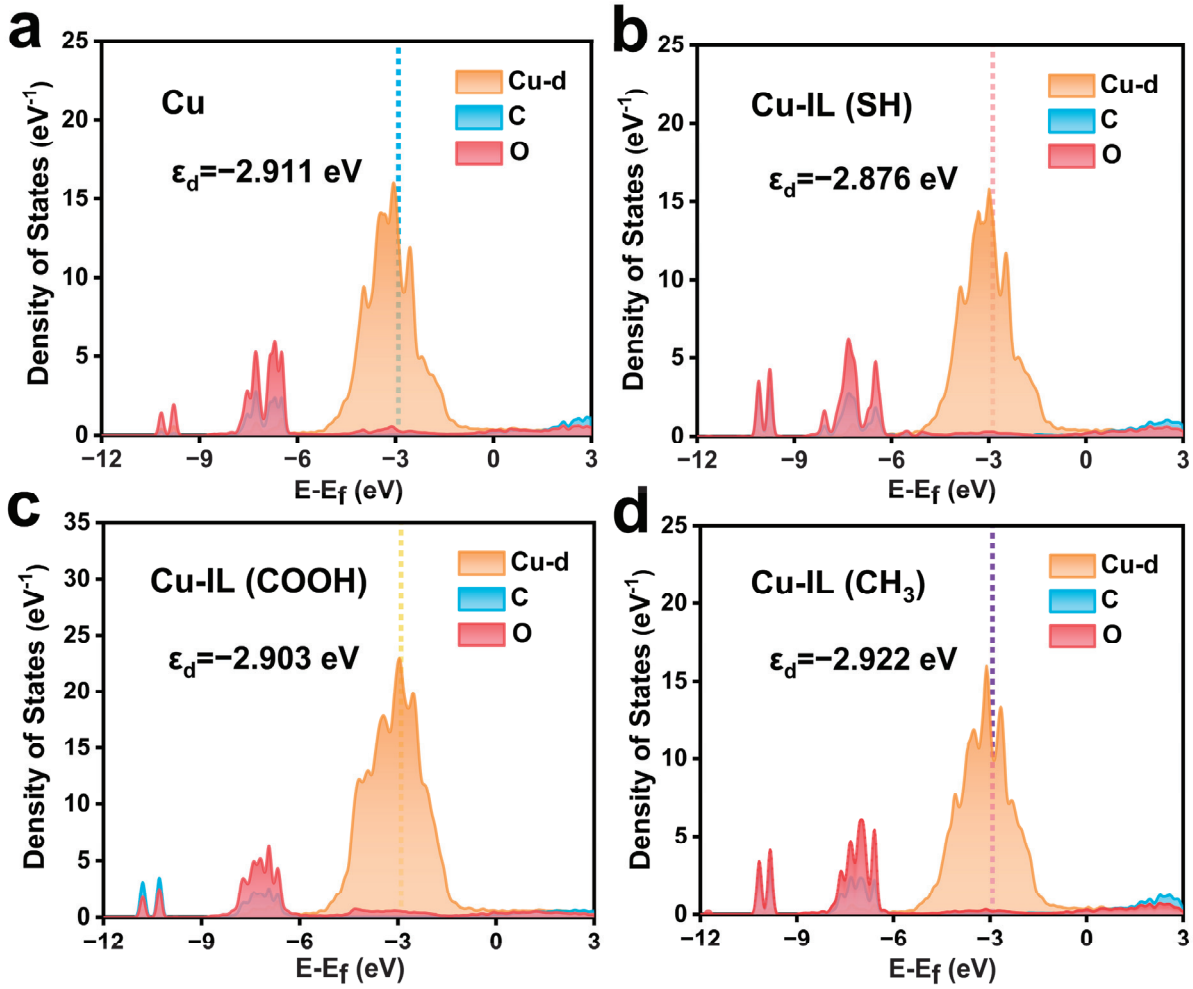

Figure 4. The DOS plots of the d orbitals of Cu and the total orbitals of C and O of adsorbed *CO + *CO in the initial state of C–C coupling. (**a**) Cu, (**b**) Cu–IL (SH), (**c**) Cu–IL (COOH), and (**d**) Cu–IL (CH_3).

To provide further orbital-level insight into Cu–intermediate interactions, we carried out the calculation of the crystal orbital Hamiltonian population (ICOHP) [49] for the Cu–C bonds at the initial stage of *CO–*CO coupling (Figure 5). The ICOHP value of Cu–C in the pure Cu is −1.270 eV, indicating a moderate bonding strength. Upon IL modification, the Cu–C ICOHP becomes more negative for Cu–IL (SH) (−1.408 eV) and Cu–IL (COOH) (−1.316 eV), signifying stronger bonding interactions. Conversely, Cu–IL (CH_3) exhibits a less negative value of −1.193 eV, further confirming weakened orbital overlap and diminished Cu–C coupling.

These electronic structure trends are closely correlated with the corresponding geometric configurations. At the initial state of C–C coupling (Table 1), the Cu–C bond lengths shorten from 1.999 Å on pristine Cu to 1.975 Å and 1.990 Å in the Cu–IL (SH) and Cu–IL (COOH) systems, respectively, while extending to 2.016 Å in Cu–IL (CH_3). A similar trend is observed for the initial C–C distances (Table S1), with Cu–IL (SH) exhibiting the shortest separation between reactive carbon atoms. These optimized structural features collectively lower the reaction barrier and stabilize the transition state, thereby facilitating C–C bond formation. At the final state, the C–C bond in the Cu–IL (SH) system remains the shortest (1.919 Å), reflecting the most stable coupling configuration among the catalysts examined.

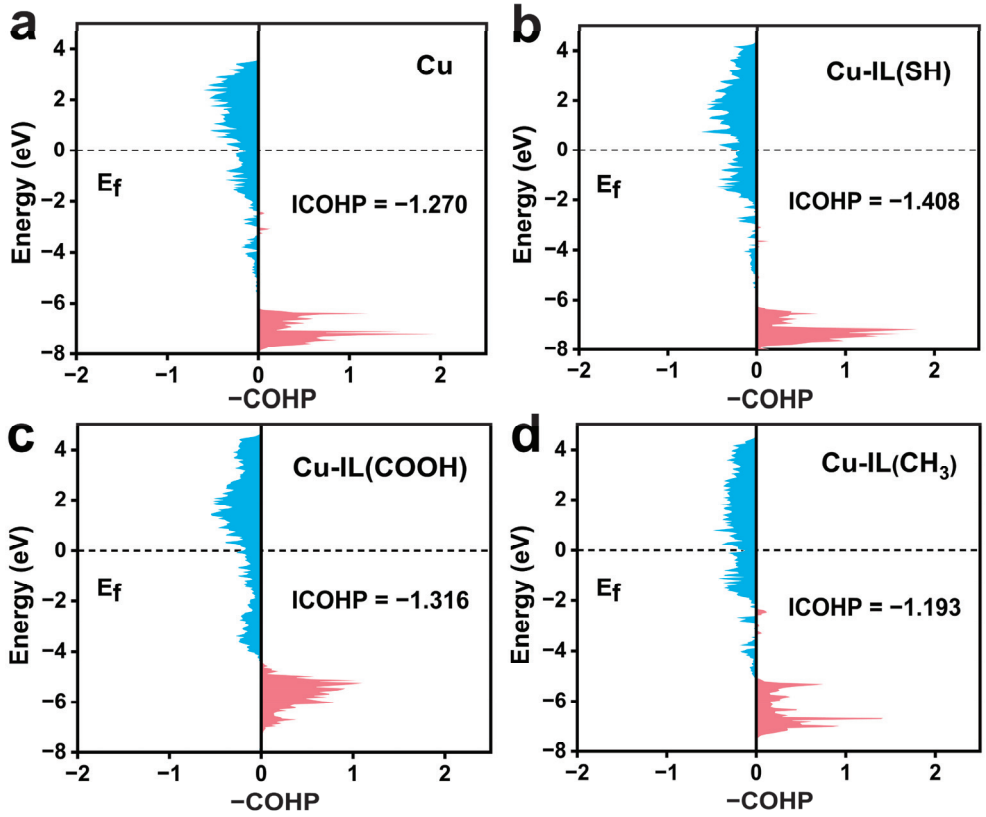

Figure 5. The projected COHP results of the overlap states between the *C atom of *CO + *CO and the adsorbed Cu atoms in the initial state of C–C coupling. (**a**) Cu, (**b**) Cu–IL (SH), (**c**) Cu–IL (COOH), and (**d**) Cu–IL (CH_3).

Table 1. The bond length of Cu–C or distance of Cu to C.

State / Sample	IS	TS	FS
Cu	1.999 Å	1.972 Å	2.025 Å
Cu–IL (SH)	1.975 Å	1.967 Å	2.021 Å
Cu–IL (COOH)	1.990 Å	1.975 Å	2.026 Å
Cu–IL (CH_3)	2.016 Å	1.979 Å	2.029 Å

In summary, IL functionalization modulates the Cu surface electronic structure through synergistic charge transfer, d-band center modulation, and orbital hybridization. These changes manifest in stronger Cu–intermediate interactions, more compact adsorption geometries, and enhanced *CO–*CO coupling, particularly in the –SH- and –COOH-functionalized systems. This mechanistic understanding provides a robust rationale for the superior C–C coupling performance observed in Cu–IL (SH).

3.3. IL-Mediated Modulation of Coupling Barriers and Product Selectivity in CO_2RR on Cu-Based Catalysts—Dual Modulation of Thermodynamics and Kinetics in C–C Coupling by ILs

To elucidate the key role of ILs in modulating the rate-determining C–C coupling step during CO_2 electroreduction on Cu-based catalysts, we performed comprehensive thermodynamic and kinetic calculations on pristine Cu and three IL-modified Cu surfaces. The transition state configurations and charge redistributions of the intermediates were obtained for the four catalyst systems, revealing the dynamic evolution of charge density on *CO intermediates throughout the reaction trajectory—from the initial state to transition state and final coupled state.

From a thermodynamic perspective, the reaction ΔG diagram for *CO–*CO coupling on pristine Cu was calculated to be 0.911 eV (Figure 6e). Upon IL modification, this value significantly decreased to 0.884 eV for Cu–IL (COOH) and 0.856 eV for Cu–IL (CH_3), respectively, with Cu–IL (SH) achieving the most favorable thermodynamics energy of 0.802 eV. This trend suggests that IL-induced interfacial environments can lower the thermodynamic barrier for *CO–*CO coupling, with Cu–IL (SH) exhibiting the most pronounced enhancement.

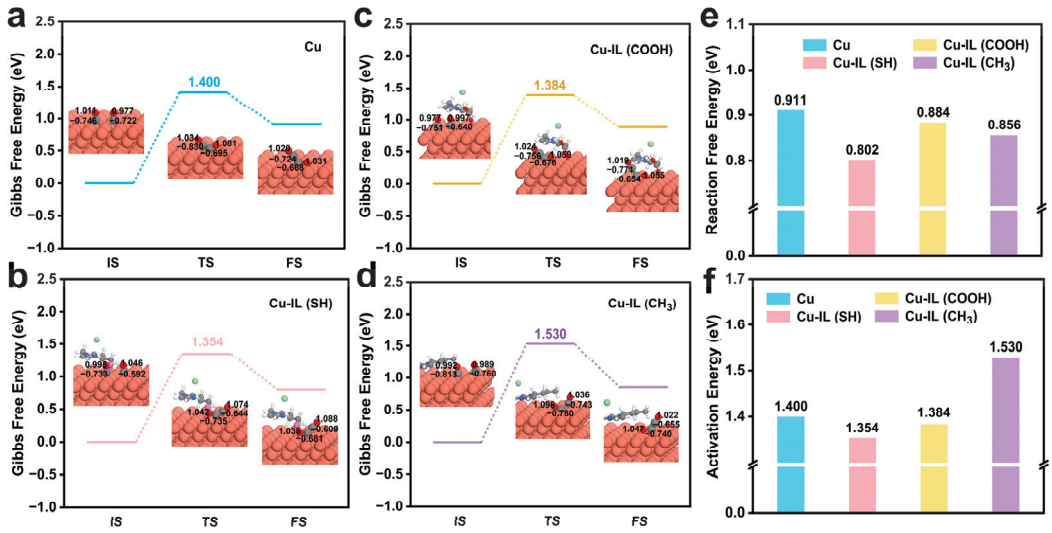

Figure 6. (**a**–**d**) Gibbs free energy of *CO + *CO → *COCO. (**a**) Cu, (**b**) Cu–IL (SH), (**c**) Cu–IL (COOH), and (**d**) Cu–IL (CH_3). (**e**) Reaction free energy of *CO + *CO → *COCO. (**f**) Activation energy of *CO + *CO → *COCO.

Particularly, to probe the kinetic effects of ILs, NEB was employed to accurately map the minimum energy pathways (MEPs) and obtain the corresponding activation energy barriers for pristine Cu and IL-modified systems. As shown in Figures 6a–d,f and S9, among all systems, Cu–IL (SH) exhibits the lowest activation energy barrier of 1.354 eV, indicating the most favorable kinetics for *CO–*CO coupling. In stark contrast, Cu–IL (CH_3) shows the highest barrier of 1.530 eV, reflecting a kinetically unfavorable pathway. Cu–IL (COOH) exhibits a moderately reduced barrier of 1.384 eV, falling between the values of pristine Cu and the most active Cu–IL (SH) system. These results demonstrate that ILs, particularly those bearing polar or coordinating groups, can simultaneously reduce both the reaction energy and the activation barrier, thereby enhancing both the thermodynamic driving force and the kinetic feasibility of C–C bond formation.

Structural analysis further supports these findings (Table S1). Among all systems, Cu–IL (SH) exhibits the shortest C–C bond length at the transition state (1.675 Å), reflecting a stronger and more stable coupling interaction between the two *CO intermediates. This structural feature correlates well with the enhanced thermodynamic driving force combined and a lowered activation barrier, which highlights the dual role of ILs in facilitating C–C bond formation.

Notably, the charge asymmetry between the two *CO intermediates induced by ILs at the adsorption sites strongly correlates with the efficiency of C–C coupling. In the Cu–IL (SH) system, the two *CO moieties exhibit the most uneven charge difference (0.192 e), compared to a smaller difference of 0.131 e in Cu–IL (COOH) and a nearly symmetrical charge distribution in the pristine Cu system (Table S2). This charge imbalance likely breaks the repulsive symmetry between two negatively charged *CO species, promoting directional electron flow, orbital overlap, and dipole-assisted coupling.

Taken together, these findings highlight a dual promotional effect of ILs on C–C coupling, as follows: (i) through the thermodynamic stabilization of the final *COCO product, and (ii) through kinetic acceleration by lowering the transition-state energy barrier. Among the systems studied, Cu–IL (SH) exhibits the most advantageous combination of charge asymmetry, transition-state geometry, and energy profile, making it the most promising candidate for selective CO_2-to-C_2 conversion.

3.4. IL-Guided Pathway Divergence and Suppression of Hydrogen Evolution Reaction of Cu-Based Catalysts for CO_2RR Products

3.4.1. Competitive Reaction Pathways Toward C_1 and C_2 Products of CO_2RR on IL-Modified Cu

Building on their role in enhancing *CO–*CO coupling, ILs also regulate the SDS of product formation in CO_2RR. To further reveal the intrinsic role of ILs in regulating product selectivity, we conducted a comparative calculation of the C_2 (C_2H_4 and C_2H_5OH) and C_1 product (CH_3OH) formation pathways, as well as the competing HER on pristine and IL-modified Cu surfaces. After the formation of the *CO intermediate, two distinct and competitive pathways become accessible; hydrogenation generates *CHO species that drive C_1 product formation such as methane, while coupling reactions produce *COCO—the crucial precursor for C_2 compound synthesis. This branching point constitutes the SDS of CO_2RR. The relative Gibbs free energies of these two competing pathways govern the product distribution.

As shown in Figures 7a,b and S10, the free energy change for *CO → *CHO on pristine Cu is 0.919 eV, which increases to 0.971 eV and 1.100 eV for Cu–IL (SH) and Cu–IL (CH_3), respectively, indicating a thermodynamic disfavoring of C_1 formation. In contrast, Cu–IL (COOH) lowers the energy of this step to 0.795 eV, thereby promoting C_1 product formation. Meanwhile, for the *CO–*CO coupling step, all IL-modified systems exhibit reduced reaction free energies compared to pristine Cu. Among them, Cu–IL (SH) exhibits the most favorable thermodynamic bias toward C_2 product formation, with a Gibbs energy difference (ΔG) of −0.287 eV between the *CO–*CO coupling and *CO hydrogenation steps. The corresponding ΔG values for Cu–IL (CH_3), Cu–IL (COOH), and pristine Cu are −0.124 eV, 0.020 eV, and 0.135 eV, respectively (Figure 7c).

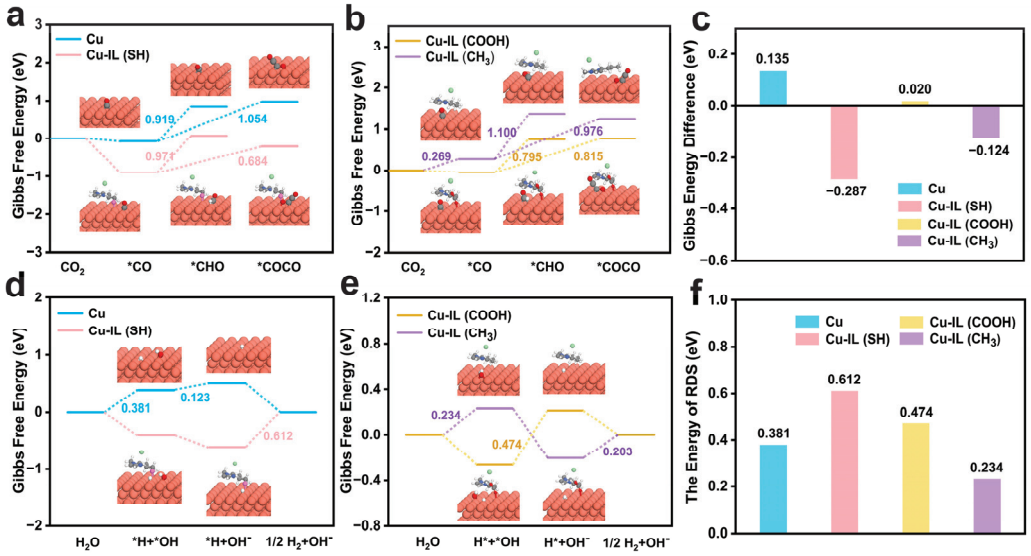

Figure 7. (**a**,**b**) Gibbs free energy of *CO → *CHO and *CO → *COCO on Cu, Cu–IL (SH), Cu-IL (COOH), and Cu-IL (CH_3). (**c**) The difference of Gibbs free energy between the *CO–*CO coupling and *CO hydrogenation steps. (**d**,**e**) Gibbs free energy of HER on Cu, Cu–IL (SH), Cu-IL (COOH), and Cu-IL (CH_3). (**f**) The energy of RDS of HER.

3.4.2. Suppression of HER

In addition to regulating the selectivity-determining step between the C_1 and C_2 pathways, ILs also play a pivotal role in suppressing the HER, a major side reaction that competes with CO_2 reduction. HER not only consumes electrons and protons that would otherwise contribute to CO_2 reduction, but also perturbs the interfacial microenvironment, altering the pH, surface potential, and charge density, all of which can influence the stability and reactivity of CO_2RR intermediates. Consequently, uncontrolled HER lowers the C_2H_4 and C_2H_5OH yield, complicates product separation, and compromises energy efficiency. It is equally critical to evaluate their influence on HER, which can profoundly impact product selectivity and faradaic efficiency. We evaluated the HER pathways by calculating the Gibbs free energy profiles for pristine and IL-modified Cu surfaces (Figure 7d,e). The reaction pathway is divided into three thermodynamically distinct steps: (i) water dissociation ($*H_2O \rightarrow *H + *OH$); (ii) *OH desorption ($*OH \rightarrow OH^-$); and (iii) hydrogen evolution. The initial water dissociation steps are thermodynamically facilitated on all IL-functionalized surfaces compared to that on pristine Cu, including Cu–IL (SH), Cu–IL (COOH), and Cu–IL (CH_3), indicating that ILs' modification promotes the surface availability of reactive hydrogen species. However, the subsequent desorption steps exhibit significant thermodynamic variation.

The RDS of HER significantly depends on the surface functionalization of Cu with different ILs (Figure 7f). On pristine Cu, the RDS is the initial water dissociation step, with a Gibbs free energy change of 0.381 eV, indicating moderate HER activity in the absence of interfacial tuning. Upon ILs modification, distinct shifts in the RDS are observed. Cu–IL (SH) presents the highest Gibbs free energy change of 0.612 eV among all systems, associated with the hydrogen evolution step involving the recombination and release of surface-bound hydrogen. As the thermodynamic rate-limiting step in the HER pathway, it reflects the pronounced suppression of HER on the Cu–IL (SH) surface. In contrast, the Cu–IL (COOH) system exhibits its highest Gibbs free energy change (0.474 eV) during hydroxide desorption, indicating that the removal of surface-bound *OH constitutes the thermodynamic rate-limiting step. This suggests that HER is suppressed by the stabilization of *OH intermediates, which delays site regeneration for subsequent proton transfer. In contrast, all elementary steps in the Cu–IL (CH_3) system along the HER pathway exhibit low Gibbs free energy changes, with the highest being only 0.234 eV. The uniformly low energy barriers suggest a facile HER process without a clear thermodynamic bottleneck.

These findings underscore the critical role of IL functional groups in modulating the thermodynamic bottleneck of the HER pathway. Polar moieties such as –SH and –COOH elevate the rate-limiting free energy by stabilizing adsorbed hydrogen or hydroxide species, thereby suppressing HER through distinct desorption-limited mechanisms. In contrast, the nonpolar $–CH_3$ group exerts minimal impact on the HER energy landscape, leaving the pathway largely unimpeded. The ability of –SH- and –COOH-functionalized ILs to increase the energetic threshold of the rate-determining step provides a mechanistic basis for their enhanced CO_2RR selectivity, achieved through the effective suppression of the competing HER process.

4. Conclusions

This work systematically elucidates the mechanism of 1-(3-X-propyl)-3-methylimidazolium-based ILs in modulating the electrocatalytic behavior of Cu electrodes toward C_2H_4 and C_2H_5OH formation in CO_2RR. Theoretical investigations reveal that ILs bearing different terminal functional groups can trigger the interfacial electronic reconstruction, change the position of the d-band center, and affect the adsorption strength and configuration of key intermediates. In particular, Cu–IL (SH) exhibits the most favorable

electronic modulation, enhancing *CO adsorption, stabilizing the *CO–*CO coupling configuration through stronger Cu–C interactions, and ultimately promoting efficient C–C bond formation. Thermodynamic and kinetic analyses further confirm that Cu–IL (SH) has the lowest reaction free energy and activation barrier for the rate-determining C–C coupling step, underscoring the pivotal role of electronic structure regulation in enhancing catalytic performance. In addition, IL modification also substantially improves the product selectivity by directing the reaction pathway towards C_2H_4 and C_2H_5OH while simultaneously suppressing undesired C_1 formation and the competitive HER.

These findings demonstrate that the catalytic enhancement in CO_2RR arises from a synergistic mechanism involving IL-induced interfacial electronic modulation, thermodynamic stabilization, and the kinetic promotion of the rate-determining C–C coupling step. The consistent trends observed across d-band shifts, adsorption energies, and energy barriers establish a robust structure–function relationship governed by ILs' polarity. This study not only advances the fundamental understanding of Cu–IL catalyst interactions but also provides a broadly applicable framework for the rational design of IL-modified electrocatalysts toward highly selective and energy-efficient CO_2 conversion. While this work focuses on Cu as a model system, we envision that the rational design of ionic liquid functional groups—considering the dipole moment, donor/acceptor character, and binding affinity—could be extended to tailor interfacial interactions on other metallic surfaces. Such molecular-level tuning may enable the application of ionic liquid-assisted catalysis in a broader range of fields.

Supplementary Materials: The following supporting information can be downloaded at: https://www.mdpi.com/article/10.3390/molecules30112352/s1, Figure S1: The configuration of (a) pristine Cu, (b) Cu–IL (SH), (c) Cu–IL (COOH), and (d) Cu–IL (CH_3) (top view); Figure S2: The configuration of (a) pristine Cu, (b) Cu–IL (SH), (c) Cu–IL (COOH), and (d) Cu–IL (CH_3) (side view); Figure S3: Bader charge at some Cu points (a) pristine Cu, (b) Cu–IL (SH), (c) Cu–IL (COOH), and (d) Cu–IL (CH_3); Figure S4: The configuration of initial state of C–C coupling on (a) pristine Cu, (b) Cu–IL (SH), (c) Cu–IL (COOH), and (d) Cu–IL (CH_3) (top view); Figure S5: The configuration of initial state of C–C coupling on (a) pristine Cu, (b) Cu–IL (SH), (c) Cu–IL (COOH), and (d) Cu–IL (CH_3) (side view); Figure S6: The configuration of final state of C–C coupling on (a) pristine Cu, (b) Cu–IL (SH), (c) Cu–IL (COOH), and (d) Cu–IL (CH_3) (top view); Figure S7: The configuration of final state of C–C coupling on (a) pristine Cu, (b) Cu–IL (SH), (c) Cu–IL (COOH), and (d) Cu–IL (CH_3) (side view); Figure S8: The different charges of the *CO + *CO and Cu/Cu–IL surfaces in pure Cu and three IL-modified catalyst systems in the initial state of C–C coupling, with cyan and yellow areas representing charge depletion and charge accumulation, respectively. (a) pristine Cu, (b) Cu–IL (SH), (c) Cu–IL (COOH), (d) Cu–IL (CH_3); Figure S9: The configuration of transition state of C–C coupling on (a) pristine Cu, (b) Cu–IL (SH), (c) Cu–IL (COOH), and (d) Cu–IL (CH_3) (side view); Figure S10: The energy of RDS of *CO–*CO coupling and *CO hydrogenation steps; Table S1: The bond length of C–C or distance of C to C; Table S2: The difference between the bader charges of two *CO.

Author Contributions: Conceptualization, C.Z. and C.W.; methodology, C.Z.; software, C.Z. and C.W.; validation, C.Z., Z.W., and J.M.; formal analysis, C.Z. and C.W.; investigation, C.W.; resources, C.Z. and Z.W.; data curation, C.W. and W.Z.; writing—original draft preparation, C.Z. and C.W.; writing—review and editing, C.Z. and C.W.; visualization, C.W.; supervision, C.Z.; project administration, C.Z.; funding acquisition, C.Z. All authors have read and agreed to the published version of the manuscript.

Funding: This research was funded by the Natural Science Foundation in Shandong Province of China (Grant No. ZR2022MB141).

Institutional Review Board Statement: Not applicable.

Informed Consent Statement: Not applicable.

Data Availability Statement: Data are contained within the article and Supplementary Materials.

Conflicts of Interest: The authors declare no conflicts of interest.

References

1. Yin, Z.-Z.; Huang, T.-T.; Shao, Z.-B.; Zhao, B. Development of fire-resistant PVA films with superior toughness, self-healing, and antibacterial properties via a phosphazene molecule. *Prog. Org. Coat.* **2025**, *198*, 108881. [CrossRef]
2. Li, X.-J.; Ning, K.; Huang, T.-T.; Shao, Z.-B.; Zhao, B. Arone-containing cyclomatrix-type polyphosphazene hybrid microspheres for epoxy resin: Enhancing fire safety and mechanical properties. *Colloids Surf. A Physicochem. Eng. Asp.* **2024**, *692*, 133988. [CrossRef]
3. Birdja, Y.Y.; Pérez-Gallent, E.; Figueiredo, M.C.; Göttle, A.J.; Calle-Vallejo, F.; Koper, M.T.M. Advances and challenges in understanding the electrocatalytic conversion of carbon dioxide to fuels. *Nat. Energy* **2019**, *4*, 732–745. [CrossRef]
4. Xie, W.F.; Li, B.K.; Liu, L.; Li, H.; Yue, M.Z.; Niu, Q.M.; Liang, S.Y.; Shao, X.D.; Lee, H.Y.Y.; Lee, J.Y.; et al. Advanced systems for enhanced CO_2 electroreduction. *Chem. Soc. Rev.* **2025**, *54*, 898–959. [CrossRef]
5. Guo, W.W.; Liu, S.J.; Tan, X.X.; Wu, R.Z.; Yan, X.P.; Chen, C.J.; Zhu, Q.G.; Zheng, L.R.; Ma, J.Y.; Zhang, J.; et al. Highly Efficient CO_2 Electroreduction to Methanol through Atomically Dispersed Sn Coupled with Defective CuO Catalysts. *Angew. Chem. Int. Ed.* **2021**, *60*, 21979–21987. [CrossRef]
6. He, X.Y.; Lin, L.; Li, X.Y.; Zhu, M.Z.; Zhang, Q.H.; Xie, S.J.; Mei, B.B.; Sun, F.F.; Jiang, Z.; Cheng, J.; et al. Roles of copper(I) in water-promoted CO_2 electrolysis to multi-carbon compounds. *Nat. Commun.* **2024**, *15*, 9923. [CrossRef]
7. Wang, Q.; Wei, H.; Liu, P.; Su, Z.; Gong, X.-Q. Recent advances in copper-based catalysts for electrocatalytic CO_2 reduction toward multi-carbon products. *Nano Res. Energy* **2024**, *3*, e9120112. [CrossRef]
8. Calle-Vallejo, F.; Koper, M.T.M. Theoretical Considerations on the Electroreduction of CO to C_2 Species on Cu(100) Electrodes. *Angew. Chem. Int. Ed.* **2013**, *52*, 7282–7285. [CrossRef]
9. Li, M.; Hu, Y.; Wu, T.; Sumboja, A.; Geng, D. How to enhance the C_2 products selectivity of copper-based catalysts towards electrochemical CO_2 reduction?—A review. *Materials Today* **2023**, *67*, 320–343. [CrossRef]
10. Ma, Z.; Yang, Z.; Lai, W.; Wang, Q.; Qiao, Y.; Tao, H.; Lian, C.; Liu, M.; Ma, C.; Pan, A.; et al. CO_2 electroreduction to multicarbon products in strongly acidic electrolyte via synergistically modulating the local microenvironment. *Nat. Commun.* **2022**, *13*, 7596. [CrossRef]
11. Pan, F.; Duan, X.; Fang, L.; Li, H.; Xu, Z.; Wang, Y.; Wang, T.; Li, T.; Duan, Z.; Chen, K.-J. Long-Range Confinement-Driven Enrichment of Surface Oxygen-Relevant Species Promotes C−C Electrocoupling in CO_2 Reduction. *Adv. Energy Mater.* **2024**, *14*, 2303118. [CrossRef]
12. Huang, P.; He, B.; Dong, Y.; Zhou, J.; Xu, J.; Pan, C.; Lou, Y.; Wang, Y.; Zhang, Y.; Huang, H.; et al. Preferentially Stabilizing the Watershed Intermediates by Adsorbate-adsorbate Interaction to Accelerate CO_2 Electroreduction to Ethanol. *Adv. Funct. Mater.* **2024**, *25*, 2424583. [CrossRef]
13. De Gregorio, G.L.; Burdyny, T.; Loiudice, A.; Iyengar, P.; Smith, W.A.; Buonsanti, R. Facet-Dependent Selectivity of Cu Catalysts in Electrochemical CO_2 Reduction at Commercially Viable Current Densities. *ACS Catal.* **2020**, *10*, 4854–4862. [CrossRef]
14. Zhang, G.; Zhao, Z.-J.; Cheng, D.; Li, H.; Yu, J.; Wang, Q.; Gao, H.; Guo, J.; Wang, H.; Ozin, G.A.; et al. Efficient CO_2 electroreduction on facet-selective copper films with high conversion rate. *Nat. Commun.* **2021**, *12*, 5745. [CrossRef] [PubMed]
15. Kim, J.Y.; Park, W.; Choi, C.; Kim, G.; Cho, K.M.; Lim, J.; Kim, S.J.; Al-Saggaf, A.; Gereige, I.; Lee, H.; et al. High Facets on Nanowrinkled Cu via Chemical Vapor Deposition Graphene Growth for Efficient CO_2 Reduction into Ethanol. *ACS Catal.* **2021**, *11*, 5658–5665. [CrossRef]
16. Piqué, O.; Low, Q.H.; Handoko, A.D.; Yeo, B.S.; Calle-Vallejo, F. Selectivity Map for the Late Stages of CO and CO_2 Reduction to C_2 Species on Copper Electrodes. *Angew. Chem. Int. Ed.* **2021**, *60*, 10784–10790. [CrossRef] [PubMed]
17. Chen, C.; Yan, X.; Wu, Y.; Liu, S.; Sun, X.; Zhu, Q.; Feng, R.; Wu, T.; Qian, Q.; Liu, H.; et al. The in situ study of surface species and structures of oxide-derived copper catalysts for electrochemical CO_2 reduction. *Chem. Sci.* **2021**, *12*, 5938–5943. [CrossRef]
18. Dutta, A.; Montiel, I.Z.; Erni, R.; Kiran, K.; Rahaman, M.; Drnec, J.; Broekmann, P. Activation of bimetallic AgCu foam electrocatalysts for ethanol formation from CO_2 by selective Cu oxidation/reduction. *Nano Energy* **2020**, *68*, 104331. [CrossRef]
19. Chen, C.; Li, Y.; Yu, S.; Louisia, S.; Jin, J.; Li, M.; Ross, M.B.; Yang, P. Cu-Ag Tandem Catalysts for High-Rate CO_2 Electrolysis toward Multicarbons. *Joule* **2020**, *4*, 1688–1699. [CrossRef]
20. Herzog, A.; Bergmann, A.; Jeon, H.S.; Timoshenko, J.; Kühl, S.; Rettenmaier, C.; Lopez Luna, M.; Haase, F.T.; Roldan Cuenya, B. Operando Investigation of Ag-Decorated Cu_2O Nanocube Catalysts with Enhanced CO_2 Electroreduction toward Liquid Products. *Angew. Chem. Int. Ed.* **2021**, *60*, 7426–7435. [CrossRef]
21. Huang, T.-T.; Ning, K.; Zhao, B. Two birds, one stone: Enhancement of flame retardancy and antibacterial property of viscose fabric using an aminoazole-based cyclotriphosphazene. *Int. J. Biol. Macromol.* **2023**, *253*, 126875. [CrossRef] [PubMed]

22. Lu, X.; Zhu, C.; Wu, Z.; Xuan, J.; Francisco, J.S.; Wang, H. In Situ Observation of the pH Gradient near the Gas Diffusion Electrode of CO_2 Reduction in Alkaline Electrolyte. *J. Am. Chem. Soc.* **2020**, *142*, 15438–15444. [CrossRef]
23. Monteiro, M.C.O.; Dattila, F.; Hagedoorn, B.; García-Muelas, R.; López, N.; Koper, M.T.M. Absence of CO_2 electroreduction on copper, gold and silver electrodes without metal cations in solution. *Nat. Catal.* **2021**, *4*, 654–662. [CrossRef]
24. Li, M.; Garg, S.; Chang, X.; Ge, L.; Li, L.; Konarova, M.; Rufford, T.E.; Rudolph, V.; Wang, G. Toward Excellence of Transition Metal-Based Catalysts for CO_2 Electrochemical Reduction: An Overview of Strategies and Rationales. *Small Methods* **2020**, *4*, 2000033. [CrossRef]
25. Lei, Q.; Zhu, H.; Song, K.; Wei, N.; Liu, L.; Zhang, D.; Yin, J.; Dong, X.; Yao, K.; Wang, N.; et al. Investigating the Origin of Enhanced C_{2+} Selectivity in Oxide-/Hydroxide-Derived Copper Electrodes during CO_2 Electroreduction. *J. Am. Chem. Soc.* **2020**, *142*, 4213–4222. [CrossRef] [PubMed]
26. Cui, Y.; He, B.; Liu, X.; Sun, J. Ionic Liquids-Promoted Electrocatalytic Reduction of Carbon Dioxide. *Ind. Eng. Chem. Res.* **2020**, *59*, 20235–20252. [CrossRef]
27. Mu, S.; Li, L.; Zhao, R.; Lu, H.; Dong, H.; Cui, C. Molecular-Scale Insights into Electrochemical Reduction of CO_2 on Hydrophobically Modified Cu Surfaces. *ACS Appl. Mater. Interfaces* **2021**, *13*, 47619–47628. [CrossRef]
28. Wang, W.; Ma, Z.; Fei, X.; Wang, X.; Yang, Z.; Wang, Y.; Zhang, J.; Ning, H.; Tsubaki, N.; Wu, M. Joint tuning the morphology and oxygen vacancy of Cu_2O by ionic liquid enables high-efficient CO_2 reduction to C_2 products. *Chem. Eng. J.* **2022**, *436*, 135029. [CrossRef]
29. Cai, H.; Yang, H.; Feng, J.; Zhou, K.; Liu, C.; Hu, Q.; He, C. Ionic Liquid-Induced Product Switching in CO_2 Electroreduction on Copper Reaction Interface. *Adv. Funct. Mater.* **2024**, *34*, 2404102. [CrossRef]
30. Zhang, X.-D.; Liu, T.; Liu, C.; Zheng, D.-S.; Huang, J.-M.; Liu, Q.-W.; Yuan, W.-W.; Yin, Y.; Huang, L.-R.; Xu, M.; et al. Asymmetric Low-Frequency Pulsed Strategy Enables Ultralong CO_2 Reduction Stability and Controllable Product Selectivity. *J. Am. Chem. Soc.* **2023**, *145*, 2195–2206. [CrossRef]
31. Coskun, O.K.; Dongare, S.; Doherty, B.; Klemm, A.; Tuckerman, M.; Gurkan, B. Tailoring Electrochemical CO_2 Reduction on Copper by Reactive Ionic Liquid and Native Hydrogen Bond Donors. *Angew. Chem. Int. Ed.* **2024**, *63*, e202312163. [CrossRef] [PubMed]
32. Shaikh, A.R.; Vidal-López, A.; Brotons-Rufes, A.; Pajski, J.J.; Zafar, S.; Mahmood, R.A.; Khan, M.U.; Poater, A.; Chawla, M.; Cavallo, L. Amino acid ionic liquids as efficient catalysts for CO_2 capture: A combined static and dynamic approach. *Results Surf. Interfaces* **2024**, *14*, 100175. [CrossRef]
33. Wang, R.; Qi, C.; Jian, Z.; Zhao, H.; Zhang, P.; An, S.; Li, Q.; Wang, L. Development of dual-functionalized ionic liquids for biphasic solvents: Enhancing the CO_2 absorption through two-stage reaction and promoting the energy-saving regeneration. *Fuel* **2024**, *359*, 130382. [CrossRef]
34. Dai, C.; Yang, Y.; Fisher, A.; Liu, Z.; Cheng, D. Interaction of CO_2 with metal cluster-functionalized ionic liquids. *J. CO_2 Util.* **2016**, *16*, 257–263. [CrossRef]
35. Wang, Y.; Hatakeyama, M.; Ogata, K.; Wakabayashi, M.; Jin, F.; Nakamura, S. Activation of CO_2 by ionic liquid EMIM–BF_4 in the electrochemical system: A theoretical study. *Phys. Chem. Chem. Phys.* **2015**, *17*, 23521–23531. [CrossRef]
36. Chang, Q.; Lee, J.H.; Liu, Y.; Xie, Z.; Hwang, S.; Marinkovic, N.S.; Park, A.-H.A.; Kattel, S.; Chen, J.G. Electrochemical CO_2 Reduction Reaction over Cu Nanoparticles with Tunable Activity and Selectivity Mediated by Functional Groups in Polymeric Binder. *JACS Au* **2021**, *2*, 214–222. [CrossRef]
37. Li, X.-Q.; Duan, G.-Y.; Chen, J.-W.; Han, L.-J.; Zhang, S.-J.; Xu, B.-H. Regulating electrochemical CO_2RR selectivity at industrial current densities by structuring copper@poly(ionic liquid) interface. *Appl. Catal. B Environ.* **2021**, *297*, 120471. [CrossRef]
38. Kresse, G.; Furthmüller, J. Efficiency of ab-initio total energy calculations for metals and semiconductors using a plane-wave basis set. *Comput. Mater. Sci.* **1996**, *6*, 15–50. [CrossRef]
39. He, R.; Huang, K.; Yang, X.; Xu, J.; Tong, Z. Copper electrocatalyst modified with pyridinium-based ionic liquids for the efficient synthesis of ethylene through electrocatalytic CO_2 reduction reaction. *Chem. Eng. J.* **2024**, *502*, 158067. [CrossRef]
40. Sha, Y.; Zhang, J.; Cheng, X.; Xu, M.; Su, Z.; Wang, Y.; Hu, J.; Han, B.; Zheng, L. Anchoring Ionic Liquid in Copper Electrocatalyst for Improving CO_2 Conversion to Ethylene. *Angew. Chem. Int. Ed.* **2022**, *61*, e202200039. [CrossRef]
41. Duan, G.Y.; Li, X.Q.; Ding, G.R.; Han, L.J.; Xu, B.H.; Zhang, S.J. Highly Efficient Electrocatalytic CO_2 Reduction to C_{2+} Products on a Poly(ionic liquid)-Based Cu^0–Cu^1 Tandem Catalyst. *Angew. Chem. Int. Ed.* **2022**, *61*, e202110657. [CrossRef] [PubMed]
42. Choi, C.; Kwon, S.; Cheng, T.; Xu, M.; Tieu, P.; Lee, C.; Cai, J.; Lee, H.M.; Pan, X.; Duan, X.; et al. Highly active and stable stepped Cu surface for enhanced electrochemical CO_2 reduction to C_2H_4. *Nat. Catal.* **2020**, *3*, 804–812. [CrossRef]
43. Zhong, D.; Zhao, Z.-J.; Zhao, Q.; Cheng, D.; Liu, B.; Zhang, G.; Deng, W.; Dong, H.; Zhang, L.; Li, J.; et al. Coupling of Cu(100) and (110) Facets Promotes Carbon Dioxide Conversion to Hydrocarbons and Alcohols. *Angew. Chem. Int. Ed.* **2021**, *60*, 4879–4885. [CrossRef] [PubMed]
44. Kresse, G.; Furthmüller, J. Efficient iterative schemes for ab initio total-energy calculations using a plane-wave basis set. *Phys. Rev. B* **1996**, *54*, 11169–11186. [CrossRef]

45. Blöchl, P.E. Projector augmented-wave method. *Phys. Rev. B* **1994**, *50*, 17953–17979. [CrossRef]
46. Perdew, J.P.; Burke, K.; Ernzerhof, M. Generalized Gradient Approximation Made Simple. *Phys. Rev. Lett.* **1996**, *77*, 3865–3868. [CrossRef]
47. Raybaud, P.; Hafner, J.; Kresse, G.; Kasztelan, S.; Toulhoat, H. Structure, Energetics, and Electronic Properties of the Surface of a Promoted MoS_2 Catalyst: An ab Initio Local Density Functional Study. *J. Catal.* **2000**, *190*, 128–143. [CrossRef]
48. Henkelman, G.; Jónsson, H. A dimer method for finding saddle points on high dimensional potential surfaces using only first derivatives. *J. Chem. Phys.* **1999**, *111*, 7010–7022. [CrossRef]
49. Deringer, V.L.; Tchougréeff, A.L.; Dronskowski, R. Crystal Orbital Hamilton Population (COHP) Analysis as Projected from Plane-Wave Basis Sets. *J. Phys. Chem. A* **2011**, *115*, 5461–5466. [CrossRef]

molecules

MDPI

Article

Multipotent Effect of Clozapine on Lipopolysaccharide-Induced Acetylcholinesterase, Cyclooxygenase-2,5-Lipoxygenase, and Caspase-3: In Vivo and Molecular Modeling Studies

Minhajul Arfeen [1,*], Devendra Kumar Dhaked [2] and Vasudevan Mani [3]

[1] Department of Medicinal Chemistry and Pharmacognosy, College of Pharmacy, Qassim University, Buraydah 51452, Saudi Arabia
[2] Department of Pharmacoinformatics, National Institute of Pharmaceutical Education and Research (NIPER)-Kolkata, Kolkata 700054, India; dkdhaked@niperkolkata.edu.in
[3] Department of Pharmacology and Toxicology, College of Pharmacy, Qassim University, Buraydah 51452, Saudi Arabia; v.samy@qu.edu.sa
* Correspondence: m.arfeen@qu.edu.sa; Tel.: +966-536439056

Abstract: Dual inhibition of cyclooxygenase-2 (COX-2) and lipoxygenase (LOX) is a recognized strategy for enhanced anti-inflammatory effects in small molecules, offering potential therapeutic benefits for individuals at risk of dementia, particularly those with neurodegenerative diseases, common cancers, and diabetes type. Alzheimer's disease (AD) is the most common cause of dementia, and the inhibition of acetylcholinesterase (AChE) is a key approach in treating AD. Meanwhile, Caspase-3 catalyzes early events in apoptosis, contributing to neurodegeneration and subsequently AD. Structure-based virtual screening of US-FDA-approved molecules from the ZINC15 database identified clozapine (CLOZ) as the dual inhibitor of COX-2 and AChE, with significant binding affinity. Further molecular docking of CLOZ in the active site of LOX and Caspase-3 also showed significant binding potential. Further, the results from molecular docking were validated using molecular dynamics simulation (MDS) studies, confirming the results from molecular docking. The results from MDS showed good binding potential and interactions with key residues. The CLOZ was further assessed using lipopolysaccharide (LPS)-challenged rats treated for thirty days at doses of 5 and 10 mg/kg, p.o. The results demonstrated modulation of COX-2, 5-LOX, AChE, Caspase-3, and MDA in LPS-induced brains. Additionally, the expression level of IL-10 was also measured. Our results showed a significant decrease in the levels of COX-2, 5-LOX, AChE, Caspase-3, and MDA. Our results also showed a significant decrement in the pro-inflammatory markers NF-κB, TNF-α, and IL-6 and an improvement in the levels of anti-inflammatory markers IL-10 and TGF-β1. Overall, the findings indicate that CLOZ has potential for neuroprotective effects against LPS-treated rats and can be explored.

Keywords: clozapine; molecular docking simulation; virtual screening; inflammation; neurodegenerative disorder; diabetes; Alzheimer's diseases

1. Introduction

Dementia is a disorder characterized by a significant decline from one's previous level of cognition and is the seventh leading cause of death among all diseases. As per the report published by the WHO in the year 2024, over 55 million people are living with dementia across the globe, and around 10 million new cases emerge annually. This number is projected to increase up to 78 and 139 million by the years 2030 and 2050,

respectively [1]. Alzheimer's disease (AD) is the most common cause of dementia. The economic burden of managing AD in the U.S. is substantial, with care costs estimated at USD 305 billion in 2020, rising to USD 360 billion by 2024. Projections indicate these costs could surpass USD 1 trillion by 2050, reflecting the disease's growing prevalence and healthcare demands [2]. Cholinergic transmission plays an important role in central nervous system functions, particularly learning and memory. Brains with dementia with characterized by elevated levels of inflammation, and recent findings demonstrate COX-2 in the center of the inflammatory response. Numerous studies have documented Caspases-mediated apoptosis as an early event in AD. The activation of Caspase not only contributes to neuronal cell death, but also facilitates the underlying etiology of the disease. AD is accompanied by oxidative stress, and malonaldehyde (MDA) is a very well-documented bio-marker for oxidative stress. Lipoxygenases (LOX), particularly 5-LOX, have been documented to promote neuroinflammation, oxidative stress, and amyloid-beta (Aβ) and disrupt neuronal and vascular integrity [3,4]. Inhibition of the above-mentioned targets along with AChE is a well-established and promising strategy for the treatment and prevention of AD.

AD is a multifactorial disease, i.e., under diseased conditions, several molecular targets are either upregulated or downregulated [5]. In this context, several reports were published that displayed multi-target action for improvement of AD. For example, Al-Fadly et al. reported Tetrahydroacridine-triazole (**1**, Figure 1) and thiosemicarbazide (**2**) hybrids as COX-2, 15-Lipooxygenase (LOX) hBChE, and hAChE inhibitors to serve as multi-target directed ligands for AD treatment [6]. Javed et al. performed structural modifications on pyrimidine and pyrrolidone cores for the inhibition of COX-2, 5-LOX, BChE, and AChE [7]. Nadeem et al. reported indole derivatives carrying 2-arylidene derivatives of thiazolopyrimidine (**3**) as multitarget inhibitors of monoamine oxidase (MAO)-A, MOA-B, BChE, and AChE [8]. Martinez et al. evaluated terpenes from industrial orange juice by-products against the inhibition of LOX, BChE, and AChE for AD [9]. Razavi et al. reviewed the potential of licofelone (**4**, an NSAID) for the treatment of neurological disorders including AD. It is relevant to mention that licofelone is an established COX and LOX inhibitor [10]. Alqahtani et al. extracted stigmasta-7,22-diene-3-one (**5**) from Isodon rugosus for the inhibition of COX, LOX, BuChE, and AChE [11]. Fang et al. reported donepezil coupled with conventional NSAIDs (**6**) for the inhibition of COX-1, COX-2, BuChE, and AChE [12]. Javed et al. reported diclofenac derivatives (**7**) as concomitant inhibitors of AChE, MAO, COX-2, and 5-LOX for the potential agents against AD [13]. Kalra et al. demonstrated that modulation of COX and LOX inflammatory pathways provides mitoprotection to AD rats using Zafirlukast (**8**) and valdecoxib (**9**) [14]. Dias et al. reported a hybrid of feruloyl-donepezil (**10**) as the multi-target inhibitory ligand for COX-1, COX-2, 5-LOX, and AChE [15]. Zhang et al., while reviewing the nine important strategies for improved treatment of AD, highlighted the importance of dual inhibition of COX and LOX [16]. Similarly, Cornec et al. reviewed multitargeted imidazoles as potential therapeutic leads for AD and other neurodegenerative diseases and outlined the importance of COX and LOX pathway modulation in improved AD treatment [17].

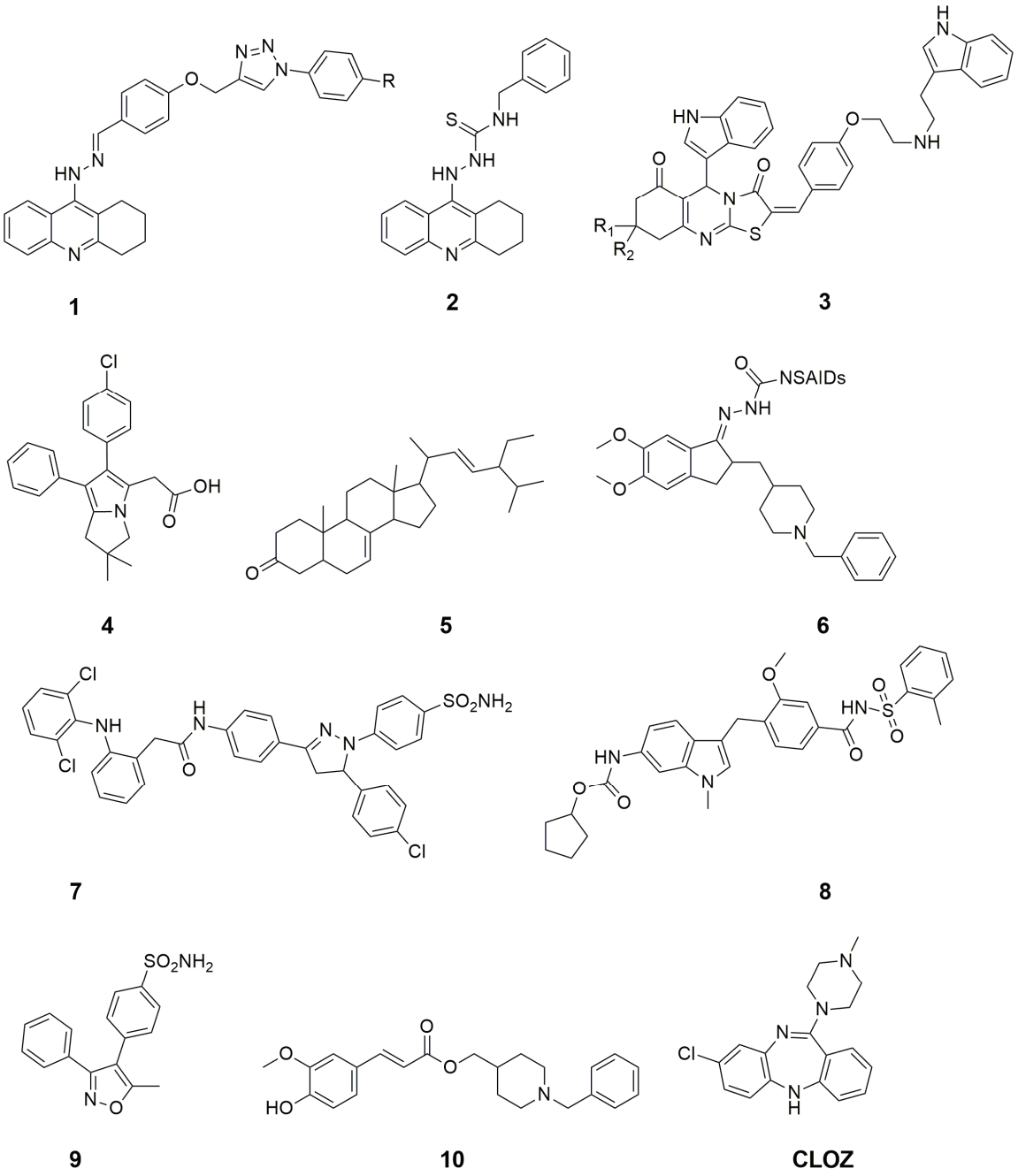

Figure 1. Chemical structures of the few ligands with multi-target action.

Clozapine (CLOZ) is an FDA-approved atypical tricyclic anti-psychotic molecule used for the treatment of schizophrenia. However, its use is limited due to the associated agranulocytosis and toxic hepatitis in a few cases. Because clozapine displays a promising therapeutic profile, it can be used as a template to develop new chemical entities devoid of agranulocytosis. Repurposing existing drugs, including those derived from chemically diverse natural products, presents a cost-effective and efficient strategy to address unmet medical needs. The inherent chemo-diversity of natural products, with their unique structural complexity and functional variability, serves as a valuable resource for identifying new therapeutic applications. Similarly, by leveraging the established pharmacodynamics and pharmacokinetics profile of known molecules, this approach can significantly accelerate the drug development pipeline [18,19]. In this work, structure-based virtual screening of US-FDA-approved molecules from the ZINC15 database identified CLOZ

as a dual inhibitor of COX-2 and AChE. Further molecular docking was performed into the active sites of 5-LOX, 15-LOX, and Caspase-3. The binding potential of CLOZ against the above-mentioned proteins was also evaluated using molecular dynamics simulation (MDS), followed by biological evaluation using in vivo model. As AD is characterized by inflammation oxidative stress, clozapine was also evaluated for downstream inflammatory markers like NF-κB, TNF-α, IL-6, IL-10, and TGF-β1. To the best of our knowledge, the above-mentioned molecular targets are not very well documented for CLOZ. This study aims to provide additional evidence that COX-2, 5-LOX AChE, and Caspase-3 are molecular targets and can be modulated by the first atypical antipsychotic CLOZ discovered in the year 1958. Figure 2 shows the workflow taken up in this report.

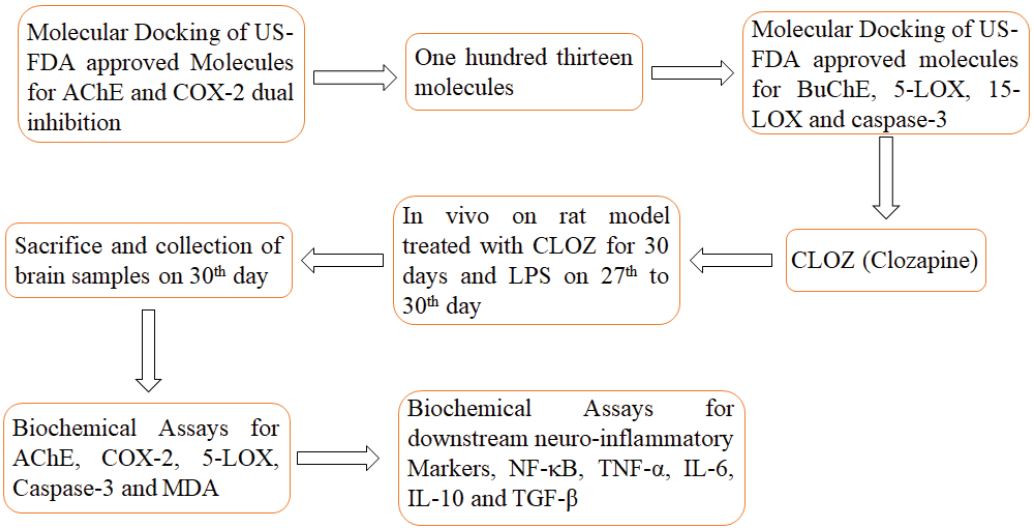

Figure 2. Workflow utilized in this report.

2. Results

2.1. Molecular Docking

The molecular docking of US-FDA-approved molecules obtained from the ZINC15 database were docked into the active sites of AChE and COX-2. The results identified CLOZ as a promising dual inhibitor of both AChE and COX-2. The CLOZ was further docked into the active sites of BuChE, 5-LOX, 15-LOX and Caspase-3. The CLOZ demonstrated notable binding affinities with AChE and BuChE, registering binding scores around 9.1 and 9.2 kcal/mol, respectively, as shown in Table 1. These scores were comparable to the co-crystallized ligands for AChE and COX-2, which had affinities of approximately 12.1 and 10.1 kcal/mol. Besides cholinesterases AChE and BuChE, CLOZ was also docked into the active sites of COX-2, 5-LOX, 15-LOX, and Caspase-3. The predicted binding affinities of CLOZ against the above-mentioned enzymes were 7.9, 7.6, 8.8, and 7.4 kcal/mol, respectively. The predicted binding affinities of the co-crystallized ligand for the aforementioned enzymes were 9.1, 9.7, 5.8, and 8.2 kcal/mol, respectively. Analysis of CLOZ's low-energy conformations indicated that its most stable binding poses interacted with key residues across multiple docked complexes.

Table 1. Predicted binding affinity (kcal/mol) of the co-crystallized ligand and CLOZ.

Sr. No.	Ligands	AChE	BuChE	COX-2	5-LOX	15-LOX	Caspase-3
1	Co-CL	12.1	10.9	9.1	9.7	5.8	8.2
2	CLOZ	9.1	9.2	7.9	7.6	8.8	6.7

2.2. Molecular Dynamics

MDS is crucial for exploring the dynamic interactions within protein–inhibitor complexes, revealing stability, binding interactions, and conformational flexibility. Unlike static docking, MD captures how temperature, solvent, and pressure affect molecular movements over time. This approach provides detailed insights into transient interactions such as hydrogen bonds and hydrophobic contacts, which are essential for understanding protein inhibition and enhancing inhibitor design in drug discovery. Therefore, in this work, the CLOZ complexed with AChE, BuChE, COX-2, 5-LOX, 15-LOX, and Caspase-3 was considered for MDS to evaluate their stability and binding interaction under dynamical conditions.

2.2.1. Root Mean Square Deviations

Figure 3 and Table 2 show RMSD values and the average RMSD values calculated over 150 ns of a simulation run for the complexes CLOZ complexed with AChE, BuChE, COX-2, 5-LOX, 15-LOX, and Caspase-3. The average RMSD value of backbone atoms across all the complexes varied in the range of 0.21 to 0.33 Å, while the standard deviation value varied in the range of 0.02 to 0.06 Å. Similarly, the average RMSD value for CLOZ varied in the range of 0.11 to 0.33 Å, and the standard deviation value for the calculated RMSD's of ligand was in the range of 0.05 to 0.09 Å. These low values of RMSDs across all complexes indicate that the backbone structure remained close to the reference conformation across the simulation run. Similarly, the low value of the standard deviation indicates minimal fluctuations around the average RMSD values, thus further consolidating the stability of the backbone in all complexes. Similarly, the low average RMSD and standard deviation values of the ligand in all complexes indicates good stability of the CLOZ across all enzyme complexes.

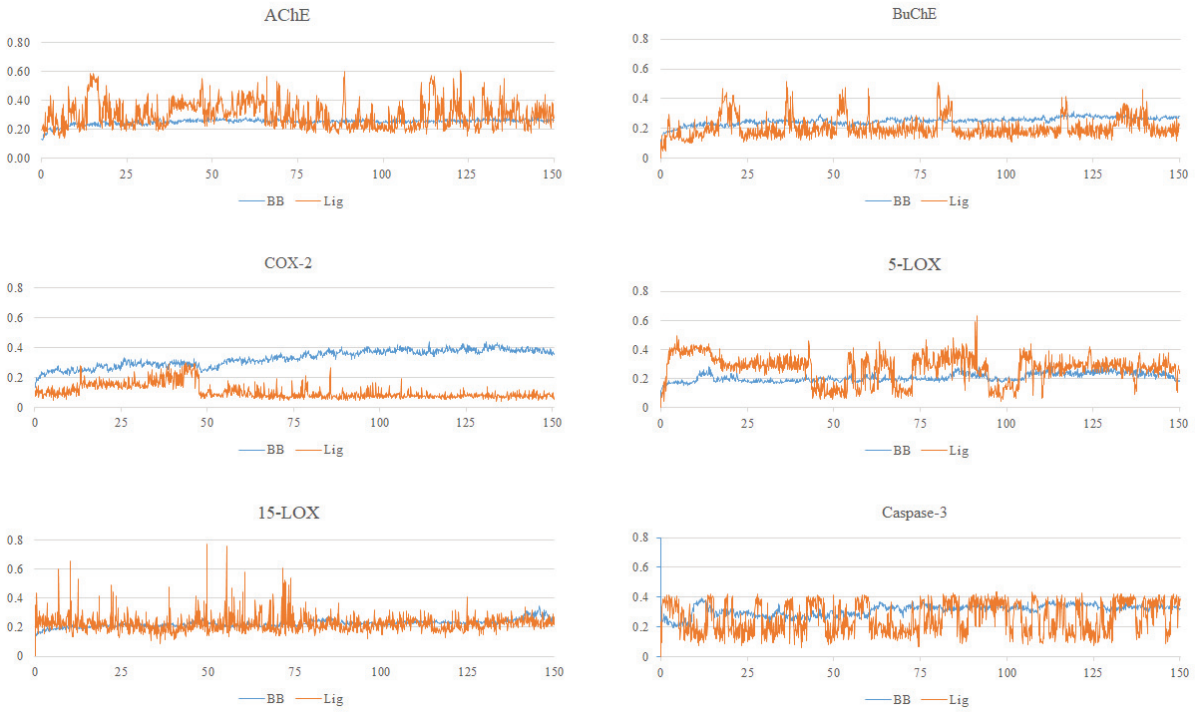

Figure 3. RMSD plots for CLOZ complexed with AChE, BuChE, COX-2, 5-LOX, and 15-LOX. The *x*-axis represents the simulation time in nanoseconds (ns), and the *y*-axis represents RMSD in nanometers (nm).

Table 2. Root mean square deviation (RMSD) values and standard deviation (SD) values for backbone atoms and ligands calculated across a simulation run of 150 ns.

	Enzyme	AChE	BuChE	COX-2	5-LOX	15-LOX	Caspase-3
Backbone	RMSD (Avg)	0.25	0.25	0.33	0.21	0.22	0.31
	SD	0.02	0.02	0.06	0.03	0.02	0.03
Ligand	RMSD (Avg)	0.30	0.20	0.11	0.27	0.22	0.26
	SD	0.09	0.07	0.05	0.09	0.06	0.10

2.2.2. Radius of Gyration

To assess the stability of the CLOZ–protein complexes, the radius of gyration (Rg) was used. A significant persistent Rg value for the protein inhibitor complex over the simulation period indicates that the overall shape and size of the protein were unaffected upon ligand binding. This could further be interpreted as proving that the binding event did not cause any significant structural folding rearrangements or unfolding processes within the protein. The persistent value of Rg may further imply that the protein structure was inherently robust or that the ligand binding took place without inducing any major conformational changes. For all complexes, the values ranged from 1.8 to 2.85 nm, with standard deviations between 0.01 and 0.02 nm, suggesting minimal fluctuation around the mean. Additionally, the standard error of the mean was between 0.0002 and 0.0004 nm, further confirming the consistency of values and indicating stable protein structures in the presence of CLOZ (Table 3). Figure 4 shows the variation in the Rg for all protein complexes calculated for 150 ns of a simulation run.

Table 3. Radius of gyration (Rg, nm) average values, standard deviation, and standard error of mean values for all proteins complexed with CLOZ.

	AChE	BuChE	COX-2	5-LOX	15-LOX	Caspase-3
Rg (Avg)	2.34	2.35	2.49	2.82	2.83	1.82
SD	0.01	0.01	0.01	0.02	0.01	0.01
SEM	0.000172	0.000237	0.000366	0.000427	0.000279	0.000319

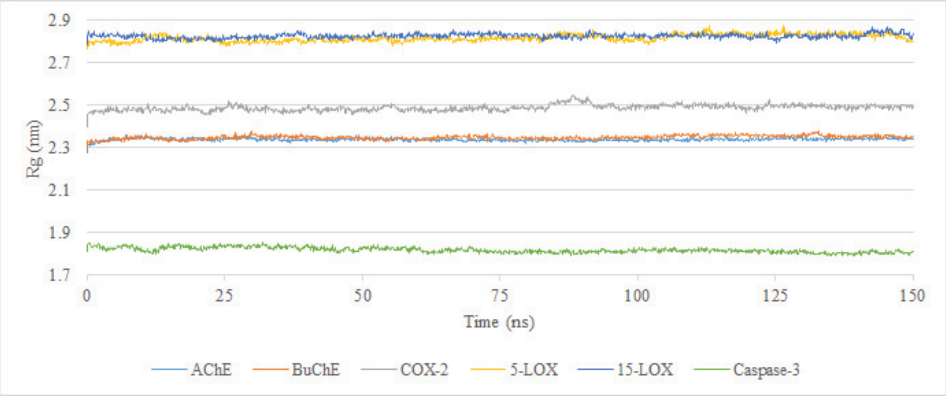

Figure 4. Radius of gyration (Rg, nm) for all proteins complexed with CLOZ.

2.2.3. Root Mean Square Fluctuation (RMSF)

RMSF is a commonly used metric in molecular dynamics (MD) simulations to quantify the flexibility of individual residues within a protein. RMSF represents the average deviation of each residue or atom from its mean position over the course of the simulation, indicating the extent of fluctuations in different regions of the molecule. Higher RMSF values typically correspond to flexible regions, such as loops or surface-exposed areas,

while lower values suggest more rigid, structurally stable regions, often in the protein's core. RMSF analysis helps to pinpoint flexible and stable areas, providing insights into the protein's structural dynamics and functional sites. The RMSF values for all proteins in consideration varied in the range of 0.2 to 0.5 nm. For AChE, the RMSF values showed significant fluctuations for residues at the N-terminal region, with the peak of residue 43 reaching 3.5 nm. Beyond residue 43, the RMSF value stabilized around 1 nm with minor fluctuations at the C terminal, indicating that the N-terminal of the AChE is highly flexible, with the rest of the protein being relatively stable. For BuChE, the RMSF values were lower and remained below 0.5 nm. Periodic spikes were observed, indicating the regions of flexibility, especially towards the C-terminal end of the protein. Overall, the BuChE displayed uniform stability, with minor fluctuations throughout the protein. For the complex of COX-2, the fluctuations were observed to be marginally higher at the N-terminal regions, with residues around 72 displaying values of 0.5 nm. Beyond residue 72, the RMSF values decreased to 0.2 nm, with peaks scattered across the protein suggesting that the N-terminal region of the COX-2 is marginally flexible while the rest of the protein is stable. For 5-LOX, the RMSF fluctuations for most of the residues stayed around 0.2 nm, with residue 133 displaying highest the RMSF value of 0.35 nm, in addition to the few minor peaks that were observed throughout the protein structure. Overall, the 5-LOX displayed general stability across the protein. The residues of 15-LOX displayed moderate fluctuations, with residues 22, 292, and 372 displaying the highest RMSF values of 0.4 nm. As observed for 5-LOX, most of the fluctuations were minor, suggesting stable regions with flexible areas in between. Overall, AChE displayed the highest flexibility among the proteins, particularly at the N-terminus, while COX-2, 5-LOX, and 15-LOX showed more moderate fluctuations. BuChE appeared to be the most stable, with fewer regions of high flexibility. Figure 5 shows the RMSFs for all complexes.

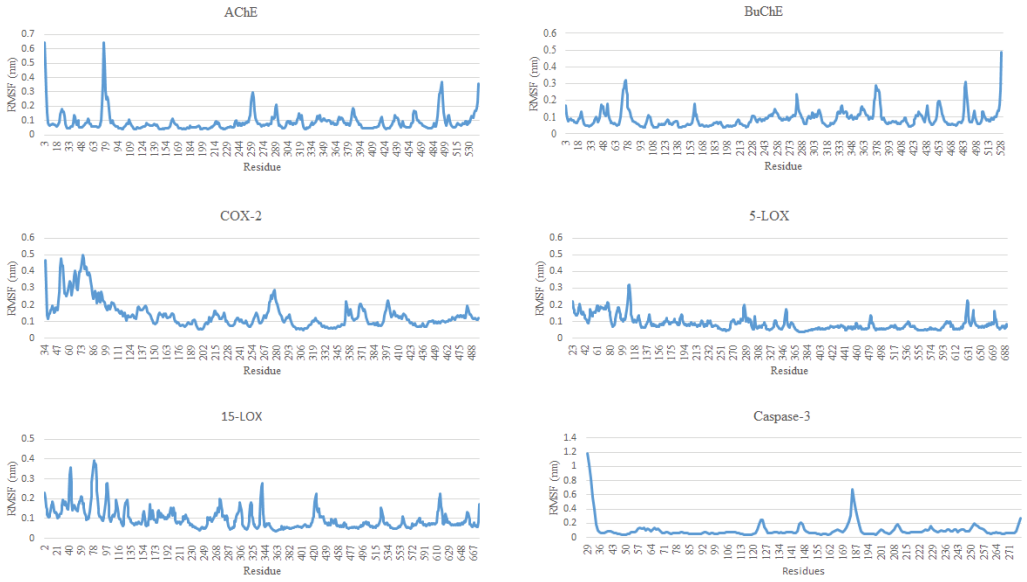

Figure 5. Root mean square fluctuations for residues of all the complexes.

2.2.4. Binding Energy

Binding energy is a critical parameter that quantifies the strength and stability of the complex formed between a receptor and its ligand. Figure 6 shows the binding energy calculated for the CLOZ complexed with the AChE, BuChE, COX-2, 5-LOX, and 15-LOX using the Generalized Born Surface Area (GBSA) approach, a popular method in MDS. The gas phase energy (ΔE (gas)) includes contributions from Van der Waals (ΔE_{VDW}) and electrostatic energy (ΔE_{EL}) and represents energies from the direct interaction of protein

and CLOZ in the absence of solvent. The solvent phase energy (ΔE_{solv}) is split into polar solvation energy (ΔE_{GB}) and non-polar solvation energy (ΔE_{surf}). ΔE_{Bind} represents the net binding energy, combining both gas-phase and solvent-phase energy to predict the overall favorability of the protein–CLOZ binding. It should be noted that the binding energies shown in this work do not include entropy contributions and, hence, represent the enthalpy contributions to binding free energy. The total binding energy of CLOZ for all complexes varied in the range of ~8 to ~32 kcal/mol, with COX-2 and 5-LOX displaying the highest binding energy of 32 kcal/mol. The binding energy of CLOZ for cholinesterase was found to be ~25 kcal/mol. The binding energy of CLOZ for Caspase-3 was the lowest, with a value of ~8 kcal/mol. The individual contributions to the binding energy were also calculated. The gas-phase VDW energies were negative across all the complexes, indicating favorable hydrophobic interactions. The gas-phase EEL values were strongly negative for all complexes except for COX-2 and Caspase-3, indicating significant electrostatic interactions across AChE, BuChE, 5-LOX, and 15-LOX. A high amount of polar solvation energy was noted across all the enzymes except COX-2 and Caspase-3, indicating significant resistance from the solvent molecules during the binding of CLOZ with AChE, BuChE, 5-LOX, and 15-LOX. The non-polar solvation energy was found to be marginally negative across all the complexes, indicating minor favorable contributions to the binding energy from solvation of the ligand. The gas-phase energy was found to be a highly favorable protein–ligand interaction. The solvent-phase energy was found to highly unfavorable, except for COX-2 and Caspase-3. Overall, the binding of CLOZ to AChE, BuChE, 5-LOX, and 15-LOX was driven by both by electrostatic and VDW despite a high amount of solvation penalties. The binding of CLOZ to COX-2 and Caspase-3 was mainly driven by hydrophobic interactions. Further, the CLOZ displayed the highest amount of binding energy for COX-2 and 5-LOX.

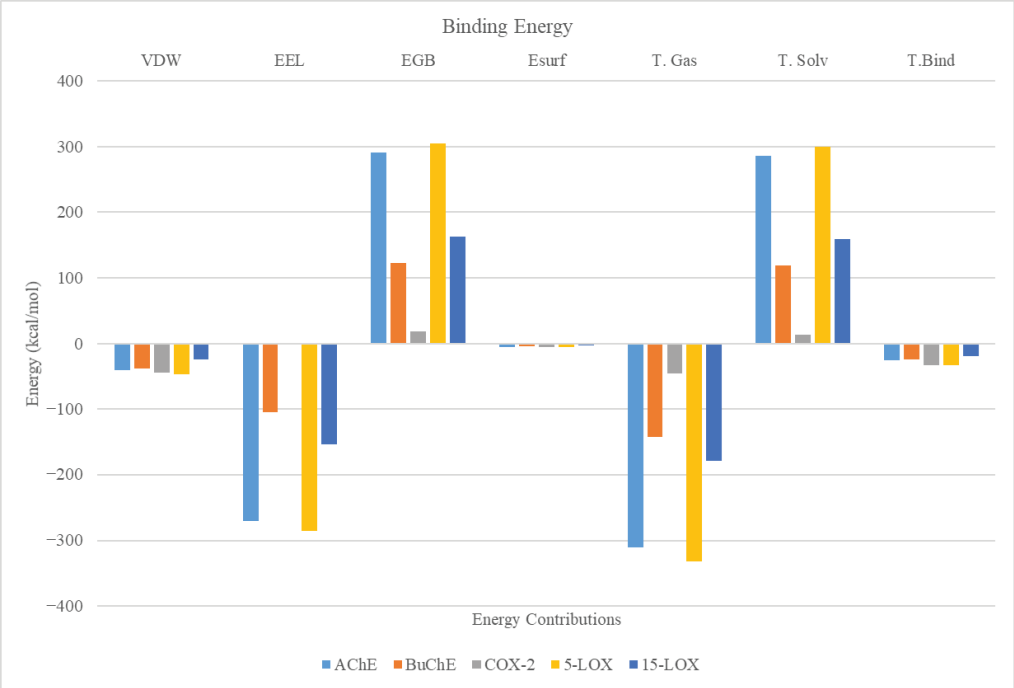

Figure 6. Individual contributions to the binding energy for all complexes taken up for MDS.

Figure 7 presents the per-residue energy decomposition analysis for the interactions of ligands with AChE, BuChE, COX-2, 5-LOX, and 15-LOX. The results indicate significant contributions from specific residues to the binding energy across all targets. For AChE, Trp85 exhibited the strongest interaction, contributing approximately −2.5 kcal/mol, while

Asn86 and Gly120 provided moderate stabilization (~1.0 kcal/mol). In BuChE, Phe329, Pro285, and Trp231 were the major contributors, with energies around −1.6, −1.4, and −1.2 kcal/mol, respectively. For COX-2, Ser530 displayed the highest contribution at approximately −3.0 kcal/mol, followed by Val349 (−2.2 kcal/mol), Leu531 (−1.7 kcal/mol), and Ala527 (−1.4 kcal/mol). The interaction profile of 5-LOX showed notable contributions from residues His385, Leu432, and Phe439, with energy values approximately −2.0 kcal/mol. Additionally, Gln381, His390, Asn443, Gln575, Ala621, and Leu625 made notable contributions (~−1.0 kcal/mol). In 15-LOX, Tyr185, Ala188, and Phe192 were the most significant contributors, with interactions around −1.6 kcal/mol. In Caspase-3, Tyr204 and Phe256 made notable contributions. The contribution of the ligand (Figure 8) to the binding energy across all proteins reveal the strongest affinity towards AChE and 5-LOX kcal/mol, followed by COX-2 and BuChE, with values above ~−20.00 and −15 kcal/mol, respectively. The ligand contributions to the binding energy of 15-LOX and Caspase-3 were found to be ~−12 and −5 kcal/mol. These insights highlight critical residues driving ligand binding, providing a basis for rational modifications to improve specificity and binding efficacy.

Figure 7. Residue contributions to the binding energy in all six complexes.

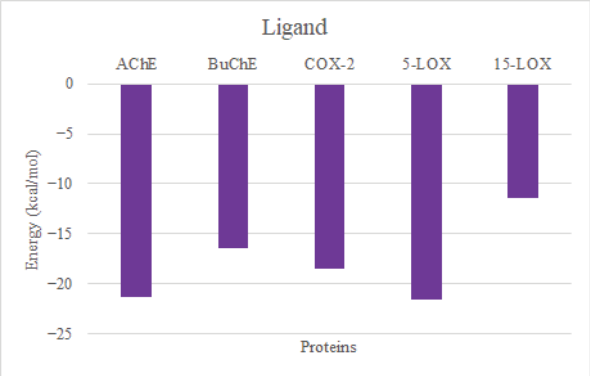

Figure 8. CLOZ contributions to the binding energy in all six complexes.

2.3. Biochemical Analysis

Figure 9 shows the effects of CLOZ on various biochemical markers related to inflammation, oxidative stress, and cell death in LPS-induced rats. These markers include COX-2, 5-LOX, AChE, Caspase-3, and MDA. The figure displays data for four groups—Control, LPS, and CLOZ + LPS—at two different doses (C5 + L and C10 + L for 5 and 10 mg/kg, respectively). Statistical significance was assessed by one-way ANOVA followed by Tukey–Kramer multiple comparisons. The results showed that COX-2 levels were significantly increased in the LPS group compared to the control group ($p < 0.01$), indicating an inflammatory response induced by LPS. CLOZ treatment at both doses significantly reduced COX-2 levels compared to the LPS group ($p < 0.01$ for C5 + L and $p < 0.05$ for C10 + L), suggesting that CLOZ can mitigate the LPS-induced upregulation of COX-2. Similar to COX-2, 5-LOX levels were also significantly high in the LPS group ($p < 0.01$ vs. control), reflecting enhanced inflammation. CLOZ treatment significantly lowered 5-LOX levels ($p < 0.05$ for C5 + L and $p < 0.01$ for C10 + L vs. LPS), indicating that CLOZ also reduced 5-LOX levels, with the higher dose demonstrating a more substantial effect. As observed for COX-2 and 5-LOX, AChE levels were significantly increased in the LPS group compared to the control group ($p < 0.001$), suggesting potential neuroinflammatory or neurotoxic effects of LPS. Both doses of CLOZ significantly decreased AChE levels ($p < 0.001$ for C5 + L and C10 + L vs. LPS), indicating that CLOZ can counteract LPS-induced AChE upregulation, with the higher dose showing a stronger effect. Caspase-3 levels, a marker of apoptosis, were also significantly higher in the LPS group compared to the control ($p < 0.01$), suggesting that LPS induces cell death pathways. Treatment with CLOZ significantly reduced Caspase-3 levels ($p < 0.01$ for C5 + L and C10 + L), highlighting CLOZ's potential anti-apoptotic effect, particularly at the higher dose. MDA, a marker of lipid peroxidation and oxidative stress, was significantly increased in the LPS group compared to the control ($p < 0.001$), indicating oxidative damage induced by LPS. CLOZ treatment reduced MDA levels ($p < 0.05$ for C5 + L and C10 + L), demonstrating CLOZ's role in mitigating oxidative stress, with the higher dose again showing a greater effect.

Figure 10 shows the effects of CLOZ on neuroinflammatory-related parameters in LPS-induced rats. The data are presented as mean ± SEM for various pro- and anti-inflammatory markers, including NF-κB, TNF-α, IL-6, IL-10, and TGF-β1, across four groups. NF-κB levels were significantly elevated in the LPS group compared to the control group ($p < 0.001$), indicating a marked inflammatory response due to LPS. Treatment with CLOZ at both doses (C5 + L and C10 + L) significantly reduced NF-κB levels compared to the LPS group ($p < 0.01$ and $p < 0.001$, respectively), suggesting that CLOZ effectively attenuated the LPS-induced activation of NF-κB, with the higher dose (C10 + L) showing a stronger reduction. LPS treatment also resulted in a significant increase in TNF-α levels ($p < 0.01$ vs. CON), another pro-inflammatory marker. CLOZ treatment at both doses

significantly decreased TNF-α levels compared to the LPS group ($p < 0.01$ for C5 + L and $p < 0.05$ for C10 + L). This decrease indicated the anti-inflammatory action of CLOZ on TNF-α expression in LPS-induced neuroinflammation. Similarly to NF-κB and TNF-α, the levels of another pro-inflammatory marker, IL-6, were significantly higher in the LPS group compared to the control ($p < 0.001$), consistent with an inflammatory response. Only the higher dose of CLOZ effectively reduced IL-6 levels ($p < 0.01$ for C10 + L vs. LPS), confirming its role in mitigating LPS-induced IL-6 upregulation, with the higher CLOZ dose again providing a greater reduction.

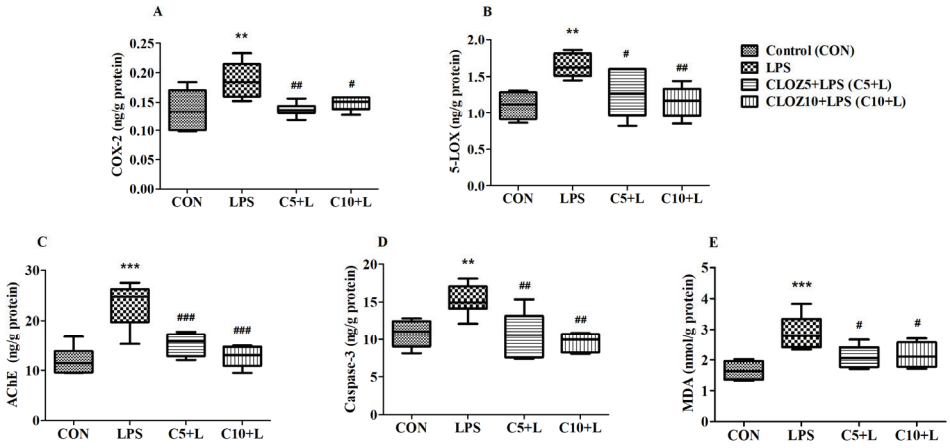

Figure 9. Effect of clozapine (CLOZ) on (**A**) COX-2, (**B**) 5-LOX, (**C**) AChE, (**D**) Caspase-3, and (**E**) MDA in LPS-induced rats. The results are expressed by mean ± SEM ($n = 6$). One-way ANOVA followed by Tukey–Kramer multiple comparisons test. ** $p < 0.01$ and *** $p < 0.001$ vs. control group; # $p < 0.05$, ## $p < 0.01$, and ### $p < 0.001$ vs. LPS-induced group.

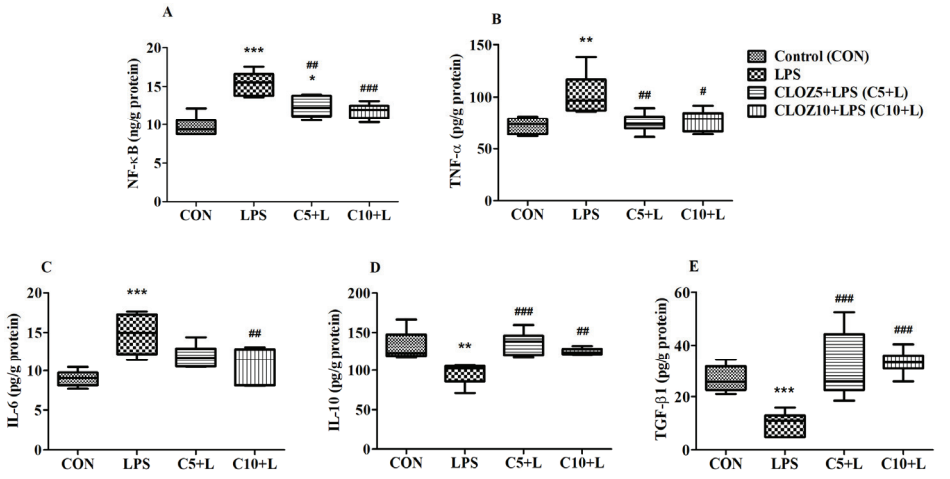

Figure 10. Effect of clozapine (CLOZ) on neuroinflammatory parameters: (**A**) NF-κB, (**B**) TNF-α, (**C**) IL-6, (**D**) IL-10, and (**E**) TGF-β1 in LPS-induced rats. The results are expressed by mean ± SEM ($n = 6$). One-way ANOVA followed by Tukey–Kramer multiple comparisons test. * $p < 0.05$, ** $p < 0.01$, and *** $p < 0.001$ vs. control group; # $p < 0.05$, ## $p < 0.01$, and ### $p < 0.001$ vs. LPS-induced group.

3. Discussion

The "one drug, one target" paradigm has long been the cornerstone of drug development, emphasizing the design of highly selective molecules to modulate a single biological target with precision. While this approach has led to significant breakthroughs in treating diseases with well-defined molecular mechanisms, it presents notable limitations when addressing complex, multifactorial conditions such as AD [20]. A network of interrelated

pathological processes characterizes AD, including Aβ accumulation, tau hyperphosphorylation, oxidative stress, neuroinflammation, and synaptic dysfunction. Targeting a single molecule or pathway often fails to address the interconnected nature of these pathological drivers, leading to suboptimal therapeutic outcomes. Moreover, compensatory mechanisms within the disease network can undermine the efficacy of single-target therapies [5,16,21]. Recent clinical failures of drugs focused solely on Aβ clearance underscore these challenges and highlight the need for more holistic strategies. The intricate and progressive nature of AD necessitates approaches that account for a multifaceted disease pathology, favoring multi-target or pathway-modulating drugs over highly selective agents. Recognizing these limitations has spurred interest in the identification of multi-targeted ligands for the treatment of complex disorders like AD. Therefore, this work employed structure-based virtual screening of US-FDA-approved drugs to identify the dual inhibitor of COX-2 and AChE. The identified molecules were further docked into the active sites of BuChE, 5-LOX, 15-LOX, and Caspase-3. The molecular docking results identified CLOZ as one of the potential molecules to modulate multiple targets. Further, the docked complexes of CLOZ were subjected to MDS for stability assessment. The efficacy of CLOZ for the targeted enzymes was further evaluated using an in vivo rat model treated with CLOZ for thirty days and with LPS for four days, i.e., from the 27th to 30th days.

Molecular docking is a vital tool in early drug development, offering a cost-effective alternative to traditional high-throughput screening [22]. Advances in algorithms and scoring functions have enhanced its accuracy in predicting binding poses and affinities, making it invaluable for hit identification, lead optimization, and assessing off-target interactions [23]. Its integration with computational and experimental methods has revolutionized drug discovery, enabling the exploration of mechanisms of action and addressing complex therapeutic challenges. Our initial molecular docking results identified CLOZ as the potential dual inhibitor of COX-2 and AChE. In addition to AChE and COX-2, the CLOZ was docked into the active sites of BuChE, 5-LOX, 15-LOX, and Caspase-3. The molecular docking results against molecular targets in consideration showed binding affinities comparable to the co-crystallized ligands. The binding mode analysis revealed that lowest energy docked conformation of CLOZ interacted with key residues and, hence, were taken up for MDS for 150 ns. Parameters like RMSD, radius of gyration, RMSF, binding energy, energy contributions, and residue-wise energy contributions to the binding energy were calculated. The low average RMSD values and minimal standard deviations for both the backbone atoms and the ligand across all enzyme complexes highlight the structural stability of the CLOZ complexes. These results further emphasize that CLOZ maintains a consistent binding pose, reinforcing its potential as a stable modulator of the studied enzymes. The consistent Rg values across all CLOZ–protein complexes, with minimal fluctuations and low standard errors, underscore the structural stability of the proteins over the 150 ns simulation. These results indicate that ligand binding does not induce significant conformational changes, further supporting the inherent robustness of the protein–CLOZ complexes. The RMSF analysis highlights distinct flexibility patterns among the CLOZ–protein complexes, with AChE exhibiting the highest fluctuations, particularly at the N-terminus, while BuChE demonstrated the greatest stability across its residues. The marginally flexible N-terminal regions in COX-2, along with the generally stable profiles observed for 5-LOX and 15-LOX, suggest that these proteins maintain their structural integrity with localized flexibility that may contribute to functional adaptability. The binding energy analysis highlights that CLOZ exhibits strong and favorable binding with COX-2 and 5-LOX, driven predominantly by hydrophobic interactions and supported by significant van der Waals contributions. Despite the solvation penalties observed for AChE, BuChE, 5-LOX, and 15-LOX, the favorable gas-phase interactions, including electrostatics and van der Waals forces, ensured

stable binding, underscoring the importance of these interactions in the overall binding mechanism. Further, per-residue energy decomposition analysis revealed key amino acids contributing significantly to CLOZ binding across all protein targets, highlighting their roles in stabilizing the complexes. For AChE, Trp86, Gly120, and Gly121 emerged as significant contributors to the binding energy. Notably, Trp86 is a key residue in the peripheral aromatic binding site which plays a crucial role in the interaction with small molecules and substrates. Meanwhile, Gly120 and Gly121, along with Ala204, form part of the oxyanion binding site, a critical component of the catalytic machinery involved in the hydrolysis of ACh. For BuChE, the residues Trp231, Pro285, Val288, Phe329, and Gly117 play critical roles in ligand binding. Notably, Trp231, Pro285, and Phe329 have been documented for collectively creating a complementary binding environment within the active site. This synergy is vital for effective substrate recognition, stabilization, and catalysis [24,25]. In the case of COX-2, Val349, Ala527, Ser530, and Leu531 are key contributors in the binding of CLOZ, each contributing uniquely to the function and interaction of COX-2 with substrates and inhibitors. Val349 and Leu531 shape the hydrophobic environment and define the side pocket unique to COX-2, enabling selective inhibitor binding. Ala527, with its smaller side chain compared to the corresponding residue in COX-1, expands the active site cavity, further facilitating COX-2 specificity. Ser530 plays a catalytic role and is the site of irreversible acetylation by aspirin, blocking substrate access and prostaglandin synthesis. Collectively, these residues are critical for COX-2's enzymatic activity, substrate specificity, and inhibitor binding, making them focal points in anti-inflammatory action [24–26]. For the case of 5-LOX, notable contributors are His367, Leu414, Phe421, Gln363, His372, Asn425 Gln557, Ala603, and Leu607, which play crucial roles in ligand binding by forming a network of interactions that stabilize ligands and facilitate enzymatic activity. His367 and His372 are central to the catalytic mechanism, as they coordinate the non-heme iron essential for oxygenation reactions, ensuring the proper alignment of ligands with the catalytic core [27]. Leu414, Phe421, Ala603, and Leu607 contribute to the hydrophobic environment of the active site, stabilizing hydrophobic ligands such as CLOZ. Gln363, Asn425, and Gln557 are involved in forming hydrogen bonds and polar interactions, enhancing ligand specificity and stabilization. These residues play a dynamic role in orienting ligands within the active site, ensuring proper positioning for catalytic efficiency [28]. In 15-LOX, Tyr185, Ala188, and Phe192 contributed significantly to CLOZ binding and were similar to the interactions reported in previous studies [29,30]. For Caspase-3, Tyr204 and Phe256 played notable roles in the binding of CLOZ and have been reported as unique residues present in the S2 subsite of Caspase-3 [31]. The contribution of a ligand to the binding energy is crucial in determining the strength, stability, and specificity of its interaction with a target protein. This aspect is particularly important as it reflects the ligand's ability to form strong and favorable interactions with the active-site residues. A ligand with a high contribution to binding energy enhances the overall binding affinity, which is key for achieving potent inhibition of the target. In this study, CLOZ demonstrated a significant contribution to the binding energy of AChE, BuChE, COX-2, and 5-LOX, highlighting its potential as a multitarget inhibitor. This underscores the promising role of CLOZ in modulating key enzymes associated with AD and neuroinflammation.

The dual inhibition of COX-2 and 5-LOX represents a promising therapeutic strategy for managing inflammation-driven diseases, including neurodegenerative conditions such as AD [10,17]. COX-2 and 5-LOX are critical enzymes in the arachidonic acid metabolic pathway, responsible for producing pro-inflammatory mediators like prostaglandins and leukotrienes, respectively. Chronic neuroinflammation, driven in part by these mediators, is increasingly recognized as a central factor in the pathogenesis and progression of AD. While selective COX-2 inhibitors have shown potential in alleviating neuroinflammation [32,33],

their long-term use is associated with cardiovascular risks, necessitating safer alternatives. Similarly, 5-LOX inhibitors have demonstrated benefits in reducing leukotriene-mediated oxidative stress and Aβ accumulation in preclinical models of AD [7,34,35]. Dual inhibition of COX-2 and 5-LOX offers a synergistic approach by targeting both arms of the inflammatory cascade, potentially providing enhanced neuroprotection and mitigating adverse effects linked to single-target therapies [36]. Therefore, taking into consideration the results from molecular docking and dynamics, the CLOZ was evaluated for its efficacy using an in vivo rat model treated with two doses of 5 mg/kg and 10 mg/kg for thirty days and with LPS on the 27th to 30th days. Our results showed significant decreases in the levels of both the inflammatory enzymes COX-2 and 5-LOX. CLOZ's capacity to markedly reduce COX-2 and 5-LOX expression highlights its strong anti-inflammatory potential. This property could be instrumental in suppressing the production of prostaglandins and leukotrienes, as they are major contributors to driving the inflammatory cascade.

The simultaneous modulation of COX-2 and 5-LOX by CLOZ exhibited a significant impact on key inflammatory mediators, including NF-κB, TNF-α, and IL-6, as well as anti-inflammatory mediators such as IL-10 and TGF-β1 (Figures 9 and 10, Section 2.3), thereby demonstrating a broad-spectrum anti-inflammatory effect. COX-2 and 5-LOX products, such as prostaglandins (e.g., PGE2) and leukotrienes (e.g., LTB4), play essential roles in activating NF-κB [37,38], a transcription factor that regulates the expression of various pro-inflammatory genes. NF-κB activation occurs in response to inflammatory stimuli and is perpetuated by positive feedback mechanisms driven by prostaglandins and leukotrienes. The reduction in the levels of COX-2 and 5-LOX by CLOZ reduces the production of these mediators, thereby attenuating NF-κB activation. This suppression limits the transcription of downstream pro-inflammatory cytokines and enzymes, such as TNF-α, IL-6, and additional COX-2 expression, creating a cascade of reduced inflammation. The modulation of NF-κB levels also prevents chronic inflammation, a hallmark of neurodegenerative disorders like AD [39]. TNF-α is a central pro-inflammatory cytokine involved in amplifying the inflammatory response [40]. Its production is regulated by NF-κB activation and is further enhanced by the presence of leukotrienes and prostaglandins [41–43] Elevated TNF-α levels are implicated in neuroinflammation, contributing to neuronal damage and progression of AD [44]. By suppressing both NF-κB activation and the direct inflammatory effects of leukotrienes and prostaglandins, dual modulation of COX-2 and 5-LOX can significantly lower TNF-α levels. This reduction in TNF-α not only decreases the inflammatory burden but may also protect neurons from cytokine-induced apoptosis, offering neuroprotective benefits in AD. IL-6 is another pro-inflammatory cytokine highly regulated by NF-κB [45]. It is a key player in chronic inflammation and is often elevated in AD and other neurodegenerative diseases [46]. Prostaglandins and leukotrienes can further stimulate IL-6 production, perpetuating the inflammatory loop [43,47]. The inhibition of COX-2 and 5-LOX interrupts this loop by reducing the upstream mediators driving IL-6 expression. Lower levels of IL-6 can mitigate systemic and neuroinflammation, reducing the neuronal damage and glial activation commonly observed in AD. IL-10 is an anti-inflammatory cytokine that acts as a counter-regulator of pro-inflammatory responses [48]. While COX-2 and 5-LOX inhibition primarily targets pro-inflammatory pathways, their suppression indirectly promotes an anti-inflammatory environment that can enhance IL-10 production. This shift toward an anti-inflammatory milieu can help restore immune homeostasis and reduce chronic inflammation. The upregulation of IL-10, facilitated by the reduced inflammatory pressure, may also limit the activation of microglia and astrocytes in the brain, further contributing to neuroprotection and resolution of inflammation in AD. TGF-β1 is a multifunctional cytokine with both pro- and anti-inflammatory roles, depending on the context. In neuroinflammatory conditions, TGF-β1 often plays a protective role by

promoting tissue repair, dampening excessive immune responses, and supporting neuronal survival [49]. Dual inhibition of COX-2 and 5-LOX reduces the production of inflammatory prostaglandins and leukotrienes, which can help maintain TGF-β1's anti-inflammatory and reparative functions. This modulation supports a balanced immune response, allowing TGF-β1 to contribute to neuroprotection and recovery without exacerbating inflammation.

Caspase-3 is a critical executioner enzyme in the apoptotic pathway, playing a central role in programmed cell death [50]. Elevated expression of Caspase-3 is often linked with neuroinflammatory and oxidative stress conditions, making it a key marker of neurodegeneration in conditions like AD [51–53]. Chronic inflammation, driven by mediators like NF-κB, TNF-α, and IL-6, creates a pro-apoptotic environment that sustains caspase-3 activation, often leading to excessive apoptosis, TNF-α, in particular, directly activates caspase-3 through the extrinsic apoptotic pathway. The modulation of COX-2 and 5-LOX by CLOZ, leading to the reduction in inflammatory mediators such as NF-κB, TNF-α, and IL-6, can influence Caspase-3 activity by mitigating the pro-apoptotic environment typically driven by chronic inflammation. Furthermore, the upregulation of anti-inflammatory mediators like IL-10 and TGF-β1 can promote cellular survival pathways, reducing the likelihood of Caspase-3 activation. This dual regulation of inflammatory and anti-inflammatory mediators may contribute to the preservation of neuronal integrity and the attenuation of apoptosis, highlighting the therapeutic potential of CLOZ targeting COX-2 and 5-LOX in reducing Caspase-3 mediated neuronal damage in neurodegenerative diseases.

AChE plays a critical role in regulating the cholinergic system by hydrolyzing acetylcholine (ACh), a neurotransmitter essential for learning, memory, and other cognitive functions. AChE regulates the cholinergic system by hydrolyzing ACh in the synaptic cleft, terminating neurotransmission and preventing overstimulation of postsynaptic receptors. This process ensures efficient signal transmission and maintains neural homeostasis. Dysregulation of AChE activity is linked to neurodegenerative diseases like Alzheimer's and is targeted therapeutically with AChE inhibitors to enhance cholinergic function. In AD, increased AChE activity exacerbates the cholinergic deficit, contributing to cognitive decline. Inflammation, a hallmark of AD, is intricately linked to the cholinergic system [54]. Pro-inflammatory mediators such as TNF-α, IL-6, and NF-κB activation disrupt ACh signaling by promoting neuronal damage and reducing ACh synthesis. Furthermore, inflammation upregulates AChE expression, compounding the cholinergic deficit and worsening cognitive dysfunction. The modulation of COX-2 and 5-LOX pathways by CLOZ can mitigate this inflammatory burden by suppressing key mediators while enhancing anti-inflammatory cytokines like IL-10 and TGF-β1. This reduction in inflammation not only protects cholinergic neurons, but may also help restore ACh levels by limiting the overactivity of AChE. The dual inhibition of COX-2 and 5-LOX thus represents a promising strategy to address the interplay between inflammation and the cholinergic system, potentially alleviating cognitive symptoms and slowing the progression of neurodegeneration in AD.

MDA is a key biomarker of lipid peroxidation, reflecting oxidative damage to cell membranes caused by reactive oxygen species (ROS), often elevated in neurodegenerative diseases such as AD [55]. It influences cellular integrity, mitochondrial function, and systemic inflammatory responses. MDA is a by-product of ROS attacking lipids, indicating the severity of oxidative stress. It contributes to cellular damage by forming adducts with DNA and proteins, impairing their functions and perpetuating mitochondrial dysfunction. MDA activates pro-inflammatory pathways by interacting with Toll-like receptors (TLRs) and promoting cytokine release (e.g., TNF-α, IL-6). This amplifies the oxidative–inflammatory cycle, contributing to chronic inflammation in conditions like AD [56]. Elevated MDA not only signifies oxidative damage but also contributes to neuronal dysfunction by disrupting membrane integrity and promoting apoptosis [57]. The dual inhibition of COX-2 and

5-LOX by CLOZ can mitigate oxidative stress by reducing inflammatory pathways that amplify ROS production. Additionally, anti-inflammatory mediators such as IL-10 and TGF-β1, promoted through this inhibition, may counteract oxidative damage and protect neuronal integrity. By targeting both inflammation and oxidative stress, CLOZ has the potential to lower MDA levels, providing neuroprotective effects and alleviating oxidative damage associated with AD progression.

4. Materials and Methods

4.1. Molecular Docking

Molecular docking studies were performed using previous studies. The crystal structures of target proteins, COX-2 (4EY7), AChE (5-IKR), BuChE (4TPK), 5-LOX (6N2W), 15-LOX (4NRE), and Caspase-3 (1GFW), were acquired from the Protein Data Bank (PDB), while the chemical structure of CLOZ was obtained from PubChem in SDF format and converted to PDB format using Open Babel. Molecular docking studies were conducted with AutoDock Vina (version 1.1.2, La Jolla, CA, USA) [58]. Protein and ligand preparations were carried out using AutoDock tools (ADT) from MGLTools (version 1.5.6) [59]. The protein preparation involved removing heteroatoms, water molecules, and nonpolar hydrogens, then adding polar hydrogens and Kollman charges and finally converting them to PDBQT format. Similarly, the ligand preparation included minimization using a universal force field, defining torsions, adding Gasteiger charges, and converting them to PDBQT format. The grid boxes for docking were defined in AutoGrid4 (version 4.2.6), with centers aligned to the co-crystallized ligands, and grid dimensions were set to encompass all atoms of each co-crystallized ligand. Docking simulations generated ten binding modes for each target, and the top three scoring modes, based on binding affinity in kcal/mol, were selected for detailed analysis. From these, the binding mode chosen for further discussion and MDS was based on key residues cited in previous studies. To visualize hydrogen bonds and hydrophobic interactions in the docked complexes, a free version of Discovery Studio was employed.

4.2. Molecular Dynamics

MDS were performed using GROMACS 2023 version 5 (KTH Royal Institute of Technology, Stockholm, Sweden). CHARMM36 (version 4.6) and generalized AMBER force field (GAFF, version 2.11) were used to prepare the topology file protein and ligand, respectively. The simulation system was prepared in a cubic water box with dimensions of 11.92885 × 11.92885 × 11.92885 nm, ensuring a minimum solute–box distance of 1.0 nm, and solvated with 161,646 TIP3P water molecules to mimic an aqueous environment. The molecular dynamics simulation was initiated with energy minimization (EM) to resolve steric clashes and optimize the system geometry. The steepest descent algorithm was employed, with the minimization halting when the maximum force fell below 1000 kJ/mol. A step size of 0.01 was used, and the process was limited to a maximum of 50,000 steps. Electrostatic interactions were modeled using the Particle Mesh Ewald (PME) method with a cutoff distance of 1.2 nm, while van der Waals interactions employed a cutoff distance of 1.2 nm as well. Periodic boundary conditions were applied in all three dimensions to mimic infinite system behavior. After energy minimization, counterions were added to neutralize the system, and an additional minimization was performed using the same steepest descent algorithm, with a cutoff of 1.0 nm for both electrostatics and van der Waals interactions. Next, the system underwent equilibration in two phases, beginning with constant volume and temperature (NVT) equilibration. The leap-frog integrator was used with a 2 fs time step over 50,000 steps, corresponding to 100 ps of simulation time. Temperature coupling was achieved using a modified Berendsen thermostat, maintaining

the protein–ligand and solvent groups at 300 K. Long-range electrostatic interactions were treated using PME with a cutoff of 1.2 nm, and van der Waals interactions were modeled with the same cutoff distance. Following NVT, constant pressure and temperature (NPT) equilibration was conducted using the same integrator and time step over 100,000 steps (200 ps). The pressure was regulated using the Berendsen barostat at 1.0 bar, with an isothermal compressibility of 4.5×10^{-5} bar^{-1}. Temperature coupling was maintained as in the NVT phase, and position restraints were applied to the protein and ligand to stabilize the structure during equilibration. Finally, the production molecular dynamics (MD) simulation was performed to collect data over 150 ns. The leap-frog integrator was used with a 2 fs time step across 75,000,000 steps. Temperature coupling was maintained at 300 K for both the protein–ligand and solvent groups, while pressure was controlled at 1.0 bar using the Parrinello–Rahman barostat. Electrostatics were modeled with PME using a 1.2 nm cutoff, and van der Waals interactions employed the same cutoff distance. Bond constraints, including those involving hydrogen atoms, were applied using the LINCS (Linear Constraint Solver) algorithm. Energies and coordinates were saved every 10 ps, ensuring detailed output for subsequent analyses. This multi-step workflow ensured a robust and reliable molecular dynamics simulation. The root mean square deviation (RMSD), radius of gyration (Rg), and root mean square fluctuations of trajectory files in the analysis were performed using in-built tools. Molecular Mechanics Generalized Born Surface Area (MMGBSA) was used to calculate the binding energy and residue-wise interaction analysis.

4.3. Animal Study

4.3.1. Animals

Thirty adult male albino rats, each weighing between 150 and 170 g and aged 11–12 weeks, were obtained from the animal facility at the College of Pharmacy, Qassim University, KSA. The rats were divided into four groups of six and housed in cages with three rats per cage. They were kept on a 12 h light/dark cycle and had unrestricted access to food and water. A one-week acclimatization period was provided prior to the initiation of drug treatments to ensure adjustment to the laboratory setting. Ethical approval for animal use in this research was secured from the Committee of Health Research Ethics, Deanship of Scientific Research, Qassim University, under research ID 23-24-18 and grant number 2023-SDG-1-HMSRC-35893.

4.3.2. Treatment and Experimental Schedule

CLOZ and lipopolysaccharide (LPS) from *Escherichia coli* (O111:B4) were sourced from Sigma-Aldrich Co. (St. Louis, MO, USA) and dissolved in a 0.09% *w*/*v* normal saline (NS) solution. To investigate CLOZ's protective effects against LPS-induced neurotoxicity, the rats were divided into four experimental groups. In the control group (CON; Group 1), animals received daily oral NS (0.1 mL/100 mg) from days 1 to 30 and were administered four intraperitoneal (i.p.) doses of NS (1 mg/kg) from days 27 to 30 to ensure standardized treatments. Group 2 (LPS) served as the LPS-only group, receiving NS orally each day and i.p. injections of LPS (1 mg/kg) on days 27 to 30 to induce neurotoxic effects. Groups 3 (CLOZ5 + LPS) and 4 (CLOZ10 + LPS) received daily oral doses of CLOZ at 5 mg/kg and 10 mg/kg, respectively, from day 1 to day 30, paired with LPS injections on the same days as Group 2. The dosing regimens for CLOZ and LPS were taken up from the previous studies [24,60,61]. The brain tissue samples were collected for ELISA analyses on the 30th day.

4.3.3. Preparation of Brain Homogenate

On day 30 of the treatment, all rats were euthanized with a combination of ketamine (100 mg/kg) and xylazine (10 mg/kg) and administered i.p. for anesthesia, followed by cervical decapitation. Brain tissues were immediately removed, cut into small sections, and rinsed thoroughly with ice-cold phosphate-buffered saline (PBS, pH 7.4) to clear any blood residues. The tissues were then weighed and homogenized in PBS on ice, maintaining a 1:9 tissue-to-PBS ratio (1 g of tissue in 9 mL PBS), using a glass homogenizer. The resulting homogenates were collected for subsequent ELISA analysis to assess specific biomarkers. Total protein concentrations in each brain homogenate were measured by the biuret colorimetric assay, following the protocol provided by Crescent Diagnostics (Jeddah, Saudi Arabia).

4.3.4. Biochemical Assays

The biochemical assays in this study were conducted using specific rat enzyme-linked immunosorbent assay (ELISA) kits obtained from MyBioSource Inc. (San Diego, CA, USA). The analyzed parameters included AChE (MBS2709297); neuroinflammatory markers such as COX-2 (MBS266603), 5-LOX (MBS2602074), NF-κB (MBS453975), TNF-α (MBS162068), IL-6 (MBS2701082), IL-10 (MBS702776), and TGF-β1 (MBS824788); apoptotic protein like Caspase-3 (MBS763727); and oxidative stress marker MDA (MBS268427). The ELISA protocols employed were based on either competitive or sandwich immunoassay principles. For each assay, specific antibodies, conjugates (such as horseradish peroxidase [HRP]), and detection systems were used to quantify the respective biomolecules. Rat brain homogenates or other relevant biological samples were prepared according to the manufacturer's instructions and stored appropriately until analysis. Standards provided with the kits were used to construct calibration curves. All reagents, including biotinylated detection antibodies and streptavidin-HRP (SABC), were prepared as per the kit instructions. Wells of the ELISA plates were allocated for samples, standards, and blanks. A fixed volume (typically 100 μL) of homogenate or standard was added to the respective wells. The plates were incubated at room temperature for a specific period, allowing for antigen–antibody binding. Post-incubation, wells were washed thoroughly with the provided washing buffer to remove unbound components. A substrate solution was added to initiate a colorimetric reaction. The reaction was stopped after the recommended time, and the developed color intensity was measured at 450 nm using a BioTek microplate reader (BioTek Instruments, Santa Clara, CA, USA). Concentrations of the analytes were determined by comparing the absorbance values to standard curves generated from known concentrations of the respective biomolecules.

4.3.5. Statistical Analysis

Results of the ELISA analysis are reported as mean values with standard error mean (SEM). Statistical evaluations were carried out using one-way ANOVA, followed by the Tukey–Kramer post hoc test to detect significant differences among the groups. All statistical analyses were performed using GraphPad version 9.0 (GraphPad Software Inc., San Diego, CA, USA), with significance defined at $p < 0.05$.

5. Conclusions

In summary, molecular docking and molecular dynamics revealed the potential of CLOZ as a multifunctional therapeutic agent. MDS studies highlighted the strong binding affinity of CLOZ with COX-2, 5-LOX, AChE, and BuChE and considerable binding affinity for 15-LOX, suggesting its potential to modulate key pathways associated with neuroinflammation and neurodegeneration. In addition to that, CLOZ also demonstrated

binding affinity with Caspase-3 in MDS. The biochemical analysis of brain samples from LPS- and CLOZ-treated rats demonstrated that CLOZ may exert neuroprotective effects in an LPS-induced neurotoxicity model. These effects include suppression of inflammatory response, improvement in the cholinergic system, and protection against apoptotic as well as oxidative stress pathways. The observed reductions in COX-2, 5-LOX, AChE, NF-κB, TNF-α, IL-6, Caspase-3, and MDA, as well as the improvement in the levels of IL-10 and TGF-β1, underscore its potential as a neuroprotective agent with anti-inflammatory, anti-apoptotic, and antioxidant properties. These findings provide a compelling basis for further exploration of CLOZ as a candidate for treating neurodegenerative diseases, particularly AD, where its ability to target multiple pathological mechanisms could offer substantial therapeutic benefits. However, the study has certain limitations, which include the absence of in vitro evaluations to validate its activity against the target enzymes. Addressing this gap would strengthen the case for advancing CLOZ with an aim toward clinical investigations.

Author Contributions: Conceptualization, M.A. and V.M.; methodology, M.A., D.K.D., and V.M.; software, M.A. and D.K.D.; validation, M.A., D.K.D., and V.M.; formal analysis, M.A. and V.M.; investigation, M.A., D.K.D., and V.M.; resources, M.A. and V.M.; data curation, M.A., D.K.D., and V.M.; writing—original draft preparation, M.A., D.K.D., and V.M.; writing—review and editing, M.A., and V.M.; visualization, M.A. and V.M.; supervision, M.A. and V.M.; project administration, M.A. and V.M.; funding acquisition, M.A. and V.M. All authors have read and agreed to the published version of the manuscript.

Funding: This research was funded by the Deanship of Scientific Research, Qassim University, Saudi Arabia, under project number (2023-SDG-1-HMSRC-35893) during the academic year 1445 AH/2023 AD.

Institutional Review Board Statement: The animal study protocol was approved by the Committee of Research Ethics, Deanship of Scientific Research, Qassim University, under research proposal number 23-24-18 dated 9 February 2023. Further, the study proposal was revised by the Deanship of Scientific Research under project number 2023-SDG-1-HMSRC-35893 and approved for funding dated 26 November 2023.

Informed Consent Statement: Not applicable.

Data Availability Statement: The data presented in this study are available from the corresponding author upon reasonable request. The data are not publicly available due to privacy issues.

Acknowledgments: The authors gratefully acknowledge Qassim University, represented by the Deanship of Scientific Research, on the financial support for this research under the number (2023-SDG-1-HMSRC-35893) during the academic year 1445 AH/2023 AD.

Conflicts of Interest: The authors declare no conflicts of interest.

References

1. Alzheimer's Disease International. World Alzheimer Report 2024: Global Perspectives on Attitudes Toward Dementia. 2024. Available online: https://www.alzint.org/resource/world-alzheimer-report-2024/ (accessed on 4 January 2025).
2. 2024 Alzheimer's Disease Facts and Figures. *Alzheimer's Dement.* **2024**, *20*, 3708–3821. [CrossRef] [PubMed]
3. Chu, J.; Praticò, D. Involvement of 5-Lipoxygenase Activating Protein in the Amyloidotic Phenotype of an Alzheimer's Disease Mouse Model. *J. Neuroinflamm.* **2012**, *9*, 127. [CrossRef] [PubMed]
4. Joshi, Y.B.; Praticò, D. The 5-Lipoxygenase Pathway: Oxidative and Inflammatory Contributions to the Alzheimer 's Disease Phenotype. *Front. Cell. Neurosci.* **2015**, *8*, 436. [CrossRef] [PubMed]
5. Cavalli, A.; Bolognesi, M.L.; Minarini, A.; Rosini, M.; Tumiatti, V.; Recanatini, M.; Melchiorre, C. Multi-Target-Directed Ligands To Combat Neurodegenerative Diseases. *J. Med. Chem.* **2008**, *51*, 347–372. [CrossRef] [PubMed]

6. Alfadly, E.D.; Elzahhar, P.A.; Tramarin, A.; Elkazaz, S.; Shaltout, H.; Abu-serie, M.M.; Janockova, J.; Soukup, O.; Ghareeb, D.A.; El-yazbi, A.F.; et al. Tackling Neuroin Fl Ammation and Cholinergic de Fi Cit in Alzheimer' s Disease: Multi-Target Inhibitors of Cholinesterases, Cyclooxygenase-2 and 15-Lipoxygenase. *Eur. J. Med. Chem.* **2019**, *167*, 161–186. [CrossRef] [PubMed]
7. Javed, M.A.; Ashraf, N.; Saeed Jan, M.; Mahnashi, M.H.; Alqahtani, Y.S.; Alyami, B.A.; Alqarni, A.O.; Asiri, Y.I.; Ikram, M.; Sadiq, A.; et al. Structural Modification, In Vitro, In Vivo, Ex Vivo, and In Silico Exploration of Pyrimidine and Pyrrolidine Cores for Targeting Enzymes Associated with Neuroinflammation and Cholinergic Deficit in Alzheimer's Disease. *ACS Chem. Neurosci.* **2021**, *12*, 4123–4143. [CrossRef] [PubMed]
8. Shahid Nadeem, M.; Azam Khan, J.; Kazmi, I.; Rashid, U. Design, Synthesis, and Bioevaluation of Indole Core Containing 2-Arylidine Derivatives of Thiazolopyrimidine as Multitarget Inhibitors of Cholinesterases and Monoamine Oxidase A/B for the Treatment of Alzheimer Disease. *ACS Omega* **2022**, *7*, 9369–9379. [CrossRef]
9. Sánchez-Martínez, J.D.; Bueno, M.; Alvarez-Rivera, G.; Tudela, J.; Ibañez, E.; Cifuentes, A. In Vitro Neuroprotective Potential of Terpenes from Industrial Orange Juice By-Products. *Food Funct.* **2021**, *12*, 302–314. [CrossRef]
10. Razavi, S.M.; Khayatan, D.; Arab, Z.N.; Momtaz, S.; Zare, K.; Jafari, R.M.; Dehpour, A.R.; Abdolghaffari, A.H. Licofelone, a Potent COX/5-LOX Inhibitor and a Novel Option for Treatment of Neurological Disorders. *Prostaglandins Other Lipid Mediat.* **2021**, *157*, 106587. [CrossRef]
11. Alqahtani, Y.S. Bioactive Stigmastadienone from Isodon Rugosus as Potential Anticholinesterase, α -Glucosidase and COX/LOX Inhibitor: In-Vitro and Molecular Docking Studies. *Steroids* **2021**, *172*, 108857. [CrossRef]
12. Fang, L.; Shen, S.; Liu, Q.; Liu, Z.; Zhao, J. Combination of NSAIDs with Donepezil as Multi-Target Directed Ligands for the Treatment of Alzheimer's Disease. *Bioorg. Med. Chem. Lett.* **2022**, *75*, 128976. [CrossRef] [PubMed]
13. Javed, M.A.; Bibi, S.; Jan, M.S.; Ikram, M.; Zaidi, A.; Farooq, U.; Sadiq, A.; Rashid, U. Diclofenac Derivatives as Concomitant Inhibitors of Cholinesterase, Monoamine Oxidase, Cyclooxygenase-2 and 5-Lipoxygenase for the Treatment of Alzheimer's Disease: Synthesis, Pharmacology, Toxicity and Docking Studies. *RSC Adv.* **2022**, *12*, 22503–22517. [CrossRef]
14. Kalra, J.; Kumar, P.; Majeed, A.B.A.; Prakash, A. Modulation of LOX and COX Pathways via Inhibition of Amyloidogenesis Contributes to Mitoprotection against β-Amyloid Oligomer-Induced Toxicity in an Animal Model of Alzheimer's Disease in Rats. *Pharmacol. Biochem. Behav.* **2016**, *146–147*, 1–12. [CrossRef] [PubMed]
15. Dias, K.S.T.; de Paula, C.T.; dos Santos, T.; Souza, I.N.O.; Boni, M.S.; Guimarães, M.J.R.; da Silva, F.M.R.; Castro, N.G.; Neves, G.A.; Veloso, C.C.; et al. Design, Synthesis and Evaluation of Novel Feruloyl-Donepezil Hybrids as Potential Multitarget Drugs for the Treatment of Alzheimer's Disease. *Eur. J. Med. Chem.* **2017**, *130*, 440–457. [CrossRef]
16. Zhang, P.; Xu, S.; Zhu, Z.; Xu, J. Multi-Target Design Strategies for the Improved Treatment of Alzheimer's Disease. *Eur. J. Med. Chem.* **2019**, *176*, 228–247. [CrossRef] [PubMed]
17. Cornec, A.S.; Monti, L.; Kovalevich, J.; Makani, V.; James, M.J.; Vijayendran, K.G.; Oukoloff, K.; Yao, Y.; Lee, V.M.-Y.; Trojanowski, J.Q.; et al. Multitargeted Imidazoles: Potential Therapeutic Leads for Alzheimer's and Other Neurodegenerative Diseases. *J. Med. Chem.* **2017**, *60*, 5120–5145. [CrossRef] [PubMed]
18. Paquot, A.; Deprez, B.; Beghyn, T. Drug repurposing and phenotypic screening: Innovative strategies for treating ultra-rare disorders. *Front. Med.* **2024**, *11*, 1489094. [CrossRef] [PubMed]
19. Casertano, M.; Genovese, M.; Paoli, P.; Santi, A.; Aiello, A.; Menna, M.; Imperatore, C. Insights into Cytotoxic Behavior of Lepadins and Structure Elucidation of the New Alkaloid Lepadin L from the Mediterranean Ascidian *Clavelina lepadiformis*. *Mar. Drugs* **2022**, *20*, 65. [CrossRef]
20. Zhou, J.; Jiang, X.; He, S.; Jiang, H.; Feng, F.; Liu, W.; Qu, W.; Sun, H. Rational Design of Multitarget-Directed Ligands: Strategies and Emerging Paradigms. *J. Med. Chem.* **2019**, *62*, 8881–8914. [CrossRef] [PubMed]
21. Medina-Franco, J.L.; Giulianotti, M.A.; Welmaker, G.S.; Houghten, R.A. Shifting from the Single to the Multitarget Paradigm in Drug Discovery. *Drug Discov. Today* **2013**, *18*, 495–501. [CrossRef] [PubMed]
22. Morris, G.M.; Lim-Wilby, M. Molecular Docking. In *Molecular Modeling of Proteins*; Kukol, A., Ed.; Humana Press: Totowa, NJ, USA, 2008; pp. 365–382, ISBN 978-1-59745-177-2.
23. Li, J.; Fu, A.; Zhang, L. An Overview of Scoring Functions Used for Protein–Ligand Interactions in Molecular Docking. *Interdiscip. Sci. Comput. Life Sci.* **2019**, *11*, 320–328. [CrossRef]
24. Mani, V.; Arfeen, M.; Dhaked, D.K.; Mohammed, H.A.; Amirthalingam, P.; Elsisi, H.A. Neuroprotective Effect of Methanolic Ajwa Seed Extract on Lipopolysaccharide-Induced Memory Dysfunction and Neuroinflammation: In Vivo, Molecular Docking and Dynamics Studies. *Plants* **2023**, *12*, 934. [CrossRef]
25. Mani, V.; Arfeen, M.; Rabbani, S.I.; Shariq, A.; Amirthalingam, P. Levetiracetam Ameliorates Doxorubicin-Induced Chemobrain by Enhancing Cholinergic Transmission and Reducing Neuroinflammation Using an Experimental Rat Model and Molecular Docking Study. *Molecules* **2022**, *27*, 7364. [CrossRef] [PubMed]
26. Arfeen, M.; Srivastava, A.; Srivastava, N.; Khan, R.A.; Almahmoud, S.A.; Mohammed, H.A. Design, Classification, and Adverse Effects of NSAIDs: A Review on Recent Advancements. *Bioorg. Med. Chem.* **2024**, *112*, 117899. [CrossRef] [PubMed]

27. He, Z.; Tao, D.; Xiong, J.; Lou, F.; Zhang, J.; Chen, J.; Dai, W.; Sun, J.; Wang, Y. Phosphorylation of 5-LOX: The Potential Set-Point of Inflammation. *Neurochem. Res.* **2020**, *45*, 2245–2257. [CrossRef]
28. Liu, Y.; Wang, K.; Cao, F.; Gao, N.; Li, W. Interactions between Inhibitors and 5-Lipoxygenase: Insights from Gaussian Accelerated Molecular Dynamics and Markov State Models. *Int. J. Mol. Sci.* **2024**, *25*, 8295. [CrossRef] [PubMed]
29. Kothayer, H.; Rezq, S.; Abdelkhalek, A.S.; Romero, D.G.; Elbaramawi, S.S. Triple Targeting of Mutant EGFRL858R/T790M, COX-2, and 15-LOX: Design and Synthesis of Novel Quinazolinone Tethered Phenyl Urea Derivatives for Anti-Inflammatory and Anticancer Evaluation. *J. Enzyme Inhib. Med. Chem.* **2023**, *38*, 2199166. [CrossRef]
30. Alzarea, S.I.; Elmaidomy, A.H.; Saber, H.; Musa, A.; Al-Sanea, M.M.; Mostafa, E.M.; Hendawy, O.M.; Youssif, K.A.; Alanazi, A.S.; Alharbi, M.; et al. Potential Anticancer Lipoxygenase Inhibitors from the Red Sea-Derived Brown Algae Sargassum Cinereum: An In-Silico-Supported In-Vitro Study. *Antibiotics* **2021**, *10*, 416. [CrossRef] [PubMed]
31. Lee, D.; Long, S.A.; Murray, J.H.; Adams, J.L.; Nuttall, M.E.; Nadeau, D.P.; Kikly, K.; Winkler, J.D.; Sung, C.M.; Ryan, M.D.; et al. Potent and Selective Nonpeptide Inhibitors of Caspases 3 and 7. *J. Med. Chem.* **2001**, *44*, 2015–2026. [CrossRef] [PubMed]
32. Shah, M.; Parmar, R.; Patel, K.; Nagani, A. Indole-Based COX-2 Inhibitors: A Decade of Advances in Inflammation, Cancer, and Alzheimer's Therapy. *Bioorg. Chem.* **2024**, *153*, 107931. [CrossRef] [PubMed]
33. Moussa, N.; Dayoub, N. Exploring the Role of COX-2 in Alzheimer's Disease: Potential Therapeutic Implications of COX-2 Inhibitors. *Saudi Pharm. J.* **2023**, *31*, 101729. [CrossRef]
34. Hussain, F.; Tahir, A.; Jan, M.S.; Fatima, N.; Sadiq, A.; Rashid, U. Exploitation of the Multitarget Role of New Ferulic and Gallic Acid Derivatives in Oxidative Stress-Related Alzheimer's Disease Therapies: Design, Synthesis and Bioevaluation. *RSC Adv.* **2024**, *14*, 10304–10321. [CrossRef] [PubMed]
35. Di Francesco, A.; Arosio, B.; Gussago, C.; Dainese, E.; Mari, D.; D'Addario, C.; Maccarrone, M. Involvement of 5-Lipoxygenase in Alzheimer's Disease: A Role for DNA Methylation. *J. Alzheimer's Dis.* **2013**, *37*, 3–8. [CrossRef] [PubMed]
36. Jacob, P.J.; Manju, S.L.; Ethiraj, K.R.; Elias, G. Safer Anti-Inflammatory Therapy through Dual COX-2/5-LOX Inhibitors: A Structure-Based Approach. *Eur. J. Pharm. Sci.* **2018**, *121*, 356–381. [CrossRef]
37. Irrera, N.; Bitto, A. Evidence for Using a Dual COX 1/2 and 5-LOX Inhibitor in Neurodegenerative Diseases. *Neural Regen. Res.* **2017**, *12*, 1077–1078. [CrossRef] [PubMed]
38. Jatana, M.; Giri, S.; Ansari, M.A.; Elango, C.; Singh, A.K.; Singh, I.; Khan, M. Inhibition of NF-KB Activation by 5-Lipoxygenase Inhibitors Protects Brain against Injury in a Rat Model of Focal Cerebral Ischemia. *J. Neuroinflamm.* **2006**, *3*, 12. [CrossRef] [PubMed]
39. Liu, X.; Wang, K.; Wei, X.; Xie, T.; Lv, B.; Zhou, Q.; Wang, X. Interaction of NF-KB and Wnt/β-Catenin Signaling Pathways in Alzheimer's Disease and Potential Active Drug Treatments. *Neurochem. Res.* **2021**, *46*, 711–731. [CrossRef]
40. Zelová, H.; Hošek, J. TNF-α Signalling and Inflammation: Interactions between Old Acquaintances. *Inflamm. Res.* **2013**, *62*, 641–651. [CrossRef] [PubMed]
41. Roy, M.; Singh, R. TRIMs: Selective Recruitment at Different Steps of the NF-KB Pathway—Determinant of Activation or Resolution of Inflammation. *Cell. Mol. Life Sci.* **2021**, *78*, 6069–6086. [CrossRef]
42. Khan, H.; Gupta, A.; Singh, T.G.; Kaur, A. Mechanistic Insight on the Role of Leukotriene Receptors in Ischemic–Reperfusion Injury. *Pharmacol. Rep.* **2021**, *73*, 1240–1254. [CrossRef] [PubMed]
43. Wautier, J.L.; Wautier, M.P. Pro- and Anti-Inflammatory Prostaglandins and Cytokines in Humans: A Mini Review. *Int. J. Mol. Sci.* **2023**, *24*, 9647. [CrossRef] [PubMed]
44. Novoa, C.; Salazar, P.; Cisternas, P.; Gherardelli, C.; Vera-Salazar, R.; Zolezzi, J.M.; Inestrosa, N.C. Inflammation Context in Alzheimer's Disease, a Relationship Intricate to Define. *Biol. Res.* **2022**, *55*, 39. [CrossRef] [PubMed]
45. Brasier, A.R. The Nuclear Factor-KB–Interleukin-6 Signalling Pathway Mediating Vascular Inflammation. *Cardiovasc. Res.* **2010**, *86*, 211–218. [CrossRef] [PubMed]
46. Rothaug, M.; Becker-Pauly, C.; Rose-John, S. The Role of Interleukin-6 Signaling in Nervous Tissue. *Biochim. Biophys. Acta Mol. Cell Res.* **2016**, *1863*, 1218–1227. [CrossRef] [PubMed]
47. Rola-Pleszczynski, M.; Stankova, J. Leukotriene B4 Enhances Interleukin-6 (IL-6) Production and IL-6 Messenger RNA Accumulation in Human Monocytes In Vitro: Transcriptional and Posttranscriptional Mechanisms. *Blood* **1992**, *80*, 1004–1011. [CrossRef] [PubMed]
48. Lobo-Silva, D.; Carriche, G.M.; Castro, A.G.; Roque, S.; Saraiva, M. Balancing the Immune Response in the Brain: IL-10 and Its Regulation. *J. Neuroinflamm.* **2016**, *13*, 297. [CrossRef] [PubMed]
49. Rustenhoven, J.; Aalderink, M.; Scotter, E.L.; Oldfield, R.L.; Bergin, P.S.; Mee, E.W.; Graham, E.S.; Faull, R.L.M.; Curtis, M.A.; Park, T.I.-H.; et al. TGF-Beta1 Regulates Human Brain Pericyte Inflammatory Processes Involved in Neurovasculature Function. *J. Neuroinflamm.* **2016**, *13*, 37. [CrossRef] [PubMed]
50. D'Amelio, M.; Sheng, M.; Cecconi, F. Caspase-3 in the Central Nervous System: Beyond Apoptosis. *Trends Neurosci.* **2012**, *35*, 700–709. [CrossRef] [PubMed]

51. Zhang, H.; Li, N.; Li, Z.; Li, Y.; Yu, Y.; Zhang, L. The Involvement of Caspases in Neuroinflammation and Neuronal Apoptosis in Chronic Pain and Potential Therapeutic Targets. *Front. Pharmacol.* **2022**, *13*, 898574. [CrossRef]
52. Anuradha, C.D.; Kanno, S.; Hirano, S. Oxidative Damage to Mitochondria Is a Preliminary Step to Caspase-3 Activation in Fluoride-Induced Apoptosis in HL-60 Cells. *Free Radic. Biol. Med.* **2001**, *31*, 367–373. [CrossRef]
53. Yang, K.T.; Pan, S.F.; Chien, C.L.; Hsu, S.-M.; Tseng, Y.Z.; Wang, S.M.; Wu, M.L. Mitochondrial Na^+ Overload Is Caused by Oxidative Stress and Leads to Activation of the Caspase 3-Dependent Apoptotic Machinery. *FASEB J.* **2004**, *18*, 1442–1444. [CrossRef] [PubMed]
54. Benfante, R.; Di Lascio, S.; Cardani, S.; Fornasari, D. Acetylcholinesterase Inhibitors Targeting the Cholinergic Anti-Inflammatory Pathway: A New Therapeutic Perspective in Aging-Related Disorders. *Aging Clin. Exp. Res.* **2021**, *33*, 823–834. [CrossRef] [PubMed]
55. Radi, E.; Formichi, P.; Battisti, C.; Federico, A. Apoptosis and Oxidative Stress in Neurodegenerative Diseases. *J. Alzheimer's Dis.* **2014**, *42*, S125–S152. [CrossRef] [PubMed]
56. Teleanu, D.M.; Niculescu, A.-G.; Lungu, I.I.; Radu, C.I.; Vladâcenco, O.; Roza, E.; Costăchescu, B.; Grumezescu, A.M.; Teleanu, R.I. An Overview of Oxidative Stress, Neuroinflammation, and Neurodegenerative Diseases. *Int. J. Mol. Sci.* **2022**, *23*, 5938. [CrossRef] [PubMed]
57. Olufunmilayo, E.O.; Gerke-Duncan, M.B.; Holsinger, R.M.D. Oxidative Stress and Antioxidants in Neurodegenerative Disorders. *Antioxidants* **2023**, *12*, 517. [CrossRef]
58. Trott, O.; Olson, A.J. AutoDock Vina: Improving the Speed and Accuracy of Docking with a New Scoring Function, Efficient Optimization, and Multithreading. *J. Comput. Chem.* **2010**, *31*, 455–461. [CrossRef] [PubMed]
59. Morris, G.M.; Huey, R.; Lindstrom, W.; Sanner, M.F.; Belew, R.K.; Goodsell, D.S.; Olson, A.J. AutoDock4 and AutoDockTools4: Automated Docking with Selective Receptor Flexibility. *J. Comput. Chem.* **2009**, *30*, 2785–2791. [CrossRef] [PubMed]
60. Ertuğrul, A.; Özdemir, H.; Vural, A.; Dalkara, T.; Meltzer, H.Y.; Saka, E. The Influence of N-Desmethylclozapine and Clozapine on Recognition Memory and BDNF Expression in Hippocampus. *Brain Res. Bull.* **2011**, *84*, 144–150. [CrossRef]
61. Andrabi, S.S.; Vishnoi, S.; Madan, R.; Bhardwaj, N.; Tabassum, H.; Akram, M.; Parvez, S. Clozapine Improves Behavioral and Biochemical Outcomes in a MK-801-Induced Mouse Model of Schizophrenia. *J. Environ. Pathol. Toxicol. Oncol.* **2020**, *39*, 1–12. [CrossRef]

molecules

MDPI

Article

Utilization of Tea Polyphenols as Color Developers in Reversible Thermochromic Dyes for Thermosensitive Color Change and Enhanced Functionality of Polyester Fabrics

Weimian Zhou [1], Qun Yang [1,2,3,*], Sixuan Tao [1], Jin Cui [4], Jie Zhu [1], Siyu Zhou [1], Ruimiao Li [1], Juan Su [1], Ning Zhang [1], Lihui Xu [1], Hong Pan [1] and Jiping Wang [1,3]

[1] School of Textiles and Fashion, Shanghai University of Engineering Science, Shanghai 201620, China; zhouweimian2022@163.com (W.Z.)
[2] Key Laboratory of Textile Fiber and Products (Wuhan Textile University), Ministry of Education, Wuhan 430200, China
[3] Shanghai Engineering Research Center for Clean Production of Textile Chemistry, Shanghai 201620, China
[4] Shanghai Evershine Co., Ltd., Shanghai 201600, China
* Correspondence: yangqun@sues.edu.cn

Abstract: Thermochromic textiles possess the capability to indicate ambient temperature through color changes, enabling real-time temperature monitoring and providing temperature warnings for body heat management. In this study, three thermochromic dyes—blue, red, and yellow—were synthesized using crystalline violet lactone (CVL), 6′-(diethylamino)-1′,3′-dimethyl-fluoran (DDF), and 3′,6′-dimethoxyfluoran (DOF) as leuco dyes, respectively, with biomass tea polyphenol serving as the color developer and tetradecanol as the phase change material. The chemical structures of these dyes were characterized using UV spectroscopy, infrared spectroscopy, Raman spectroscopy and ^{1}H NMR. The thermochromic mechanisms were investigated, revealing that the binding bonds between the leuco dyes and the color developer broke and reorganized with temperature changes, imparting reversible thermochromic property. Polyester fabrics were dyed using an impregnation method to produce three reversible thermochromic fabrics in blue, red, and yellow. The structure and properties of these fabrics were analyzed, showing a significant increase in the UPF value from 26.3 to approximately 100, indicating enhanced UV resistance. Water contact angle measurements revealed that the contact angle of undyed polyester fabrics was 139°, while that of dyed polyester fabrics decreased by about 40°, indicating improved hydrophilicity. Additionally, the fabric inductive static tester showed that the static voltage half-life of dyed polyester fabric was less than 1 s, demonstrating a significant antistatic effect. Infrared thermal imaging results indicated that during the warming and cooling process, the thermochromic polyester fabric exhibited specific energy storage and insulation effects at 38 °C, close to the human body temperature. This study presented a novel approach to developing smart color-changing textiles using biomass-derived thermochromic dyes, offering diverse materials for personal thermal management, and intelligent insulation applications.

Keywords: reversible thermochromic dyes; tea polyphenols; polyester; phase change energy storage; smart textile

1. Introduction

Color is a visual effect of light perceived through the eye, brain, and life experiences. Innovative color-changing materials have garnered significant attention due to their environmental adaptability, altering color in response to ambient temperature, humidity, pH, and other factors. The reversible color change or discoloration based on temperature variation is known as thermochromism. Thermochromic materials have been widely utilized in military applications, intelligent windows, architectural coatings, and textiles [1–4]. In extreme weather conditions, the thermal homeostasis of the human body can be disrupted.

Thermochromic garments can function as temperature sensors, transmitting thermal signals to the wearer and monitoring body temperature in real-time [5,6]. Tarek M. Abou Elmaaty et al. [7] have printed thermochromic pigments (blue and red) on specially designed cotton children's garments using flat screen-printing techniques. The garments exhibited noticeable color changes in response to body temperature, maintaining fastness to light, washing, and rubbing. Liu et al. [8] utilized biomass-based three-component thermochromic dyes for dyeing linen fabrics by vacuum impregnation. The dyed fabrics demonstrated changes in color, surface wettability, strength, and thermal insulation with the temperature change. Contrastingly, Yu et al. [9] developed conductive fibers with thermochromic effects through a combination of Joule heating and solar absorption modulation. These fibers, capable of electro-thermal conversion, can monitor the thermal environment of the human body. Silk, known for its excellent mechanical properties and breathability compared to synthetic polymer fibers, was used by Wang et al. [10] to create high-performance thermochromic silk fabrics. These fabrics, produced through a cost-effective, sustainable, and efficient finishing process, exhibited excellent thermochromic response properties.

Three-component thermochromic materials typically consist of a leuco dye, a color developer (electron donor), and a phase change solvent carrier. During dye synthesis, the lactone ring of leuco dye broke as the temperature increased, resulting in electron loss and complexation with the color developer to form a colored complex. At the same time, organic solvents served as equilibrium media for these three-component thermochromic materials. Among color developer systems, bisphenol A (BPA) has been widely used due to its structural advantages, ability to enhance the conversion rate of thermochromic dyes, and low cost [11,12]. However, BPA's chemical structure is similar to estrogen, allowing it to bind to estrogen receptors (ER) and disrupt natural endocrine functions, leading to biotoxic effects such as breast cancer, endometriosis, and infertility [13,14]. Consequently, the production and use of BPA have been severely restricted to minimize adverse health effects. Several new BPA analogues have been developed and widely adopted as replacements. Tea polyphenols, as a biomass material with multiple phenolic hydroxyl groups, can be compounded with leuco dyes to achieve thermochromic effects, making them a promising alternative to BPA. Additionally, phase change materials (PCMs) can store and release latent heat during the phase transitions and were widely used in thermal management and storage [15]. Solid/liquid PCMs offered significant advantages, including high latent heat storage capacity and minimal volume change during phase transitions [16]. For example, tetradecanol (TD) is an essential organic solid/liquid PCM with a large storage capacity and a phase change temperature close to human body temperature (approximately 38 °C). Therefore, it has been extensively used in residential air conditioning, solar heating, waste heat recovery, and building energy efficiency [17–20].

Polyester fabrics exhibit excellent wrinkle resistance and shape retention properties. Additionally, polyester fibers possess high strength and elastic recovery, contributing to the fabric's robustness and durability. However, they also present challenges, such as poor moisture absorption and susceptibility to static electricity. To address these issues, researchers have implemented several modifications. Zhang et al. [21] enhanced the hydrophilic and hygroscopic properties of polyester fabrics by combining pozzolanic materials with polydopamine-modified polyester. Furthermore, Fan et al. [22] utilized a novel graphene oxide-doped disperse dye for one-bath dyeing of polyester fabrics, imparting antistatic properties. The reduction of graphene oxide at 2% for 30 min achieved a class A antistatic standard, thereby improving the performance and suitability of polyester fabrics.

In this study, three thermochromic dyes—blue, red, and yellow—were synthesized using crystalline violet lactone (CVL), 6′-(diethylamino)-1′,3′-dimethyl-fluoran (DDF), and 3′,6′-dimethoxyfluoran (DOF) as leuco dyes, respectively. Biomass tea polyphenol served as the color rendering agent, while tetradecanol was utilized as the phase-change material. The chemical structures and thermochromic mechanisms of these dyes were thoroughly investigated. The synthesized thermochromic dyes were applied to polyester fabrics via the impregnation method. The thermal stability, hydrophilicity, hydrostatic half-life, and

other properties of these three thermochromic polyester fabrics were evaluated. This environmentally friendly approach to creating thermochromic fabrics using biomass-derived dyes presented a novel pathway for intelligent color-changing textiles, offering innovative thermal insulation and enhancing diversity in personal heat management materials.

2. Results and Discussion

2.1. Structure of Biomass Thermochromic Dyes and Thermochromic Mechanism

The reversible thermochromic dyes' behavior was primarily influenced by the melting point of the phase change solvent. To determine the color change temperatures of the synthesized blue, red, and yellow dyes, a series of heating experiments were conducted with real-time monitoring. The results indicated that the discoloration temperatures for the three dyes fell within the range of 39–42 °C, which aligned with the phase transition temperature of the solvent tetradecanol, as illustrated in Figure 1. A reversible thermochromic system consists of leuco dyes, a color-developer and a cosolvent [23]. The interaction among these components is pivotal, with tetradecanol playing a crucial role in modulating the thermochromic response of the dyes.

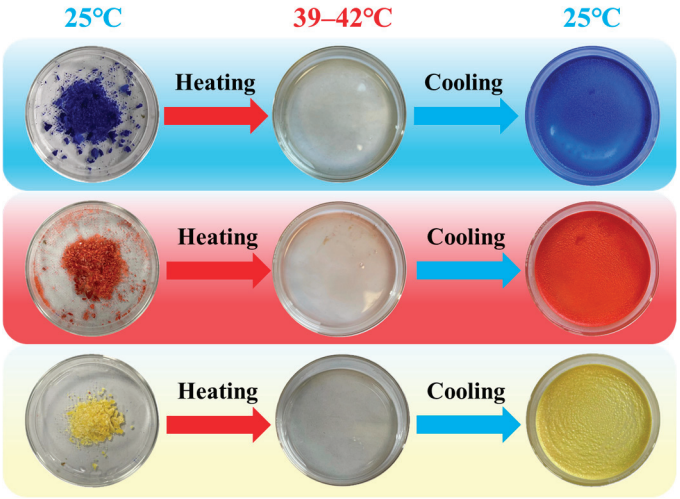

Figure 1. Temperature thresholds for color transitions in three reversible thermochromic dyes.

The UV absorption spectra of the three biomass thermochromic dyes at 25 °C and 50 °C were analyzed using in situ UV spectroscopy. As shown in Figure 2a–c, the dyes TC-CVL (Figure 2a), TC-DDF (Figure 2b) and TC-DOF (Figure 2c) exhibited distinct absorptions at 560–630 nm, 490–550 nm, and 425–470 nm, respectively, indicating the color of blue, red, and yellow at 25 °C. Upon increasing the temperature to 50 °C, the absorbance at these wavelengths decreases significantly. The absorbance at 560–630 nm, 500–550 nm, and 440–470 nm became comparable to other wavelengths, suggesting that the chromophore groups of TC-CVL, TC-DDF, and TC-DOF were disrupted upon heating, rendering the dyes colorless. This observation aligned with the macroscopic appearance of the dyes, which are blue, red, and yellow at lower temperatures but become colorless upon heating (Figure 2a–c, upper left corner of the curve).

The results shown in Figure 2d–f were in situ Raman spectroscopy at 25 °C and 50 °C, which indicated significant absorption near 2800 cm^{-1} at 25 °C, suggesting the presence of quinone and C=N structures. However, at 50 °C, the peak intensities near 2800 cm^{-1} decreased significantly, indicating temperature-induced changes in quinone and C=N structures. Additionally, changes in C=O vibration induced by alterations in the lactone ring structure at 1500 cm^{-1} were also observed in the Raman figure. The C–O–C vibration absorption peaks at 1060 cm^{-1} and 1120 cm^{-1} of the three dyes were close to the vibration absorption peaks in the infrared spectrum.

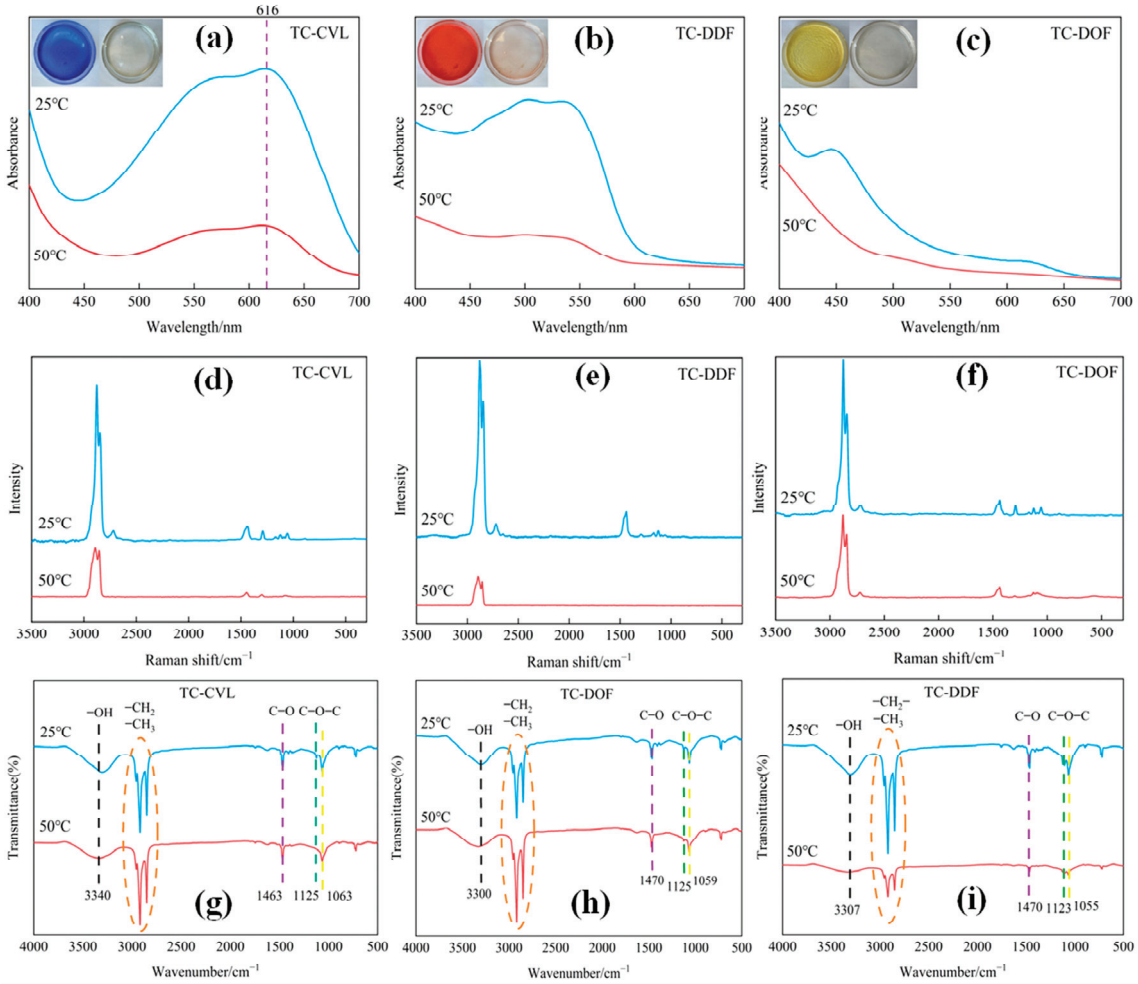

Figure 2. Structural analysis of three thermochromic dyes at 25 °C and 50 °C, respectively: (**a**–**c**) UV absorption spectra; (**d**–**f**) Raman spectra; (**g**–**i**) FTIR spectra.

Figure 2g–i shows in situ infrared spectroscopy of the three dyes at 25 °C and 50 °C. For instance, in Figure 2d for TC-CVL, the broad peak at 3340 cm^{-1} was primarily attributed to the –OH group of the phase change solvent tetradecanol. This peak also indicates the presence of intermolecular and intramolecular hydrogen bonds within the thermochromic dye system. At 25 °C, the lactone group of CVL formed intramolecular hydrogen bonds with the phenolic hydroxyl group of tea polyphenol, resulting in the formation of the TC-CVL colored complex. As the temperature increased from 25 °C to 50 °C, the intensity of the broad peak at 3340 cm^{-1} diminished, indicating a weakening of intermolecular and intramolecular hydrogen bonding in the thermochromic dyes. This change was due to the transformation of the tetradecanol from a solid to a liquid state. In liquid tetradecanol, CVL and tea polyphenols dissolved and existed as two colorless complexes. The C–O–C vibrational absorption peaks of CVL at 1125 cm^{-1} and 1063 cm^{-1}, along with the peaks at 1390 cm^{-1} and 1540 cm^{-1}, correspond to the C–O asymmetric stretching vibrations associated with the ring-opening carboxylate structure in CVL [24]. These observed peaks remained largely unaffected by variations in temperature.

To further verify the structure of thermochromic dyes and the changes in their molecular structure before and after heating, the three dyes—TC-CVL, TC-DDF, and TC-DOF were characterized using a solid-state NMR at 25 °C and 50 °C, respectively, as shown in Figure 3. TC-CVL in Figure 3a as an example, the absorption peaks of each hydrogen atom at 25 °C were δ15.12 ppm, δ13.23 ppm, δ12.57 ppm, δ7.09 ppm, δ6.72 ppm, δ3.87 ppm, δ2.01 ppm, and δ1.31 ppm. In contrast, at an elevated temperature of 50 °C, the absorption peaks were δ15.21 ppm, δ13.27 ppm, δ12.59 ppm, δ12.30 ppm, δ7.83 ppm, δ7.11

ppm, δ6.67 ppm, δ6.38 ppm, δ5.70 ppm, δ3.94 ppm, δ3.76 ppm, δ3.27 ppm, δ1.98 ppm, δ1.31 ppm, δ1.02 ppm, and δ0.62 ppm. Based on the structural analysis of CVL and tea polyphenols, the peak at δ12.3 ppm corresponded to the phenolic hydroxyl active hydrogen of tea polyphenols. This was attributed to the phase transition of tetradecanol from solid to liquid state at 50 °C, which weakened the interaction between CVL and tea polyphenols. Consequently, the conjugated colorimetric structure was dissociated, and the hydrogen bonds between CVL and tea polyphenols broke as the temperature increased. The phenolic hydroxyl active hydrogen of tea polyphenols was influenced by the CVL conjugated structure, leading to a decrease in the extra-nuclear electron cloud density, a weakened shielding effect, an increased effective magnetic field, and a higher chemical shift. The analysis of Figure 3b,c indicated that TC-DDF and TC-DOF exhibited similar changes. This indicated that the three thermochromic dyes—TC-CVL, TC-DDF, and TC-DOF exhibited reversible thermochromic behavior. This behavior was facilitated by the disruption and subsequent reformation of hydrogen bonds between the cryptochromic dyes and tea polyphenols [25].

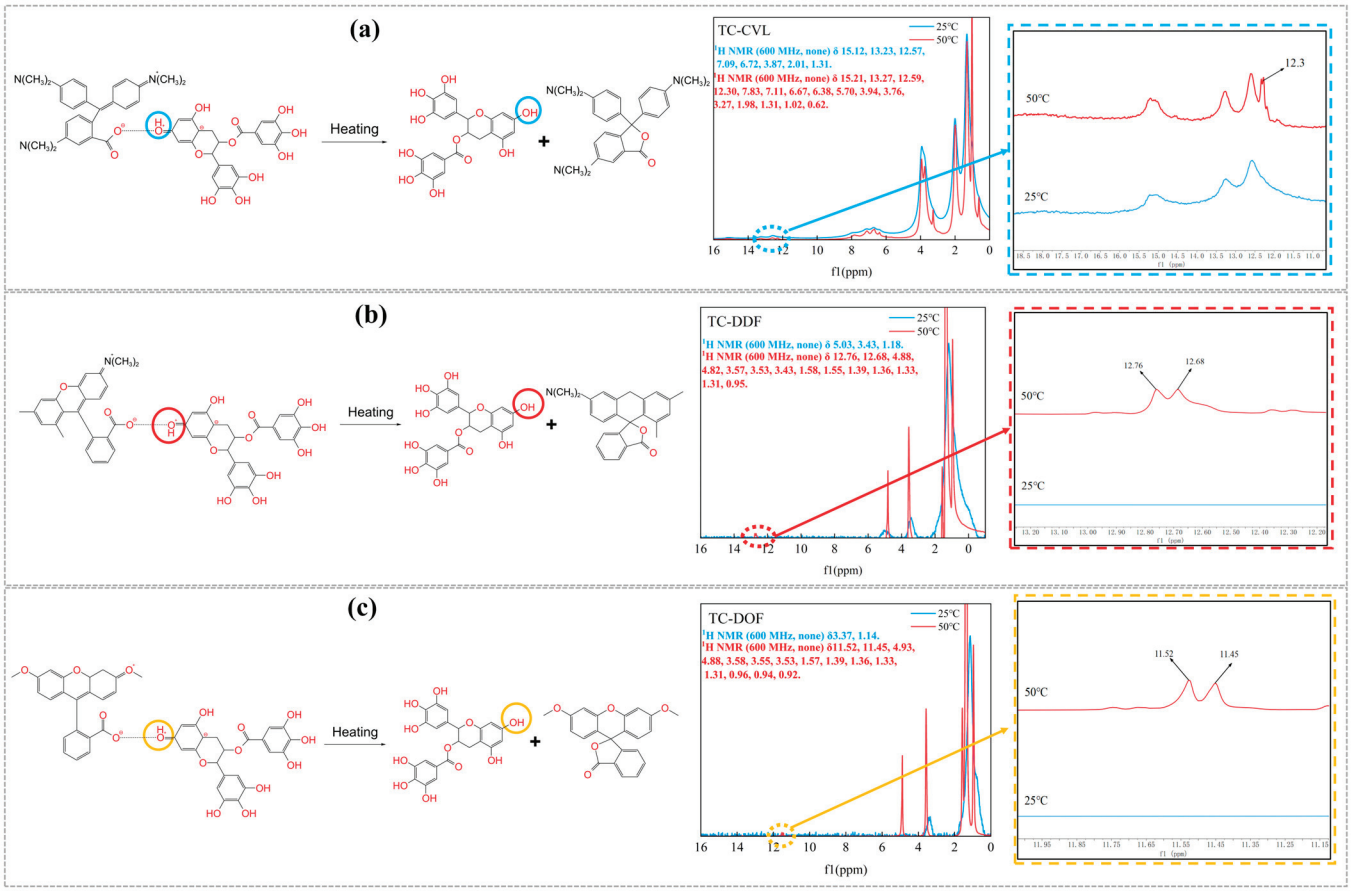

Figure 3. ^{1}H NMR spectra of three thermochromic dyes at 25 °C and 50 °C: (**a**) TC-CVL; (**b**) TC-DOF; (**c**) TC-DOF.

The mechanism of thermochromic change can be described as follows: At low temperatures, the binding force between the leuco dyes and the color developer was strong. With the temperature increased or decreased, the hydroxyl groups (–OH) in tetradecanol underwent reversible transformations with quinone, while the lactone ring transformed with an open-loop acid by gaining or losing H^{+} ions. These transformations involved hydrogen transfer isomerization. The conjugation degree of the system was adjusted through associations and dissociations facilitated by hydrogen bonds between the carbonyl oxygen, hydroxyl oxygen, and hydroxyl hydrogen in open-loop acid, as well as hydroxyl oxygen and hydroxyl hydrogen in mixed alcohols (tetradecanol). Additional electrical effects

between the carbonyl carbon in the open-loop acid and hydroxyl oxygen in tetradecanols were used and played a role in achieving a "crystallization-melting" cycle of eutectic phase within a specific heating-cooling temperature range [26]. The structural changes under varying temperatures are illustrated in Figure 4. For biomass thermochromic dyes, the lactone ring of the cryptochrome dye opened under the influence of temperature, forming a quinone-like structure. This structural transformation altered the coupling system of the dye, resulting in a color change.

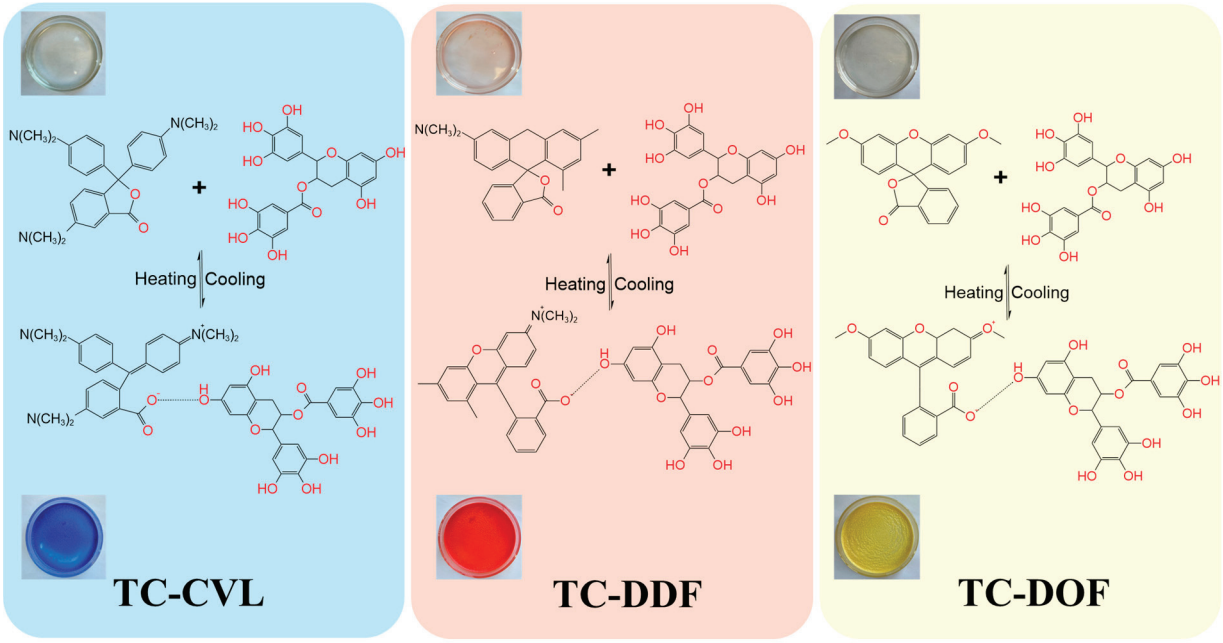

Figure 4. Molecular structure changes of three thermochromic dyes—TC-CVL, TC-DDF, and TC-DOF with heating and cooling.

2.2. Reversible Thermochromism of Dyed Polyester Fabric

Tetradecanol was utilized as a solvent for multi-component thermochromic materials, offering excellent solid/liquid phase change properties along with being environmentally friendly, cost-effective, and readily available. Polyester fabrics were dyed by impregnation to produce three reversible thermochromic fabrics in blue, red, and yellow using TC-CVL, TC-DDF, and TC-DOF dyes, respectively (as shown in Figure 5b). Tetradecanol served as the dyeing medium, leveraging its solid/liquid phase change properties.

FTIR spectroscopy analysis of the chemical structures of undyed polyester fabric and thermochromic polyester fabrics revealed that, in the spectra of thermochromic polyester fabrics (Figure 5a), the intramolecular and intermolecular hydrogen bonding of the three thermochromic dyes was observed at 3284 cm^{-1}. Additionally, the vibration peaks of the endo-methylene and methylene groups of the thermochromic dyes were detected at 2912 cm^{-1} and 2848 cm^{-1}. Compared to undyed polyester fabrics, the vibration peaks at 1712 cm^{-1} in thermochromic polyester fabrics were weakened, indicating that the stretching vibration of C=O in the lactone ring carbonyl of the three thermochromic dyes has a specific effect on the polyester fabrics. The variations in K/S values of the three dyed fabrics across different wavelengths are illustrated in Figure 5c. It was evident that the blue, red, and yellow fabrics exhibited their highest K/S values at their respective characteristic wavelengths. This indicated that each fabric achieved maximum color strength at specific wavelengths, corresponding to the peak absorption of the thermochromic dyes used. These findings highlighted the effectiveness of the dyeing process and the distinct optical properties of the thermochromic fabrics.

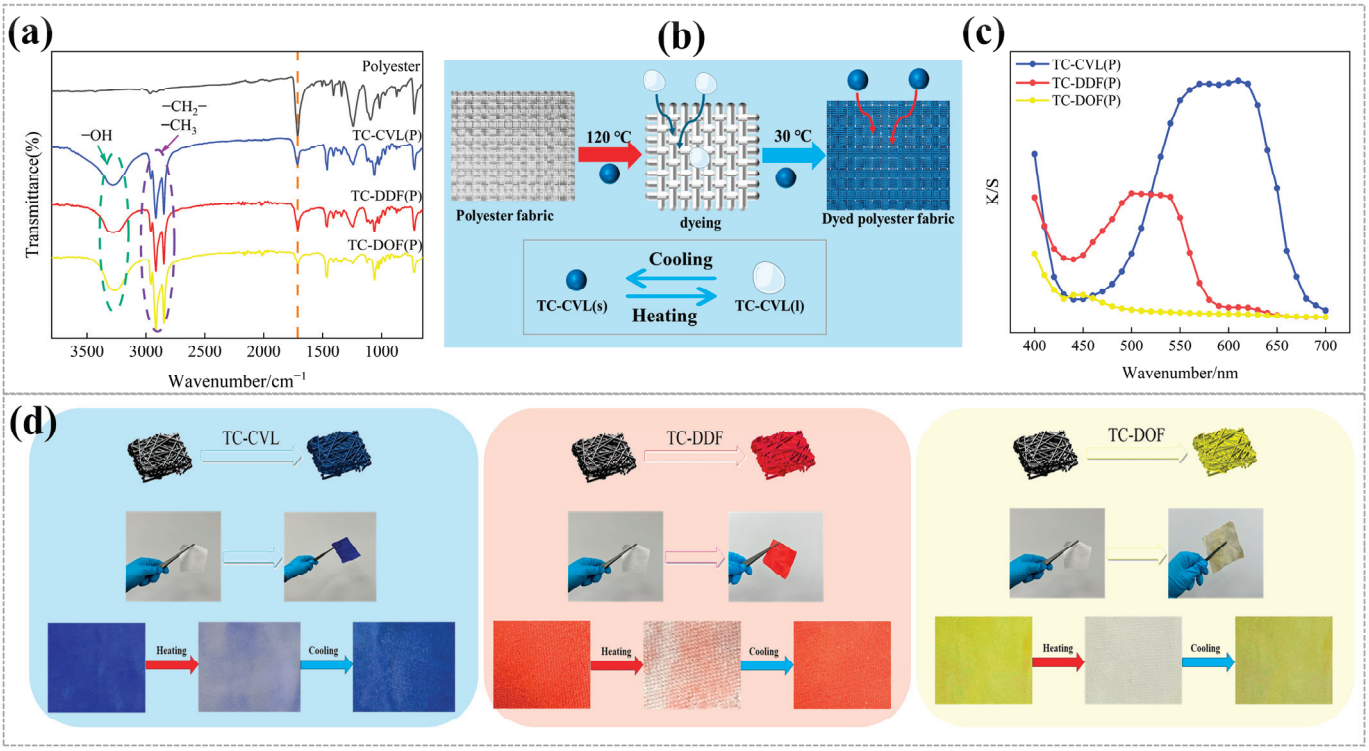

Figure 5. (**a**) FTIR spectra of both untreated and thermochromic polyester fabrics; (**b**) dyeing process methodology; (**c**) K/S values of three thermochromic polyester fabrics; (**d**) comparative analysis of fabrics pre- and post-dyeing, highlighting their reversible thermochromic properties under thermal cycling.

At room temperature, the dyed polyester fabrics exhibited blue, red, and yellow, respectively. Upon heating, the polyester fabrics became colorless, demonstrating a significant thermochromic response. When the heating plate was turned off, the dyed polyester fabrics reverted to their original blue, red, and yellow with the temperature decreased, as illustrated in Figure 5d. After numerous cycles of heating and cooling, the dyed polyester fabrics consistently demonstrated the same reversible thermochromic effect as observed during the initial cycle. This stability in performance underscored the durability and reliability of the thermochromic dyes used. The fabrics maintained their ability to change color upon heating and revert to their original blue, red, and yellow upon cooling, indicating a robust and repeatable thermochromic response. These findings indicated the potential of these materials in applications requiring long-term reversible color changes, such as smart textiles and temperature-sensitive indicators.

2.3. Performance of Thermochromic Polyester Fabrics

Ultraviolet (UV) radiation is categorized into two types: UVB (ultraviolet B) and UVA (ultraviolet A). The UVA band, with a wavelength of 320–400 nm, UVB band, with wavelengths from 280 to 320 nm. UVB has distinct biological effects, particularly impacting the skin during outdoor activities. The anti-UV performance of dyed polyester fabrics was analyzed, as shown in Figure 6a,b. The results demonstrated a reduction in UV transmittance, indicating that these fabrics possess inherent UV resistance properties. By calculating the ultraviolet protection factor (UPF) values of the polyester fabrics before and after dyeing, it was found that the UPFs of polyester fabrics dyed by TC-CVL, TC-DDF, and TC-DOF were 103.61, 96.57, and 94.11, respectively (Figure 6b). In contrast, the UPF of the undyed polyester fabric was only 26.3. This significant increase in UPF values demonstrated the enhanced UV resistance of polyester fabrics due to the dyeing process with these thermochromic dyes.

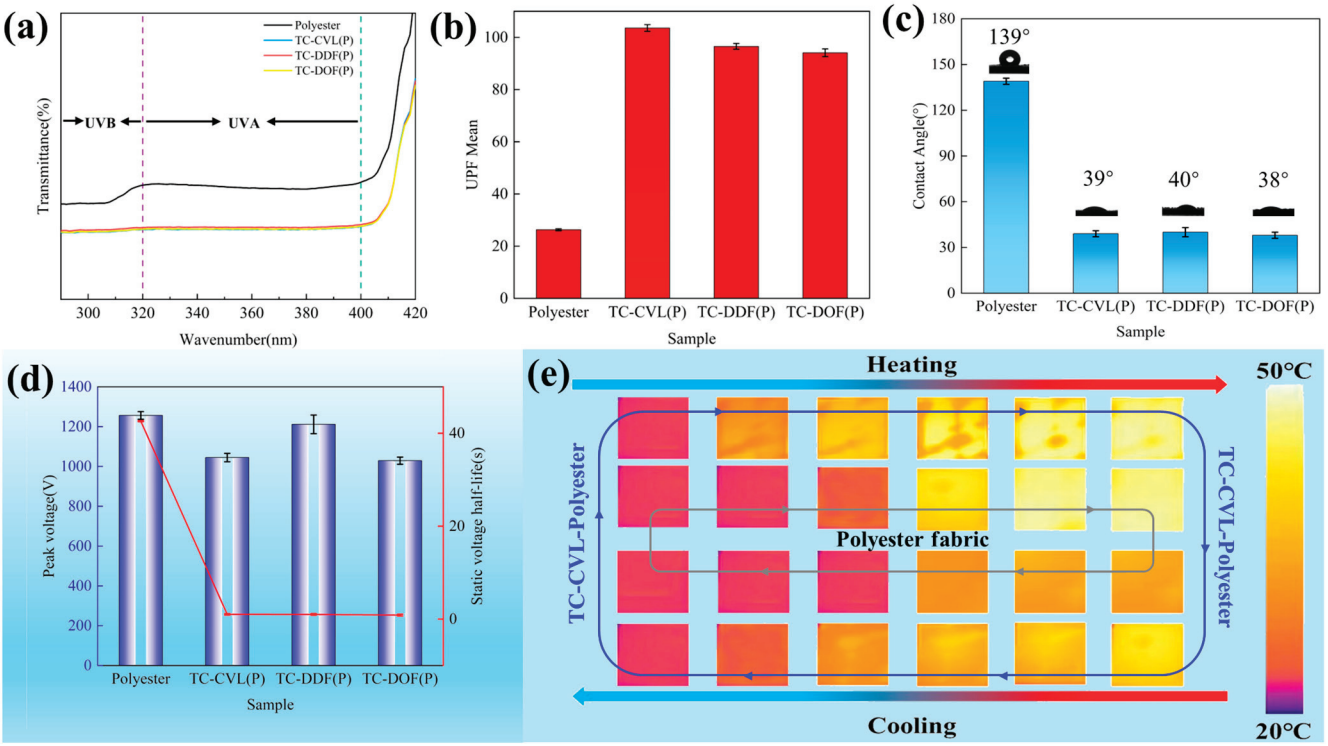

Figure 6. Performances of polyester fabrics before and after dyeing: (**a**) UV transmittance; (**b**) UPF values; (**c**) water contact angle; (**d**) peak voltage and static voltage half-life. (**e**) Infrared thermogram comparisons of polyester and thermochromic polyester fabrics (TC-CVL dyeing) under heating and cooling cycle.

Polyester fibers are known for their poor hydrophilicity and inadequate hygroscopicity, which can lead to the accumulation of static electricity in dry environments. This static buildup results in the adsorption of dust and fluff, causing pilling and negatively affecting the fabric's appearance. The application of multi-component biomass thermochromic dyes, utilizing tetradecane as a carrier, significantly enhanced the surface hydrophilicity of polyester fabrics. During the dyeing process, the hydroxyl groups of long-chain alcohols interact with the polyester fibers, improving their hydrophilicity. This interaction not only enhanced the moisture absorption capacity of the fabrics but also effectively reduced static electricity. Consequently, the dyed polyester fabrics exhibited better performance in terms of comfort and durability, making them more suitable for various applications where static resistance and moisture management are critical.

The contact angles of both undyed and dyed polyester fabrics were measured to assess their hydrophilicity. The water contact angle of undyed polyester fabrics was approximately 139°, indicating significant hydrophobicity. In contrast, the water contact angle of dyed polyester fabrics was reduced to 40° (Figure 6c), demonstrating that the application of reversible thermochromic dyes imparted considerable hydrophilicity to the polyester fabrics. This enhancement effectively addressed the inherent hydrophobic deficiencies of polyester fabrics. Furthermore, the antistatic properties of polyester fabrics before and after dyeing were evaluated (Figure 6d). Due to the high crystallinity, small amorphous zone, and low moisture return (0.4%) of polyester fabrics [27], there was a tendency for static charge accumulation on their insulating surfaces. The lack of polar hydrophilic groups also contributed to static electricity buildup [28–30]. Improved hydrophilicity reduced static charge accumulation, thereby enhancing the antistatic performance of the fibers. Static half-life measurements revealed that the static voltage of dyed polyester fabrics remained similar to that of undyed fabrics, around 1000–1200 V. However, the static half-life of dyed polyester fabrics was significantly reduced to less than 1 s, compared to 42.6 s for undyed

fabrics. This substantial decrease indicated that the dyed polyester fabrics exhibited strong antistatic properties, making them more suitable for applications.

Based on the analysis of the above data, thermochromic dyes transitioned from solid particles to a liquid state and adhered to the fabrics as the temperature increased during the dyeing process. Upon completion of dyeing and subsequent washing, the dyes within the fiber voids and on the surfaces reverted to a solid state (Figure 5b). The inclusion of tetradecanol in the dye formulation imparted hydrophilic and antistatic properties to the fabric. The presence of dye particles within the fiber voids enhanced the UV resistance of the polyester fabrics.

Phase change materials (PCMs) have the ability to absorb or release substantial amounts of heat while maintaining a constant temperature during the phase transition. The infrared thermography of undyed polyester fabric and reversible thermochromic polyester fabrics is presented in Figure 6e. The initial temperature of the fabrics was set at 25 °C. Upon heating, the surface temperature of the undyed polyester fabric (inner ring in Figure 6e) increased significantly faster than that of the reversible thermochromic polyester fabric (TC-CVL polyester) (outer ring in Figure 6e), where the lighter colors indicated the higher temperatures. The reversible thermochromic polyester fabric demonstrated superior thermal regulation. During the cooling phase, the rate of surface temperature change in the TC-CVL polyester was lower, indicating its thermal insulation properties. This was primarily due to the phase change solvent in the thermochromic polyester fabric, which can store and release thermal energy through solid/liquid phase transitions, thereby endowing the thermochromic polyester fabric with effective thermal insulation capabilities [31].

To further verify the thermal insulation and energy storage capabilities of thermochromic polyester fabrics, temperature–time curves were generated. Both undyed polyester and the three thermochromic polyester fabrics were placed on a heating plate, which was set at 55 °C. After heating, fabrics were permitted to cool for 150 s under ambient conditions (25 °C, 55% RH). An infrared thermal imager recorded the surface temperature of the fabrics in real-time, as shown in Figure 7. The results indicated that the temperature of the undyed polyester fabric increased linearly during the heating process (Figure 7a). In contrast, the polyester fabrics dyed with TC-CVL, TC-DDF, and TC-DOF thermochromic dyes exhibited an inflection point near 38 °C (Figure 7b–d). At this temperature, the rate of temperature change in the dyed fabrics decreased relative to the undyed fabric, primarily due to the solid/liquid phase transitions of tetradecane. During this phase transition, tetradecane absorbed a substantial amount of heat, stabilizing the temperature until the phase transition was complete. After this point, the temperature of the dyed fabrics continued to rise to approximately 55 °C.

Similarly, during the cooling process, the temperature of the fabrics dropped rapidly as the ambient temperature was lower than the fabric temperature. When the fabric temperature approached 38 °C, the cooling rate slowed significantly. This was because the ambient temperature (25 °C) was lower than the internal temperature of tetradecane, causing the thermal movement within the dye molecules to decrease. Consequently, tetradecane began to release heat and gradually solidified, resulting in a flattened cooling curve near 38 °C and a reduced cooling rate. The duration of this phase for the polyester fabrics dyed with TC-CVL, TC-DDF, and TC-DOF was 35 s, 57 s, and 38 s (between two dotted purple lines in Figure 7b–d), respectively, indicating that tetradecane was undergoing a liquid-solid phase transition during this period. Once the phase transition was completed, the temperature of the dyed fabrics continued to drop. After cooling for 150 s, the temperature of the undyed polyester fabric (28.8 °C) was lower than that of the dyed polyester fabric (33.9 °C, 33.3 °C, 33.2 °C) (Figure 7b–d). Under identical conditions, the dyed polyester fabrics exhibited the exothermic duration and the heat preservation effect at 38 °C. In contrast, the undyed polyester fabric demonstrated no energy storage or heat retention during the cooling process. Tetradecane, chosen as the phase change solvent for the three-component thermochromic dye, exhibited a solid/liquid phase change temperature of 37–38 °C, closely aligning with human body temperature. This

characteristic made these thermochromic fabrics suitable for personal thermal management and intelligent thermal insulation applications.

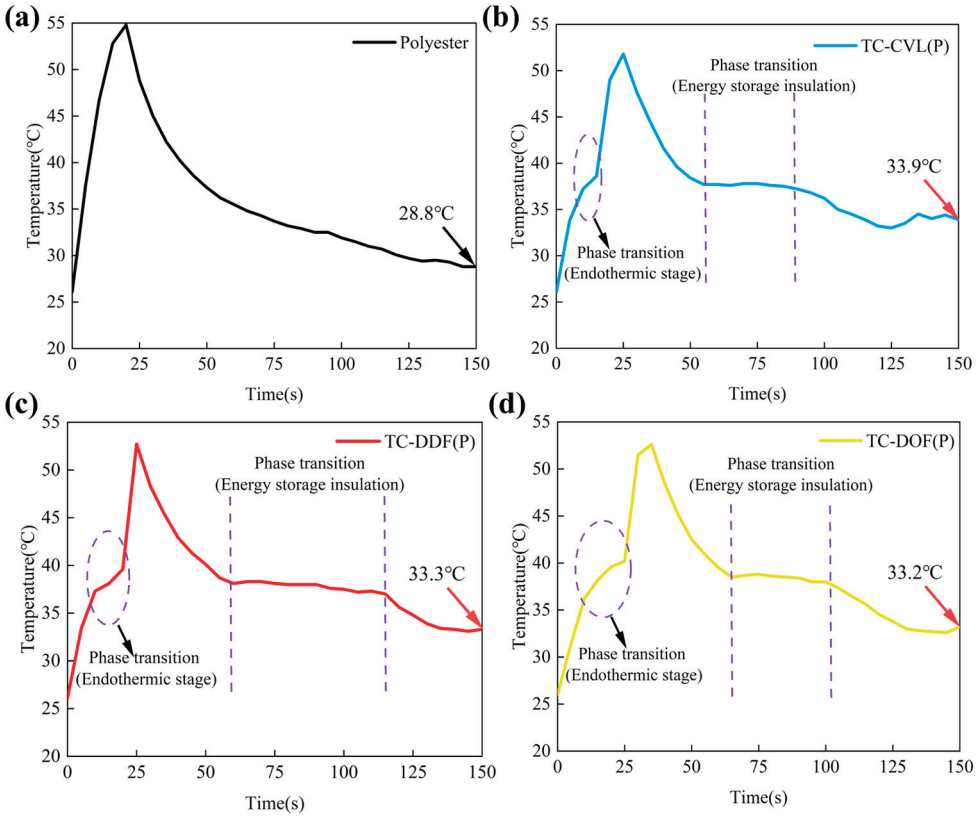

Figure 7. Temperature–time curve analysis for both polyester and thermochromic polyester fabrics: (**a**) polyester fabric; (**b**) TC-CVL-polyester fabric; (**c**) TC-DDF(P)-polyester fabric; (**d**) TC-DOF(P)-polyester fabric.

3. Materials and Methods

3.1. Materials

Tea polyphenols were chemically pure and procured from Aladdin Chemical Reagents Ltd., (Shanghai, China). Crystalline violet lactone (CVL), 6′-(diethylamino)-1′,3′-dimethylfluoran (DDF), 3′,6′-dimethoxyfluoran (DOF), and tetradecanol (TD), all of chemically pure, were purchased from Sinopharm Chemical Reagent Co. Ltd (Shanghai, China). Polyester fabric was provided by Zhejiang Silk Technology Co. Ltd (Zhengjiang, China).

3.2. Preparation of Reversible Thermochromic Dyes

The materials listed in Table 1 were individually added to the dissolved state of tetradecane and subjected to stirring at 300 rpm for 2 h at 90 °C, ensuring the formation of a homogeneous solution. Subsequently, the tea polyphenol was uniformly incorporated into the above solution, followed by an additional 2 h of stirring at 90 °C. The mixture was then maintained at a constant temperature for 0.5 h before cooling to room temperature, resulting in the formation of biomass thermochromic dyes, as illustrated in Figure 8. These three biomass thermochromic dyes exhibited reversible thermochromic behavior, making them suitable for various applications in intelligent textiles. The synthesis process not only ensured the uniform distribution of the dye components but also enhanced the thermal stability and color-changing properties of the resulting materials.

Table 1. Components of three thermochromic dyes.

Samples	Leuco Dyes	Chromogenic Agents	Solvent
TC-CVL	Crystal violet lactone	Tea polyphenols	Tetradecanol
TC-DDF	6′-(Diethylamino)-1′,3′-dimethyl-fluoran	Tea polyphenols	Tetradecanol
TC-DOF	3′,6′-Dimethoxyfluoran	Tea polyphenols	Tetradecanol

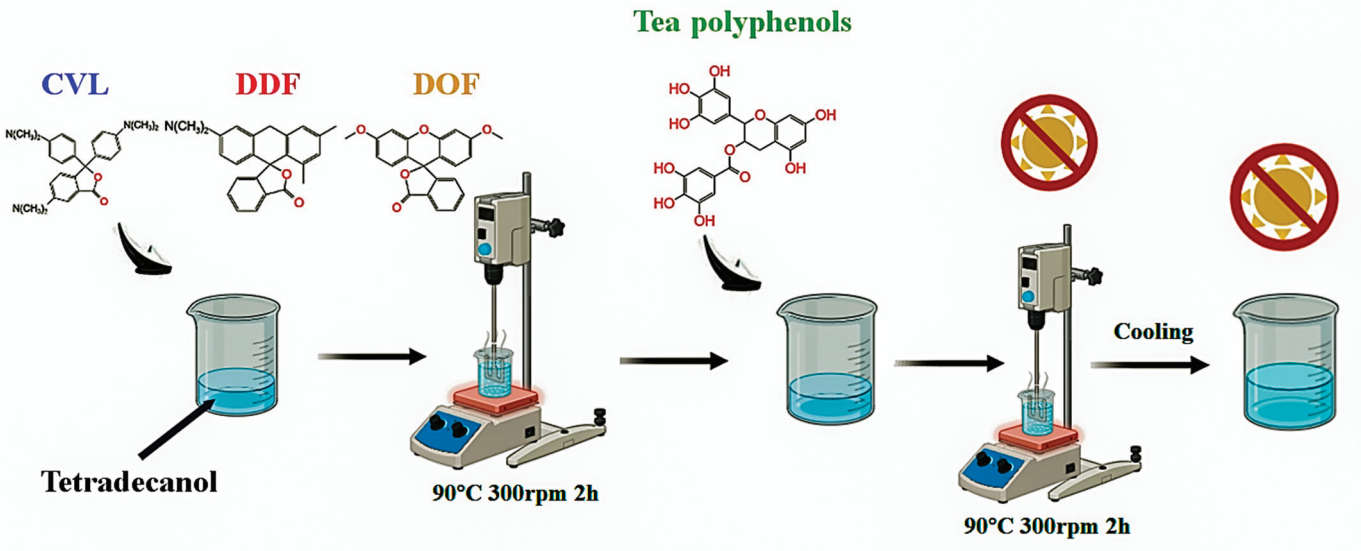

Figure 8. Schematic representation of the thermochromic dye synthesis process.

3.3. Dyeing of Polyester Fabric Using Reversible Thermochromic Dyes

The polyester fabric was dyed using the three prepared thermochromic dyes; the dyeing process is illustrated in Figure 9. After dyeing, the polyester samples were carefully extracted and subjected to a washing procedure for 10 min to remove any residual dye. Subsequently, the samples were air-dried at room temperature for 1 h. This methodical approach ensured the production of thermochromic polyester fabrics.

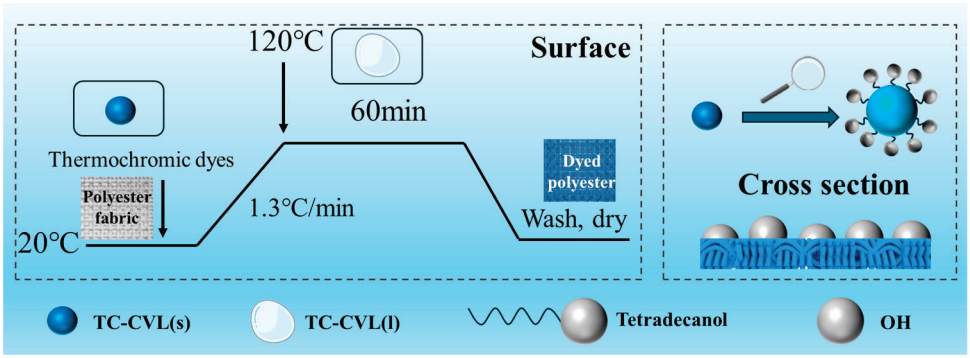

Figure 9. Dyeing process of thermochromic polyester fabrics.

3.4. Characterization

To analyze the molecular structure changes of the three reversible thermochromic dyes before and after heating, several advanced spectroscopic techniques were employed. The absorbance of the biomass thermochromic dyes was measured using in-situ ultraviolet spectroscopy (PerkinElmer Lambda 950, Waltham, USA) at 25 °C and 50 °C, respectively, within the wavelength range of 400–700 nm. In situ Raman measurements (Ecopia Hall effect tester HMS-7000) were conducted at both 25 °C and 50 °C, covering the wavelength range

of 300–3500 cm^{-1}. Additionally, an in-situ Fourier transform infrared (FTIR) spectrometer (Thermo Nicolet iS50, Madison, WI, USA) was used to characterize three thermochromic dyes, obtaining spectra at 25 °C and 50 °C across the wavelength range of 400–4000 cm^{-1}. High-resolution solid-state nuclear magnetic resonance (NMR) spectra were acquired using high-temperature solid-state NMR spectrometer (Agilent 600M, Santa Clara, CA, USA). A standard Agilent magic-angle spinning (MAS) probe with a 4 mm zirconium oxide rotor was employed for recordings at various temperatures on an Agilent DSX-300 spectrometer, facilitating the analysis of chemical structure changes and elucidating the color change mechanism of the biomass thermochromic dyes. The Datacolor SF650 Color Measurement and Matching instrument (10○ standard viewer, CIE D65 Light Measurement, Datacolor, Lawrenceville, USA) was used to measure the K/S values of blue, red, and yellow fabrics at room temperature. The ultraviolet reflectance (UV-R) of the reversible thermochromic polyester fabrics was determined using a UV spectrophotometer with a resolution of 4 cm^{-1}, in accordance with the European standard for sun-protective clothing (EN:13758-1 standard) [32]. The static water contact angle of the fabrics was measured using a Water Contact Angle Analyzer (Drop Shape Analyzer–DSA 25, Hamburg, Germany) with a 10 μL water droplet. The antistatic properties were evaluated using the YG—401 fabric inductive static tester according to the test methods for electrostatic propensity—Part 1: Test method using corona charging (GB/T12703.1–2021 standard) [33]. The evaluation involved measuring the peak voltage decay and decay time of fabrics through the corona charging method, with the acceleration voltage sat at 10 KV. An electric heating plate and an infrared thermal imager were employed to observe the color and temperature changes of the fabrics during heating and cooling cycles, thereby assessing their thermal responsiveness.

4. Conclusions

In this study, three thermochromic dyes were prepared using biomass—derived tea polyphenols as color developers. The molecular structures of these dyes were analyzed before and after the thermochromic transition to elucidate the mechanism of color change. The results revealed that the bonds between the leuco dyes and the color developer dissociated upon heating and reformed upon cooling, thereby imparting reversible thermochromic properties. Additionally, polyester fabrics dyed with these reversible thermochromic dyes indicated that the water contact angle of the dyed polyester fabrics decreased from 139° to approximately 40°, demonstrating improved wettability. The UPF value of the dyed polyester fabrics increased from 29.3 to about 100, enhancing the UV resistance. Furthermore, a comparative analysis of the electrostatic voltage and electrostatic half-life of polyester fabrics before and after dyeing revealed a significant enhancement in antistatic properties. The electrostatic voltage half-life of undyed polyester fabric was measured at 42.6 s, whereas the dyed polyester fabrics exhibited a markedly reduced half-life of approximately 1 s. Additionally, infrared thermography demonstrated that the dyed polyester fabrics possessed notable energy storage and insulation capabilities. This method of fabricating thermochromic polyester textiles showed significant promise for the development of advanced smart color-changing textiles, especially for applications in personal thermal management and intelligent insulation.

Author Contributions: W.Z. Investigation, Project administration, writing—original draft; Q.Y. conceptualization, supervision, funding acquisition, writing—review and editing; S.T. writing—original draft; J.C. data curation, project administration; J.Z. data curation, writing—original draft; S.Z. and R.L. project administration; J.S. and N.Z. data curation; L.X. formal analysis, methodology; H.P. methodology, writing—review and editing; J.W. methodology, conceptualization. All authors have read and agreed to the published version of the manuscript.

Funding: This work was supported by the Key Laboratory of Textile Fiber and Products (Wuhan Textile University), Ministry of Education (Project Number Fzxw2023003), Foundation of Shanghai University of Engineering Science (0239-E3-0507-19-05165), Songjiang District Science and Technology Research Project (24SJJBGS2) and Cooperative Project ((23)FZ-032).

Institutional Review Board Statement: Not applicable.

Informed Consent Statement: Not applicable.

Data Availability Statement: The experimental data used to support the findings of this study are included in the article.

Conflicts of Interest: Author J.C. was employed by the company Shanghai Evershine Co., Ltd. The remaining authors declare that the research was conducted in the absence of any commercial or financial relationships that could be construed as a potential conflict of interest.

References

1. Viková, M.; Pechová, M. Study of adaptive thermochromic camouflage for combat uniform. *Text. Res. J.* **2020**, *90*, 2070–2084. [CrossRef]
2. Wu, S.; Sun, H.; Duan, M.; Mao, H.; Wu, Y.; Zhao, H.; Lin, B. Applications of thermochromic and electrochromic smart windows: Materials to buildings. *Cell Rep. Phys. Sci.* **2023**, *4*, 101370. [CrossRef]
3. Liu, H.; Jiang, T.; Wang, F.; Ou, J.; Li, W. Thermochromic superhydrophobic coatings for building energy conservation. *Energy Build.* **2021**, *251*, 111374. [CrossRef]
4. Zhang, J.; Zhang, Y.; Wu, S.; Ji, Y.; Mao, Z.; Wang, D.; Xu, Z.; Wei, Q.; Feng, Q. Weavable coaxial phase change fibers concentrating thermal energy storage, photothermal conversion and thermochromic responsiveness toward smart thermoregulatory textiles. *Chem. Eng. J.* **2024**, *483*, 149281. [CrossRef]
5. Wang, C.; Gong, X.; Li, J.; Chen, Y.; Li, B.; Zhang, L.; Fu, S. Ultrahigh-sensitivity thermochromic smart fabrics and flexible temperature sensors based on intramolecular proton-coupled electron transfer. *Chem. Eng. J.* **2022**, *446*, 136444.
6. Cheng, Z.; Lei, L.; Zhao, B.; Zhu, Y.; Yu, T.; Yang, W.; Li, Y. High performance reversible thermochromic composite films with wide thermochromic range and multiple colors based on micro/nanoencapsulated phase change materials for temperature indicators. *Compos. Sci. Technol.* **2023**, *240*, 110091. [CrossRef]
7. Abou Elmaaty, T.M.; Abdeldayem, S.A.; Elshafai, N. Simultaneous Thermochromic pigment printing and Se-NP multifunctional finishing of cotton fabrics for smart childrenswear. *Cloth. Text. Res. J.* **2020**, *38*, 182–195. [CrossRef]
8. Liu, J.; Tan, J.; Liu, H.; Yin, Y.; Wang, C. Multicolor-tunable biomass thermochromic dyes utilizing tea polyphenols color developer for temperature-controlled linen fabric. *Ind. Crops Prod.* **2023**, *204*, 117254. [CrossRef]
9. Yu, S.; Zhang, Q.; Liu, L.; Ma, R. Thermochromic conductive fibers with modifiable solar absorption for personal thermal management and temperature visualization. *ACS Nano* **2023**, *17*, 20299–20307. [CrossRef]
10. Wang, Y.; Ren, J.; Ye, C.; Pei, Y.; Ling, S. Thermochromic silks for temperature management and dynamic textile displays. *Nano-Micro Lett.* **2021**, *13*, 72. [CrossRef]
11. Wang, X.; Dong, L.; Li, J.; Wang, S.; Yao, B.; Chen, Y.; Yang, H. Reversible thermochromic properties of bisphenol A aromatic phenolic resin's composite natural rubber film. *Opt. Mater.* **2024**, *147*, 114698. [CrossRef]
12. Geng, X.; Li, W.; Wang, Y.; Lu, J.; Wang, J.; Wang, N.; Li, J.; Zhang, X. Reversible thermochromic microencapsulated phase change materials for thermal energy storage application in thermal protective clothing. *Appl. Energy* **2018**, *217*, 281–294. [CrossRef]
13. Simonelli, A.; Guadagni, R.; De Franciscis, P.; Colacurci, N.; Pieri, M.; Basilicata, P.; Pedata, P.; Lamberti, M.; Sannolo, N.; Miraglia, N. Environmental and occupational exposure to bisphenol A and endometriosis: Urinary and peritoneal fluid concentration levels. *Int. Arch. Occup. Environ. Health* **2016**, *90*, 49–61. [CrossRef] [PubMed]
14. Stolz, A.; Schönfelder, G.; Schneider, M.R. Endocrine Disruptors: Adverse Health Effects Mediated by EGFR? *Trends Endocrinol. Metab.* **2018**, *29*, 69–71. [CrossRef] [PubMed]
15. Umair, M.M.; Zhang, Y.; Iqbal, K.; Zhang, S.; Tang, B. Novel strategies and supporting materials applied to shape-stabilize organic phase change materials for thermal energy storage—A review. *Appl. Energy* **2019**, *235*, 846–873. [CrossRef]
16. Huang, X.; Chen, X.; Li, A.; Atinafu, D.; Gao, H.; Dong, W.; Wang, G. Shape-stabilized phase change materials based on porous supports for thermal energy storage applications. *Chem. Eng. J.* **2019**, *356*, 641–661. [CrossRef]
17. Zhao, L.; Li, M.; Yu, Q.; Zhang, Y.; Li, G.; Huang, Y. Improving the thermal performance of novel low-temperature phase change materials through the configuration of 1-dodecanol-tetradecane nanofluids/expanded graphite composites. *J. Mol. Liq.* **2021**, *322*, 114948. [CrossRef]
18. Hou, M.; Kong, X.; Li, H.; Yang, H.; Chen, W. Experimental study on the thermal performance of composite phase change ventilated roof. *J. Energy Storage* **2021**, *33*, 102060. [CrossRef]
19. Hsieh, S.; Omu, A.; Orehounig, K. Comparison of solar thermal systems with storage: From building to neighbourhood scale. *Energy Build.* **2017**, *152*, 359–372. [CrossRef]
20. Yang, H.; Wang, Y.; Yu, Q.; Cao, G.; Yang, R.; Ke, J.; Di, X.; Liu, F.; Zhang, W.; Wang, C. Composite phase change materials with good reversible thermochromic ability in delignified wood substrate for thermal energy storage. *Appl. Energy* **2018**, *212*, 455–464. [CrossRef]
21. Zhang, X.; Tong, W.; Feng, F.; Wang, Z.; Wang, X.; Zhang, Y. Polydopamine-assisted load of palygorskite on polyester fabric for moisture absorption and perspiration. *Appl. Clay Sci.* **2022**, *230*, 106720. [CrossRef]

22. Fan, L.; Tan, Y.; Amesimeku, J.; Yin, Y.; Wang, C. A novel functional disperse dye doped with graphene oxide for improving antistatic properties of polyester fabric using one-bath dyeing method. *Text. Res. J.* **2019**, *90*, 655–665. [CrossRef]
23. Panák, O.; Držková, M.; Kaplanová, M. Insight into the evaluation of colour changes of leuco dye based thermochromic systems as a function of temperature. *Dye. Pigment.* **2015**, *120*, 279–287. [CrossRef]
24. Panák, O.; Držková, M.; Kaplanová, M.; Novak, U.; Klanjšek Gunde, M. The relation between colour and structural changes in thermochromic systems comprising crystal violet lactone, bisphenol A, and tetradecanol. *Dye. Pigment.* **2017**, *136*, 382–389. [CrossRef]
25. Zhu, C.F.; Wu, A.B. Studies on the synthesis and thermochromic properties of crystal violet lactone and its reversible thermochromic complexes. *Thermochim. Acta* **2005**, *425*, 7–12. [CrossRef]
26. Zhou, W.M.; Yang, Q.; Tao, S.X.; Zhou, S.Y.; Zhu, J.; Li, R.M.; Xu, L.H.; Pan, H.; Zhang, H.J.; Zhao, H.; et al. Fabrication and reversible thermotropic characterization of polyurethane/dye microcapsules composite films for thermal management. *Colloids Surf. A Physicochem. Eng. Aspect.* **2024**, *703*, 135226. [CrossRef]
27. Pei, L.; Li, H.; Zhang, H.; Wang, Z.; Wang, J. Migration and chemical characterization of cyclic oligomers from polyester fiber in waterless dyeing system. *Fibers Polym.* **2022**, *23*, 2648–2656. [CrossRef]
28. Tang, X.; Zhang, X.; Zhang, H.; Zhuang, X.; Yan, X. Facile dip-coating process towards multifunctional nonwovens: Robust noise reduction, abrasion resistance and antistatic electricity. *Text. Res. J.* **2017**, *88*, 2568–2578. [CrossRef]
29. Elabid, A.E.A.; Zhang, J.; Shi, J.; Guo, Y.; Ding, K.; Zhang, J. Improving the low temperature dyeability of polyethylene terephthalate fabric with dispersive dyes by atmospheric pressure plasma discharge. *Appl. Surf. Sci.* **2016**, *375*, 26–34. [CrossRef]
30. Hu, C.C.; Chang, S.S.; Liang, N.-Y. Fabrication and characterization of antistatic fiber with segmented pie structure. *Text. Res. J.* **2015**, *86*, 1828–1836. [CrossRef]
31. kaplan, Ö.; gökşen Tosun, N.; Gökçe, İ.; Alkan, C. Diacid esters of 1-dodecanol as new alternatives to solid-liquid phase change materials for solar heat storage systems. *Energy Sources Part A Recovery Util. Environ. Eff.* **2023**, *45*, 608–622. [CrossRef]
32. Gambichler, T.; Laperre, J.; Hoffmann, K. The European standard for sun-protective clothing: EN 13758. *J. Eur. Acad. Dermatol. Venereol. JEADV* **2006**, *20*, 125–130. [CrossRef]
33. *GBT127031-2021*; Textiles—Test Methods for Electrostatic Propensity—Part 1 Test Method Using Corona Charging. China National Standardization Administration: Beijing, China, 2021.

molecules

MDPI

Article

Experiment and Molecular Dynamic Simulation on Interactions between 3,4-Bis(3-nitrofurazan-4-yl) Furoxan (DNTF) and Some Low-Melting-Point Explosives

Junming Yuan *, Runsheng Huang, Jinying Wang, Xiwei Xing, Jing Wang, Tao Han, Qi Yang and Jia Yang

School of Environmental and Safety Engineering, North University of China, Taiyuan 030051, China; 17835131200@163.com (R.H.); wjywzhy@126.com (J.W.); 15903412016@163.com (X.X.); wj1872691402@163.com (J.W.); h3581305@163.com (T.H.); m17636191448@163.com (Q.Y.); 16603596671@163.com (J.Y.)

* Correspondence: yuanjm@nuc.edu.cn

Abstract: 3,4-bis(3-nitrofurazan-4-yl) furoxan (DNTF) is an explosive with excellent performance, and the use of DNTF as a high-energy component is of great significance for improving the comprehensive performance of weapons. To explore the effect of DNTF on low-melting-point molten carrier explosives, the compatibility between DNTF and other low-melting-point explosives was analyzed by differential scanning calorimetry, and mechanical sensitivity was tested. The compatibility and cohesive energy density between DNTF and other low-melting-point explosives were calculated by Materials Studio. The results showed that DNTF has good compatibility with most low-melting-point explosives, and the peak temperature change of the mixed system formed by melt-casting is not obvious. Among them, DNTF has the best compatibility with MTNP, TNT, and DNAN; moderate compatibility with DFTNAN and DNP; and the worst compatibility with DNMT. The sensitivity test results indicate that the combination of DNTF and TNT has the most significant reduction in mechanical sensitivity. DFTNAN and MTNP have better stability than DNTF and can generate strong interaction forces with DNTF. Other low-melting-point explosives mixed with DNTF have lower intermolecular forces than DNTF. The DNTF/MTNP system requires the most energy to phase change when heated compared to other mixed systems and is the least sensitive to heat. The DNTF/DNMT system has the lowest cohesive energy density and is the most sensitive to heat.

Keywords: low-melting-point explosives; molecular dynamic simulation; interaction; compatibility; mechanical sensitivity

1. Introduction

3,4-bis(3-nitrofurazan-4-yl) furoxan (DNTF) is a new type of high-energy-density material [1–3], which has a stronger working ability compared to octahydro-1,3,5,7-tetranitro-1,3,5,7-tetrazocine (HMX) [4] and has a significant accelerating effect on metals. DNTF benefits from high detonation velocity and energy, high density, good oxygen balance, a low melting point, and moderate sensitivity. It can be used as the main component of cast explosives [5–8] and high-energy propellants [9–11] and has broad application prospects [12,13]. Therefore, DNTF has received widespread attention and research.

DNTF is a hydrogen-free explosive with a low melting point, moderate sensitivity, good thermal stability, and indirect steam heating that does not decompose for a long time. It is suitable for melting and casting explosive formulations. DNTF can be mixed with 2,4,6-trinitrotoluene (TNT) explosives to form low-cocrystal compounds that can be formulated into liquid carriers with different melting points and energy requirements [14]. By replacing TNT with DNTF as a liquid phase carrier, the energy of mixed explosives will rise to a new level, which is of great significance for improving the overall performance of weapons [15]. As a low-melting-point and high-energy explosive, DNTF meets the

requirements of the casting process itself, but its high sensitivity greatly increases the hazard of the explosive. The chemical and crystal structures of DNTF explosive molecules are shown in Figure 1 [16].

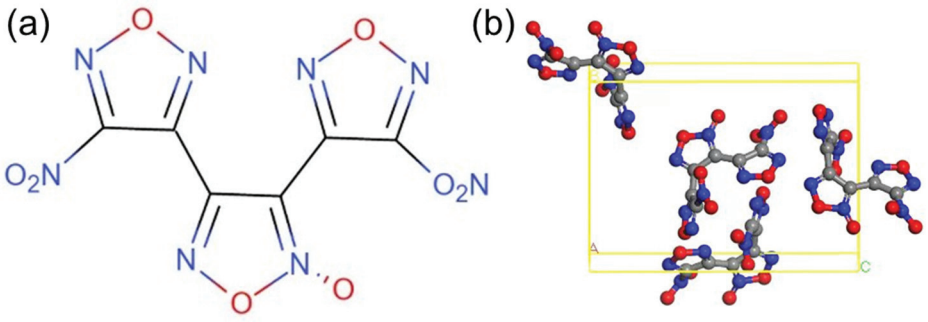

Figure 1. The structures of DNTF: (**a**) chemical structure; (**b**) crystal structure.

The use of DNTF as a high-energy component has the following advantages: (1) It has better solid-phase uniformity compared to the addition of solid particles to the melt-cast carrier at lower temperatures. High-sensitivity explosives and low-sensitivity explosives can be melted and cast to improve their sensitivity; (2) Compared with the addition of high-energy solid particles to the melt-cast carrier, DNTF and the melt-cast carrier together melt-cast to form a lower hardness and better ductility, which means it has better mechanical properties; (3) DNTF has excellent detonation performance and higher energy than hexahydro-1,3,5-trinitro-1,3,5-triazine (RDX).

According to current research on the compatibility of DNTF, it has been found that DNTF/TNT and DNTF/5-ATEZN (5-Amino-tetrazolium Nitrate) have good compatibility, DNTF/NTO (3-Nitro-1,2,4-triazol-5-one) and DNTF/TATB (2,4,6-Triamino-1,3,5-trinitrobenzene) have moderate compatibility, and DNTF/LLM-105 (2,6-Diamino-3,5-Dinitropyrazine-1-Oxide) and DNTF/PVAC (Polyvinyl Acetate) have poor compatibility [17–19]. The mechanical and thermal sensitivity of DNTF-based binary cocrystal materials decreases with increasing DNTF content. The maximum bond length of the N-O bond initiated by DNTF can serve as a theoretical criterion for the relative mechanical sensitivity and thermal safety of DNAN/DNTF binary cocrystal materials [20].

Existing research has shown that the addition of other substances has a significant impact on the performance of DNTF [21]. For example, molecular dynamics simulation methods are used to establish molecular models of NC (Nitrocotton)/DNTF [22] and GAP (Glycidyl azide polymer)/DNTF [16] blends to explore the interaction between additives and explosives.

The above research results are related to the performance of DNTF explosives and their compatibility with other explosives. Similar research methods have also been found in the literature [23–26], which respectively explore the compatibility issues of 2,3-bis (hydroxymethyl)-2,3-dinitro-1,4-butanediol tetranitrate (DNTN), dihydroxylamonium 5,5′-bistetrazole-1,1′-diolate (TKX-50), tetraethylammonium decahydrocarbonate (BHN), and trans-1,4,5,8-tetranitro1,4,5,8-tetrazadecalin (TNAD) with other energetic components and inert materials. These studies have important reference significance for the research of this paper. In addition, the ab initio molecular dynamic method can also be used to study the compatibility between components of energetic materials [27,28].

In this article, a mixture of DNTF and six types of low-melting-point explosives was prepared. The compatibility and interaction between DNTF and other low-melting-point explosives was investigated using electron microscopy morphology characterization and DSC analysis. Combined with experimental characterization and molecular dynamics simulation calculations, the physical and chemical interactions between DNTF and low-melting-point explosives were studied at different temperature ranges. The research results can provide certain theoretical support for the safe use of DNTF.

2. Experimental Methods

2.1. Materials and Equipment

Materials: 3,4-bis(3-nitrofurazan-4-yl) furozan (DNTF), 1-methyl-3,4,5-trinitropyrazole (MTNP), 1-methyl-3,5-dinitro-1,2,4-triazole (DNMT), 2,4,6-trinitrotoluene (TNT), 2,4-dinitroanisole (DNAN), and 3,4-dinitropyrazole (DNP) samples were provided by Xi'an Modern Chemistry Research Institute and purified by recrystallization in alcohol whose mass fraction purity was greater than 0.995. 3,5-difluoro-2,4,6-trinitroanisole (DFTNAN) was produced by the North University of China. The mixtures of DNTF and some low-melting-point explosives were prepared according to a mass ratio of 1:1.

Equipment: EM-30 scanning electron microscope from COXEM Company in Daejeon, South Korea; HCT-1 differential scanning calorimeter from Beijing Hengjiu Technology Co., Ltd. (Beijing, China).

2.2. Performance Characterization Methods

SEM: The particle morphology of DNTF and low-melting-point-explosive samples was observed by scanning electron microscopy (SEM) and compared with the morphology of DNTF raw materials. The samples were treated with gold spray and accelerated to a voltage of 15 kV.

Mechanical sensitivity: In accordance with methods 601.2 and 602.1 of GJ772A-97, the impact sensitivity and friction sensitivity of DNTF and DNTF with low-melting-point-explosive samples were tested using an MYG-I impact sensitivity tester and an MYG-I friction sensitivity tester, respectively. The characteristic drop height test used a 5.000 ± 0.005 kg drop hammer with a dosage of 30 ± 1 mg; the friction sensitivity test pressure was 3.92 MPa, the swing angle was 90°, and the dosage was 20 mg.

DSC: The thermal performance parameters and thermal decomposition process of the samples were tested and analyzed using DSC HQC-1. DNTF, DNMT, TNT, DNAN, DNP, MTNP, and DNTF mixed with low-melting-point explosives were tested and analyzed using DSC at a heating rate of 10 °C/min. The temperature range was 30–350 °C, with a dosage of 3 ± 0.1 mg. The experiment used a sealed alumina crucible and an empty crucible as reference material.

2.3. Evaluated Standard of Compatibility for Mixtures

The evaluated standards [23] of compatibility are listed in Table 1.

Table 1. Evaluation standards of the compatibility for explosives and contact materials.

Criteria ΔTp (°C)	Rating	Note
Less than or equal to 2	A, compatible or good compatibility	Safe for use in any explosive design
3~5	B, slightly sensitized or fair compatibility	Safe for use in testing or when the device will be used for a very short period of time; not to be used as a binder material or when long-term storage is desired
6~15	C, sensitized or poor compatibility	Not recommended for use with explosive items
Above 15	D, hazardous or bad compatibility	Hazardous. Do not use under any conditions

The temperature change of the decomposition peak is calculated as:

$$\Delta T_p = \left| T_{p1} - T_{p2} \right| \quad (1)$$

where ΔT_p is the change in decomposition peak temperature of the system alone relative to the mixed system, K; T_{p1} is the decomposition peak temperature of the separate system, K; and T_{p2} is the decomposition peak temperature of the mixed system, K.

3. Molecular Dynamic Simulation

3.1. DNTF/Low-Melting-Point Explosives Mixed Models

The molecular structural formulas and configurations of six low-melting-point explosives provided by the laboratory—DFTNAN, TNT, DNMT, DNAN, MTNP, and DNP—are shown in Figure 2.

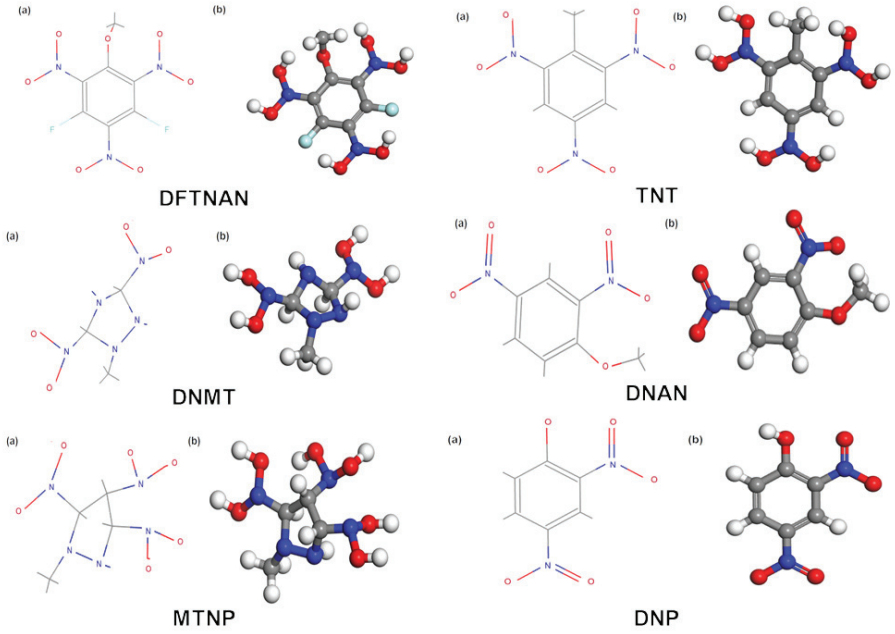

Figure 2. Molecular structural formulas (**a**) and configurations (**b**) of six low-melting-point explosives.

The amorphous cell is used to create an amorphous model of DNTF and low-melting-point explosives, ensuring that the density of the model is close to the theoretical density. The initial model established is shown in Figure 3.

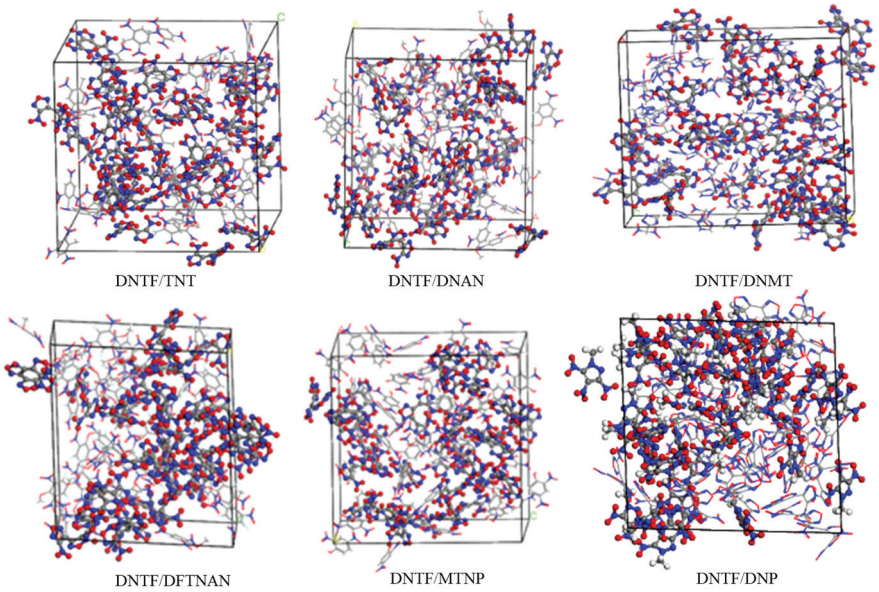

Figure 3. Initial models of DNTF and low-melting-point explosives.

The established initial model parameters are shown in Table 2.

Table 2. Initial parameters of calculation model of mixed system.

	Sample	Molecular Number of Low-Melting-Point Explosive	Molecular Number of DNTF	Atom Number	Density ($g \cdot cm^{-3}$)
I	DNTF	30	30	1320	1.853
II	DNTF/DFTNAN	34	30	1386	1.821
III	DNTF/TNT	42	30	1542	1.689
IV	DNTF/DNMT	54	30	1470	1.727
V	DNTF/DNAN	48	30	1600	1.595
VI	DNTF/MTNP	43	30	1434	1.803
VII	DNTF/DNP	47	30	1510	1.687

3.2. Molecular Dynamics Calculations

The interaction between DNTF and low-melting-point-explosive components at low temperatures was studied by molecular dynamics simulation using Materials Studio2019 software. The COMPASS force field and a smart minimization method were used to optimize the geometry of the amorphous model with a convergence limit of 0.001 kcal/mol. The MD simulation used the Nosé–Hoover temperature control method and the Berendsen pressure control method. The van der Waals and electrostatic interactions were calculated using the atom-based and Ewald methods, respectively. The cutoff radius was set to 12.5 Å, the spline width was set to 0.1 nm, the buffer width was set to 0.05 nm, the step size was set to 1 fs, and the isothermal isobaric (NPT) ensemble was selected. The temperature was 298.15 K, and the pressure was 101 KPa. The total simulation time was 300 ps. In order to eliminate the influence of unreasonable energy and volume on the calculation results, a balanced system of 100 ps was selected to calculate the relevant performance.

4. Results and Discussion

4.1. Electron Microscopy Morphology

SEM was used to characterize the microstructure of DNTF explosive particles mixed with low-melting-point-explosive particles. The electron microscope photos of the morphology characteristics of DNTF explosive grains are shown in Figure 4a,b, which are photos of DNTF grains magnified by 200 and 500 times, respectively. Overall, the DNTF crystal exhibits a layered morphology, and the surface of the uncoated DNTF is relatively smooth and flat. The particles have a regular polyhedral shape with slightly smaller grains attached to the surface without any other attachments.

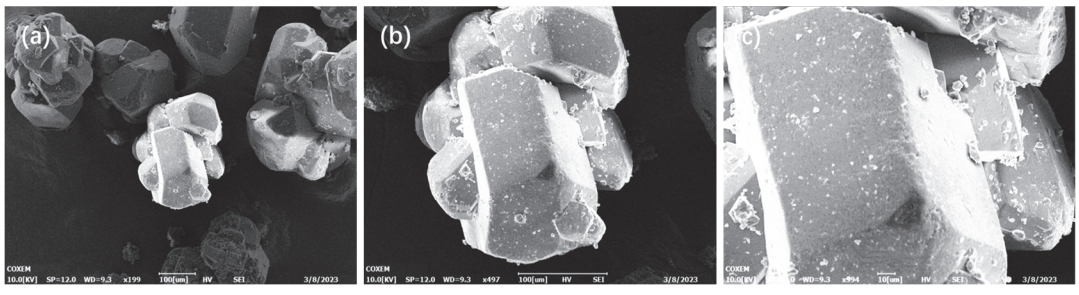

Figure 4. DNTF morphology: (**a**) 200 times; (**b**) 500 times; (**c**) 1000 times.

The electron microscopy morphology characterization of DNTF and low-melting-point explosives is shown in Figure 5. The surface of DNTF/MTNP is the smoothest, with very few small particles, indicating the best compatibility between DNTF and MTNP. After mixing DNTF with TNT and DNMT, the surface roughness increases, and crystalline particles appear on the surface, with the DNTF/DNMT phenomenon being more obvious. The surface roughness of DNTF, DNAN, and DNP is more pronounced, and the surface is clustered. Compared to DNTF/DNAN, DNTF/DNP has smoother surfaces and less

clustering. The surface of mixed DNTF and DFTNAN is the roughest, and the crystal surface adheres to incompletely melted explosive particles, indicating the worst compatibility between the two.

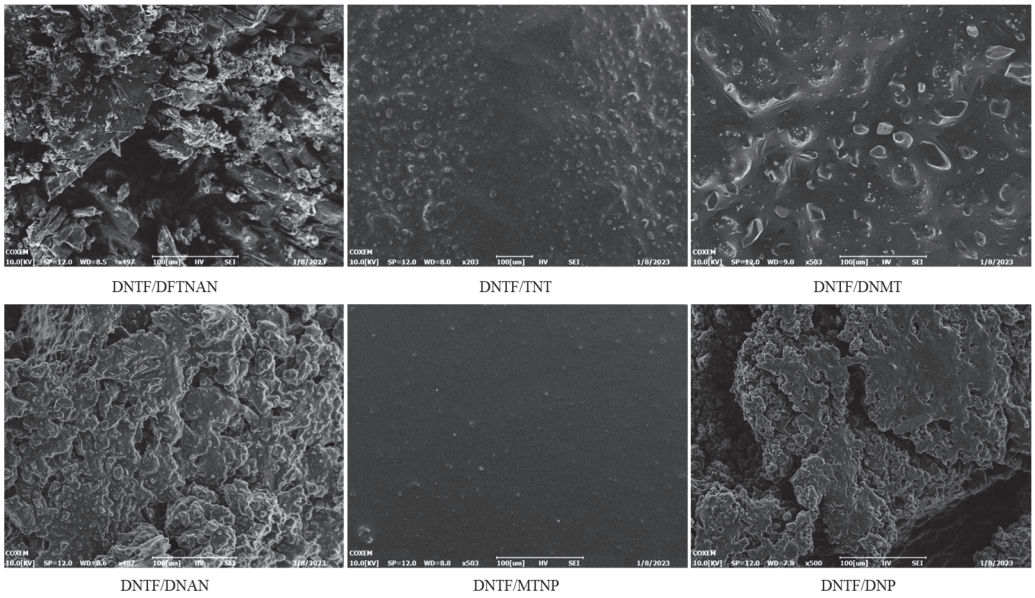

Figure 5. Morphology of the mixtures with DNTF and low-melting-point explosives (500 times).

4.2. DSC Analysis

The thermal degradation of explosives is a complex process that typically involves multiple mechanisms, triggered by similar activation barriers and occurring at close rates. Only one reaction will initiate decomposition and continue for a considerable period of time, especially in the case of crystals. One mechanism usually dominates the other reaction, and even when the two reactions start slightly later, they can switch at higher temperatures to become the main reaction. The differential thermal curves between DNTF and low-melting-point explosives are shown in Figure 6.

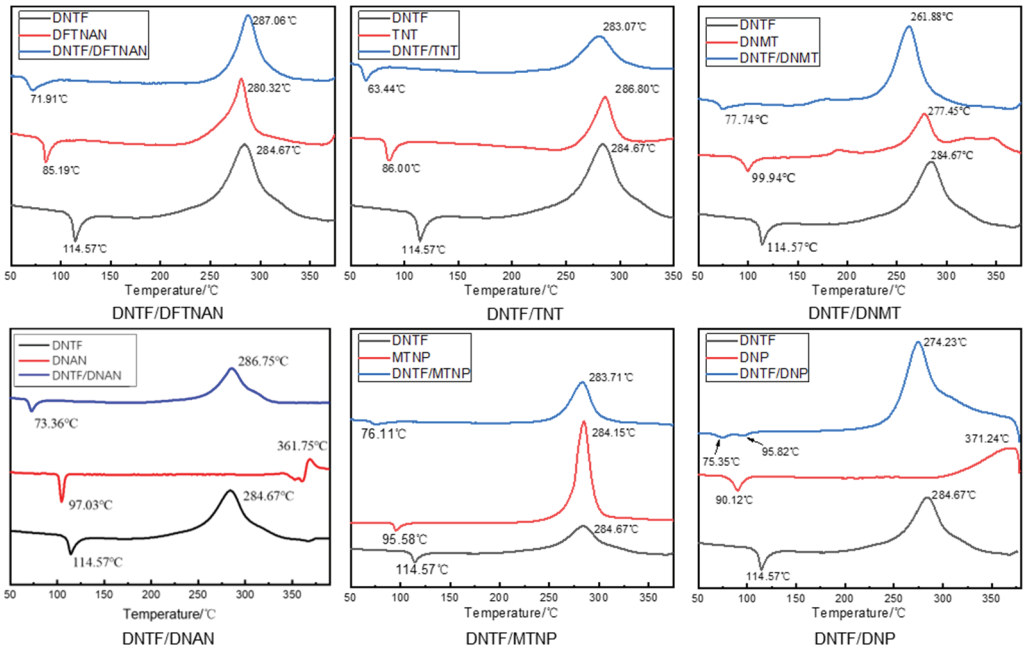

Figure 6. DSC curve of the mixtures with DNTF and low-melting-point explosives.

According to the DSC curve in Figure 6, the thermal decomposition process of DNTF and low-melting-point explosives is mainly divided into two stages: an endothermic melting stage and an exothermic decomposition stage. The DSC curve of DNTF/DFTNAN shows a single exothermic peak, and the initial decomposition temperature and thermal decomposition peak temperature are significantly higher than those of DNTF. After mixing DFTNAN and DNTF, DNTF and DFTNAN decompose almost simultaneously, and there is an exothermic peak in the DSC curve of the mixture. In the DNTF/DFTNAN mixed system, the peak decomposition temperature of DNTF/DFTNAN was 2.39 °C higher than that of the DNTF alone. According to the compatibility criteria, the mixed system of DNTF and DFTNAN can be considered compatible, and the compatibility evaluation is B. Similarly, the compatibility between DNTF explosives and other low-melting-point explosives was determined according to the ABCD compatibility criterion, and the discrimination results are listed in Table 3.

Table 3. Decomposition temperatures of binary systems obtained by DSC.

Binary System	Single System	Peak Temperature			
		Tp1 (°C)	Tp2 (°C)	ΔTp (°C)	Rating
DNTF/DFTNAN	DNTF	284.67	287.06	2.39	B
DNTF/TNT	DNTF	284.67	283.07	1.60	A
DNTF/DNMT	DNTF	284.67	261.88	22.79	D
DNTF/DNAN	DNTF	284.67	286.75	2.08	B
DNTF/MTNP	DNTF	284.67	283.71	0.96	A
DNTF/DNP	DNTF	284.67	274.23	10.44	C

Note: Binary system, DNTF/low-melting-point-explosive binary system; single system, DNTF single-energetic-material system; T_{p1}, maximum exothermic peak temperature of a single system; maximum exothermic peak temperature of mixture system; $\Delta T_p = \left|T_{p1} - T_{p2}\right|$.

After mixing TNT, MTNP, and DNTF, the exothermic decomposition peak temperature of the mixed system did not cause a significant shift compared to pure DNTF, and the temperature difference of the exothermic decomposition peak was less than 2 °C. The exothermic decomposition peak temperature of DNTF/DNAN and DNTF/DFTNAN mixed systems was slightly shifted compared to pure DNTF, while the exothermic decomposition peak temperature of DNTF/DNMT and DNTF/DNP mixed systems was significantly shifted compared to pure DNTF. Based on the above compatibility criteria, DNTF has good compatibility with most low-melting-point explosives, and the thermal decomposition peak temperature shift of the mixed system formed by melting and casting is relatively small. Based on the electron microscopy characterization results, DNTF has the best compatibility with MTNP, good compatibility with TNT, moderate compatibility with DNP and DNAN, and a slight deviation in morphology characterization and compatibility results between DNTF, DFTNAN, and DNMT.

4.3. Mechanical Sensitivity

The impact friction sensitivity test results of DNTF, low-melting-point explosives, and the mixed system of DNTF and low-melting-point explosives are listed in Table 4.

After mixing DNTF and low-melting-point explosives, the impact sensitivity of the mixed system is arranged in the following order: H_{50}(DNTF/DNAN) > H_{50} (DNTF/TNT) > H_{50}(DNTF/MTNP) > H_{50}(DNTF/DFTNAN) > H_{50}(DNTF/DNMT) > H_{50} (DNTF/DNMT) > H_{50} (DNTF/DNP). The order of the friction sensitivity of the DNTF/low-melting-point explosive mixed system is as follows: P (DNTF + TNT) > P (DNTF + DNAN) > P (DNTF/MTNP) > P (DNTF + DNP) > P (DNTF + DNMT) > P (DNTF + DFTNAN).

Combining the sensitivity test results of pure DNTF and pure low-melting-point explosives, the addition of DFTNAN, DNMT, MTNP, and DNP all improved the impact sensitivity of DNTF, while TNT and DNAN slightly decreased the impact sensitivity of DNTF. The friction sensitivity data show that the friction sensitivity of the DNTF and

low-melting-point explosive mixture system is reduced compared to pure DNTF, with the DNTF/TNT mixture system showing the most significant reduction in friction sensitivity. The results of the mechanical sensitivity data indicate that the addition of TNT and DNAN can effectively reduce the mechanical sensitivity of DNTF. For explosives such as DFTNAN, TNT, DNAN, and MTNP that have good compatibility with DNTF, the addition of low-melting-point explosives significantly reduces the friction sensitivity of DNTF explosives. The impact sensitivity of DNTF/TNT and DNTF/DNAN mixed systems is lower than that of pure DNTF, while the impact sensitivity of DNTF/DFTNAN and DNTF/MTNP mixed systems is improved.

Table 4. Summary of impact sensitivity and friction sensitivity results.

Sample (Ratio)	Friction Sensitivity	Impact Sensitivity
	P/%	H_{50}/cm
DNTF	100%	43.65
DFTNAN	0%	40.97
TNT	15%	≥100
DNMT	60%	92.7
DNAN	16%	≥100
MTNP	0%	≥100
DNP	32%	≥100
DNTF/DFTNAN	60%	39.80
DNTF/TNT	24%	46.67
DNTF/DNMT	52%	38.90
DNTF/DNAN	36%	47.86
DNTF/MTNP	40%	40.56
DNTF/DNP	44%	35.48

Combining the results of DNTF and low-melting-point explosive mechanical sensitivity, it can be found that the DNTF/TNT composite system has the most significant effect on reducing mechanical sensitivity. After the addition of TNT, the friction sensitivity of DNTF decreased by 76%, the drop height increased by 3.02 cm, and the impact sensitivity decreased. The impact sensitivity of pure DNTF explosives is not high, like HMX (H_{50} = 43.56 cm), but the high friction sensitivity of DNTF makes it susceptible to friction ignition and explosion, leading to detonation. The addition of TNT significantly reduces the friction sensitivity of DNTF, which helps improve the safety of DNTF explosives.

4.4. Binding Energy Calculation

Binding energy (E_{bind}) is defined as the amount of work required to pull each component of the system from "zero distance" to "infinity". E_{bind} is an important parameter to measure the size of the interaction force between different components in the composite system, and it can also predict the compatibility between different components. The higher the E_{bind} value, the more precise the combination between components in the composite system, the stronger the interaction force, the higher the thermodynamic stability of the system, and the more stable the formed structure. The mathematical expression is given in (2):

$$E_{bind} = -E_{inter} = -(E_{total} - E_{DNTF} - E_{LMPE}) \quad (2)$$

where E_{inter} is the interaction energy between the two components; E_{total} is the total energy of the system at equilibrium; and E_{DNTF} and E_{LMPE} are the energies of the remaining parts in the composite system after removing the respective components of DNTF and Layer 1, respectively.

Based on the MD simulation of the substituted models, the corrected binding energies Eb* are summarized in Table 5. The binding energy Eb* is a measure of the interaction strength of the components [29]. It might affect the structural stability of the cocrystal—

the larger the Eb* value, the more stable the cocrystal becomes—and provide a general evaluation for screening the preferred substitution pattern and molecular ratio.

Table 5. Corrected binding energy of the substituted models with different molecular molar ratios.

System	E_{total}/kJ·mol^{-1}	E_{DNTF}/kJ·mol^{-1}	E_{layer2}/kJ·mol^{-1}	E_{bind}/kJ·mol^{-1}
DNTF/DFTNAN	−3994.21	−686.26	−2212.49	1095.46
DNTF/TNT	−1321.95	2016.10	−2150.20	1187.85
DNTF/DNMT	−9630.89	−6611.40	−2186.12	813.37
DNTF/DNAN	−741.00	2511.64	−2080.46	1172.18
DNTF/MTNP	−7354.68	−4039.98	−2126.76	1187.94
DNTF/DNP	−1322.16	1886.79	−2202.72	1016.23

Note: E_{DNTF} and E_{LMPE} are the residual energy of DNTF and low-melting-point explosives in the mixed system, respectively. E_{bind} is the interaction energy between the two components. E_{total} is the total interaction energy.

The compatibility of the composite system was calculated by molecular dynamics simulation. According to the numerical results of the modified binding energy, it was found that the law is as follows: Eb * (DNTF/MTNP) > Eb * (DNTF/TNT) ≈ Eb * (DNTF/DNAN) > Eb * (DNTF/DFTNAN) > Eb * (DNTF/DNMT) > Eb * (DNTF/DNMT). The binding energy of DNTF with MTNP, TNT, and DNAN composite systems is relatively high, while the binding energy with DNMT is the lowest. Based on the compatibility between DNTF and the low-melting-point explosive composite system in Table 3, MTNP, TNT, DNAN, and DNTF have good compatibility. The binding energy of the three systems is higher than that of other low-melting-point-explosive systems, and the calculation law of binding energy is consistent with the DSC compatibility discrimination results.

At the same time, the binding energy of the composite system at 2000 K and 3000 K is calculated by MS, and the binding energy results with respect to 300 K temperature are presented in Tables 6–8.

Table 6. Corrected binding energy Eb* of the substituted models with different molecular molar ratios (300 K).

System	E_{total}/kJ·mol^{-1}	E_{DNTF}/kJ·mol^{-1}	E_{layer2}/kJ·mol^{-1}	E_{bind}/kJ·mol^{-1}
DNTF/DFTNAN	−3994.21	−686.26	−2212.49	1095.46
DNTF/TNT	−1321.95	2016.10	−2150.20	1187.85
DNTF/DNMT	−9640.82	−6365.79	−2461.84	813.19
DNTF/DNAN	−741.00	2511.64	−2080.46	1172.18
DNTF/DNP	−1332.17	1886.80	−2202.72	1016.25

Table 7. Corrected binding energy Eb* of the substituted models with different molecular molar ratios (2000 K).

System	E_{total}/kJ·mol^{-1}	E_{DNTF}/kJ·mol^{-1}	E_{LMPE}/kJ·mol^{-1}	E_{bind}/kJ·mol^{-1}
DNTF/DFTNAN	4656.87	3433.6	1293.33	70.06
DNTF/TNT	7988.16	6686.18	1389.42	87.44
DNTF/DNMT	−1002.00	−2225.50	1300.39	76.89
DNTF/DNAN	8653.11	7494.62	1279.60	121.11
DNTF/DNP	7733.31	6341.74	1454.05	62.48

Table 8. Corrected binding energy Eb* of the substituted models with different molecular molar ratios (3000 K).

System	E_{total}/kJ·mol^{-1}	E_{DNTF}/kJ·mol^{-1}	E_{LMPE}/kJ·mol^{-1}	E_{bind}/kJ·mol^{-1}
DNTF/DFTNAN	−1592.53	−1386.14	799.27	1005.66
DNTF/TNT	1442.12	1356.91	878.81	793.6
DNTF/DNMT	−4211.64	−4087.31	784.02	908.35
DNTF/DNAN	1479.18	1653.01	884.42	1058.25

The calculation results indicate that the binding energy between DNTF and DFTNAN, TNT, DNAN, and DNP systems is higher at a temperature of 300 K, while the binding energy between DNTF and DNMT systems is the smallest, which is consistent with the compatibility discrimination results. Under high-temperature conditions of 2000 and 3000 K, the interaction between DNTF and low-melting-point explosives is affected. A typical representative is TNT and DNAN, which have good compatibility with DNTF. The binding energy of the TNT system decreases with increasing temperature compared to other low-melting-point explosives, while the binding energy of the DNTF/DNAN composite system is higher than that of other low-melting-point-explosive systems. As for the DNMT with the worst compatibility, the binding energy of the DNTF/DNMT system at 2000 K is higher than that of the DFTNAN system with better compatibility, and the binding energy of the DNMT system at 3000 K is higher than that of the TNT system with better compatibility.

4.5. Cohesive Energy Density

Cohesive energy density (CED) is a parameter used to measure intermolecular forces, which is the energy required per unit volume of 1 mole of a condensate to overcome intermolecular forces and become gaseous [30]. It characterizes the energy required for condensed state gasification, which in MD simulation is the sum of van der Waals energy and electrostatic energy, i.e., the non-bonding energy between molecules. The lower the CED value of the explosive, the less energy is required for the explosive to undergo a phase transition when heated, which indirectly indicates that the explosive is more sensitive to heat under the same conditions. Based on the MD simulation calculation of the cohesive energy density, the results are shown in Table 9.

Table 9. Cohesive energy density of the substituted models with molecular molar ratios.

Model	CED (Kcal/cm^3)	Evdw (Kcal/cm^3)	Eelectrostatic (Kcal/cm^3)
DNTF/MTNP	10.894	3.7936	6.9849
DNTF/DNAN	7.8535	3.7790	3.9722
DNTF/TNT	8.9443	3.5996	5.2394
DNTF/DNP	8.6095	4.0168	4.6480
DNTF/DNMT	7.5919	3.8999	3.6920
DNTF/DFTNAN	9.7717	3.6557	6.0040

Note: CED = E_{vdw} + $E_{electrostatic}$.

According to the calculation results in Table 9, the cohesive energy density is as follows: DNTF/MTNP > DNTF/DFTNAN > DNTF/TNT > DNTF/DNP > DNTF/DNAN > DNTF/DNMT. The cohesive energy density of the MTNP/DNTF composite system is the highest, indicating that the combination of MTNP and DNTF requires the highest energy to undergo phase transition when heated compared to other mixed systems and is the least sensitive to heat under the same conditions. However, the DNTF/DNMT system requires the least energy to undergo a phase transition when heated and is the most heat sensitive under the same conditions. The cohesive energy density of the TNT composite system, which is consistent with the compatibility discrimination results of MTNP, is lower than that of the DFTNAN hybrid system with moderate compatibility. The compatibility discrimination results of DNAN and DFTNAN are consistent, while the cohesive energy density value of the DNTF/DNAN system is lower than that of DNP with poor compatibility and is close to the CED value of the DNMT system, with the worst compatibility.

5. Conclusions

By analyzing the comprehensive performance of DNTF explosive, it was confirmed that its mechanical and thermal sensitivity are relatively high, which affects its promotion and use in the ammunition field. In response to this issue, some low-melting-point explosives and DNTF explosives were selected for mixed preparation in this paper, and

their morphology, thermal performance, and mechanical sensitivity were characterized and tested. In addition, molecular dynamics was used to simulate and analyze the binding energy of the mixture. Based on the above research work, some conclusions have been drawn, as follows:

(1) Combining electron microscopic characterization and DSC analysis, it can be concluded that DNTF has good compatibility with most low-melting-point explosives, and the peak temperature change of the composite system formed by melting casting is not significant. Among them, DNTF has the best compatibility with MTNP, TNT, DNAN, and DFTNAN, moderate compatibility with DNP, and the worst compatibility with DNMT.

(2) Comparing DNTF with several low-melting-point-explosive systems, it can be found that the combination of DNTF and TNT has the most significant effect on reducing mechanical sensitivity. The friction sensitivity decreased by 76%, the drop height increased by 3.02 cm, and the impact sensitivity decreased. Due to the high friction sensitivity of DNTF, it is prone to friction ignition and explosion, resulting in detonation. The addition of TNT significantly reduces the friction sensitivity of DNTF, helping to improve the safety of DNTF explosives.

(3) The simulation results of binding energy are almost in agreement with the compatibility test, indicating that many explosives with good compatibility can be screened by calculating the binding energy. DFTNAN and MTNP are more stable than DNTF and have stronger intermolecular forces when combined with DNTF. The intermolecular force generated by mixing other low-melting-point explosives with DNTF is lesser than that of DNTF. The MTNP/DNTF composite system has the highest cohesive energy density and requires the highest amount of energy to undergo phase transition when heated compared to other mixed systems, making it the least sensitive to heat. However, the DNTF/DNMT system has the lowest cohesive energy density and is the most sensitive to heat.

Author Contributions: Conceptualization, J.Y. (Junming Yuan); methodology, J.Y. (Junming Yuan); validation, R.H., X.X., J.W. (Jinying Wang), and Q.Y.; formal analysis, J.W. (Jinying Wang), J.Y. (Junming Yuan), and T.H.; data curation, J.Y. (Jia Yang) and J.W. (Jing Wang); writing—original draft preparation, R.H., X.X., and J.Y. (Jia Yang); writing—review and editing, J.Y. (Junming Yuan) and R.H.; visualization, R.H. and J.W. (Jing Wang) All authors have read and agreed to the published version of the manuscript.

Funding: This research was funded by Robust Munitions Center, CAEP, grant number RMC2014B03 and the Open Cooperative Innovation Fund Project of Xi'an Institute of Modern Chemistry, grant number 204J20190387.

Institutional Review Board Statement: This project has been approved by North University of China, with approval number 1912200039HX.

Informed Consent Statement: Informed consent was obtained from all subjects involved in the study.

Data Availability Statement: Data are contained within the article.

Conflicts of Interest: The authors declare no conflicts of interest.

References

1. Wang, Q.H.; Zhang, Y.A.; Jin, D.Y. Energy and castability of DNTF explosive. *Chin. J. Explos. Propellants* **2004**, *27*, 14–16.
2. Zhao, F.Q.; Chen, P.; Hu, R.Z.; Yang, L.; Zhang, Z.Z.; Zhou, Y.S.; Yang, X.W.; Gao, Y.; Gao, S.L.; Shi, Q.Z. Thermochemical properties and non-isothermal decomposition reaction kinetics of 3,4-dinitrofurazanfuroxan (DNTF). *J. Hazard. Mater.* **2004**, *113*, 71.
3. Li, Y.; Yuan, J.M.; Zhao, W.; Qu, Y.; Xing, X.W.; Meng, J.W.; Liu, Y.C. Application and Development of 3,4-Bis(3-nitrofurazan-4-yl)furoxan (DNTF). *Russ. J. Gen. Chem.* **2021**, *91*, 445–455. [CrossRef]
4. Zhan, C.; Shu, Y.; Wang, X.; Zhao, X. A Computational Investigation of a Novel Explosive: DNTF. *Cent. Eur. J. Energ. Mater.* **2005**, *2*, 45–53.
5. Wang, Q. Properties of DNTF-based melt-cast explosives. *Chin. J. Explos. Propellants* **2003**, *26*, 57–59.

6. Xiong, X.F.; Wang, H.; Gao, J.; Luo, Y.; Wang, H. Metal accelerating ability of DNTF-based melt-cast explosive. *Chin. J. Explos. Propellants* **2011**, *34*, 32–34.
7. Wang, Q. Overview of carrier explosive for melt-cast composite explosive. *Chin. J. Explos. Propellants* **2011**, *34*, 25–28.
8. Hang, G.Y.; Lu, C.; Wang, J.T.; Xue, H.J.; Wang, T.; Yu, W.L.; Shen, H.M. Theoretical Prediction on Properties of 3,4-Bisnitrofurazanfuroxan (DNTF) Crystal and its Polymer Bonded Explosives (PBXs) Through Molecular Dynamics (MD) Simulation. *J. Mol. Model.* **2023**, *29*, 169. [CrossRef]
9. Zheng, W.; Wang, J.N.; Ren, X.N.; Zhang, L.; Zhou, Y. An Investigation on Thermal Decomposition of DNTF-CMDB Propellants. *Propellants Explos. Pyrotech. Int. J. Deal. Sci. Technol. Asp. Energ. Mater.* **2007**, *32*, 520–524. [CrossRef]
10. Li, L.L.; Wang, J.N.; Liu, Z.R. Effects of DNTF contents on dynamic mechanical properties of modified double-base propellant. *Chin. J. Energ. Mater.* **2010**, *18*, 174–179.
11. Zheng, W.; Wang, J.N. Review on 3,4-bisnitrofurazanfuroxan (DNTF). *Chin. J. Energ. Mater.* **2011**, *14*, 463–466.
12. Sinditskii, V.P.; Burzhava, A.V.; Sheremetev, A.B.; Aleksandrova, N.S. Thermal and Combustion Properties of 3,4-Bis(3-nitrofurazan-4-yl)furoxan (DNTF). *Propellants Explos. Pyrotech.* **2012**, *37*, 575–580. [CrossRef]
13. Zhang, G.; Jin, S.; Li, L.; Li, Y.; Li, Z.; Wang, D.; Zhang, B.; Jing, B.; Shu, Q. Thermal stability assessment of 3,4-bis(3-nitrofurazan-4-yl)furoxan (DNTF) by accelerating rate calorimeter (ARC). *J. Therm. Anal. Calorim.* **2016**, *126*, 1185–1190. [CrossRef]
14. Hu, H.X.; Zhang, Z.Z.; Zhao, F.Q.; Xiao, C.; Wang, Q.H.; Yuan, B.H. A study on the properties and application of high energy density material DNTF. *Acta Armamentarii* **2004**, *25*, 155–158.
15. Ma, Q.; Shu, Y.J.; Luo, G.; Wen, M.P.; Gao, D.-Y.; Zheng, B.-H.; Shu, Y.-J. Toughening and Elasticizing Route of TNT Based Melt Cast Explosives. *Chin. J. Energ. Mater.* **2012**, *20*, 618–629.
16. Qin, Y.; Yuan, J.M.; Sun, H.; Liu, Y.; Zhou, H.; Wu, R.; Chen, J.; Li, X. Experiment and Molecular Dynamic Simulation on Performance of 3,4-Bis(3-nitrofurazan-4-yl)furoxan (DNTF) Crystals Coated with Energetic Binder GAP. *Crystals* **2023**, *13*, 327. [CrossRef]
17. Gao, H.X.; Zhao, F.Q.; Li, S.W.; Luo, Y.; Zhang, Z.; Zhong, Y.; Zhang, R.; Gao, Y. Physico-chemical properties of 3,4-dinitrofurazanfuroxan (DNTF) and its effect on combustion properties of smokeless propellant. In Proceedings of the 2007 International Autumn Seminar on Propellants Explosives and Pyrotechnics, Xi'an, China, 23–26 October 2007; pp. 606–609.
18. Li, X.; Wang, B.L.; Lin, Q.H.; Chen, L.P. Compatibility study of DNTF with some insensitive energetic materials and inert materials. *J. Energ. Mater.* **2016**, *34*, 409–415. [CrossRef]
19. Sun, S.; Zhang, H.; Xu, J.; Wang, S.; Zhu, C.; Wang, H.; Ding, R.; Yu, Z.; Sun, J. Two novel melt-cast cocrystal explosives based on 2, 4-dinitroanisole with significantly decreased melting point. *Cryst. Growth Des.* **2019**, *19*, 6826–6830. [CrossRef]
20. Gao, J.; Wang, H.; Jin, D.; Guo, X.; Wang, W. Safety of DNAN/DNTF Binary Eutectic under Thermal Stimulation and Mechanical Stimulation. *Explos. Mater.* **2021**, *50*, 35–39.
21. Shao, H.Y.; Ren, X.N.; Liu, Z.R.; Zhang, X. Ternary phase diagrams of DNTF and TNAZ and their eutectics. *J. Therm. Anal. Calorim.* **2011**, *103*, 617–623. [CrossRef]
22. Meng, L.L.; Qi, X.F.; Wang, J.N. Molecular dynamics simulation and experimental study of DNTF on plasticizing properties of NC. *Chin. J. Explos. Propellants* **2015**, *38*, 86–89.
23. Pang, W.; Wang, K.; DeLuca, L.T.; Trache, D.; Fan, X.; Li, J.; Li, H. Experiments and simulations on interactions between 2,3-bis(hydroxymethyl)-2, 3-dinitro-1, 4-butanediol tetranitrate (DNTN) with some energetic components and inert materials. *FirePhysChem* **2021**, *1*, 166–173. [CrossRef]
24. Huang, H.; Shi, Y.; Yang, J.; Li, Y.B. Compatibility Study of dihydroxylammonium 5,5′-Bistetrazole-1,1′-diolate (TKX-50) with some energetic materials and inert materials. *J. Energ. Mater.* **2015**, *33*, 66–72. [CrossRef]
25. Pang, W.; Fan, X.; Xue, Y.; Xu, H.; Zhang, W.; Zhang, X.; Li, Y.; Li, Y.; Shi, X. Study on the compatibility of tetraethylammonium decahydrodecaborate (BHN) with some energetic components and inert materials. *Propellants Explos. Pyrotech.* **2013**, *38*, 278–285. [CrossRef]
26. Yan, Q.-L.; Li, X.-J.; La-Ying, Z.; Ji-Zhen, L.; Hong-Li, L.; Zi-Ru, L. Compatibility study of trans-1,4,5,8-tetranitro1,4,5,8-tetraazadecalin (TNAD) with some energetic components and inert materials. *J. Hazard. Mater.* **2008**, *34*, 529–534. [CrossRef]
27. Isayev, O.; Gorb, L.; Qasim, M.; Leszczynski, J. Ab initio molecular dynamics study on the initial chemical events in nitramines: Thermal decomposition of CL-20. *J. Phys. Chem. B* **2008**, *112*, 11005–11013. [CrossRef]
28. Biswas, S.; Wong, B.M. High-temperature decomposition of diisopropyl methylphosphonate on alumina: Mechanistic predictions from ab initio molecular dynamics. *J. Phys. Chem. C* **2021**, *125*, 21922–21932. [CrossRef]
29. Li, Y.X.; Chen, S.S.; Ren, F.D.; Jin, S.-H. Theoretical Insight into the Influence of Molecular Ratio on the Stability, Mechanical Property, Solvent Effect and Cooperativity Effect of HMX/DMI Cocrystal Explosive. *Chin. J. Struct. Chem.* **2017**, *36*, 13.
30. Song, X.Y.; Xing, X.L.; Zhao, S.X.; Ju, X.H. Molecular dynamics simulation on TKX-50/fluoropolymer. *Model. Simul. Mater. Sci. Eng.* **2020**, *28*, 015004. [CrossRef]

molecules

MDPI

Article

Microscopic Understanding of Interfacial Performance and Antifoaming Mechanism of REP Type Block Polyether Nonionic Surfactants

Yifei Zhao, Chunlong Xue, Deluo Ji, Weiqian Gong, Yue Liu and Ying Li *

Key Lab. of Colloid and Interface Chemistry of State Education Ministry, School of Chemistry and Chemical Engineering, Shandong University, Jinan 250100, China
* Correspondence: yingli@sdu.edu.cn

Abstract: In many practical applications involving surfactants, achieving defoaming without affecting interfacial activity is a challenge. In this study, the antifoaming performance of REP-type block polymer nonionic surfactant C12EOmPOn was determined, and molecular dynamics simulation method was employed to investigate the molecular behaviors of surfactants at a gas/water interface, the detailed arrangement information of the different structural segments of the surfactant molecules and the inter-/intra-interactions between all the structural motifs in the interfacial layer were analyzed systematically, by which the antifoaming mechanisms of the surfactants were revealed. The results show that the EO and PO groups of REP-type polyether molecules are located in the aqueous phase near the interface, and the hydrophobic tails distribute separately, lying almost flat on the gas/water interface. The interaction between the same groups of EOs and POs is significantly stronger than with water. REP block polyethers with high polymerization degrees of EO and PO are more inclined to overlap into dense layers, resulting in the formation of aggregates resembling "oil lenses" spreading on the gas/water interface, which exerts a stronger antifoaming effect. This study provides a smart approach to obtaining efficient antifoaming performance at room temperature without adding other antifoam ingredients.

Keywords: propylene oxide; ethylene oxide; antifoam; interfacial molecular behaviors; molecular dynamics simulation; foam properties

1. Introduction

The application of foam is extensive in both daily life and industrial production, encompassing fields such as foam fire suppression, mineral flotation, enhanced oil recovery, detergents, and cosmetics [1–4]. But in many practical processes, foam generation is a double-edged sword; in some cases, the formation of foams can be harmful [5–7]. For instance, the presence of excessive foam can have detrimental effects on product quality, impede production efficiency, disrupt process operations, and potentially cause equipment damage, thereby posing safety hazards [5,8,9]. In the field of detergents, producing abundant foam used to be a major requirement for showing product performance in the hand-washing process. In the present day, the utilization of low-foam detergents is more favored, which can effectively shorten rinsing time, resulting in substantial water and electricity conservation while also reducing sewage discharge [10–12]. On many occasions like this, the achievement of effective antifoaming while maintaining the interfacial activity of the surfactant systems is of great importance, which is still a challenge.

The antifoaming phenomena are intrinsically related to defoaming. Basically, defoamers are utilized to destroy existing foam, while antifoamers are used to prevent foam generation [13]. Antifoamers can act as defoamers, while not all defoamers have the ability to prevent foaming. The two effects could be intersected in many situations, and

effective applications of both effects need to be based on a clear understanding of the mechanisms [14], which are necessary to be further extended.

The currently used defoaming approaches can be broadly classified into two categories: physical and chemical methods. The physical methods mainly involve applying external forces to alter the physical states of the formed foam and cause its rupture, such as mechanical stirring, ultrasonic treatment, electrostatic action, and thermal treatment. [8,9,15,16]. The chemical methods typically employ chemical additives as defoamers, which has become the most commonly employed approach in modern industrial productions due to its advantages, such as rapid defoaming, prolonged duration, and cost-effectiveness [9]. Physical defoaming methods are hard to use in antifoaming. While most of the currently employed defoamers include mineral oil, fatty acids, fatty alcohols, surfactants, silicone compounds (silicone oil or polysiloxane), solid hydrophobic particles, etc. [6,17–19], might be antifoamfers, though the mechanisms of different types of defoamers are quite different. Reducing the solubility of surfactants is the most commonly used defoaming category. For example, the addition of oppositely charged electrolytes to anionic surfactant systems was demonstrated, in certain studies, to result in foam rupture [20,21]. Solid particles and oil droplets could exhibit a defoaming effect through a bridging-stretching mechanism, the spreading-fluid entrainment mechanism, and the spreading-wave generation mechanism [9,17,22,23].

In all the possible methods, the approaches only using surfactants without the need for additional antifoaming ingredients are more expected, while it is also very difficult to achieve and control. For example, the combination of cationic and anionic surfactants can lead to a defoaming effect by means of precipitation or phase separation resulting from the electrostatic interactions between the head groups [24,25], while the interfacial activity would be greatly reduced and even disappeared. Nonionic surfactants could exhibit defoaming properties at high temperatures above their cloud point; the condensed phase formed from the insoluble surfactants acts as oil droplets bridged onto the foam film, facilitating its defoaming action corresponding to temperature rising [26–28]. Maintaining the interfacial activity of the surfactant systems while inhibiting its foamability is a tricky problem and a big challenge, especially at room temperature.

In recent years, a new REP-type of block polyether nonionic surfactant has been developed. REP-type block polyethers are a class of polymers with epoxy structure, such as repeated units of ethylene oxide (EO) or propylene oxide (PO) groups, synthesized by polymerization reaction triggered by initiators, and their molecular structure is RO-$(EO)_x$-$(PO)_y$-H, where R stands for hydrophobic alkyl chain [29,30]. They have been employed as antifoamers in detergent formulations, showing many advantages, such as well-regulated molecular structure, the absence of precipitation, and cost-effectiveness [31]. Its capabilities in emulsification and solubilization processes also attracted some attention [32,33]. However, the related microscopic-level mechanisms are scarce, and their effective application is limited. Understanding the structure–performance relationship of such surfactants is meaningful for further optimization and the development of efficient antifoaming approaches.

In this paper, the equilibrium and dynamic surface activities and foam properties of pure REP-type nonionic surfactants and the compound systems with anionic surfactant sodium dodecyl sulfate (SDS) were experimentally determined, and molecular dynamic simulations were employed to elucidate the behavior of the surfactant molecules at the gas/water interface. The excellent foamability of SDS can introduce obvious differences in foam properties to the experimental results of the composite system. By analyzing the tilt angle of each component towards the z-axis, the hydrogen bonds between EO/PO chains and water, examining the radial distribution function, and investigating intermolecular interactions among different groups, a comprehensive understanding of the arrangement and aggregation behavior of REP-type polyether molecules at the gas/water interface was provided, by which the antifoaming mechanisms were analyzed. A common nonionic surfactant, AEO-9, with similar hydrophobic tails, was used as a reference. This work

might provide a theoretical basis and guidance for the design and application of low foam systems with high surface activity.

2. Results and Discussion

2.1. Surface Activity and Foaming Properties of REP Type Block Polyether Nonionic Surfactants

The equilibrium surface tension curves of the three nonionic surfactants, AEO-9, C12E5P4, and C12E14P8, are shown in Figure 1a. The equilibrium surface activity parameters, such as the maximum surface excess (Γ_{max}) and the minimum area per molecule (A_{min}) of surfactant at the air–water interface, are calculated according to Equations (1) and (2), and these parameters are shown in Table 1.

$$\Gamma_{max} = -\frac{1}{2.303nRT}\left(\frac{d\gamma}{dlgc}\right)_T \quad (1)$$

$$A_{min} = \frac{1}{N_A\Gamma_{max}} \quad (2)$$

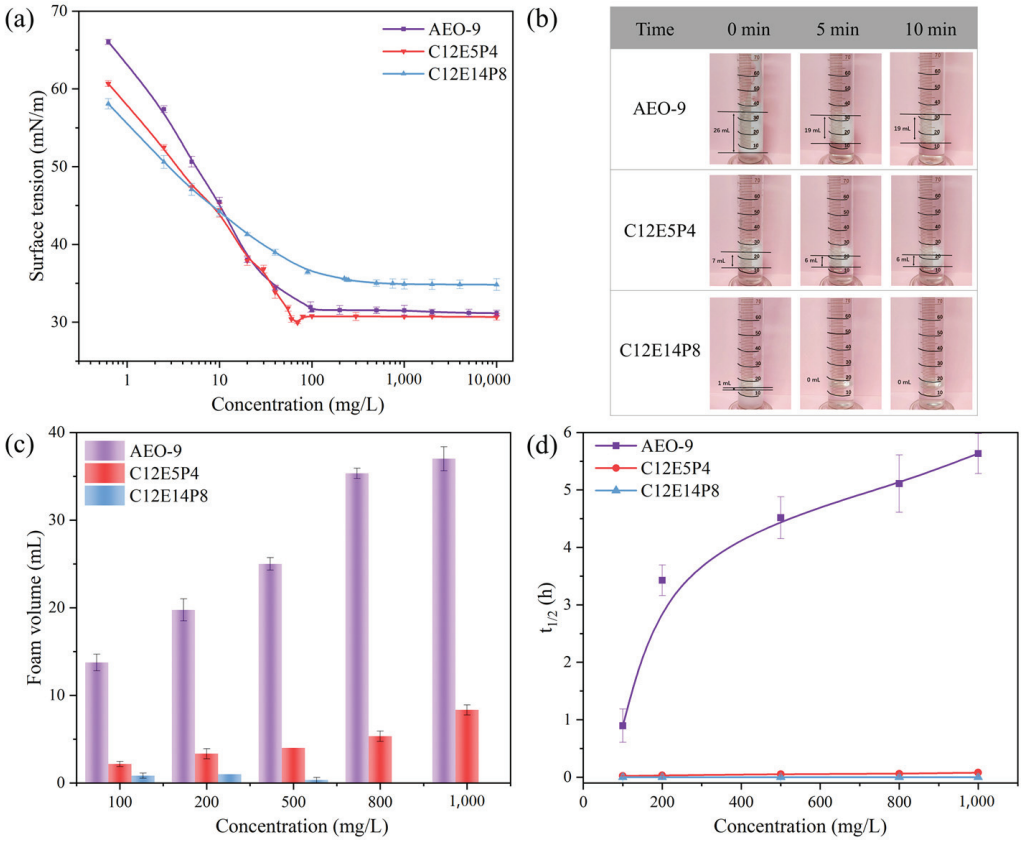

Figure 1. The surface activity and foam properties of AEO-9, C12E5P4, and C12E14P8 solutions. (**a**) The variation of equilibrium surface tension as a function of surfactant concentration at 298 K. (**b**) The photos of foam column taken at different times after foam generation at 298 K. The concentration of surfactant is 500 mg/L. (**c**) Foaming ability of different types of surfactants represented by the initial foam volume at 298 K. (**d**) Foam stability of different types of surfactants represented by foam half-life time $t_{1/2}$ at 298 K.

According to the results in Figure 1a and Table 1, AEO-9 and C12E5P4 have similar γ_{CMC} and CMC. The structural difference between AEO-9 and C12E5P4 is not much, so it is reasonable their surface activity is similar.

Table 1. Values of critical micelle concentration (CMC), equilibrium surface tension at CMC (γ_{CMC}), surface excess (Γ_{max}), and minimum area per molecule (A_{min}) for surfactant AEO-9, C12E5P4, and C12E14P8 at 298 K.

Surfactant	CMC (mg/L)	γ_{CMC} (mN/m)	Γ_{max} (μmol/m^2)	A_{min} (nm^2)
AEO-9	94.64	31.54	2.660	0.63
C12E5P4	63.46	30.77	2.605	0.64
C12E14P8	246.69	34.85	1.190	1.40

Generally speaking, foam properties of surfactants are closely related to surface activity [25]. It can be seen from the results in Figure 1b–d that there is a significant difference in the foaming capacity and foam stability between AEO-9 and C12E5P4. The AEO-9 exhibits excellent foam stabilization capability, whereas the foam ability of C12E5P4 is low, and the generated foam bursts rapidly. It indicates that the introduction of four propylene oxide groups in the C12E5P4-replacing EO groups causes significant differences in foam properties, which is very interesting and provides perfect comparative systems to explore the influence of interfacial behavior of surfactants with different molecular structures on foam properties, which is further investigated in the later section.

Comparing the two REP-type nonionic surfactants, it can be observed that C12E14P8 exhibits a little larger CMC and higher γ_{CMC} compared to C12E5P4 and AEO-9, while the Γ_{max} is much larger and A_{min} is much smaller. Under the same surfactant concentration, the foaming ability and foam stability of C12E14P8 are far below AEO-9 and C12E5P4, showing strong antifoaming performance. The results demonstrate that an increase in the degree of polymerization positively impacts the antifoaming effect of REP-type nonionic surfactants.

According to the above results, it is evident that REP-type nonionic surfactants have the potential to be used as antifoamers. For the purpose of understanding the mechanisms clearly, the adsorption kinetics of the surfactants are experimentally determined, and the interfacial molecular behaviors are investigated by molecular dynamic simulations.

2.2. Dynamic Surface Activity of REP Type Block Polyether Nonionic Surfactants

The time-dependent dynamic surface tension of AEO-9, C12E5P4, and C12E14P8 solutions under identical concentrations of 500 mg/L were measured, as shown in Figure 2a. The adsorption kinetics of the surfactants were analyzed using a model proposed by Rosen et al. [34].

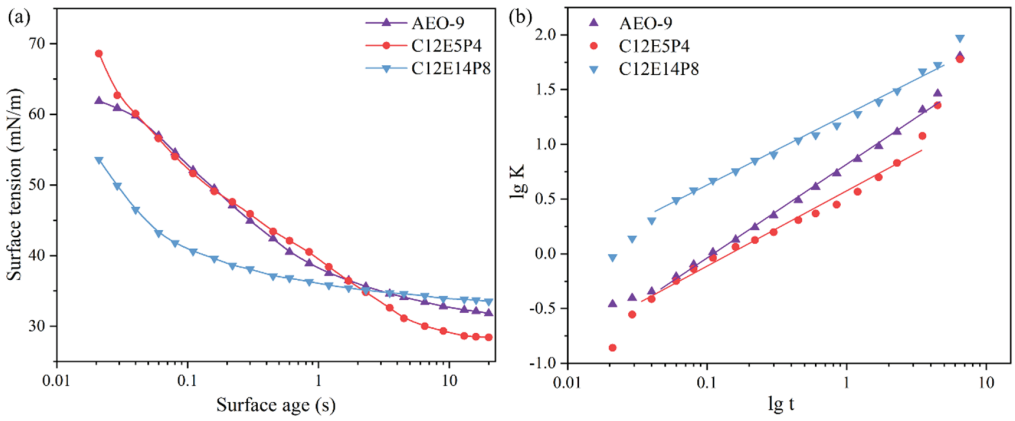

Figure 2. (**a**) Dynamic surface tension of samples under concentration of 500 mg/L at 298 K. (**b**) Dynamic surface tension parameters lgK as function of lgt for AEO-9, C12E5P4, and C12E14P8 at 298 K.

The dynamic surface tension curves of the two nonionic surfactants, AEO-9 and C12E5P4, exhibit similar trends at this concentration, as depicted in Figure 2a, but are

different from that of C12E14P8. The interpretation of the dynamic surface tension data are facilitated using the empirical equation proposed by Rosen et al. [35]:

$$\frac{\gamma_0 - \gamma_t}{\gamma_t - \gamma_m} = \left(\frac{t}{t^*}\right)^n \tag{3}$$

The surface tension of the solvent is denoted as γ_0, while the surface tension of the solution at time t is represented by γ_t. The surface tension of the solution at equilibrium is expressed as γ_m. The constant n quantifies the surfactant's tendency to diffuse into the adsorbed layer. t* denotes the time required to reach half of the intermediate equilibrium value Π (Π = $\gamma_0 - \gamma_t$). Equation (4) is derived through a logarithmic transformation of Equation (3) [35]:

$$lg\frac{\gamma_0 - \gamma_t}{\gamma_t - \gamma_m} = nlgt - nlgt^* \tag{4}$$

The adsorption energy of the adsorption process is mainly reflected by −nlgt*. The smaller the adsorption energy, the smaller t*, reflecting that the surfactant molecules are more easily adsorbed to the interface [36]. Equation (4) simplifies lg[($\gamma_0 - \gamma_t$)/($\gamma_t - \gamma_m$)] to lgK, establishing a linear relationship with lgt as the independent variable and lgK as the dependent variable. Thus, the slope of the linear equation represents the constant n in Rosen's formula, and the intercept represents −nlgt*.

$R_{1/2}$ represents the rate at which the surface tension in the rapid descent zone drops at time t* [35]:

$$R_{1/2} = \frac{\gamma_0 - \gamma_m}{2t^*} \tag{5}$$

The faster the surface tension decreases, the greater the $R_{1/2}$ value. The calculated values of n, t*, and $R_{1/2}$ are shown in Table 2.

Table 2. Dynamic surface tension parameters of AEO-9, C12E5P4, and C12E14P8 under concentration of 500 mg/L at 298 K.

Surfactant	n	t* (s)	t_i (s)	t_m (s)	$R_{1/2}$ (mN m^{-1} s^{-1})
AEO-9	0.824	0.106	6.47×10^{-3}	1.72	185.6
C12E5P4	0.668	0.152	4.83×10^{-3}	4.75	140.8
C12E14P8	0.652	0.012	3.40×10^{-4}	0.40	1643.7

The t* of C12E14P8 is the smallest at the same concentration, indicating a lower adsorption barrier and stronger adsorption tendency. The time required for the surfactant molecules to diffuse from the bulk solution to reach the surface is the shortest and could reach an intermediate equilibrium state faster. A smaller value of n corresponds to a stronger diffusion trend. Comparing the parameters of these three nonionic surfactants reveals that, at this concentration, REP-type polyether exhibits a stronger diffusion trend than AEO-9, while C12E14P8 showed even stronger diffusion trends than C12E5P4, which suggests that introducing more propylene oxide groups facilitate the increase in the diffusion and interfacial adsorption of the nonionic surfactant molecules in aqueous solutions. Combined with the foam performance, it can be considered that the diffusion of REP-type polyether nonionic surfactant in the bulk phase and the adsorption on the gas/water interface has a certain relationship with the foam inhibition performance.

2.3. Molecular Behavior of REP Type Block Polyether Nonionic Surfactants at Gas/Water Interface

A comparative analysis of molecular behaviors of REP nonionic surfactants at the gas/water interface in foam films was conducted using molecular dynamic simulations. The equilibrium configurations of foam films with different mass concentrations of C12E5P4 and AEO-9 are shown in Figure 3. In the snapshot containing a smaller number of molecules, the arrangement behavior of single characteristics could be observed, while in the snapshots

containing a larger number of molecules, the effect of inter-molecular interaction on the molecular behaviors could be noticed.

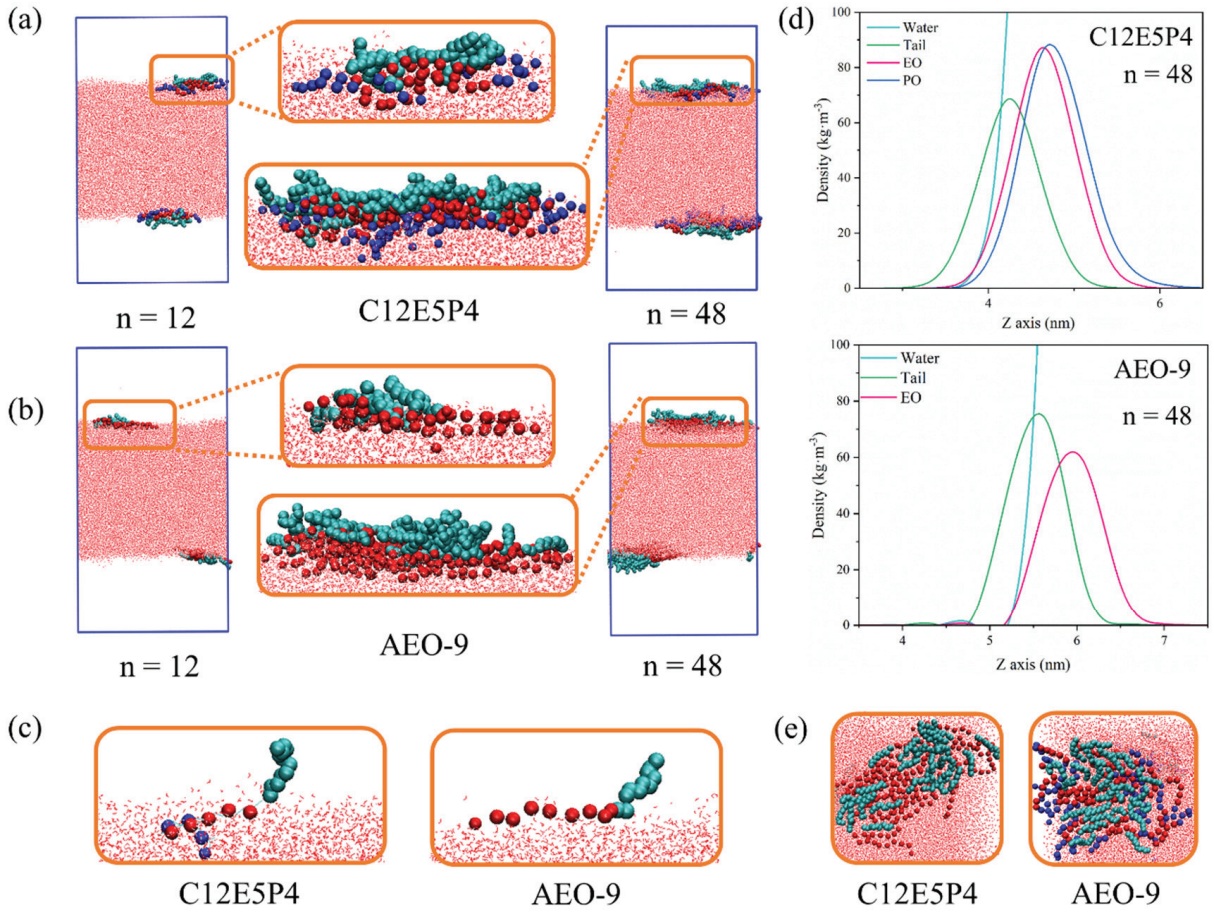

Figure 3. The side views of MD-simulated equilibrium configurations of (**a**) C12E5P4 and (**b**) AEO-9 with different molecular numbers at 298 K. (**c**) Conformation of one C12E5P4 molecule and one AEO-9 molecule at the gas/water interface extracted from (**a**,**b**). (**d**) Density of carbon chain and head groups of C12E5P4 and AEO-9. (**e**) The top views of MD simulated equilibrium configurations of C12E5P4 and AEO-9 (n = 48). (The green ball represents the C atom on the tail chain of hydrophobic carbon; the red ball represents the O atom in ethylene oxide groups; the blue balls represent the O atoms in propylene oxide groups).

Figure 3a–c show the side view of the MD simulation snapshots of C12E5P4 and AEO-9. The density distribution of the head group perpendicular to the gas/water interface plane along the z-axis was calculated to gain further insights into the structural properties of the head group, as shown in Figure 3d. It could be found that C12E5P4 and AEO-9 molecules both adsorb on the interface with their hydrophobic carbon tail chains extending into the gas phase, and EO chain segments are located near the interface in the aqueous phase, within a depth of 2 nm for both AEO-9 and C12E5P4. When the number of molecules increased, the EO groups of C12E5P4 and AEO-9 both tended to aggregate due to the strong interactions between EO groups. It was very interesting that the PO group was commonly considered hydrophobic, while the PO chains of C12E5P4 are located near the interface in the aqueous phase, too. Because C12E5P4 is terminated by hydroxyl (-OH), which is more hydrophilic than the EO group, the PO chain is pulled a little deeper into the water phase than the EO groups. Another detail that needs to be mentioned is that propylene oxide has a branched methyl group (-CH_3), resulting in significant steric hindrance that impedes aggregation between PO groups, so the PO segments aggregate looser than EO groups, so

C12E5P4 take up more space on the interface than AEO-9 when the number of molecules on the interface increases, which coincide with the results in Table 1.

The tilt angles (of which the definition was shown in Figure 4a) of the carbon chain, EO chain, and PO chain of C12E5P4 with z-axes were calculated to describe more clearly the conformation of REP-type nonionic surfactants on the interface, as shown in Figure 4b. θ_0 is relatively chaotic and disordered along the direction of the gas/water interface, ranging from 50° to 90°; even when the concentration increased, θ_0 did not change even a little, which is obviously different from the commonly excellent conformation of the hydrophobic tails of the regular surfactants. θ_1 is kept at approximately 90°; the increase in the concentration of surfactant molecules leads to a gradual reorientation of θ_1, becoming a little more perpendicular to the z-axis. θ_2 undergoes similar changes to θ_1. It could be concluded that the EO and PO segments eventually remain parallel to the gas/water interface, lying almost flat, though θ_2 exhibits a little wider distribution range. The EO and PO chains exhibit the stretching state parallelly to the interface and occupy a large interfacial area, so the hydrophobic carbon tails could only lie flat without the opportunity to interact with each other, and that is why the stability of C12E5P4 foam decreased, as shown in Figure 1.

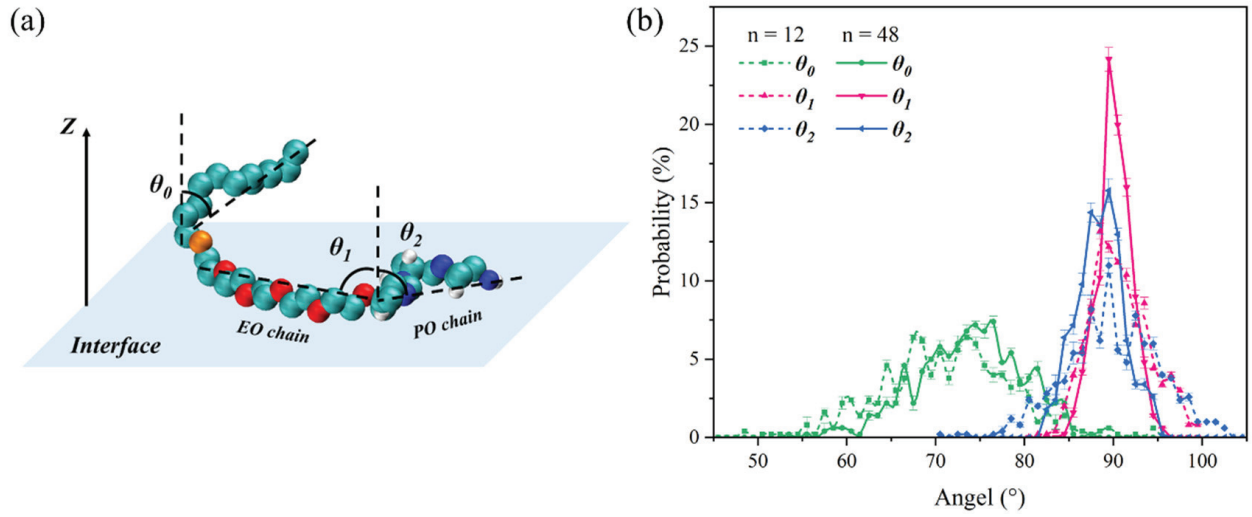

Figure 4. (**a**) Definition of the tilt angle of carbon chain, EO chains, and PO chains, θ_0, θ_1, and θ_2 are the tilt angles of carbon chain, EO chains, and PO chains. (**b**) Distribution probability of different tilt angles in two concentration systems of C12E5P4 at 298 K.

The quantification of hydrogen bonds formed between surfactants and water molecules was conducted along the PEO-PPO structure extending to the -OH, and the results are shown in Figure 5. It was found that two minor peaks are observed at the positions of O_6 and O_8, primarily due to the fact that O_6 is located at the end of the EO chain, where there is folding in the PO chain and weak aggregation between EO molecules, allowing this oxygen atom to be more exposed to the aqueous environment. Similarly, a significant molecular gap exists at position O_8 as well. The O_{10} in the -OH position forms the highest number of hydrogen bonds with water. As the number of molecules in the system increases, the average number of hydrogen bonds that each O atom forms with water decreases except O_{10}, corresponding to the inter- or intra-molecular aggregation of EO and PO groups. When n = 12, EO forms an equal number of hydrogen bonds with water as PO, and the aggregation degree of EO and PO groups are both weak. When n > 12, the clustering of EO groups is clearer than PO because the interaction between EO is stronger, so PO groups form more hydrogen bonds with water than the EO.

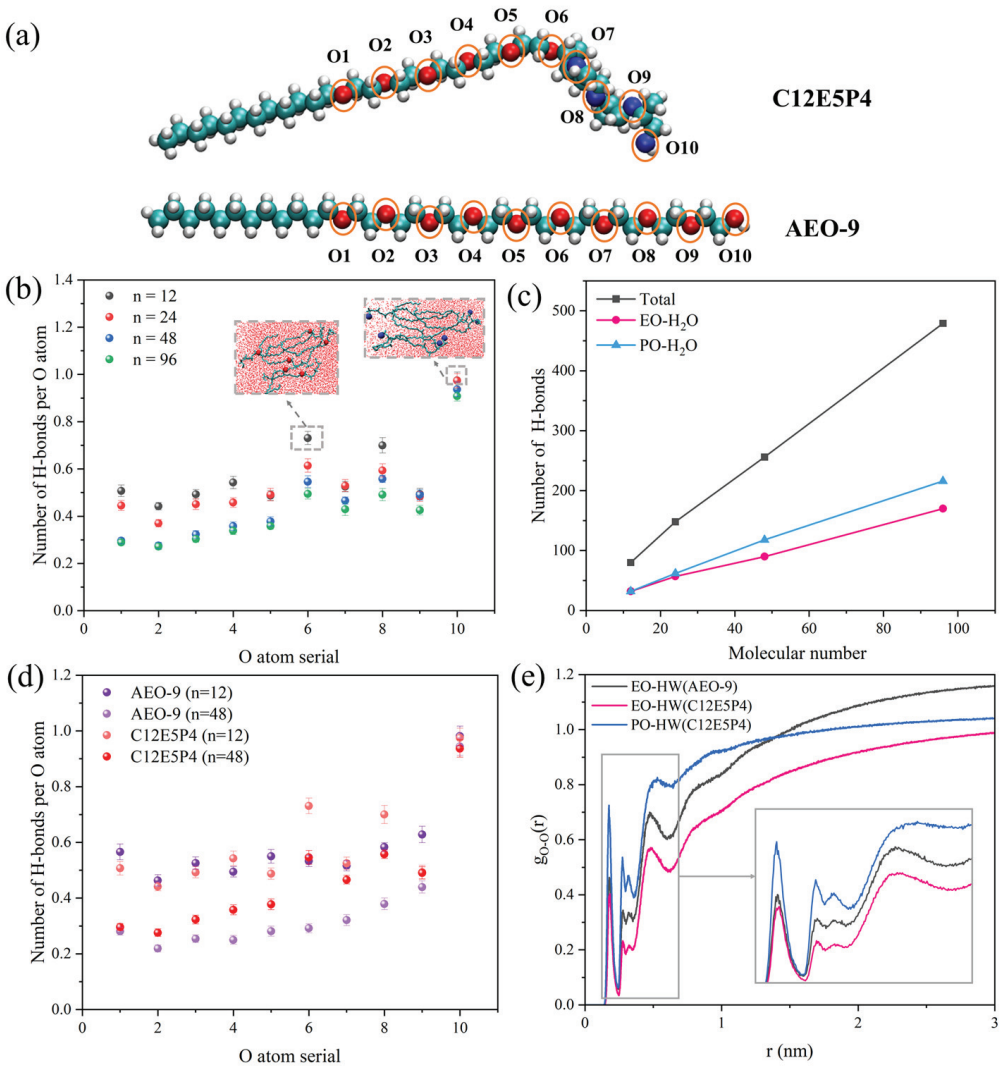

Figure 5. (**a**) Diagram of oxygen atomic number of C12E5P4 and AEO-9. (**b**) The average number of hydrogen bonds per oxygen atom in C12E5P4 system under different concentrations. (**c**) Hydrogen bonds change of C12E5P4 systems with different molecular numbers at 298 K. (**d**) The average number of hydrogen bonds per oxygen atom in C12E5P4/AEO-9 system under different concentrations at 298 K. (**e**) Radial distribution functions of ether groups and water at different positions at 298 K.

As for the results of AEO-9, which are shown in Figure 5c, the number of hydrogen bonds formed by individual oxygen atoms in AEO-9 with water is fewer than that of C12E5P4. Figure 5d illustrates variations in radial distribution functions for ether groups and water molecules at different positions within the C12E5P4 system and the AEO-9 system. The first peak of these curves is observed at 0.18 nm. The radial distribution function value of the first peak for -O-(PO) is 0.72, while the second, third, and fourth peaks occur at 0.28 nm, 0.32 nm, and 0.51 nm, respectively. The peaks of EO occur in approximately the same positions as PO, but they are weaker overall. With the increase in the number of C12E5P4 molecules, the interaction between EO and PO with water is weakened, and the influence on EO groups is greater (Figure S4). The above results suggest that the affinity between EO groups drives the close aggregation of EO groups, while the interaction between PO groups is weaker, which agrees well with the results shown in Figure 6. A comparison of the RDF peaks in Figure 6a shows that EO-EO interactions exhibit the highest intensity with a peak value of approximately 700, while PO-PO interactions are comparatively weaker with a peak value of 500. In addition, EO-PO groups display the weakest affinity, characterized by a peak value of 75. The results prove that the interaction

between EO groups is stronger, and the aggregation trend is stronger. The interaction energy between different groups is given in Figure 6b. It can be found that the interaction between the EO or PO groups is primarily dominated by the Coulomb force, which is much stronger than van der Waals force, and the Coulomb interaction energy between EO-EO groups is surely greater than that between PO-PO groups.

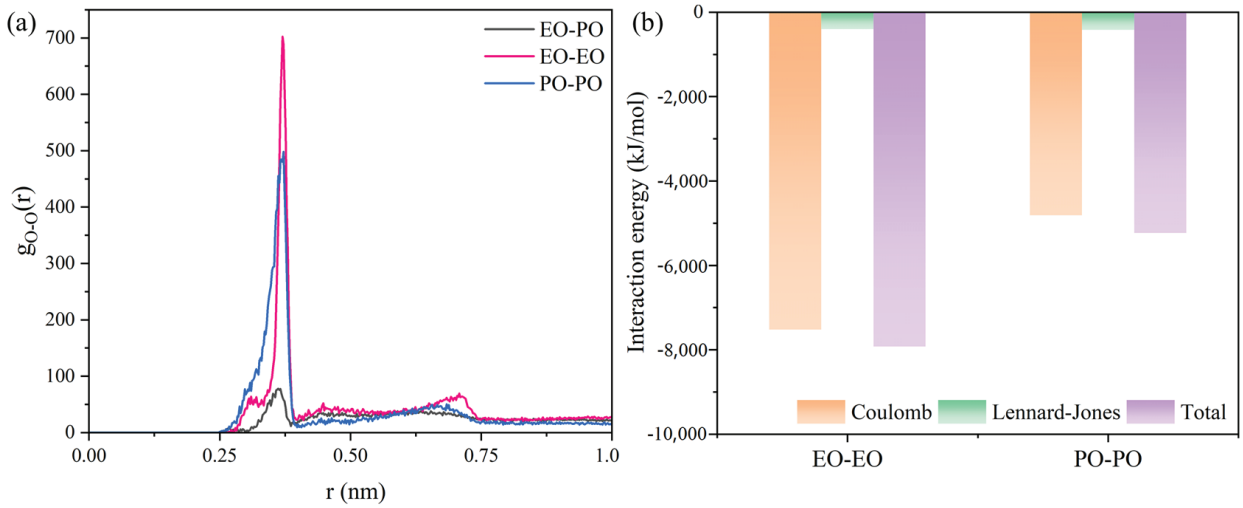

Figure 6. (**a**) Radial distribution functions of EO–PO groups, EO–EO groups, and PO–PO groups in C12E5P4 system (n = 48) at 298 K. (**b**) Coulomb interaction potential and Lennard-Jones potential between different groups in C12E5P4 system (n = 48) at 298 K.

Based on the preceding discussion, it can be inferred that the interaction between PO-PO groups is weaker than EO-EO groups, and the interaction between EO-PO groups is the weakest. The C12E5P4 occupies a larger area than AEO-9, and the hydrophobic tails of C12E5P4 could not intersect with each other to form a compacted stable interface layer like AEO-9, so the foam stability is low.

The arrangement of C12E14P8 molecules at the interface differs somewhat from that of C12E5P4 and gave out important clues on improving the antifoaming performance of REP surfactant. Here, the simulation systems with the same mass concentration of 5 wt% were constructed, and since the molecular mass of C12E14P8 is about twice that of C12E5P4, the number of the former is half that of the latter. As shown in Figure 7a, the EO segments in C12E14P8 exhibit a more compact organization, while the PO chain tends to concentrate around the aggregate formed by the EO chains, too. The arrangement of C12E14P8 molecules is a little more loosely packed compared to that of C12E5P4, as depicted in Figure 7b, while the thickness of the C12E14P8 interface layer is undoubtedly thicker. The aggregation of C12E14P8 at the interface results in the formation of aggregates resembling "oil lenses". According to the gyration radius shown in Table 3, it is observed that the size of C12E14P8 aggregates at the interface is larger than C12E5P4.

Table 3. Interfacial thickness and gyration radius (R_g) of different systems with same concentration (5 wt%) at 298 K.

Surfactant	Interface Thickness (nm)	R_g (nm)
C12E5P4	0.76	6.21
C12E14P8	1.61	7.08

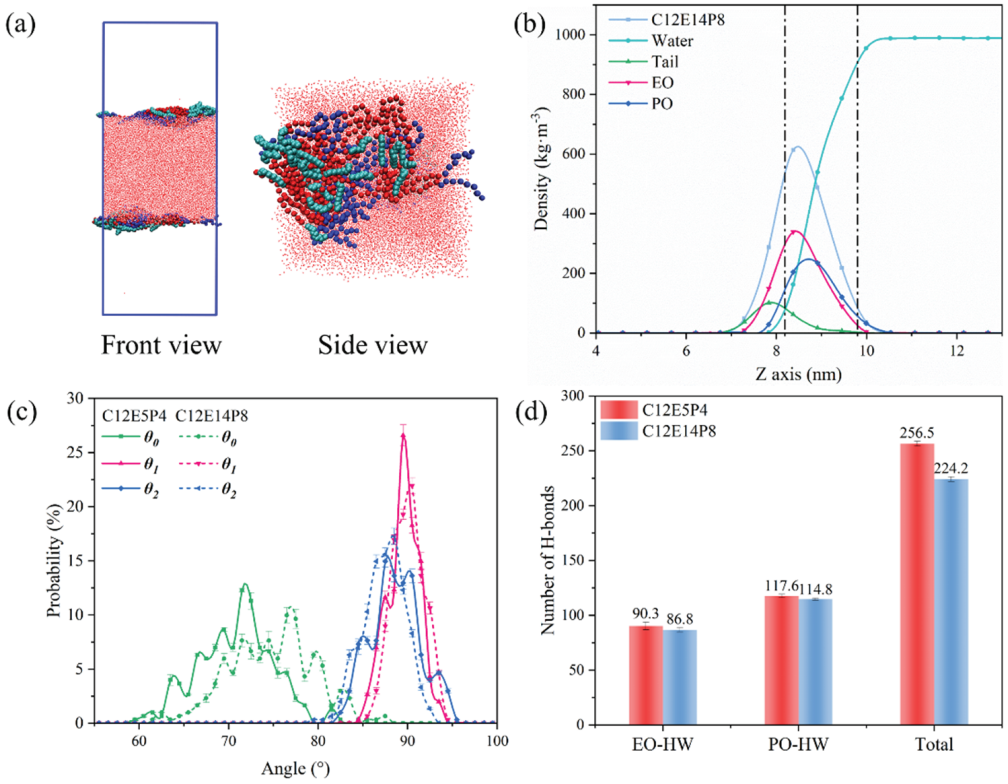

Figure 7. (**a**) The MD simulated equilibrium configuration of C12E14P8 (n = 48) at 298 K. (**b**) Density distribution of C12E14P8 under the concentration of 5 wt% at 298 K (Dotted line: interfacial thickness). (**c**) Probability distribution of tilt angle of different types of REP block polyether. (**d**) The number of hydrogen bonds formed between REP-type block polyether molecules and water.

By analyzing the tilt angle, it can be observed from Figure 7c that the carbon chain of C12E14P8 is positioned closer to the gas/water interface compared to that of C12E5P4. The interaction between REP block polyether and water was examined by analyzing the number of hydrogen bonds, and the results are shown in Figure 7d. The total number of hydrogen bonds formed by C12E14P8 with water is smaller than that of C12E5P4, especially for the EO chain, of which the average hydrogen bond formed by each EO group with water is significantly reduced. This indicates that there is a substantial increase in EO aggregation as the degree of EO polymerization increases. Similar phenomena could be observed on the PO chain.

The schematic diagram of C12E5P4 is depicted in Figure 8a. Compared with C12E5P4, with a lower degree of polymerization, and EO groups of C12E14P8, with a higher degree of polymerization, are more inclined to overlap into dense layers, and PO groups are arranged around the aggregates of EO to form larger "oil lens" at the interface (Figure 8b). The formation of an "oil lens" structure on the interface by the C12E14P8 molecules plays a role similar to oil droplets through a bridging-stretching mechanism [17], which is actually the key antifoaming mechanism of C12E14P8.

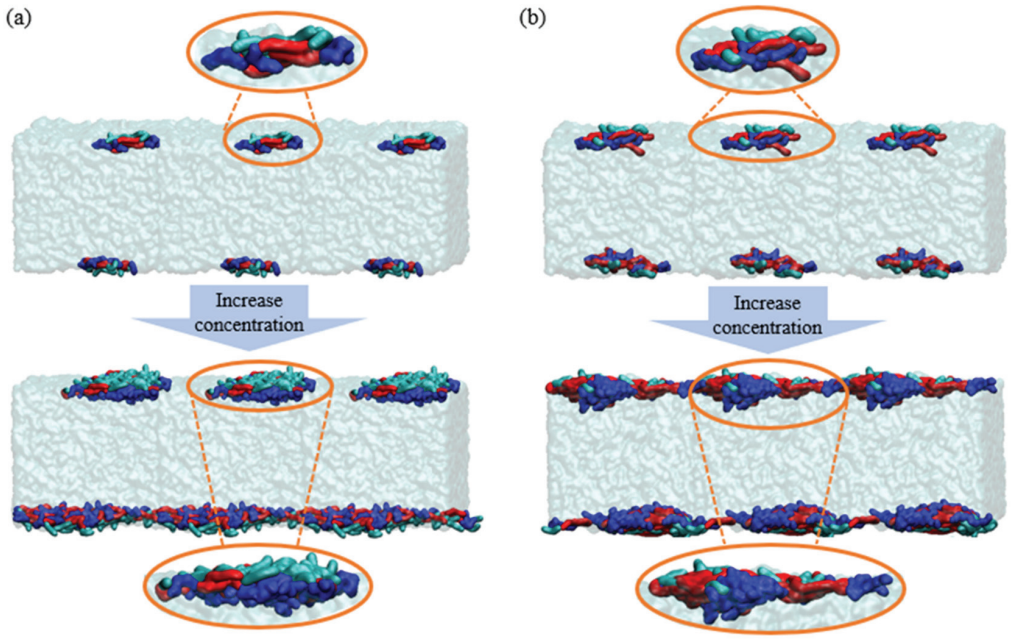

Figure 8. Distribution diagram of REP−type block polyether molecule aggregates on the foam liquid film: (**a**) C12E5P4 system; (**b**) C12E14P8 system. (Green segments represent carbon chain. Red segments represent EO chain. Blue segments represent PO chain).

2.4. Interfacial Molecular Behavior and Foam Properties of Nonionic/Anionic Surfactant Binary Mixed System

To further comprehend the antifoaming efficacy of REP surfactants in conjunction with other surfactants, foam determination experiments on pure SDS systems and SDS/nonionic surfactant compound systems were conducted. In the foam performance test, the mass concentration of pure SDS solution was 1000 mg/L, while the concentration of SDS in the binary composite system was 1000 mg/L, and the concentration of nonionic surfactant was 250 mg/L (the mass concentration ratio was 4:1). As depicted in Figure 9a, the foam formed from pure SDS system remains stable for a long time at room temperature, with a half-life time of up to 13 h. The SDS/AEO-9 system maintained similarly high foam stability. At the same time, the half-life time of the foam formed from the C12E5P4/SDS system is shortened to 1 h. C12E14P8 exhibited the best antifoaming effect in the compound systems, and the half-life time was shortened almost thirty times, reaching 28 min. At the common working temperature of a washing machine, 40 °C, the addition of C12E14P8 reduces the half-life of the compound SDS system by 110 times compared with pure SDS, as depicted in Figure 9b. This observation suggests that the incorporation of C12E14P8 significantly diminishes both the foaming ability and foam stability of the composite system, performing a nice antifoaming performance.

A molecular simulation was used to explore the antifoaming mechanism of C12E14P8 in the compound foam system at room temperature. In the pure SDS system, the SDS molecules exhibit a preference for upright orientation at the gas/water interface; with the sulfuric acid head groups penetrating into the aqueous phase, an ordered dense interface layer could be formed, even if there is electrostatic repulsion between the head groups (Figure 10a). In the compound system of C12E14P8 and SDS, C12E14P8 diffuses faster, occupying most of the interfacial area, forming dense aggregations like oil drops at the interface (Figure 10b), reducing the stability of the foam films. The RDF diagram (Figure 10c) also indicates that the existence of C12E14P8 weakens the interaction between sulfuric acid groups in SDS and water, simultaneously reducing the number of hydrogen bonds formed between sulfuric acid groups and water (Table S3). The results obtained from molecular simulation agree well with the foam determination experiments results. As it was shown by the dynamic surface tension curve of the compound surfactant in Figure 10d, the C12E14P8

does adsorb to the interface more rapidly than SDS. It is valuable to note that the interfacial activity of the C12E14P8/SDS compound system is higher than the SDS system and could be qualified as a low-foam system with high activity.

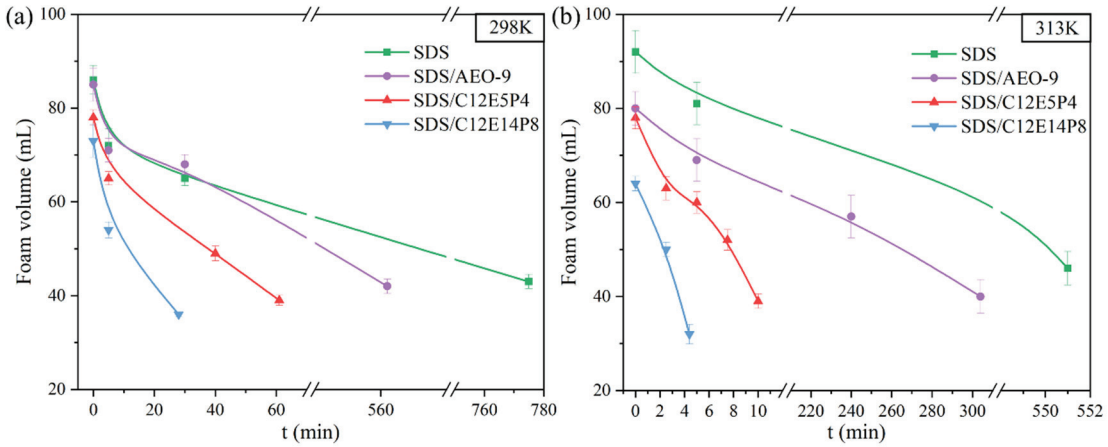

Figure 9. The variation of foam volume generated by pure SDS system and SDS compound system (mass concentration ratio is 4:1) with time (**a**) at 298 K and (**b**) at 313 K.

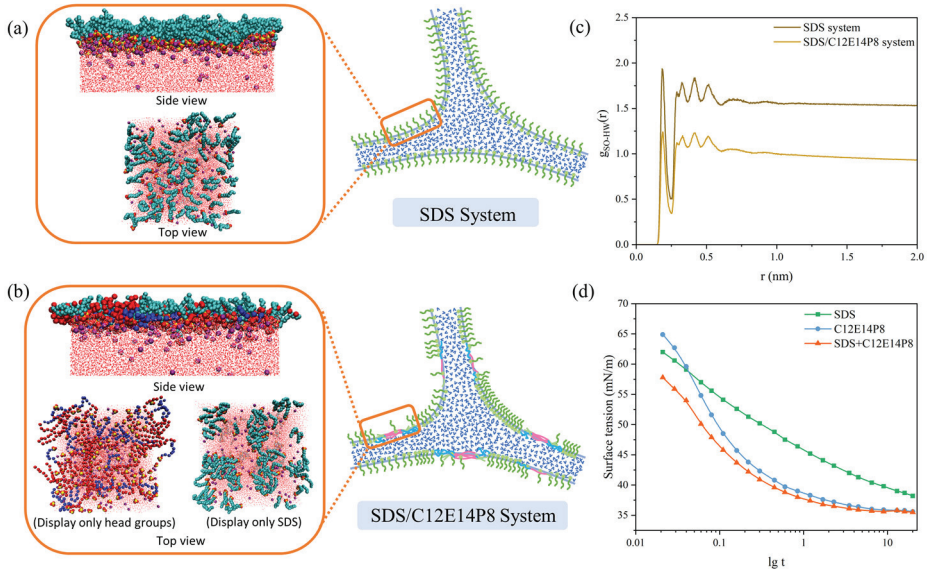

Figure 10. Top view of the molecular simulation snapshot and schematic diagram of (**a**) pure SDS foam liquid film; (**b**) C12E14P8 and SDS compound system. (**c**) Radial distribution functions of sulfuric acid groups and water in different systems at 298 K. (**d**) Dynamic surface tension curves of SDS system, C12E14P8 system, and SDS/C12E14P8 compound system at 298 K.

3. Material and Methods

3.1. Materials

Nonionic surfactant dodecyl polyoxyethylene ether (AEO-9) (content $\geq$ 99.5%, M_w~590) was purchased from BASF. The anionic surfactant sodium dodecyl sulfate (SDS) (AR, M_w~288.38) was purchased from Macklin. Nonionic surfactant dodecyl polyoxyethylene polyoxyel ether $C_{12}H_{25}O(EO)_m(PO)_nH$ (C12E5P4, m = 5, n = 4; C12E14P8, m = 14, n = 8, content $\geq$ 99.7%) were provided by Lianhong Company. The chemical structures of the surfactants are shown in Figure 11a.

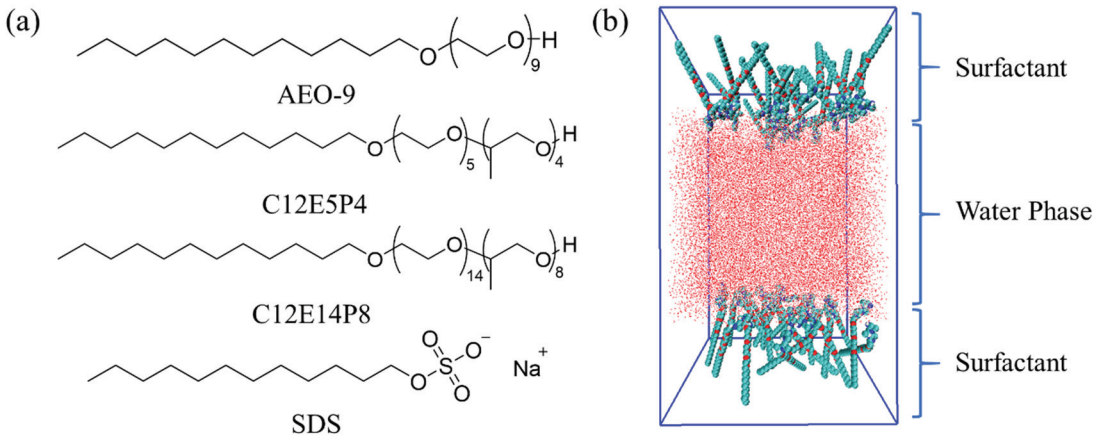

Figure 11. (**a**) Molecular structure of nonionic surfactant AEO-9, REP-type block polyether (C12E5P4 and C12E14P8) and anionic surfactant SDS. (**b**) Diagram of the initial state of the simulation system.

3.2. Static Surface Tension

Sample solutions of different mass concentrations were prepared with ultra-pure water as solvent, and the surface tension was measured by Wilhelmy plate method using Krüss K100 surface tensiometer. The experimental temperature was controlled to be 25 ± 1 °C. Three groups were selected to record the data to reduce the error.

3.3. Foam Performance

Foaming capacity: The foaming capacity was tested by Bartsch shaking method [37]. The initial foam volume is used to indicate the foaming capacity. We added 15 mL of the prepared solution into a mixing cylinder with a stopper and quickly recorded the initial foaming height after hand-shaking for 30 s. We repeated the operation three times.

Foam stability: Static foam stability is expressed by half-life. The foam half-life refers to the time when the foam volume decays to half of the initial volume, recorded as $t_{1/2}$. The above experimental temperature was controlled at 25 ± 1 °C.

3.4. Dynamic Surface Tension

Three different surfactant solutions (concentration 500 mg/L) were prepared with ultra-pure water as solvent. The dynamic surface tension was measured by SITA dynamic surface tensiometer (the maximum bubble pressure method) [38]. The temperature of the solution was controlled at 25 ± 1 °C.

3.5. Molecular Dynamic Simulation

The initial topologies of surfactants C12EmPn (Figure 11a) and SDS were optimized at B3LYP/6−31G(d) levels using the Gaussian16 software package [39]. The initial "sandwich" model of the surfactant/water system was established using the molecular packing program PACKMOL 17.125 [40]. As shown in Figure 11b, the initial configuration consists of 33,400 water molecules placed in a box with an intermediate size of 10.0 nm × 10.0 nm × 10.0 nm with different numbers of surfactant molecules on both sides of the water. In the anionic/nonionic surfactant complex system, in order to make the system electrically neutral, an equal amount of anti-ion (sodium ion) is randomly introduced into the water phase. All the systems and corresponding labels are listed in Tables S1 and S2.

All molecular dynamic calculations were performed in GROMACS 2019.6 [41]. The interatomic interaction is calculated based on the parameters and potential functions of the GROMOS 54A7 force field [42]. In this position, surfactant molecules are described by association atoms. In the simulation, the water molecules were described using the extended simple charge (SPC/E) model [43]. Periodic boundary conditions are applied to the x, y, and z axes of the box. The energy minimization step size is set to 10 fs, and the number of steps is set to 5000. Then, NVT simulation with step size of 2 fs was

run for 10 ns for confirmation and analysis [44,45]. Berendsen thermostat was used to control the temperature, and the temperature was set at 298.15 K [46]. The key length is all limited by LINCS algorithm, and the truncation radius of the neighbor list is 1.2 nm, which is updated every 10 steps [47]. The Particle Mesh Ewald (PME) method was used to calculate the long-range electrostatic interaction with mesh spacing of 0.135 nm and truncation radius of 1.2 nm [34]. The analysis tools provided by GROMACS 2019.6 were used to analyze the simulation results, including the density distribution along the z-axis, radial distribution function, interface generation energy, and water molecular diffusion coefficient. Visualization and snapshot analysis of all molecular configurations using Visual Molecular Dynamics software (VMD) 1.9.3 [48]. According to Figures S1–S3, the simulation system reaches equilibrium at about 6 ns, and the trajectory of the last 4 ns is selected for data analysis.

4. Conclusions

In this paper, the surface activity, foam property, and molecular behavior of two REP-type block polyether nonionic surfactants, C12E5P4 and C12E14P8, at the gas/water interface was studied by combining experiment and molecular dynamics simulation methods for the purpose of better understanding the antifoaming mechanism. The experimental results show that REP-type polyether molecules have a high interfacial adsorption tendency, while the foaming property and foam stability are much lower than that of AEO-9. Among them, C12E14P8 has the most significant antifoaming performance and still shows an excellent antifoaming effect after mixing with a typical foam stabilizer SDS. The simulation results showed that REP-type poly-molecules adsorbed almost flat on the gas/liquid interface, the EO and PO groups were all located in the water phase near the interface, and the hydrophobic tails distributed separately, lying almost flat on the gas/water interface. A radial distribution function and energy analysis showed that the interaction between the same kind of groups as EOs and POs is significantly stronger than that between the EO and PO groups and water. When the degree of polymerization of EO and PO increases, the EOs and POs aggregate separately to form structures similar to an "oil lens", so the foam liquid film has low stability and poor foaming ability. In the composite system with SDS, the interfacial adsorption rate of polyether molecules is faster than that of SDS, occupying the interfacial sites, which reduces the adsorption capacity and foam stability of SDS in the composite system, so it shows remarkable antifoaming performance. This study provides valuable insights for designing low-foam systems with high interface activity with bright application potentials in many related industries, such as washing.

Supplementary Materials: The following supporting information can be downloaded at: https://www.mdpi.com/article/10.3390/molecules29081816/s1, Figure S1: RMSD of SDS/C12E14P8 binary compounding system; Figure S2: (a) Density distributions of AEO-9 and C12E5P4 (n = 48) at 6−7 ns and 9−10 ns, respectively; (b) The change of inclination Angle of C12E5P4 with simulation time at two concentrations of n = 12 and n = 48; (c) Density distributions of C12E14P8 at 6−7 ns and 9−10 ns, respectively; Figure S3: The total number of hydrogen bonds in C12E5P4 system with different molecular number changes with simulation time; Figure S4: Radial distribution functions of ether groups and water in (a) EO groups and (b) PO groups in C12E5P4 systems under different concentrations; Table S1: Summaries of simulated pure polyether systems; Table S2: Summaries of simulated SDS system and SDS/C12E14P8 system; Table S3: The number of hydrogen bonds formed between sulfuric acid groups and water in different systems at 298 K.

Author Contributions: Conceptualization, Y.Z. and Y.L. (Ying Li); Methodology, Y.Z.; Software, C.X. and D.J.; Validation, Y.Z. and C.X.; Formal analysis, Y.Z.; Investigation, W.G. and Y.L. (Yue Liu); Resources, Y.Z., C.X. and W.G.; Data curation, Y.Z.; Writing—original draft, Y.Z.; Writing—review & editing, Y.Z. and Y.L. (Ying Li); Visualization, D.J.; Supervision, C.X., D.J., Y.L. (Yue Liu) and Y.L. (Ying Li); Project administration, Y.L. (Ying Li); Funding acquisition, Y.L. (Ying Li). All authors have read and agreed to the published version of the manuscript.

Funding: This work was financially supported by the National Natural Science Foundation of China (21872084, 61575109).

Institutional Review Board Statement: Not applicable.

Informed Consent Statement: Not applicable.

Data Availability Statement: Data are contained within the article and Supplementary Materials.

Conflicts of Interest: The authors declare no conflict of interest.

References

1. Malysa, K.; Lunkenheimer, K. Foams under dynamic conditions. *Curr. Opin. Colloid Interface Sci.* **2008**, *13*, 150–162. [CrossRef]
2. Farrokhpay, S. The significance of froth stability in mineral flotation—A review. *Adv. Colloid Interface Sci.* **2011**, *166*, 1–7. [CrossRef]
3. Farajzadeh, R.; Andrianov, A.; Krastev, R.; Hirasaki, G.J.; Rossen, W.R. Foam-oil interaction in porous media: Implications for foam assisted enhanced oil recovery. *Adv. Colloid Interface Sci.* **2012**, *183–184*, 1–13. [CrossRef] [PubMed]
4. Wu, M.; Liang, Y.; Zhao, Y.; Wang, W.; Hu, X.; Tian, F.; He, Z.; Li, Y.; Liu, T. Preparation of new gel foam and evaluation of its fire extinguishing performance. *Colloids Surf. A Physicochem. Eng. Asp.* **2021**, *629*, 127443. [CrossRef]
5. Ng, E.L.S.; Lau, K.K.; Partoon, B.; Lim, S.F.; Chin, S.Y. Selection criteria for antifoams used in the acid gas sweetening process. *Ind. Eng. Chem. Res.* **2021**, *60*, 13438–13462. [CrossRef]
6. Cevada, E.; Roos, K.; Alvarez, F.; Carlotti, S.; Vázquez, F. High molar mass polyethers as defoamers of heavy crude oil. *Fuel* **2018**, *221*, 447–454. [CrossRef]
7. Yang, P.; Li, L.; Qin, S.; Wu, D.; Peng, Y.; Liu, H.; Peng, X. Effects and mechanisms of foam suppression in food waste anaerobic digester using defoaming agents. *Fuel* **2023**, *342*, 127920. [CrossRef]
8. Vardar-Sukan, F. Foaming: Consequences, prevention and destruction. *Biotechnol. Adv.* **1998**, *16*, 913–948. [CrossRef]
9. Karakashev, S.I.; Grozdanova, M.V. Foams and antifoams. *Adv. Colloid Interface Sci.* **2012**, *176–177*, 1–17. [CrossRef]
10. Venkatesh, G. Dishwashers: Literature review to summarise the multi-dimensionality of sustainable production and consumption. *Sustainability* **2022**, *14*, 10302. [CrossRef]
11. Alt, T.; Boivin, D.; Altan, M.; Kessler, A.; Schmitz, A.; Stamminger, R. Exploring consumer behaviour in automatic dishwashing: A quantitative investigation of appliance usage in six european countries. *Tenside Surfactants Deterg.* **2023**, *60*, 106–116. [CrossRef]
12. Gooijer, H.; Stamminger, R. Water and energy consumption in domestic laundering worldwide—A review. *Tenside Surfactants Deterg.* **2016**, *53*, 402–409. [CrossRef]
13. Pugh, R.J. Foaming, foam films, antifoaming and defoaming. *Adv. Colloid Interface Sci.* **1996**, *64*, 67–142. [CrossRef]
14. Ross, S. Profoams and antifoams. *Colloids Surf. A Physicochem. Eng. Asp.* **1996**, *118*, 187–192. [CrossRef]
15. Chavan, P.; Sharma, P.; Sharma, S.R.; Mittal, T.C.; Jaiswal, A.K. Application of high-intensity ultrasound to improve food processing efficiency: A review. *Foods* **2022**, *11*, 122. [CrossRef] [PubMed]
16. Garrett, P.R. Defoaming: Antifoams and mechanical methods. *Curr. Opin. Colloid Interface Sci.* **2015**, *20*, 81–91. [CrossRef]
17. Denkov, N.D. Mechanisms of foam destruction by oil-based antifoams. *Langmuir* **2004**, *20*, 9463–9505. [CrossRef] [PubMed]
18. Lu, Y.; Huang, M.; Zhou, Q.; Wang, B.; Wei, W.; Chen, J. On recycling earth pressure balance shield muck with residual foaming agent: Defoaming and antifoaming investigations. *Environ. Sci. Pollut. Res.* **2024**, *31*, 8046–8060. [CrossRef] [PubMed]
19. Ren, C.; Zhang, X.; Jia, M.; Ma, C.; Li, J.; Shi, M.; Niu, Y. Antifoaming agent for lubricating oil: Preparation, mechanism and application. *Molecules* **2023**, *28*, 3152. [CrossRef]
20. Fauser, H.; von Klitzing, R. Effect of polyelectrolytes on (de)stability of liquid foam films. *Soft Matter* **2014**, *1*, 693–6916. [CrossRef]
21. Cao, X.; Xia, W.; Zhao, T.; Li, X.; Zhang, P.; Qin, X.; Bai, B.; Bian, J. Study on the dual effects of $MgCl_2$ on the characteristics of foams stabilized by sodium dodecyl sulfate. *Ind. Eng. Chem. Res.* **2023**, *62*, 16977–16989. [CrossRef]
22. Arnaudov, L.; Denkov, N.D.; Surcheva, I.; Durbut, P.; Broze, G.; Mehreteab, A. Effect of oily additives on foamability and foam stability. 1. Role of interfacial properties. *Langmuir* **2001**, *17*, 6999–7010. [CrossRef]
23. Denkov, N.D.; Marinova, K.G.; Tcholakova, S.S. Mechanistic understanding of the modes of action of foam control agents. *Adv. Colloid Interface Sci.* **2014**, *206*, 57–67. [CrossRef] [PubMed]
24. Agneta, M.; Zhaomin, L.; Chao, Z.; Gerald, G. Investigating synergism and antagonism of binary mixed surfactants for foam efficiency optimization in high salinity. *J. Pet. Sci. Eng.* **2019**, *175*, 489–494. [CrossRef]
25. Wang, R.; Li, Y.; Li, Y. Interaction between cationic and anionic surfactants: Detergency and foaming properties of mixed systems. *J. Surfactants Deterg.* **2014**, *17*, 881–888. [CrossRef]
26. Chaisalee, R.; Soontravanich, S.; Yanumet, N.; Scamehorn, J.F. Mechanism of antifoam behavior of solutions of nonionic surfactants above the cloud point. *J. Surfactants Deterg.* **2003**, *6*, 345–351. [CrossRef]
27. Lindman, B.; Medronho, B.; Karlström, G. Clouding of nonionic surfactants. *Curr. Opin. Colloid Interface Sci.* **2016**, *22*, 23–29. [CrossRef]
28. Joshi, K.S.; Jeelani, S.A.K.; Blickenstorfer, C.; Naegeli, I.; Oliviero, C.; Windhab, E.J. Nonionic block copolymer antifoams. *Langmuir* **2006**, *22*, 6893–6904. [CrossRef] [PubMed]
29. Herzberger, J.; Niederer, K.; Pohlit, H.; Seiwert, J.; Worm, M.; Wurm, F.R.; Frey, H. Polymerization of ethylene oxide, propylene oxide, and other alkylene oxides: Synthesis, novel polymer architectures, and bioconjugation. *Chem. Rev.* **2016**, *116*, 2170–2243. [CrossRef]

30. Brocas, A.; Mantzaridis, C.; Tunc, D.; Carlotti, S. Polyether synthesis: From activated or metal-free anionic ring-opening polymerization of epoxides to functionalization. *Prog. Polym. Sci.* **2013**, *38*, 845–873. [CrossRef]
31. Zhang, W.; Tan, Y.H.; Finch, J.A. Synthesis and characterization of alkyl, propoxy, ethoxy-based frothers. *Miner. Eng.* **2016**, *95*, 66–73. [CrossRef]
32. Yada, S.; Suzuki, T.; Hashimoto, S.; Yoshimura, T. Adsorption and aggregation properties of homogeneous polyoxypropylene-polyoxyethylene alkyl ether type nonionic surfactants. *Langmuir* **2017**, *33*, 3794–3801. [CrossRef]
33. Yada, S.; Suzuki, T.; Hashimoto, S.; Yoshimura, T. Adsorption dynamics of homogeneous polyoxypropylene-polyoxyethylene alkyl ether nonionic surfactants at the air/water interface. *J. Mol. Liq.* **2018**, *255*, 208–214. [CrossRef]
34. Essmann, U.; Perera, L.; Berkowitz, M.L.; Darden, T.; Lee, H.; Pedersen, L.G. A smooth particle mesh Ewald method. *J. Chem. Phys.* **1995**, *103*, 8577–8593. [CrossRef]
35. Hua, X.Y.; Rosen, M.J. Dynamic surface tension of aqueous surfactant solutions: I. Basic paremeters. *J. Colloid Interface Sci.* **1988**, *124*, 652–659. [CrossRef]
36. Gao, T.; Rosen, M.J. Dynamic surface tension of aqueous surfactant solutions: 7. Physical significance of dynamic parameters and the induction period. *J. Colloid Interface Sci.* **1995**, *172*, 242–248. [CrossRef]
37. Lee, J.; Nikolov, A.; Wasan, D. Effects of micellar structuring and solubilized oil on the kinetic stability of aqueous foams. *Ind. Eng. Chem. Res.* **2014**, *53*, 18891–18899. [CrossRef]
38. Weissenborn, P.K.; Pugh, R.J. Surface tension of aqueous solutions of electrolytes: Relationship with ion hydration, oxygen solubility, and bubble coalescence. *J. Colloid Interface Sci.* **1996**, *184*, 550–563. [CrossRef] [PubMed]
39. Marenich, A.V.; Cramer, C.J.; Truhlar, D.G. Universal solvation model based on solute electron density and on a continuum model of the solvent defined by the bulk dielectric constant and atomic surface tensions. *J. Phys. Chem. B* **2009**, *113*, 6378–6396. [CrossRef]
40. Martínez, L.; Andrade, R.; Birgin, E.G.; Martínez, J.M. PACKMOL: A package for building initial configurations for molecular dynamics simulations. *J. Comput. Chem.* **2009**, *30*, 2157–2164. [CrossRef]
41. Abraham, M.J.; Murtola, T.; Schulz, R.; Páll, S.; Smith, J.C.; Hess, B.; Lindahl, E. GROMACS: High performance molecular simulations through multi-level parallelism from laptops to supercomputers. *SoftwareX* **2015**, *1–2*, 19–25. [CrossRef]
42. Schmid, N.; Eichenberger, A.P.; Choutko, A.; Riniker, S.; Winger, M.; Mark, A.E.; van Gunsteren, W.F. Definition and testing of the GROMOS force-field versions 54A7 and 54B7. *Eur. Biophys. J.* **2011**, *40*, 843–856. [CrossRef] [PubMed]
43. Yuet, P.K.; Blankschtein, D. Molecular dynamics simulation study of water surfaces: Comparison of flexible water models. *J. Phys. Chem. B* **2010**, *114*, 13786–13795. [CrossRef] [PubMed]
44. Li, J.; Han, Y.; Qu, G.; Cheng, J.; Xue, C.; Gao, X.; Sun, T.; Ding, W. Molecular dynamics simulation of the aggregation behavior of N-dodecyl-N,N-dimethyl-3-ammonio-1-propanesulfonate/sodium dodecyl benzene sulfonate surfactant mixed system at oil/water interface. *Colloids Surf. A Physicochem. Eng. Asp.* **2017**, *531*, 73–80. [CrossRef]
45. Qu, G.; Xue, C.; Zhang, M.; Liang, S.; Han, Y.; Ding, W. Molecular dynamics simulation of sulfobetaine-type zwitterionic surfactants at the decane/water interface: Structure, interfacial properties. *J. Dispersion Sci. Technol.* **2016**, *37*, 1710–1717. [CrossRef]
46. Berendsen, H.J.C.; Postma, J.P.M.; van Gunsteren, W.F.; Dinola, A.; Haak, J.R. Molecular dynamics with coupling to an external bath. *J. Chem. Phys* **1984**, *81*, 3684–3690. [CrossRef]
47. Hess, B.; Bekker, H.; Berendsen, H.J.C.; Fraaije, J.G.E.M. LINCS: A linear constraint solver for molecular simulations. *J. Comput. Chem.* **1997**, *18*, 1463–1472. [CrossRef]
48. Humphrey, W.; Dalke, A.; Schulten, K. VMD: Visual molecular dynamics. *J. Mol. Graph.* **1996**, *14*, 33–38. [CrossRef]

molecules

MDPI

Article

Developing an Improved Cycle Architecture for AI-Based Generation of New Structures Aimed at Drug Discovery

Chun Zhang †, Liangxu Xie †, Xiaohua Lu, Rongzhi Mao, Lei Xu * and Xiaojun Xu *

Institute of Bioinformatics and Medical Engineering, School of Electrical and Information Engineering, Jiangsu University of Technology, Changzhou 213001, China; zhangchlwy@gmail.com (C.Z.); xieliangxu@jsut.edu.cn (L.X.); jsluxiaohua@outlook.com (X.L.); maorongzhi2022@outlook.com (R.M.)
* Correspondence: leixu@jsut.edu.cn (L.X.); xuxiaojun@jsut.edu.cn (X.X.)
† The authors contributed equally to this work.

Abstract: Drug discovery involves a crucial step of optimizing molecules with the desired structural groups. In the domain of computer-aided drug discovery, deep learning has emerged as a prominent technique in molecular modeling. Deep generative models, based on deep learning, play a crucial role in generating novel molecules when optimizing molecules. However, many existing molecular generative models have limitations as they solely process input information in a forward way. To overcome this limitation, we propose an improved generative model called BD-CycleGAN, which incorporates BiLSTM (bidirectional long short-term memory) and Mol-CycleGAN (molecular cycle generative adversarial network) to preserve the information of molecular input. To evaluate the proposed model, we assess its performance by analyzing the structural distribution and evaluation matrices of generated molecules in the process of structural transformation. The results demonstrate that the BD-CycleGAN model achieves a higher success rate and exhibits increased diversity in molecular generation. Furthermore, we demonstrate its application in molecular docking, where it successfully increases the docking score for the generated molecules. The proposed BD-CycleGAN architecture harnesses the power of deep learning to facilitate the generation of molecules with desired structural features, thus offering promising advancements in the field of drug discovery processes.

Keywords: deep learning; molecule generation; bidirectional; CycleGAN; attention

1. Introduction

The cornerstone of novel drug design resides in the exploration of small molecules that meet defined criteria, a task that has historically presented challenges [1–3]. Traditionally, this endeavor has heavily depended on the expertise of professionals involved with the processes of screening, synthesis, and testing, incurring considerable demands on both human resources and materials. Computer-aided drug design (CADD) has brought about improvements to this situation [4–11], culminating in notable achievements thus far. Especially since the emergence of artificial intelligence, deep learning-based molecule generation has brought about achievements as one of the advanced molecular modeling techniques. Recently, deep learning-designed drugs have entered pre-clinical trials [12–17].

In the field of computer-aided drug design (CADD), machine learning and deep learning have gained significant attention. Machine learning involves the development of algorithms that enable computers to learn and make predictions without explicit programming. Deep learning, a subset of machine learning, employs artificial neural networks with multiple layers to extract complex patterns from data. One important application of deep learning in CADD is the use of deep generative models. Deep generative models are designed to generate new data samples that resemble a given training dataset. In the context of drug discovery, these models play a crucial role in de novo molecule generation. De novo molecule generation refers to the process of designing and synthesizing entirely new molecules with desired properties.

Deep learning shows the power of prediction and generation. To make use of its generation ability, de novo molecular design methods have been developed [18,19]. These methods are based on recurrent neural networks, variational autoencoders (VAEs), generative adversarial networks (GANs), and transformers, etc. For example, Pham et al. employed conditional variational autoencoder frameworks to efficiently generate novel molecules with enhanced biological activity [20]. Wang et al. utilized generative pre-training techniques to extract contextual information from molecules, facilitating the generation of molecules with improved binding affinity to target proteins [21].

Among these widely reported methods, generative adversarial network (GAN) has emerged as a popular architecture for generating highly realistic molecules [22,23]. By simulating the potential distribution of molecules through the interplay between generators and discriminators, GAN can generate a diverse range of molecular structures. In the field of de novo molecular generation, GAN exhibits distinctive characteristics with an ability to construct variants by changing component architecture in generators and discriminators. Consequently, a multitude of GAN architectures are being explored and developed to cater to diverse requirements. The combination of reinforcement learning and GANs enables control over the attributes of generated samples, facilitating the generation of sequence data that aligns with specific target requirements [24]. LatentGAN directly incorporates the autoencoder into the GAN, employing the pre-trained autoencoder to map the molecular structure to potential vectors and to train the GAN using the potential vectors as inputs and outputs [25]. Beyond from GAN, CycleGAN employs a ring network comprising two sets of symmetric generators and discriminators, enabling dual unpaired data transformations during the generation process [26]. The Mol-CycleGAN [27] model extends CycleGAN to the junction tree variational autoencoder (JT-VAE) [28] framework to ensure that the generated compounds are always effective. The original molecular data set is fed into the "codec" structure to generate new compounds with desired pharmacological properties [27–29]. Similar to the natural language, the forward and backward directions of the input molecule would preserve sequential information as shown in Figure 1. Therefore, information from reading the input molecules from the forward direction and the backward direction should be kept.

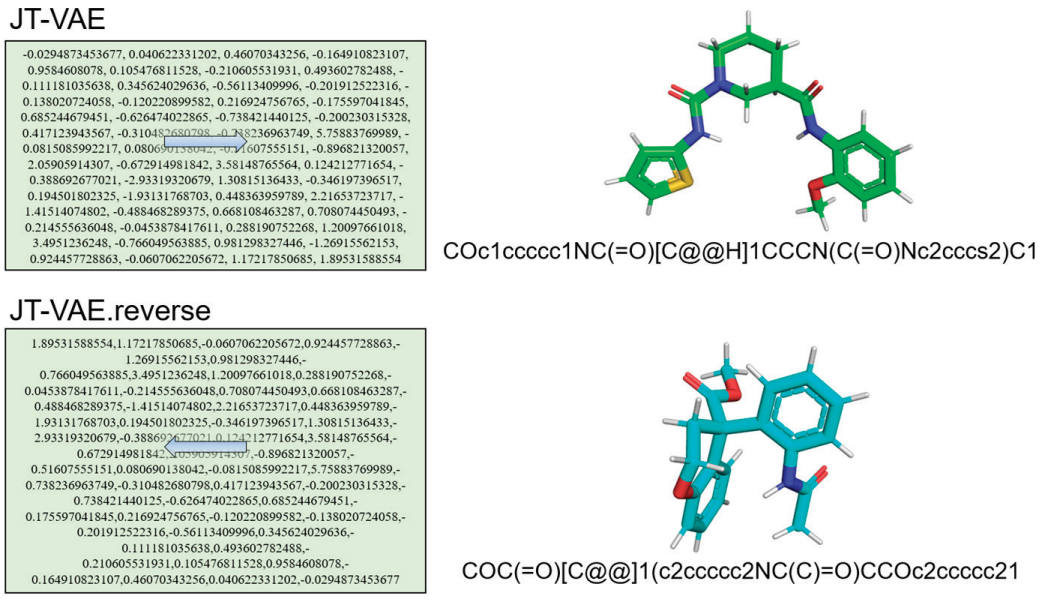

Figure 1. The schematic figures of processing of forward and reverse of JT-VAE. Reading the input from two directions (labelled as arrows) would generate different SMILES strings. The left panel shows the reading of the JT-VAE encoding in a forward and backward direction; and the right panel shows the corresponding molecules.

Herein, we propose BD-CycleGAN (Figure 2), which incorporates bi-directional long short-term memory (BiLSTM) [30] and attention mechanisms [31] into the Mol-CycleGAN generator and discriminator, respectively. BiLSTM is a type of recurrent neural network that can process information in both the forward and backward directions. The CycleGAN model is a type of deep learning model that learns to transform molecules from one form to another. In our case, it learns to generate new molecules with the desired structural features. The attention mechanism is a component used in deep learning models. It allows the model to focus on different parts of the input data while performing a task, giving more weight or attention to relevant information. Our proposed BD-CycleGAN architecture combines the strengths of the CycleGAN model, BiLSTM, and an attention mechanism to enable the generation of new molecules in drug discovery. The inclusion of BiLSTM within the generator allows for the capture of sequential context information, enabling better modeling of molecular sequence features and enhancing the generator's capability to express molecular structures. The generated molecules exhibit higher potential for the lead candidates and align more closely with the principles of pharmaceutical chemistry. The improvement in the performance of the optimized model is evaluated by the success rate, diversity, and novelty indicators.

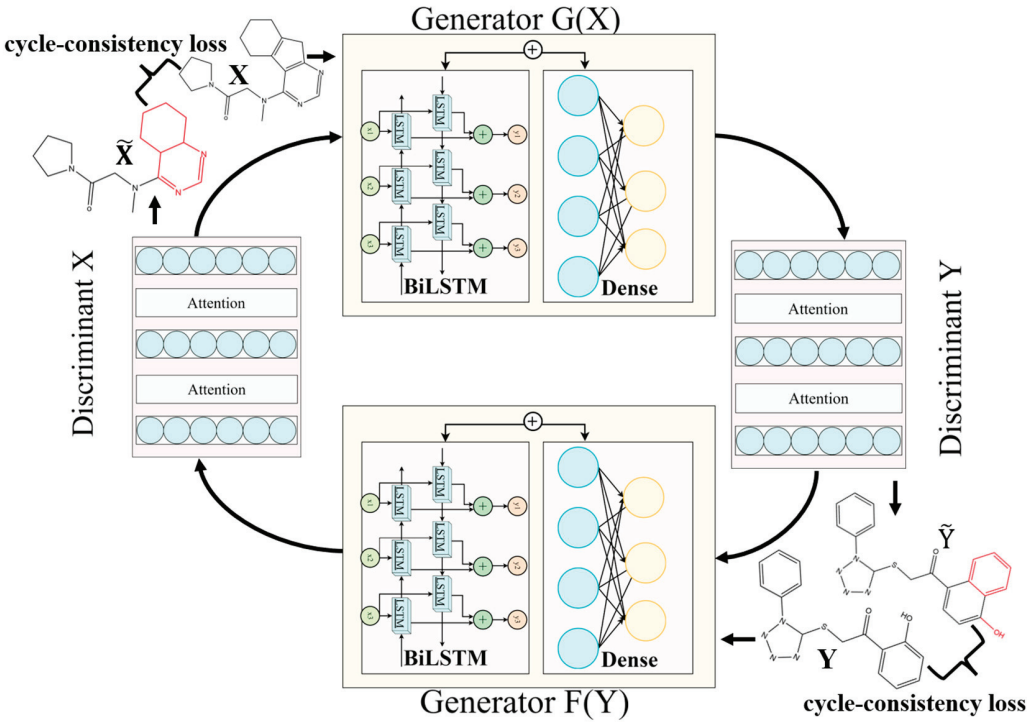

Figure 2. The proposed architecture of the BD-CycleGAN. Discriminators consist of three dense layers that connected by two Attention layers. Generators consist of one BiLSTM layer, one Dense layer and the residual connection between two layers. The cycle-consistency loss and molecules are displayed on both sides of the schematic figure to demonstrate the loss in models.

2. Results

2.1. Ablation Experiment to Identify Architecture of Model

We conduct ablation experiment on our proposed model by using the generation task of aromatic data set. To enhance the generative ability, we need to revise the generator architecture of CycleGAN. The architecture of four combination models, including BiSTM_Attention, Attention_BiLSTM, LSTM_Res, and BiLSTM_Res, are presented in Figure S1 in the Supplementary Materials Section. Figure 3 presents the success rate of the four examined models. The success rate of BiLSTM_Res is higher than that of the other three models, suggesting that the molecule generation ability of BiLSTM_Res model surpasses that of the other modules. Figure S2 shows that the BiLSTM_Res model generates a higher number of target characteristic molecules compared to the other modules combinations.

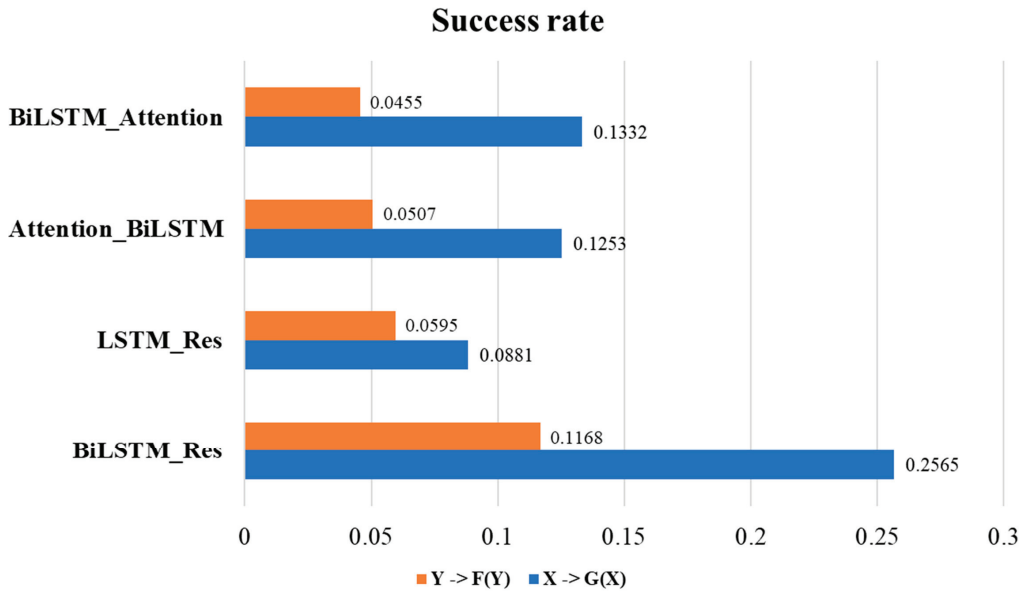

Figure 3. Success rate results for the four combined models in the ablation experiment.

In our ablation experiment, we firstly show that one layer of BiLSTM could outperform two layers of LSTM as shown in Figure 3. Secondly, the attention mechanism and residual connection are embedded in the discriminator to assist in focusing on key features. Comparing BiLSTM_Attention and BiLSTM_Res, we can see that the BiLSTM_Res will build the connection between the output of the BiLSTM and the input, which can provide more information after dimensionality reduction and will improve gradient transfer and enhance the model's learning capacity. Thereby, BiLSTM_Res enhances its discriminative ability and guides the generator in generating more realistic and diverse molecules. As a result, BiLSTM_Res is selected as the generator module for our proposed BD-CycleGAN models.

2.2. Molecular Generation with Specific Structural Group

In the lead optimization process, the pharmacodynamic functional groups need to be tuned to change the property of potential molecules. BD-CycleGAN is proposed to complete this task to transform from source molecules to target molecules. CycleGAN adopts the special cycle architecture of complete symmetry. The model will transform and reconstruct the molecular data in the two relative regions of X and Y, to realize the transformation and generation of molecular structure. As shown in Figure S3, the ZINC-250K data set was divided into six data sets based on the number of five functional groups: aromatic ring, aliphatic ring, halogen, hydrogen bond donor (HBD), and hydrogen bond acceptor (HBA). Figure 4 shows the molecular distribution of the different structural features of the generated aromatic ring, aliphatic ring, halogen, and hydrogen bond donor (HBD). Compared with molecule set X, which is the original molecular distribution, it is obvious that more generated molecules are close to the characteristics of molecule set Y. The molecules have been successfully converted from the source molecule X to the target molecule Y. The transformation is more obvious in the task of HBA_Discrete generation (shown in Figure 5). The X set only contains molecules with five hydrogen bond acceptors, while the Y set contains molecules with fewer than five hydrogen bond acceptors. The results show that the success rate of converting a single feature into multiple continuous features is improved.

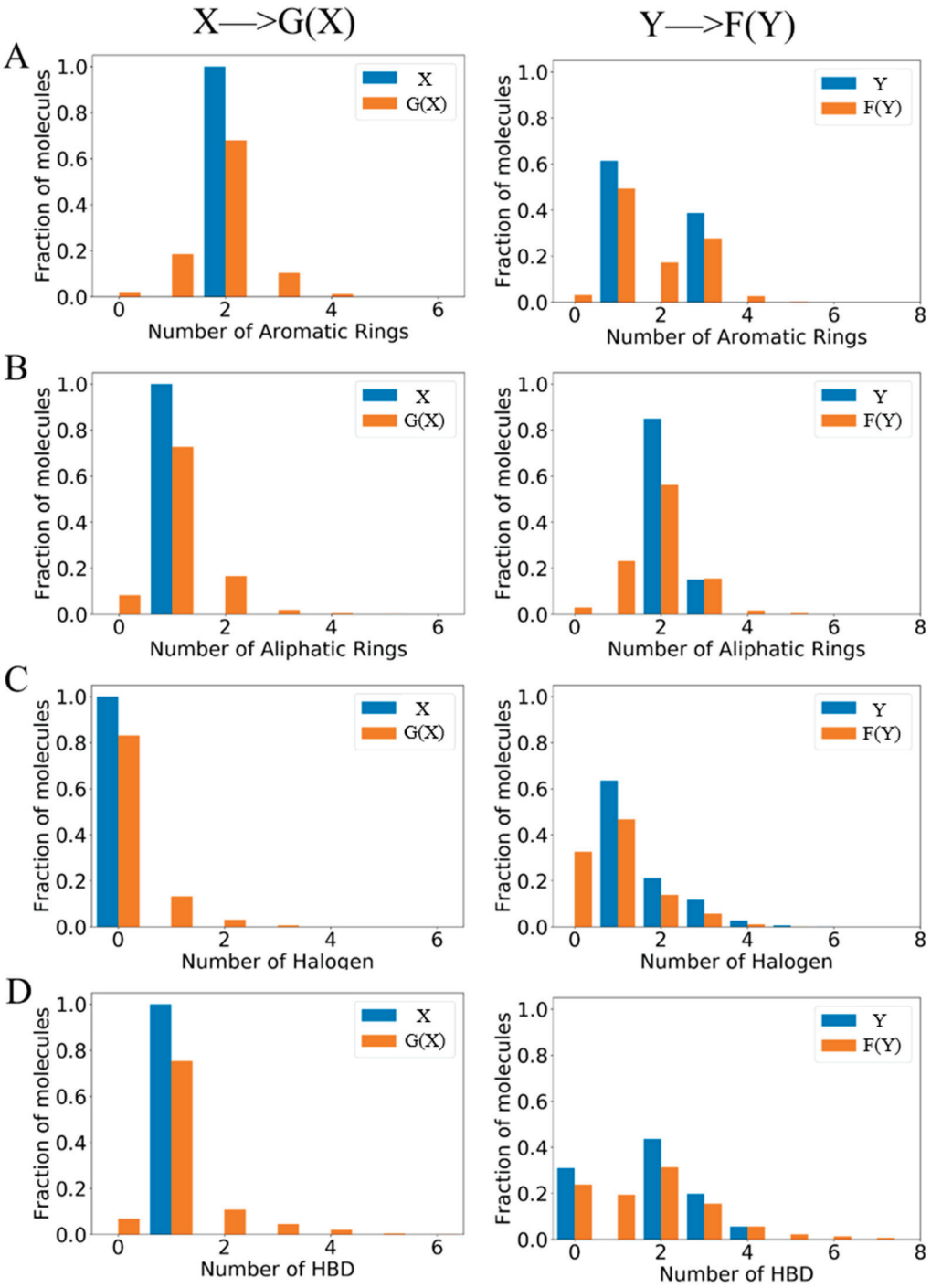

Figure 4. The distribution of the generated molecules. (**A**) Aromatic rings, (**B**) aliphatic rings, (**C**) halogen, and (**D**) HBD. In each sub-figure, the blue bars represent the original molecular distribution and the orange bars represent the generated molecular distribution.

We employed two key evaluation criteria, the ability of the model to generate the required molecules and the likelihood of successfully generating molecules with the desired functional groups. We have presented the corresponding results in Figures 4 and 5, and summarized them in Table 1. The results demonstrate our model can generate the desired molecules.

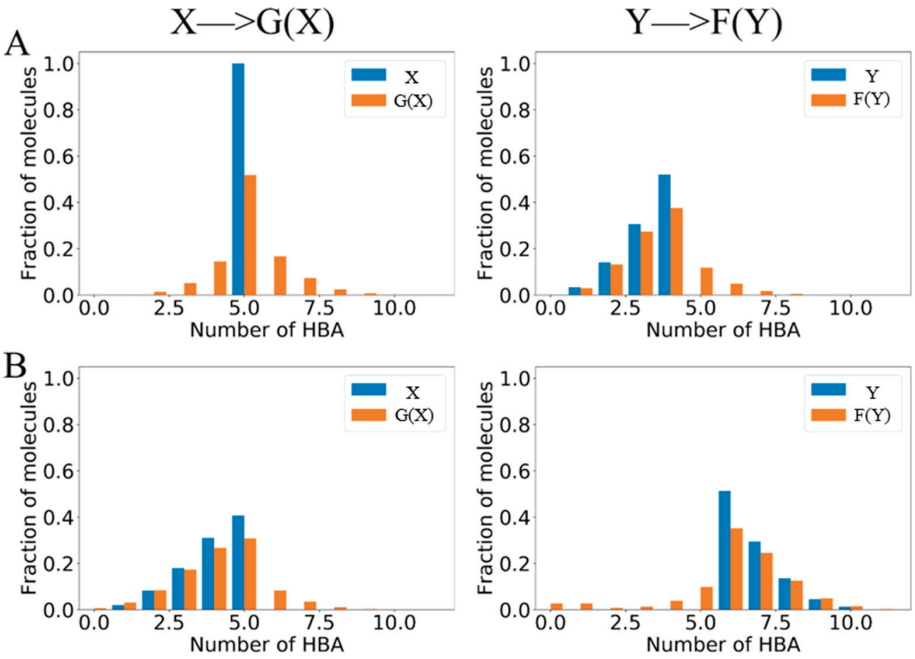

Figure 5. The distribution of the generated molecules for hydrogen bond acceptors. (**A**) HBA_Discrete and (**B**) HBA_Continuous. "HBA_Discrete" refers to the discrete representation of the number of hydrogen bond acceptors. "HBA_Continuous" refers to the continuous numerical values of the number of hydrogen bond acceptors. In each sub-figure, the blue bars represent the original molecular distribution and the orange bars represent the generated molecular distribution.

Table 1. Assessment of Structural Modifications in Generated Molecules.

Model		X—>G(X)			Y—>F(Y)		
Data	**Model**	**Success Rate**	**Diversity**	**Non-Identity**	**Success Rate**	**Diversity**	**Non-Identity**
Aromatic rings	Mol-CycleGAN	0.231	0.981	0.762	0.102	0.997	0.582
	BD-CycleGAN	0.257	0.995	0.804	0.117	0.997	0.680
Aliphatic rings	Mol-CycleGAN	0.183	0.996	0.713	0.154	0.994	0.769
	BD-CycleGAN	0.222	0.996	0.814	0.196	0.996	0.861
Halogen	Mol-CycleGAN	0.032	0.997	0.417	0.145	0.993	0.717
	BD-CycleGAN	0.121	0.994	0.714	0.257	0.991	0.793
HBD	Mol-CycleGAN	0.226	0.994	0.718	0.147	0.991	0.822
	BD-CycleGAN	0.193	0.996	0.782	0.178	0.996	0.923
HBA_Discrete	Mol-CycleGAN	0.154	0.986	0.389	0.030	0.999	0.328
	BD-CycleGAN	0.376	0.995	0.782	0.078	0.996	0.662
HBA_Continuous	Mol-CycleGAN	0.106	0.995	0.518	0.102	0.994	0.475
	BD-CycleGAN	0.085	0.974	0.662	0.142	0.966	0.662

2.3. Performance Evaluation on the Chemical Structure

The structural performance of the model is quantitatively calculated under six different feature distributions: aromatic ring, aliphatic ring, halogen, HBD, HBA_Discrete, and HBA_Continuous. The generator and discriminator are divided into two directions, so the generation of two directions is realized. The evaluation indicators for the two directions (X—>G(X) and Y—>F(Y)) are summarized in Table 1. The BD-CycleGAN model has been improved in terms of success rate, uniqueness, and non-identity. The success rate and non-identity of the aromatic ring are improved. The diversity has been improved for aromatic ring, HBD, and HBA_Discrete. Since the aromatic ring structure has a long chain-like structure, it is necessary to deal with and transfer the long-term dependence and complex spatial structure during the simulation of molecular generation. BiLSTM and the

attention mechanism can deal with this situation well, to improve the processing ability and accuracy of the molecular generation model for the aromatic ring structure.

For the halogen feature distribution, the success rate obviously improved from 0.032 to 0.121 for G(X) and from 0.145 to 0.257 for F(Y). The non-uniformity is nearly doubled, indicating that the model has a good advantage in dealing with structures with halogens. For the HBA_Discrete distribution, the molecules in the X set only have samples with five hydrogen bond acceptors. This specific restriction allows the model to capture the contextual information of the input molecules more accurately and to generate molecules that are better matched with the characteristics of the target. Therefore, the BD-CycleGAN model achieves a doubling of the success rate and non-identity in the generation task of the HBA_Discrete distribution.

To quantitatively assess the performance of the proposed model, the evaluation matrices are compared between BD-CyleGAN and Mol-CycleGAN using the MOSES benchmark. As shown in Table 2, the model was analyzed using five indicators: Filters, Valid, IntDiv, IntDiv2, and Novelty to determine the effectiveness of the model's molecular generation performance, and the diversity of the generated molecules. Among the six different feature distributions, the halogen task has the highest novelty, which means that the resulting molecules have more unique structural properties. Meanwhile, the aliphatic rings generation scored the highest, indicating that the resulting molecules are more stable in structural generation, which may have a wider range of applications and greater research value. In the filter evaluation, HBD had the highest score and the best performance. In the evaluation of molecular effectiveness, the six different distributions were significantly improved, which means that the BD-CycleGAN model can better learn the distribution of functional groups during the training process so that the generated molecules are more in line with the requirements of functional group distribution. Such molecules are more in line with the law of medicinal chemistry and biological feasibility and may be easier to synthesize and apply in practical treatment.

Table 2. The evaluation of generated molecules in terms of success rate and the validity of molecules that meet chemical rules and chemical diversity.

Structure	Model	X—>G(X)					Y—>F(Y)				
		Filters	**Valid**	**IntDiv**	**IntDiv2**	**Novelty**	**Filters**	**Valid**	**IntDiv**	**IntDiv2**	**Novelty**
Aromatic	Mol-Cycle	0.621	0.989	0.865	0.859	0.954	0.598	0.998	0.869	0.863	0.947
	BD-Cycle	0.639	0.995	0.866	0.860	0.961	0.599	0.998	0.868	0.863	0.957
Aliphatic	Mol-Cycle	0.576	0.998	0.862	0.857	0.960	0.518	0.994	0.865	0.859	0.974
	BD-Cycle	0.585	0.997	0.863	0.857	0.970	0.519	0.996	0.867	0.861	0.980
Halogen	Mol-Cycle	0.587	0.998	0.869	0.863	0.927	0.618	0.994	0.865	0.859	0.963
	BD-Cycle	0.576	0.998	0.873	0.867	0.960	0.534	0.994	0.870	0.864	0.975
HBD	Mol-Cycle	0.691	0.995	0.865	0.859	0.950	0.549	0.993	0.871	0.866	0.975
	BD-Cycle	0.699	0.997	0.863	0.857	0.956	0.554	0.997	0.874	0.868	0.986
HBA_Discete	Mol-Cycle	0.636	0.988	0.865	0.859	0.905	0.519	0.999	0.882	0.874	0.943
	BD-Cycle	0.611	0.996	0.868	0.862	0.956	0.454	0.999	0.887	0.879	0.965
HBA_Continuous	Mol-Cycle	0.533	0.997	0.880	0.873	0.939	0.647	0.997	0.863	0.857	0.940
	BD-Cycle	0.589	0.998	0.882	0.874	0.953	0.649	0.997	0.866	0.858	0.952

Mol-Cycle is the abbreviation for Mol-CycleGAN, BD-Cycle is the abbreviation for BD-CycleGAN.

2.4. Structure and Property Analysis

To evaluate the quality of the molecular generation models, one of the most important tasks is to evaluate the similarity of molecular generation. Selecting the appropriate similarity index is of great significance for evaluating the quality of the model and optimizing the generated molecules. In this paper, the similarity between the molecules generated by the BD-CycleGAN model and the molecules of the original dataset was evaluated by visualizing the Tanimoto similarity, visualizing the molecules, and the four indicators FCD, SNN, Scaff, and Frag in the MOSES platform.

As shown in Figures 6 and 7, we performed Tanimoto similarity analysis on datasets containing different functional group distributions. We can intuitively see that the BD-CycleGAN model has slightly lower similarity in the distribution of aromatic rings, aliphatic rings, and halogen than the Mol-CycleGAN model. HBD and HBA_Continuous distributions show an improved similarity. The embedded BiLSTM and attention make the model pay more attention to local structures and specific features while pursuing generative diversity and novelty. Meanwhile, some features with similar overall structures may be ignored. This makes the overall similarity of molecules generated by the BD-CycleGAN model slightly reduced. However, the HBA and HBD features in a molecule are often related to the local structure of the molecule, so the BD-CycleGAN model can generate HBA and HBD features that are more accurate and closer to the original molecule, thereby improving their similarity. Such improvements have implications for studying molecular similarity and drug design from a biological perspective.

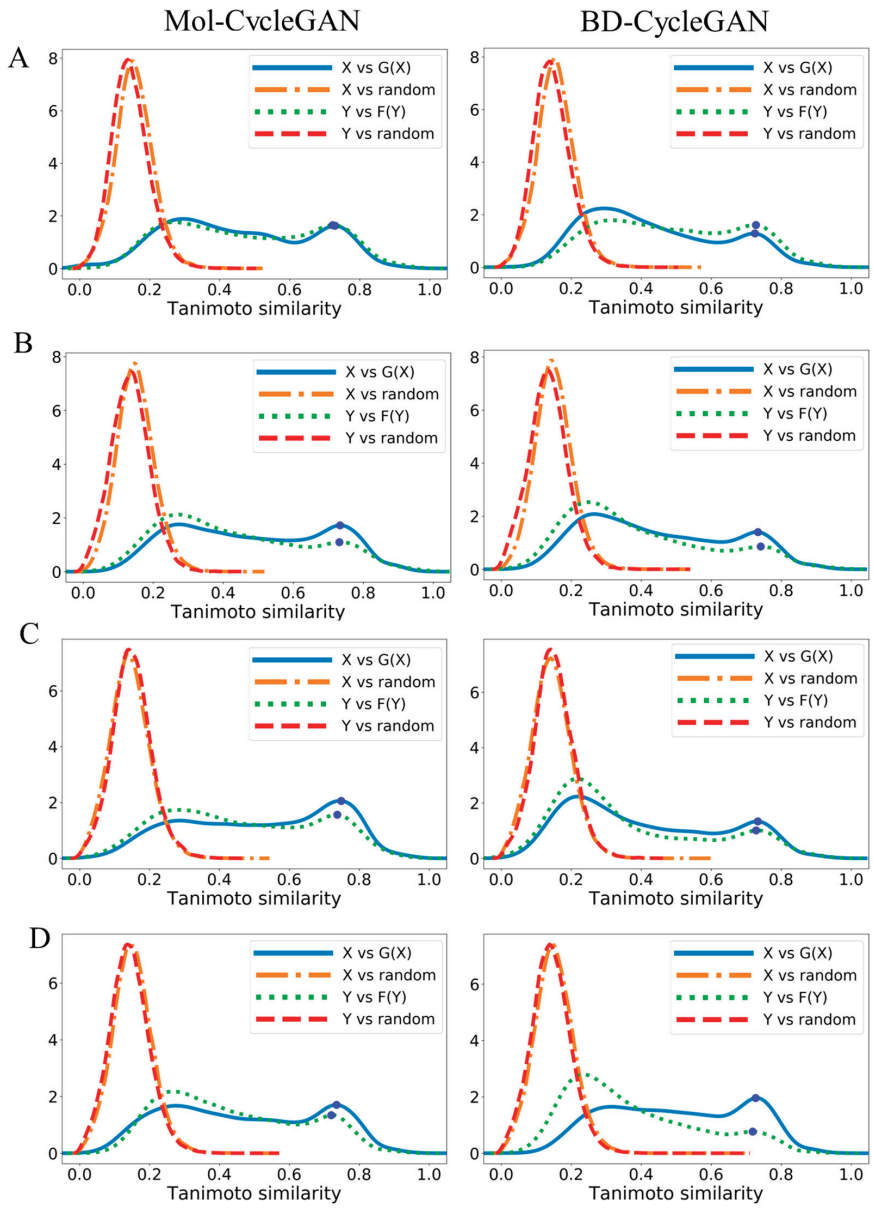

Figure 6. Density map of Tanimoto similarity. (**A**) Aromatic rings, (**B**) aliphatic rings, (**C**) halogen, and (**D**) HBD. X and Y are the original molecules and G(X) and F(Y) are the generated molecules. "random" refers to the molecules that were randomly selected from the ZINC-250K dataset. Blue dots represent the location of distribution peaks.

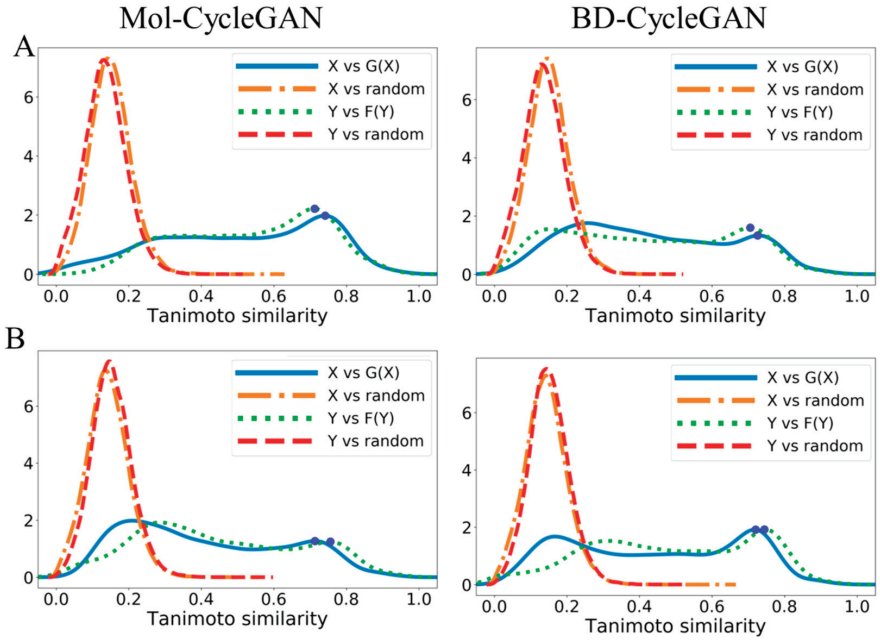

Figure 7. Density map of Tanimoto similarity. (**A**) HBA_Discrete and (**B**) HBA_Continuous. X and Y are the original molecules and G(X) and F(Y) are the generated molecules. "random" refers to the molecules that were randomly selected from the ZINC-250K dataset. Blue dots represent the location of distribution peaks.

Tables 3 and 4 show the four evaluation metrics, FCD, SNN, Frag, and Scaff, used to evaluate the similarity of the generated molecules. The test set is divided from the ZINC-250K dataset and TestSF is from the test_scaffold of MOSES. As shown in Table 3, the generated molecules with hydrogen bonds performed significantly better. Because the formation of hydrogen bonds (both HBA and HBD) usually involves specific interactions between atoms, BD-CycleGAN is better at modeling the sequences, so the similarity between HBA and HBD is higher. The similarity between aromatic and aliphatic rings, on the other hand, may be more dependent on the structure of the ring and the type of bond, and thus the similarity is relatively poor.

Table 3. The evaluation of generated molecules in terms of structural similarity and novel molecular fragment similarity in the process from X to G(X).

X—>F(X)		FCD		SNN		Scaff		Frag	
Data	**Model**	**Test**	**TestSF**	**Test**	**TestSF**	**Test**	**TestSF**	**Test**	**TestSF**
Aromatic Rings	Mol-CycleGAN	0.627	4.487	0.609	0.467	0.901	0.143	0.998	0.909
	BD-CycleGAN	0.831	4.460	0.578	0.466	0.887	0.149	0.997	0.989
Aliphatic Rings	Mol-CycleGAN	0.278	5.971	0.669	0.466	0.922	0.125	0.999	0.990
	BD-CycleGAN	0.464	6.275	0.603	0.456	0.895	0.098	0.999	0.990
Halogen	Mol-CycleGAN	0.082	5.397	0.825	0.480	0.942	0.200	0.999	0.987
	BD-CycleGAN	0.591	5.700	0.640	0.448	0.847	0.170	0.997	0.986
HBD	Mol-CycleGAN	0.419	4.08	0.653	0.476	0.907	0.138	0.998	0.993
	BD-CycleGAN	0.368	4.126	0.637	0.476	0.904	0.143	0.999	0.993
HBA_Discrete	Mol-CycleGAN	0.160	4.016	0.882	0.498	0.901	0.143	0.999	0.993
	BD-CycleGAN	0.864	4.833	0.596	0.461	0.717	0.145	0.998	0.991
HBA_Continuous	Mol-CycleGAN	0.212	6.288	0.734	0.450	0.957	0.196	0.997	0.968
	BD-CycleGAN	0.562	5.944	0.692	0.450	0.883	0.191	0.997	0.982

Table 4. The evaluation of generated molecules in terms of structural similarity and novel molecular fragment similarity in the process from Y to F(Y).

Y—>F(Y)		FCD		SNN		Scaff		Frag	
Data	**Model**	**Test**	**TestSF**	**Test**	**Test**	**Test**	**TestSF**	**Test**	**TestSF**
Aromatic Rings	Mol-CycleGAN	0.135	4.741	0.727	0.469	0.908	0.104	0.999	0.990
	BD-CycleGAN	0.175	4.915	0.675	0.465	0.887	0.101	0.999	0.991
Aliphatic Rings	Mol-CycleGAN	0.494	10.810	0.607	0.438	0.433	0.011	0.998	0.971
	BD-CycleGAN	0.633	10.403	0.538	0.428	0.371	0.018	0.997	0.974
Halogen	Mol-CycleGAN	0.558	5.778	0.638	0.462	0.841	0.135	0.998	0.984
	BD-CycleGAN	2.153	7.560	0.551	0.433	0.605	0.148	0.982	0.975
HBD	Mol-CycleGAN	0.358	5.553	0.594	0.447	0.904	0.204	0.997	0.988
	BD-CycleGAN	0.758	6.229	0.513	0.429	0.840	0.172	0.994	0.986
HBA_Discrete	Mol-CycleGAN	0.034	8.755	0.862	0.452	0.982	0.179	0.999	0.941
	BD-CycleGAN	0.470	10.012	0.674	0.422	0.927	0.182	0.977	0.880
HBA_Continuous	Mol-CycleGAN	0.272	4.975	0.755	0.483	0.824	0.106	0.999	0.994
	BD-CycleGAN	0.543	4.721	0.673	0.476	0.666	0.109	0.999	0.993

We examined the generated molecule structures with the highest Tanimoto similarity in six different data distributions generated by the BD-CycleGAN model and Mol-CycleGAN model. It can be observed from Figure 8 that the similarity between X and G(X) of the BD-CycleGAN model and the MolCycleGAN model is generally higher than the similarity between Y and F(Y). The similarity between X and G(X) of the BD-CycleGAN model is higher in the aromatic ring adjustment, while the similarity between Y and F(Y) of the BD-CycleGAN model is higher in the aliphatic ring adjustment. The model may fit in some specific tasks, indicating that a possible modification of BD-CycleGAN is to tune two generators in future work. As shown in Figures S4 and S5, HBA_Continuous obtained the highest similarity score, and the similarity was significantly improved.

The molecules generated by the BD-CycleGAN model and Mol-CycleGAN model were evaluated according to their structural properties by using the four molecular property indicators: logP, SA, QED, and weight as suggested by MOSES (Figures 9, S7 and S8). The logP metric shows similar distribution for both BD-CycleGAN and Mol-CycleGAN. SA reveals the difficulty of drug synthesis, and it is evident from Figure 9 that aliphatic rings, halogen, and discrete distributed HBA are relatively difficult to synthesize, with halogen being the most difficult. The remaining groups of compounds were less difficult to synthesize. BD-CycleGAN can reduce the synthesizability difficulty for aromatic rings, HBA_continuous, and HBD. From the QED index, it can be seen that the scores of molecules generated by the BD-CycleGAN model are generally higher, which reflects the increase in structural diversity and novelty of the generated molecules, meaning that the generated molecules are closer to drug samples and have higher drug potential and drug feasibility. From the weight index, it can be judged whether the molecules generated by the models are biased towards lighter molecules or heavier molecules. The distribution of weight does not show any obvious difference, except HBA_contiunous, suggesting that Mol-CycleGAN would tend to generate lighter molecules.

In drug design, many factors need to be optimized, such as toxicity. Therefore, we applied eToxPred [32] to compute the toxicity of the generated molecules. Both the BD-CycleGAN and Mol-CycleGAN models generated molecules with comparable levels of toxicity (Figure 9). However, to enhance the toxicity for drug development purposes, it will be necessary to reinforce the generative model by incorporating toxicity as a loss indicator. Future work needs to be conducted to facilitate the improvement of pharmacology properties.

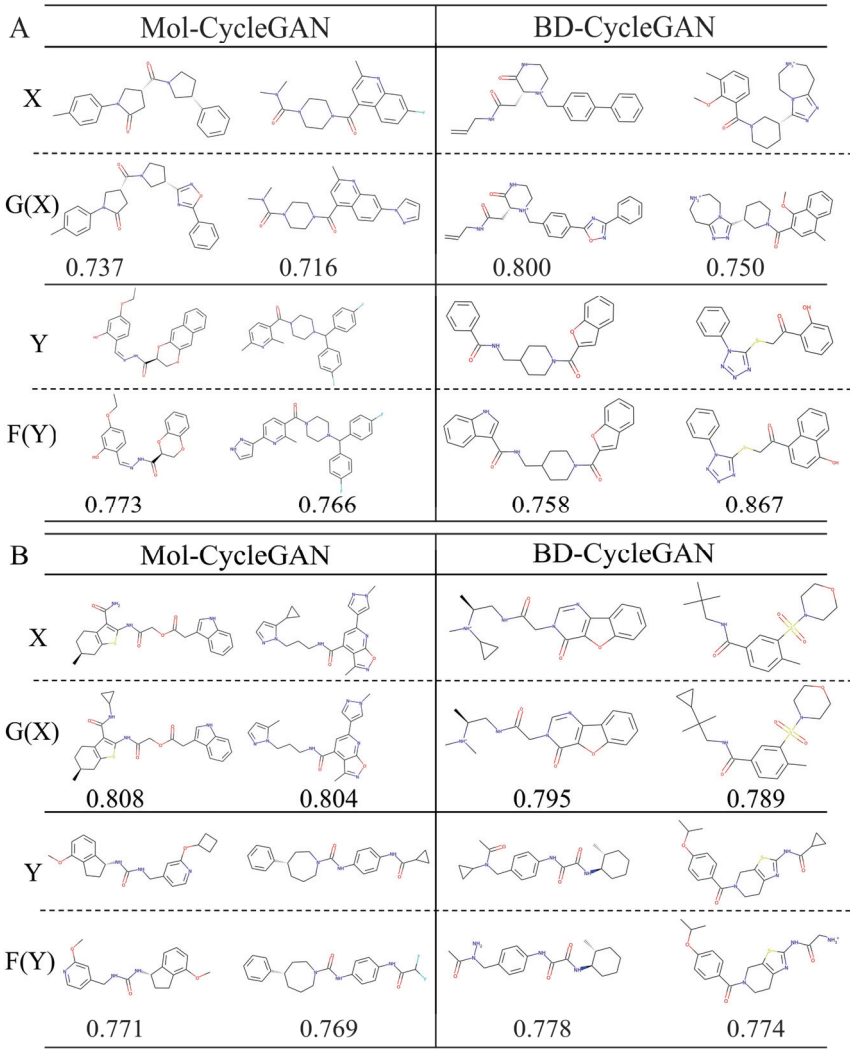

Figure 8. Structure diagram of the original and generated molecules. The molecules are generated in a cyclic manner. The model generates molecules G(X) based on input X and obtains the pharmacophore property of Y, and vice versa. X and Y are the original molecules. G(X) and F(Y) are the generated molecules. (**A**) Aromatic rings and (**B**) aliphatic rings.

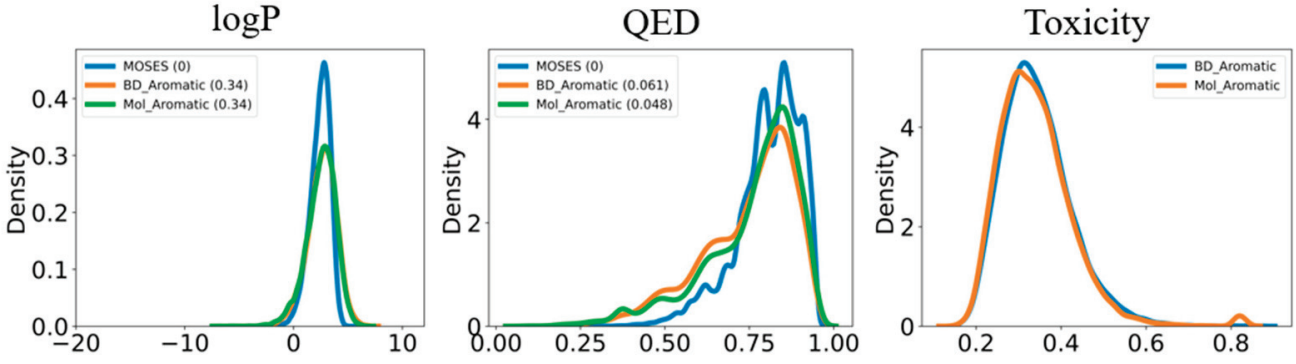

Figure 9. *Cont*.

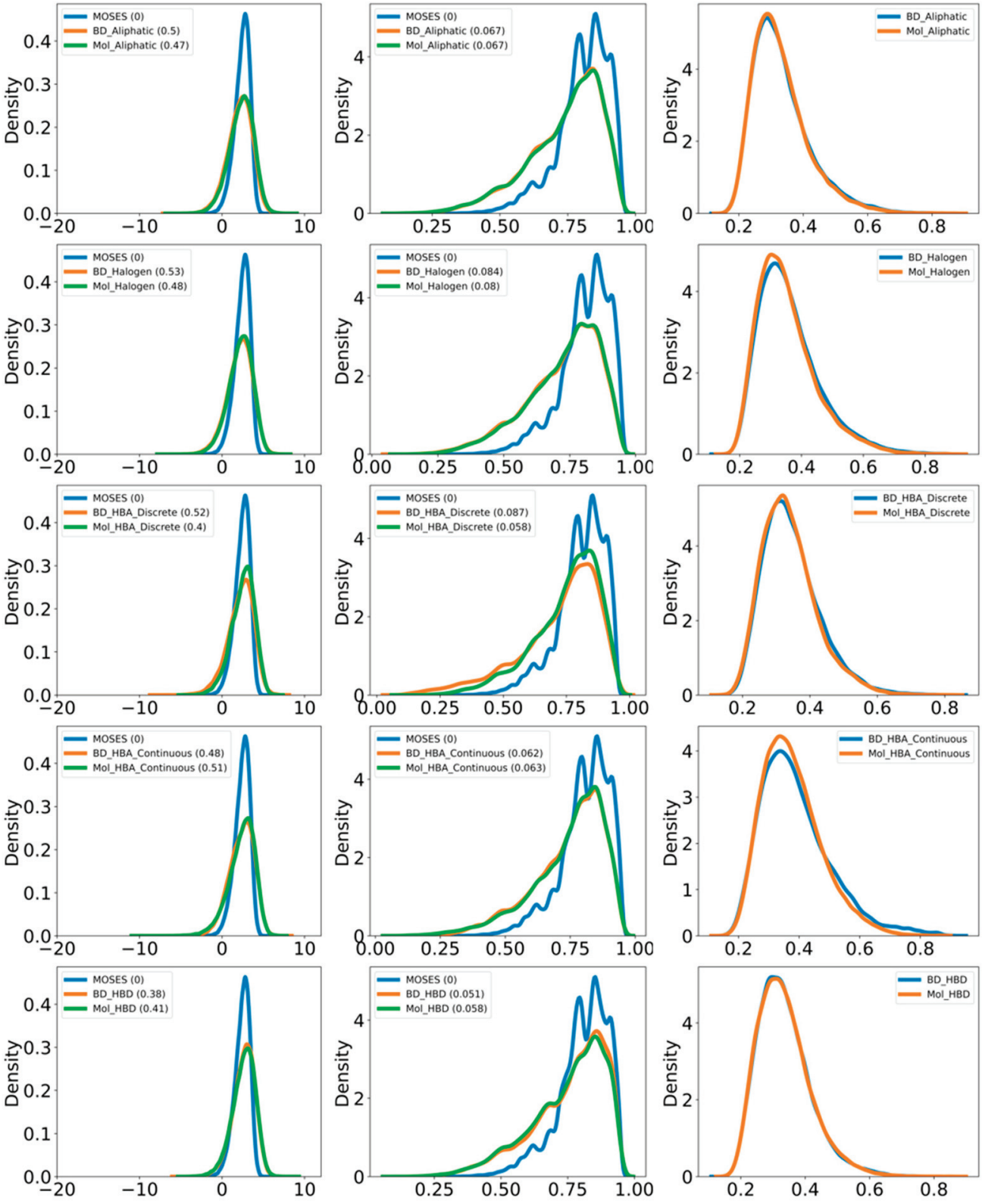

Figure 9. Property distribution of the generated molecules for Mol-CycleGAN and BD-CycleGAN. For clarity, "BD" refers to BD-CycleGAN and "Mol" refers to Mol-CycleGAN. The drug-like properties (logP, QED, and toxicity) are displayed for comparison.

2.5. Applications in Active and Decoy Generation

The advantage of BD-CycleGAN is that it inherits the advantage of CycleGAN, which can translate the source domain to the target domain. Therefore, one application of BD-CycleGAN is to perform structural transformations between two datasets; for example, transforming decoys to actives. We assess the model's generality by applying it to a molecule dataset of cyclin-dependent kinase 2 (CDK2) and the beta-site amyloid precursor protein cleaving enzyme (BACE). The BD-CycleGAN takes the active and decoy compounds as inputs and generates property-matched molecules. As shown in Figure 10, the similarity distribution between the generated molecules of the F(Y_test) and the X molecules surpasses the similarity observed between Y_test molecules and randomly generated molecules (Y_test vs. random). The results demonstrate the applicability of the model, as it is capable of generating molecules with the desired properties and that are structurally similar to the active molecules. The success of such a transformation would depend on the quality and size of the input datasets, and the specific training parameters used for the model. In future, it may be possible to use BD-CycleGAN to generate structurally diverse molecules that have the potential to be active against a given target by carefully training and optimizing the model.

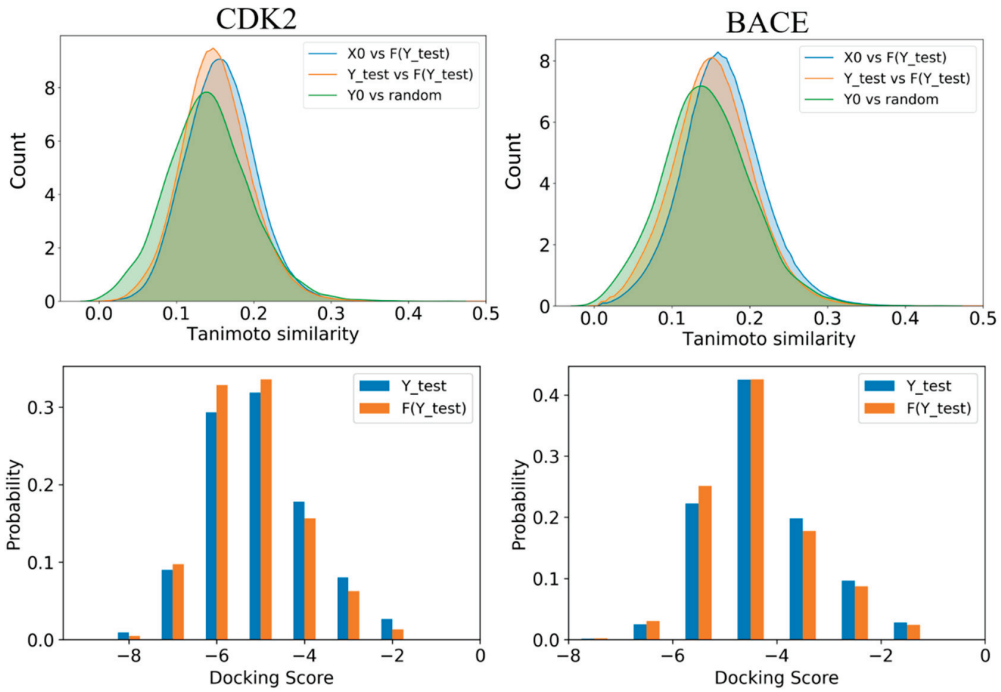

Figure 10. Molecular Tanimoto similarity and distribution of docking scoring for the original and generated molecules in the CDK2 and BACE datasets.

Our proposed model can be used in drug discovery. In this context, the input will be the known inhibitors and the random selected molecules. In the cycle generation, we anticipate that the random molecules, which may not have exhibited inhibitory properties initially, can undergo structural transformations to acquire the desired characteristics of potential inhibitors.

To illustrate the practical application of our approach, we performed molecular docking analyses on both the original molecules and the molecules generated by our model in the target of CDK2 and BACE. The original of molecules for CDK2 and BACE are from the datasets of DUD-E [33] and Enamine [34]. The results, as depicted in Figure 10, reveal a notable trend that the generated molecules (F(Y_test)) exhibit consistently higher docking scores, indicating a stronger binding affinity compared to the original molecules (Y_test). These findings suggest that our generated molecules obtain the pharmacological properties of potential inhibitors that possess favorable interactions with the target molecule of interest.

3. Discussion

We propose a molecular generative model called BD-CycleGAN, which embeds BiLSTM and residue connection in the generator and an attention mechanism in the discriminator. By introducing BiLSTM into the generator, the model deals better with the bidirectional dependencies of the sequence data while taking forward and backward contextual information into account, thereby improving the accuracy and consistency of the generated molecules. In addition, by connecting the output of the BiLSTM layer with the original input through the residual connection layer, we can include the original input information in the context features extracted by BiLSTM, preserving the local details and global semantics of the original data. Combining information from the forward and backward directions would enhance the generative ability of the generator. In the discriminator, we embedded an attention layer into the neighboring dense layer. The architecture of discriminator can enhance the feature extraction ability, focus on the key information, and improve the discrimination ability of the discriminator to distinguish between the generated samples and the real samples. Through the attention mechanism, we can determine the importance of each position more precisely and thus better judge the difference between the generated sample and the real one. In summary, the BD-CycleGAN model enables the generator and discriminator to work together more effectively, which improves the quality and accuracy of molecular generation.

Our proposed model can increase the success rate due to the inclusion of BiLSTM and an attention layer. The inclusion of BiLSTM enables the capture of bi-directional dependencies and improves the model's ability to generate diverse and accurate molecular structures. The attention layer enhances the discriminator's capability to focus on important patterns in the generated molecules, thereby improving the discrimination process. These architectural enhancements contribute to an increased success rate in generating molecules with desired structural groups. However, it is important to acknowledge the limitations of our proposed model. One notable limitation is its inability to directly optimize pharmacophore properties, such as logP (lipophilicity) and toxicity. In drug discovery, it is crucial to consider not only the structural features of molecules but also their pharmacokinetic and toxicological properties. Incorporating constraints related to properties like logP and toxicity into the molecule generation process is essential to ensuring the viability and safety of potential drug candidates. Therefore, further research is necessary to develop a framework that can generate molecules satisfying both structural requirements and specific property constraints.

4. Materials and Methods

4.1. BiLSTM for Processing of Bidirectional Molecular Representation

BiLSTM is a bidirectional long short-term memory (LSTM) neural network [35] that can be considered as two LSTMs: a forward LSTM layer and a reverse LSTM layer [36]. In Figure S5, the forward LSTM layer processes the sequence in a forward direction, while the reverse LSTM layer processes the sequence in a backward direction. In the forward LSTM layer, each time step's input consists of the current input and the hidden state from the previous time step. Conversely, in the reverse LSTM layer, the input from each time step comprises the current input and the hidden state from the subsequent time step. Consequently, the hidden states of the forward and reverse LSTMs are concatenated, yielding a comprehensive representation that serves as the output of the BiLSTM. This combined representation incorporates both forward and backward contextual information, enabling the model to effectively capture long-term dependencies within the sequence.

In molecular generation tasks, the utilization of BiLSTM enables better capturing of information within molecules. More information should facilitate the generation of more accurate and rational molecular sequences. By leveraging contextual information, BiLSTM enhances the prediction of subsequent characters or atoms, ensuring the resulting molecules exhibit sound syntactic and chemical regularity. Its implementation aids in effectively handling challenges such as the vanishing gradient problem and enables a more robust capture of long-term dependencies within the sequence.

4.2. Attention Mechanism for Focusing Molecular Information

The attention mechanism is a widely employed technique in deep learning to enhance model performance by dynamically assigning weights to different segments of input data [29–31,35–37]. In the context of chemical molecular generation tasks, the input strings often tend to be lengthy and challenging to handle. Using attention mechanism can address the bottleneck problem to utilize the most relevant information of the input [38]. In the BD-Cyc1eGAN model, the attention mechanism is incorporated into the discriminator, denoted as D, to facilitate the identification of key features within the input string. By reducing the emphasis on unnecessary information, the attention mechanism contributes to improved accuracy in classification and identification.

4.3. Residual Connection for Keeping Molecular Information

Residual connection refers to the introduction of bridge layer connections in the network, which directly transmit the original input to subsequent network layers, thereby enabling faster dissemination and retention of information. Residual connection can effectively preserve the important features and structural information of the original molecule and provide reference and assistance during the generation process. At the same time, residual connections can help alleviate the problem of vanishing or exploding gradients and improve the stability and convergence of model training.

4.4. CycleGAN for Molecular Generation in a Cycle Way

The fundamental concept of CycleGAN is to concurrently train two generators and two discriminators. Specifically, one generator is responsible for converting data from one domain to another, while the other generator facilitates the reverse conversion. The purpose of the two discriminators is to assess the authenticity of the generated data. By leveraging the structural characteristics offered by CycleGAN, it becomes possible to achieve precise feature transformations within molecules. Consequently, this capability holds promising potential for facilitating alterations in the properties and characteristics of molecules. As a result, CycleGAN exhibits promising applications in the realms of drug discovery and molecular design.

4.5. Model Selection

In molecular generation, the utilization of deep neural networks [39] can enhance the model's ability to capture information from input sequences, enabling the learning of complex molecular structures and reaction mechanisms. By incorporating BiLSTM, the model can simultaneously consider the information both preceding and following the input sequence, thereby further improving its expressive and predictive capabilities [40]. The integration of attention mechanisms assists the model in focusing on critical segments of the input sequence, leading to more accurate predictions of molecular structures and properties [41]. The combination of various models and methodologies has shown the potential in improving the similarity and success rate of molecular generation. It is important to note that these methods do not guarantee success in all scenarios. In specific applications, careful selection and adjustment of models and techniques are necessary, taking into account the characteristics of the data and tasks at hand. Ablation experiments should be conducted accordingly to achieve the desired outcomes.

Based on a comprehensive analysis of the advantages and limitations of deep neural networks, BiLSTM, attention mechanisms, and LSTM in molecular generation, four experimental groups of models were examined in this study to select the optimal molecule generation models. Figure S1 [see Supplementary Materials] illustrates the algorithm framework for these four models, which share the same discriminator but employ different generators. In the BiLSTM_Attention model, BiLSTM and the attention layer are integrated into the generator. The BiLSTM layer precedes the attention layer, allowing the data to pass through BiLSTM before the attention mechanism assigns weights. Conversely, in the Attention_BiLSTM model, the attention layer is positioned before the BiLSTM layer,

assigning weights before the data enter the BiLSTM. The LSTM_Res model incorporates an LSTM module within the generator, where the output of the LSTM layer connects to the embedding layer after passing through the dense layer. Lastly, the BiLSTM_Res model introduces a BiLSTM_block module, where the output of the BiLSTM layer is connected to the embedding layer after traversing the dense layer.

The previous model utilized connected residual layers as the generator and dense layers as the discriminator. After a systematic evaluation of the attention layer, LSTM, and BiLSTM, we introduced an additional BiLSTM layer alongside the residual connection in the generator, aiming to leverage the benefits of bidirectional LSTM for improved performance. We incorporated an attention layer between the dense layers in the discriminator. The addition of the attention layer in the discriminator helps to effectively capture important patterns in the generated molecules.

4.6. Workflow

Generation models typically use simplified molecular input line entry system (SMILES) [42,43] characters and molecular diagrams [44] to generate target molecules. However, SMILES would suffer from the problem of generating invalided molecules. Therefore, we select JT-VAE as the encoding method to ensure the generated molecules remain valid. Before model training, the SMILES are mapped to JT-VAE space.

We maintained the symmetric structure of CycleGAN in our approach. As illustrated in Figure 2, we constructed and presented two identical generators and two discriminators in a symmetrical fashion. The generator component incorporates BiLSTM as a crucial element. Initially, the potential vector obtained from the potential spatial sampling of JTVAE serves as the input for BD-CycleGAN model. The bidirectional loop architecture of BiLSTM aids in capturing contextual information about the input vectors and generating more comprehensive feature representations. Subsequently, the output of BiLSTM is dimensionally transformed through a dense layer and then fused with the original input vectors to incorporate the information from both the potential vectors and the original inputs, thereby enhancing the generator's capabilities.

The discriminator utilizes a stacked structure consisting of a dense layer and an attention mechanism layer, which is stacked a total of three times. In each stacking process, input vectors undergo feature extraction and dimension transformation through the dense layer, resulting in a set of low-dimensional feature representations. Subsequently, the attention mechanism calculates the weights for each position within this feature set, and the weighted sum of these attention weights yields the final representation of the feature set. This stacking operation is repeated three times, progressively extracting and fusing features, thereby enhancing the discriminator's sensitivity to the distinctions between the generated and the real molecules. As a result, discrimination accuracy and effectiveness are improved. The discriminator designed with this structure effectively discerns the generated molecules from the real ones, thereby enhancing the discriminative capability of the model.

4.7. Evaluation Metrics

We evaluated the model by using MOSES [45] metrics to measure the molecular structure, chemical properties, and overall similarity of the resulting molecular assemblages. The nearest neighbor similarity, fragment similarity, scaffold similarity, valley similarity, and Fréchet ChemNet Distance were calculated to evaluate the performance of the model. These indicators can help us understand how similar the generated molecule is to the target molecule, how well the chemical properties match, and how consistent the overall structure is. The evaluation indexes are provided in the Supplementary Materials. Through these evaluation indexes, we can more comprehensively evaluate the performance of the model in molecular generation tasks.

4.8. Data Set

The commonly used ZINC-250K is selected as our dataset. We select the molecules based on the functional groups. Pharmacodynamic functional groups refer to the structural units that have certain chemical properties and can affect the biological activity of molecules. The presence or absence of pharmacodynamic functional groups affects the biological activity of a molecule. Therefore, the identification and analysis of pharmacodynamic functional groups are very important in the process of drug discovery. The classification of pharmacodynamic functional groups can be carried out according to their presence, location, and number in the molecule. The classification method based on pharmacodynamic functional groups classifies molecules according to their structural characteristics, and further studies the relationship between structural characteristics and biological activities. This classification method is highly interpretable and structurally specific and can help to better understand the relationship between molecular structure and biological activity.

The pharmacodynamic category is defined by the presence or absence of these functional groups. The ZINC-250K data set was divided into training sets, validation sets, and test sets, and the number of different functional groups was selected as the basis for division. As shown in Figure S3, the ZINC-250K data set was divided into six data sets based on the number of five functional groups: aromatic ring, aliphatic ring, halogen, hydrogen bond donor (HBD), and hydrogen bond acceptor (HBA).

Aromatic Rings: Molecules with only two aromatic rings in the X dataset, while molecules with one or three aromatic rings belong in the Y dataset.

Aliphatic Rings: Molecules with only one aliphatic ring in the X dataset and two or three aliphatic rings in the Y dataset.

Halogen: Molecules in the X dataset contain no halogens (F, Cl, Br, I and CN), while molecules in the Y dataset have one, two, three, four, or five halogens.

HBD: The molecules in the X dataset contained only one hydrogen bond donor, while the molecules in the Y dataset had zero, two, three, four, or five hydrogen bond donors.

To further demonstrate the generation ability, we conduct a task by using the discrete number and the continuous number of HBA.

HBA_Discrete: The molecules in the X data set contain only five hydrogen bond acceptors, while molecules in the Y data set have zero, two, three, or four hydrogen bond acceptors.

HBA_Continuous: Molecules in the X data set have zero, one, two, three, four, or five hydrogen bond receptors, while molecules in the Y data set have 6, 7, 8, 9, or 10 hydrogen bond receptors.

Aromatic rings and aliphatic rings are used to tune the hydrophobic property in the lead optimization. HBA and HBD represent the functional group of a molecule where protons can form hydrogen bonds with other molecules, thus they play key roles in the recognition, binding, and permeation of molecules through the cell membrane. The efficiency and biological feasibility of generating molecules can be improved by changing functional groups.

Our proposed method is limited to altering the number of functional groups rather than changing the types of functional groups. This limitation is worth noting. Specifically, our approach utilizes neural network-based models to modify the quantity of functional groups in molecules. For instance, we can adjust the number of aromatic rings, aliphatic rings, halogens, hydrogen bond donors, and hydrogen bond acceptors.

4.9. Applications in Active and Decoy Generation

The proposed model can achieve cyclic molecule generation. Therefore, we assessed its application in generating active molecules from decoy compounds. We chose two popular targets for our test, these being cyclin-dependent kinase 2 (CDK2) and beta-site amyloid precursor protein cleaving enzyme (BACE). The CDK2 dataset consists of 474 actives and 27850 decoys. BACE consists of 7172 potential inhibitors from the Enamine BACE-targeted library and 7172 random selected molecules from ZINC-250K. We converted the active and decoy compounds into the JT-VAE input and generated property-matched molecules. The active molecules were labeled as X and the decoys were labeled as Y.

5. Conclusions

We proposed the BD-CycleGAN model to improve the generative ability of de novo molecule generation. The performance of our model is evaluated by generating six sets of molecules with different structural features. The results show that incorporating BiLSTM and residual connection into the generator can improve the success rate by effectively handling the bidirectional information in the sequence data. The revisions made to the generator and discriminator as part of the cycle-type GAN can further enhance the bidirectional generative ability. The experimental findings highlight two key advantages of the BD-CycleGAN model. Firstly, it exhibits improved diversity in the generated molecules, allowing for a broader exploration of chemical space. Additionally, the model achieves increased similarity between the source molecules and the generated molecules, which is required for the lead optimization process in drug design. Overall, our BD-CycleGAN model achieves better performance in terms of molecular generation, which provides a promising tool for the molecular design and discovery.

Supplementary Materials: The following supporting information can be downloaded at: https://www.mdpi.com/article/10.3390/molecules29071499/s1, Figure S1: Schematic diagram of the four combined models.; Figures S2 and S3: molecular distribution; Figures S4 and S5: structure of generated molecules; Figure S6: schematic figure of BiLSTM; Figure S7: Synthetic Accessibility (SA) distribution of generated molecules; Figure S8: Molecular weight distribution of generated molecules.

Author Contributions: L.X. (Liangxu Xie) and X.X. designed the work. C.Z. conducted the experiments. L.X. (Liangxu Xie) and C.Z. developed the algorithm. X.L. and R.M. conduct parts of analysis. L.X. (Lei Xu) and X.X. supervised the work. All authors reviewed the manuscript. All authors have read and agreed to the published version of the manuscript.

Funding: This work was supported by the National Natural Science Foundation of China under Grant Nos. 22003020 to L.Xie and 12074151 to X.X.; the Natural Science Foundation of Jiangsu Province (Grant No. BK20191032), the Changzhou Sci. & Tech. Program (Grant No. CJ20200045) to L.Xie; and the Postgraduate Research & Practice Innovation Program of Jiangsu Province (Grant No. SJCX22_1480) to RM. The funders had no role in the design of the study, in the collection, analysis, or interpretation of the data, or in the preparation of the manuscript.

Institutional Review Board Statement: Not applicable.

Informed Consent Statement: Not applicable.

Data Availability Statement: The dataset supporting the conclusions of this article is available in the ZINK250K repository, hyperlink to dataset(s): https://www.kaggle.com/datasets/basu369victor/zinc250k (accessed on 6 December 2021. The scripts of this article is available in the GitHub repository, in https://github.com/AIMedDrug/BD-CycleGAN (accessed on 15 September 2023).

Acknowledgments: We thank Xiaochen Feng for the valuable discussion. CZ acknowledges the comments and assistance from Zuode Yin and Baiyi Li.

Conflicts of Interest: The authors declare no conflicts of interest.

References

1. Walters, W.P.; Barzilay, R. Applications of Deep Learning in Molecule Generation and Molecular Property Prediction. *Acc. Chem. Res.* **2021**, *54*, 263–270. [CrossRef] [PubMed]
2. Elton, D.C.; Boukouvalas, Z.; Fuge, M.D.; Chung, P.W. Deep learning for molecular design—A review of the state of the art. *Mol. Syst. Des. Eng.* **2019**, *4*, 828–849. [CrossRef]
3. McNair, D. Artificial Intelligence and Machine Learning for Lead-to-Candidate Decision-Making and Beyond. *Annu. Rev. Pharmacol. Toxicol.* **2023**, *63*, 77–97. [CrossRef]
4. Paul, D.; Sanap, G.; Shenoy, S.; Kalyane, D.; Kalia, K.; Tekade, R.K. Artificial intelligence in drug discovery and development. *Drug Discov. Today* **2021**, *26*, 80. [CrossRef] [PubMed]
5. Zhavoronkov, A.; Vanhaelen, Q.; Oprea, T.I. Will artificial intelligence for drug discovery impact clinical pharmacology? *Clin. Pharmacol. Ther.* **2020**, *107*, 780–785. [CrossRef] [PubMed]
6. Urbina, F.; Lentzos, F.; Invernizzi, C.; Ekins, S. Dual use of artificial-intelligence-powered drug discovery. *Nat. Mach. Intell.* **2022**, *4*, 189–191. [CrossRef] [PubMed]

7. Yu, W.; MacKerell, A.D., Jr. Computer-Aided Drug Design Methods. *Methods Mol. Biol.* **2017**, *1520*, 85–106. [CrossRef] [PubMed]
8. Zhong, F.; Xing, J.; Li, X.; Liu, X.; Fu, Z.; Xiong, Z.; Lu, D.; Wu, X.; Zhao, J.; Tan, X. Artificial intelligence in drug design. *Sci. China Life Sci.* **2018**, *61*, 1191–1204. [CrossRef] [PubMed]
9. Deng, J.; Yang, Z.; Ojima, I.; Samaras, D.; Wang, F. Artificial intelligence in drug discovery: Applications and techniques. *Brief. Bioinform.* **2022**, *23*, bbab430. [CrossRef] [PubMed]
10. Delijewski, M.; Haneczok, J. AI drug discovery screening for COVID-19 reveals zafirlukast as a repurposing candidate. *Med. Drug Discov.* **2021**, *9*, 100077. [CrossRef]
11. Mokaya, M.; Imrie, F.; van Hoorn, W.P.; Kalisz, A.; Bradley, A.R.; Deane, C.M. Testing the limits of SMILES-based de novo molecular generation with curriculum and deep reinforcement learning. *Nat. Mach. Intell.* **2023**, *5*, 386–394. [CrossRef]
12. Arnold, C. Inside the nascent industry of AI-designed drugs. *Nat. Med.* **2023**, *29*, 1292–1295. [CrossRef] [PubMed]
13. Mamoshina, P.; Vieira, A.; Putin, E.; Zhavoronkov, A. Applications of Deep Learning in Biomedicine. *Mol. Pharm.* **2016**, *13*, 1445–1454. [CrossRef]
14. Lavecchia, A. Deep learning in drug discovery: Opportunities, challenges and future prospects. *Drug Discov. Today* **2019**, *24*, 2017–2032. [CrossRef] [PubMed]
15. Askr, H.; Elgeldawi, E.; Aboul Ella, H.; Elshaier, Y.A.M.M.; Gomaa, M.M.; Hassanien, A.E. Deep learning in drug discovery: An integrative review and future challenges. *Artif. Intell. Rev.* **2023**, *56*, 5975–6037. [CrossRef] [PubMed]
16. Rifaioglu, A.S.; Atas, H.; Martin, M.J.; Cetin-Atalay, R.; Atalay, V.; Doğan, T. Recent applications of deep learning and machine intelligence on in silico drug discovery: Methods, tools and databases. *Brief. Bioinform.* **2019**, *20*, 1878–1912. [CrossRef] [PubMed]
17. Özçelik, R.; van Tilborg, D.; Jiménez-Luna, J.; Grisoni, F. Structure-Based Drug Discovery with Deep Learning. *ChemBioChem* **2023**, *24*, e202200776. [CrossRef] [PubMed]
18. Das, P.; Sercu, T.; Wadhawan, K.; Padhi, I.; Gehrmann, S.; Cipcigan, F.; Chenthamarakshan, V.; Strobelt, H.; dos Santos, C.; Chen, P.-Y.; et al. Accelerated antimicrobial discovery via deep generative models and molecular dynamics simulations. *Nat. Biomed. Eng.* **2021**, *5*, 613–623. [CrossRef] [PubMed]
19. Gao, W.; Coley, C.W. The Synthesizability of Molecules Proposed by Generative Models. *J. Chem. Inf. Model.* **2020**, *60*, 5714–5723. [CrossRef] [PubMed]
20. Pham, T.-H.; Xie, L.; Zhang, P. FAME: Fragment-based Conditional Molecular Generation for Phenotypic Drug Discovery. In Proceedings of the 2022 SIAM International Conference on Data Mining (SDM), Virtually, 28–30 April 2022; pp. 720–728.
21. Wang, X.; Gao, C.; Han, P.; Li, X.; Chen, W.; Rodríguez Patón, A.; Wang, S.; Zheng, P. PETrans: De Novo Drug Design with Protein-Specific Encoding Based on Transfer Learning. *Int. J. Mol. Sci.* **2023**, *24*, 1146. [CrossRef] [PubMed]
22. Creswell, A.; White, T.; Dumoulin, V.; Arulkumaran, K.; Sengupta, B.; Bharath, A.A. Generative adversarial networks: An overview. *IEEE Signal Process. Mag.* **2018**, *35*, 53–65. [CrossRef]
23. Metz, L.; Poole, B.; Pfau, D.; Sohl-Dickstein, J. Unrolled generative adversarial networks. *arXiv* **2016**, arXiv:1611.02163.
24. Guimaraes, G.L.; Sanchez-Lengeling, B.; Outeiral, C.; Farias, P.L.C.; Aspuru-Guzik, A. Objective-reinforced generative adversarial networks (organ) for sequence generation models. *arXiv* **2017**, arXiv:1705.10843.
25. Prykhodko, O.; Johansson, S.V.; Kotsias, P.-C.; Arús-Pous, J.; Bjerrum, E.J.; Engkvist, O.; Chen, H. A de novo molecular generation method using latent vector based generative adversarial network. *J. Cheminformatics* **2019**, *11*, 74. [CrossRef] [PubMed]
26. Zhu, J.-Y.; Park, T.; Isola, P.; Efros, A.A. Unpaired image-to-image translation using cycle-consistent adversarial networks. In Proceedings of the IEEE International Conference on Computer Vision, Venice, Italy, 22–29 October 2017; pp. 2223–2232.
27. Maziarka, Ł.; Pocha, A.; Kaczmarczyk, J.; Rataj, K.; Danel, T.; Warchoł, M. Mol-CycleGAN: A generative model for molecular optimization. *J. Cheminformatics* **2020**, *12*, 2. [CrossRef] [PubMed]
28. Jin, W.; Barzilay, R.; Jaakkola, T. Junction tree variational autoencoder for molecular graph generation. *Artif. Intell. Drug Discov.* **2020**, *75*, 228.
29. Wang, F.; Feng, X.; Guo, X.; Xu, L.; Xie, L.; Chang, S. Improving de novo Molecule Generation by Embedding LSTM and Attention Mechanism in CycleGAN. *Front. Genet.* **2021**, *12*, 709500. [CrossRef] [PubMed]
30. Yulita, I.N.; Fanany, M.I.; Arymuthy, A.M. Bi-directional Long Short-Term Memory using Quantized data of Deep Belief Networks for Sleep Stage Classification. *Procedia Comput. Sci.* **2017**, *116*, 530–538. [CrossRef]
31. Niu, Z.; Zhong, G.; Yu, H. A review on the attention mechanism of deep learning. *Neurocomputing* **2021**, *452*, 48–62. [CrossRef]
32. Pu, L.; Naderi, M.; Liu, T.; Wu, H.C.; Mukhopadhyay, S.; Brylinski, M. eToxPred: A machine learning-based approach to estimate the toxicity of drug candidates. *BMC Pharmacol. Toxicol.* **2019**, *20*, 2. [CrossRef]
33. Mysinger, M.M.; Carchia, M.; Irwin, J.J.; Shoichet, B.K. Directory of useful decoys, enhanced (DUD-E): Better ligands and decoys for better benchmarking. *J. Med. Chem.* **2012**, *55*, 6582–6594. [CrossRef] [PubMed]
34. Enamine. Targeted Libraries-Enamine. Available online: https://enamine.net/compound-libraries/targeted-libraries (accessed on 8 May 2023).
35. Graves, A. (Ed.) Long short-term memory. In *Supervised Sequence Labelling with Recurrent Neural Networks*; Springer: Berlin/Heidelberg, Germany, 2012; Volume 385, pp. 37–45.
36. Wang, S.; Wang, X.; Wang, S.; Wang, D. Bi-directional long short-term memory method based on attention mechanism and rolling update for short-term load forecasting. *Int. J. Electr. Power Energy Syst.* **2019**, *109*, 470–479. [CrossRef]
37. Guo, M.-H.; Xu, T.-X.; Liu, J.-J.; Liu, Z.-N.; Jiang, P.-T.; Mu, T.-J.; Zhang, S.-H.; Martin, R.R.; Cheng, M.-M.; Hu, S.-M. Attention mechanisms in computer vision: A survey. *Comput. Vis. Media* **2022**, *8*, 331–368. [CrossRef]

38. Zheng, S.; Yan, X.; Yang, Y.; Xu, J. Identifying structure–property relationships through SMILES syntax analysis with self-attention mechanism. *J. Chem. Inf. Model.* **2019**, *59*, 914–923. [CrossRef] [PubMed]
39. Rolnick, D.; Tegmark, M. The power of deeper networks for expressing natural functions. *arXiv* **2017**, arXiv:1705.05502.
40. Lin, X.; Quan, Z.; Wang, Z.-J.; Huang, H.; Zeng, X. A novel molecular representation with BiGRU neural networks for learning atom. *Brief. Bioinform.* **2020**, *21*, 2099–2111. [CrossRef] [PubMed]
41. Xiong, Z.; Wang, D.; Liu, X.; Zhong, F.; Wan, X.; Li, X.; Li, Z.; Luo, X.; Chen, K.; Jiang, H. Pushing the boundaries of molecular representation for drug discovery with the graph attention mechanism. *J. Med. Chem.* **2019**, *63*, 8749–8760. [CrossRef]
42. Winter, R.; Montanari, F.; Steffen, A.; Briem, H.; Noé, F.; Clevert, D.-A. Efficient multi-objective molecular optimization in a continuous latent space. *Chem. Sci.* **2019**, *10*, 8016–8024. [CrossRef] [PubMed]
43. Kim, K.; Kang, S.; Yoo, J.; Kwon, Y.; Nam, Y.; Lee, D.; Kim, I.; Choi, Y.-S.; Jung, Y.; Kim, S. Deep-learning-based inverse design model for intelligent discovery of organic molecules. *Comput. Mater.* **2018**, *4*, 67. [CrossRef]
44. Li, Y.; Zhang, L.; Liu, Z. Multi-objective de novo drug design with conditional graph generative model. *J. Cheminform.* **2018**, *10*, 33. [CrossRef] [PubMed]
45. Polykovskiy, D.; Zhebrak, A.; Sanchez-Lengeling, B.; Golovanov, S.; Tatanov, O.; Belyaev, S.; Kurbanov, R.; Artamonov, A.; Aladinskiy, V.; Veselov, M. Molecular sets (MOSES): A benchmarking platform for molecular generation models. *Front. Pharmacol.* **2020**, *11*, 565644. [CrossRef]

MDPI AG
Grosspeteranlage 5
4052 Basel
Switzerland
Tel.: +41 61 683 77 34

Molecules Editorial Office
E-mail: molecules@mdpi.com
www.mdpi.com/journal/molecules

Academic Open
Access Publishing

mdpi.com

ISBN 978-3-7258-6399-0